

# Sheffield Hallam University

*Optimisation of the antimicrobial peptide Smp24 and its derivatives*

BERTELSEN, Magnus Gammelgaard

Available from the Sheffield Hallam University Research Archive (SHURA) at:

<http://shura.shu.ac.uk/32083/>

## A Sheffield Hallam University thesis

This thesis is protected by copyright which belongs to the author.

The content must not be changed in any way or sold commercially in any format or medium without the formal permission of the author.

When referring to this work, full bibliographic details including the author, title, awarding institution and date of the thesis must be given.

Please visit <http://shura.shu.ac.uk/32083/> and <http://shura.shu.ac.uk/information.html> for further details about copyright and re-use permissions.

# Optimisation of the antimicrobial peptide Smp24 and its derivatives

**Magnus Gammelgaard Bertelsen**

A thesis submitted in partial fulfilment of the requirements of  
Sheffield Hallam University  
for the degree of Doctor of Philosophy

March 2023

## Candidate Declaration

I hereby declare that:

- 1) I have not been enrolled for another award of the University, or other academic or professional organisation, whilst undertaking my research degree.
- 2) None of the material contained in the thesis has been used in any other submission for an academic award.
- 3) I am aware of and understand the University's policy on plagiarism and certify that this thesis is my own work. The use of all published or other sources of material consulted have been properly and fully acknowledged.
- 4) The work undertaken towards the thesis has been conducted in accordance with the SHU Principles of Integrity in Research and the SHU Research Ethics Policy.
- 5) The word count of the thesis is 78,512.

Name	Magnus Gammelgaard Bertelsen
Date	March 2023
Award	PhD
Research Institute	Industry and Innovation Research Institute
Director of studies	Dr. Keith Miller

## Abstract

The global increase in antimicrobial resistance development has created a critical need for the development of novel antimicrobial agents. Antimicrobial peptides (AMPs) are one such class of novel antimicrobials, but they have several disadvantages such as high manufacturing cost and low selectivity that must be addressed before they can achieve clinical use. In this study the relatively large size and high cytotoxic activity of the natural, venom derived AMP Smp24 were addressed using several different approaches.

A formulation approach was investigated by incorporation of the peptide into sol-gel coatings in order to inhibit or prevent the growth of bacterial biofilms, showing that the unique physiochemical properties of the peptide can be utilized to improve and control the properties of the coating.

Furthermore, a drug design approach was also used, based on several stages. Firstly, an investigation of the peptide structure was done creating a regional breakdown of the 3D structure and mechanism of action of the early stages of the pore formation using planar patch clamp electrophysiology. A bridge was built between the structure and mechanism via the use of molecular dynamics simulations of the peptide-bilayer interactions in order to establish a structure mechanism relationship. Based on this relationship several truncated variants of the parent peptide were designed and evaluated, first *in silico* showing that the simulations can give direct feedback during the design process and *in vitro* showing that two of the truncated analogs had both smaller size, improved antimicrobial properties and reduced cytotoxic properties compared to the parent peptide. The best analogs were further developed via amino acids substitutions in two iterations, with a total of 19 analogs evaluated *in silico* with 11 of those also being evaluated *in vitro*. Again, multiple analogs were produced with improved antimicrobial activity and selectivity.

Overall, additional insight into the structure and biophysical behaviour of Smp24 was gained and utilized to guide the design of new analogs with significantly smaller size and improved selectivity without loss of antimicrobial activity relative to the parent peptide.

# Table of Contents

Candidate Declaration.....	2
Abstract .....	3
Table of Contents .....	4
1. General introduction .....	8
1.1 Antimicrobial peptides .....	9
1.2 Mechanism of action of AMPs .....	10
1.3 Antimicrobial coatings.....	12
1.4 Sol-gel coatings.....	15
1.5 Patch clamp analysis of antimicrobial peptides .....	18
1.5.1 Live cells .....	18
1.5.2 Synthetic bilayers.....	19
1.6 Molecular dynamics simulations.....	23
1.7 Molecular dynamics simulations of antimicrobial peptides .....	26
1.8 Aims and objectives.....	27
2. Materials and methods .....	29
2.1 Materials.....	29
2.2 Production of sol-gel coating.....	29
2.3 Evaluation of antimicrobial coatings .....	29
2.3.1 Brightfield (BF) microscopy characterisation of coating structures .....	29
2.3.2 Matrix-assisted laser desorption/ionization (MALDI) mass spectrometry imaging (MSI) .....	30
2.3.3 Peptide elution from the sol-gel coating.....	30
2.3.4 Coating mediated biofilm inhibition.....	31
2.4 <i>In vitro</i> biophysical evaluation of AMPs: .....	31
2.4.1 Electro formation of GUVs.....	31
2.4.2 Patch clamp.....	32
2.5 <i>In vitro</i> biological evaluation of AMPs.....	33
2.5.1 Minimum inhibitory concentration (MIC) .....	33
2.5.2 Peptide only biofilm inhibition assay.....	33
2.5.3 Haemolysis assay .....	34
2.5.4 Cell culture .....	34
2.5.5 Cell line toxicity.....	34
2.6 <i>In silico</i> evaluation of AMPs: .....	35
2.6.1 Molecular dynamics simulations .....	35

2.6.2	<i>Ab initio</i> structure generation .....	35
2.6.3	Peptide water model .....	35
2.6.4	Peptide TFE/water mixture model .....	36
2.6.5	Bilayer models .....	36
2.7	MD simulation analysis methods .....	40
2.7.1	3D structure visualisation .....	40
2.7.2	Evaluation of peptide structure .....	40
2.7.3	Analysis of the position and orientation of the peptide relative to the bilayer .....	43
2.7.4	Energy calculations .....	48
3.	Development of a sol-gel coating as a drug delivery system for Smp24 .....	50
3.1	Introduction .....	50
3.2	Results .....	51
3.2.1	Method development .....	51
3.2.2	Formulation overview .....	55
3.2.3	Evaluation of sol-gel only coating morphology .....	56
3.2.4	MALDI-TOF profiling of the sol-gel Smp24 system .....	60
3.2.5	Evaluation of peptide distribution and integration into the sol-gel .....	64
3.2.6	Evaluation of peptide elution from the sol-gel coatings .....	68
3.2.7	Evaluation of the biofilm inhibitory properties of the coatings .....	70
3.3	Discussion .....	72
3.3.1	Evaluation of the peptide distribution using MALDI MSI .....	72
3.3.2	Peptide-matrix interactions and microscopic structure of sol-gel coatings .....	76
3.3.3	Effect of the peptide concentration on the coating behaviour .....	79
3.3.4	Optimal formulation parameters for the antimicrobial coating .....	80
3.4	Conclusions .....	81
4.	Investigation of the structure and mechanism of action of Smp24 .....	82
4.1	Introduction .....	82
4.2	Results and discussion .....	82
4.2.1	Structure of Smp24 .....	82
4.2.2	More accurate <i>In silico</i> modelling of the solution behaviour of Smp24 .....	85
4.2.3	Solution structure of Smp24 .....	87
4.2.4	Mechanism of action of Smp24 .....	94
4.2.5	Investigation of Smp24 induced pore formation using planar patch clamp electrophysiology .....	98

4.2.6 Kinetics of membrane disruption .....	101
4.2.7 Qualitative analysis of conductance events .....	103
4.3 Conclusions.....	109
5. Structure mechanism relationship of Smp24 .....	110
5.1 Introduction.....	110
5.2 Results and discussion .....	110
5.2.1 Design of MD simulations.....	110
5.2.2 Initial interactions and insertion of the peptide into the bilayer .....	115
5.2.3 Mechanism of insertion.....	119
5.2.4 Evaluation of the system equilibrium.....	124
5.2.5 Influence of membrane composition on insertion, structure and selectivity .....	134
5.2.6 Concentration dependent effects on the bilayer biophysical properties ....	142
5.2.7 Modelling of pore associated configurations of Smp24.....	145
5.2.8 Use of MD simulations to investigate the mechanism of action of AMPs ...	156
5.3 Conclusions.....	157
6. Rational design of truncated Smp24 variants.....	159
6.1 Introduction.....	159
6.2 Results and discussion .....	163
6.2.1 Selection of truncation targets .....	163
6.2.2 Truncation design .....	166
6.2.3 In silico modelling .....	168
6.2.4 Antimicrobial and cytotoxic properties of the truncated peptides.....	196
6.2.5 The truncations effect on the antimicrobial activity and selectivity.....	198
6.2.6 Use of MD simulation for the design of truncated AMPs .....	204
6.2.7 Evaluation of the antibiofilm properties of the truncated peptides.....	205
6.2.7 Biophysical evaluation of the pore formation.....	212
6.2.8 Effect of the truncations on the mechanisms of pore formation .....	217
6.3 Conclusions.....	223
7. Optimisation of the primary sequence of Smp14a.....	224
7.1 Introduction.....	224
7.1.1 Design of the first generation Smp14a analogs.....	224
7.1.2 In silico evaluation strategy .....	229
7.2 Results and discussion .....	229

7.2.1 In silico screening of Smp14a analogs .....	229
7.2.2 Selection of the most promising analogs .....	242
7.2.3 Biological evaluation of Smp14a analogs .....	246
7.2.4 Design of the second generation Smp14a analogs .....	255
7.2.5 In silico evaluation of the second generation smp14a analogs .....	258
7.2.6 In vitro evaluation of the second generation Smp14a analogs.....	266
7.2.7 Computer aided drug design of AMPs using MD simulations.....	271
7.3 Conclusions.....	273
8. General discussion and future perspectives.....	274
8.1 Advanced formulation of antimicrobial peptides .....	274
8.2 Structure activity relationship and structure based design of Smp24 and analogs .....	279
8.3 Improving the therapeutic index of Smp24 using drug design .....	282
8.4 Mechanism of membrane disruption and drug design.....	287
8.5 Further development of Smp24 and its analogs .....	289
References.....	292

## 1. General introduction

Antimicrobial resistance (AMR) is a natural phenomenon in which microorganisms exposed to the selective pressure of an antimicrobial agent will, over time, become more resistant to the effects of that compound. This occurs as the population of the bacteria which is susceptible to the antimicrobial agent will be killed or inhibited while those which are naturally more resistant or have acquired antibiotic-resistant traits will survive and multiply (1). The mechanisms behind such antibiotic-resistance traits can be due to a variety of adaptations of the bacteria such as production of enzymes that break down the antimicrobial compounds, mutations in the structure of the target of the compound leading to a reduced binding efficacy, adoption of new pathways that bypasses the target of the compound and the prevention of access of the antimicrobial agent to its target such as by excreting it from the cell via efflux pumps (2). The resulting effect of such resistance development is that common bacterial infections no longer can be easily treated with the traditionally used first line antimicrobial therapeutic. Instead, more expensive therapeutics with potentially greater risks of adverse effects are needed to successfully treat the infection. However, the bacteria can also eventually develop resistance to these alternative therapeutics leading to multidrug resistant bacteria species such as methicillin-resistant *Staphylococcus aureus* which is not only resistant to methicillin but usually also aminoglycosides, macrolides, tetracycline, chloramphenicol, and lincosamides (2).

In 2014 the UK prime minister commissioned a report on the topic of AMR, supported by the UK government and the Wellcome Trust. This report reviewed and analysed the rise of antimicrobial resistance globally and suggest actions that could help tackle it on an international level (3). This report estimates that by 2050, globally 10 million lives a year could be lost due to antimicrobial resistant infections if no proactive actions are taken to curb the increase of AMR. In addition, a more recent report from The Lancet estimates that globally 1.27 million deaths could be attributed to bacterial AMR resistance in 2019 (4). The UK government report concludes that the current supply of new medicines is insufficient to keep up with the rate of resistance development and therefore the crisis must be tackled with a multitude of approaches. These include improved public awareness, improved hygiene, reduction of unnecessary use of antimicrobials, improved surveillance of drug resistance, better diagnostics and further

promotion of the development of new alternatives to traditional small molecule antibiotics. One of these alternatives specifically highlighted in the report is antimicrobial peptides (AMPs) (3).

### 1.1 Antimicrobial peptides

AMPs are a diverse group of compounds which can be classified based on several different traits such as their source/origin, selectivity, structure or presence of specific residues. Naturally occurring AMPs can be found from many different sources ranging from microorganisms, non-mammalian animals such as amphibians, arachnids and insects where they can both play a role in the animal's immune defence or as a component in venoms and other secretions, and in mammals such as humans where they again play a role in the immune defence both due to their direct antimicrobial activity and due to their immune regulatory properties. AMPs can also have a relative wide range of selectivity with different peptides showing activity against Gram-positive and Gram-negative bacteria, fungi, viruses, parasites and tumour cells. Perhaps the most critical classification from a drug design point of view is based on their secondary structure. Four general categories exist including linear alpha-helical peptides, beta-sheet peptides, combined alpha-helical and beta-sheet peptides and linear extended/random coil peptides (5). However, the archetypal AMP is generally alpha-helical, with a cationic charge and has an overall amphiphilic nature with one side of the helix being rich in polar and charged residues while the other is rich in hydrophobic residues. This unique structure of these peptides allows them to interact with and insert into bacterial cell membranes, although some of these peptides do not adopt their helical structure until they start interacting with the membranes, being mainly unstructured while in solution (6).

One of the key reasons why AMPs are of interest as novel antimicrobial agents relates to their interplay with AMR. Although resistance development against AMPs can occur, often via modifications to membrane composition, resistance development is still less prevalent than that for small molecule antimicrobial agents, since the targets for AMPs are diverse and any changes to these targets can often significantly interfere with the normal function of the cell (7). Further evidence for this lower resistance development is that AMPs have existed in nature for millions of years, yet resistance occurrence is

still very limited (8). In addition, the use of AMPs in combination with conventional antibiotics can also lead to even lower rates of resistance development and synergistic antimicrobial effects (9).

While AMPs are a promising class of antimicrobial drug candidates, they still present several challenges that need to be overcome with further drug development.

Instability of the formulated peptides, limited selectivity leading to local or systemic toxicity, adverse inflammatory effects, high manufacturing costs and non-ideal pharmacokinetic properties all need to be addressed through a combination of improved drug design, formulation and manufacturing methodologies (9).

## 1.2 Mechanism of action of AMPs

In addition to their structure, the mechanism of action of AMPs is one of the key aspects that separates them from conventional antibiotics.

Their mechanisms of action can be split into two categories, either membrane disruptive or membrane non-disruptive. However, an individual peptide cannot always be placed into one specific category as the antimicrobial action can often be attributed to a combination of both types of mechanisms (10).

Even within the two main categories the individual mechanisms of action can vary substantially. Nucleic acids, protein synthesis, protein function and cell wall synthesis have all been identified as membrane non-disruptive targets for AMPs (10). Similarly for the membrane disruptive category the exact mechanism of action can also vary between peptides.

Traditionally 3 main mechanisms have been proposed (figure 1.1):

The barrel-stave model is based on the mechanism of action of alamethicin. In this model the peptides insert perpendicularly into the membrane and form a bundle with a central lumen like a barrel. The hydrophobic parts of the peptides align with the core of the phospholipid bilayer and as such the inner lumen of the pore is only made of the more hydrophilic regions of the peptides. Each pore can consist of different numbers of peptides thus producing a range of different pore sizes (11).

In the toroidal pore model, the peptides insert into the membrane and force the lipid bilayer to bend into a pore. As such, the pore surface will be composed of both the

phospholipid head-groups and the hydrophilic part of the peptides. Because of this, the pore size can vary more than in the barrel-stave model. The pore formation is possible due to the interaction between the phospholipid headgroups and the peptides that shields the charges of the peptides thus allowing them to associate together (11).

Lastly, in the carpet model the peptides accumulate on the surface of the membrane like a carpet. Once a critical concentration is reached the peptides will disrupt the membrane in a detergent-like manner leading to lipid removal through micelle formation (11).

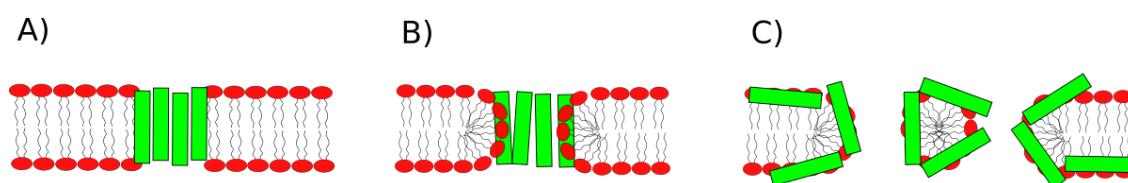


**Figure 1.1 Schematic of the three traditional models for the AMP induced membrane disruption.** A) Barrel-stave model, B) Toroidal pore model, C) Carpet model.

Although these 3 models are by far the most reported, they still cannot perfectly explain the behaviour of all AMPs and the same peptide has been described with different models by different authors (11, 12). Some also suggest that the models are not distinct but that there is a continuous graduation between ion channel, pore formation and membrane rupture (11). Bechinger et al. suggests an alternative model for membrane disruption called the in-plane diffusion model. In this model the peptides insert into the membrane surface which creates a disturbance in the properties of the bilayer in an area around them. The peptides can then move around in the plane of the bilayer and once they approach each other a critical distance is reached, leading to increased local destabilisation and transient openings in the bilayer (12-14). Further refinement by Bechinger has led to the SMART model, in which AMPs are first separated into two categories based on their amphiphilicity. Hydrophobic peptides with a low amphiphilicity such as alamethicin are said to form transmembrane helical bundles similarly to those described in the barrel-stave model, although he argues that the process is more complex than initially thought. The second set of peptides are cationic amphiphilic peptides such as melittin and magainin. Like in

the in-plane diffusion model these peptides are said to first insert into the membrane in an in plane alignment, however how this leads to the membrane disruption can vary. Bechinger argues that the mechanism of membrane disruption is not intrinsic to the peptide structure but dependent on both the peptide concentration and the properties of the lipid bilayer as both respond to each other in a transient manner. As such an individual AMP can both lead to stabilisation of a bilayer and disruption via mechanisms akin to the toroidal pore model or carpet model depending on the conditions of the system (15).

### 1.3 Antimicrobial coatings

Together with AMR, biofilm associated infections are the two major challenges related to the treatment bacterial infectious diseases. A variety of different factors associated with biofilms leads to a stark increase in the antimicrobial tolerance of these types of infections and if combined with antimicrobial resistance the infections can be very difficult to treat using traditional approaches (16, 17). Biofilms can both be associated with chronic tissue infections, such as with *P. aeruginosa* in lung tissue related to cystic fibrosis or leg ulcers, or with medical devices such urinary or venous catheters, ventilation tubes or different surgical implants, with medical device related infections being responsible for 60-70% of all hospital acquired infections (16, 17). The risk of acquiring medical device related infections can be relatively high, for example the risk of developing an infection with a urinary catheter increasing by approximately 10% for each day the catheter is in place (16). As mentioned, the treatment of biofilm associated infections can be very difficult and for some medical device related infections even require surgical procedures and as such preventative approaches could be more effective both in terms of clinical outcomes and cost (16, 17). Antimicrobial coatings could reduce the risk of medical device related infections and wound dressings could be used to fight recurring infections (16, 17).

A variety of antimicrobial coatings and wound dressings have already been developed relying on controlled localised delivery of different antimicrobial agents such as antibiotics, biocides or silver nanoparticles encased in different polymer systems (16-19). However, one group of compounds that have received less clinical attention is

AMPs, even though AMPs have great potential against biofilm infections via their metabolic independent mechanism of action and with some AMPs even showing the ability to eliminate established biofilms (20). Many different antimicrobial coatings utilising AMPs have been developed and undergone pre-clinical testing. In general, these formulations can be split up into two different approaches, either having the AMP elute from the coating in a controlled manner or having the AMP covalently immobilised onto the coating creating a surface-based killing mechanism.

Most controlled release formulations rely on the physical entrapment of the AMPs within polymer (21-30) or calcium-phosphate (31-34) networks. Several formulations also utilise the unique amphiphilic physiochemical properties of AMPs in their design such as with the addition of hydrophobic/amphiphilic compounds to entrap or influence the diffusion of the AMPs (21, 22, 24, 29, 31). One example of this is Lim et al. who designed a dual layer coating with the AMP HHC36 trapped within a poly- $\epsilon$ -caprolactone film with a 1-palmitoyl-2-oleoyl-sn-glycero-3-phosphocholine layer on top. The phospholipid layer works as a diffusion barrier and leads to a lower burst and longer overall release compared with the polymer layer itself (22). Alternatively, Shukla et al. utilises the positive charge of the AMP Ponericin G1 to encapsulate the peptide within their multilayer film due to interactions with different negatively charged polymers (25).

As the main mechanism of action of AMPs is not dependent on internalisation into the bacterial cell, a unique form of drug delivery systems can be made where the peptides are immobilized rather than released from the coating (35). This type of coating has the potential to be active for a very long time period as the AMPs are not lost over time and the constraint can lower the risk of degradation by enzymes (34). However, one challenge with this approach is that the killing mechanism is approximation based and if proteins and dead bacteria build up on the surface of the coating the efficacy will be drastically reduced and allow for biofilm formation (36). To counter this, many formulations utilise antiadhesive components such as hydrophilic polymers, multilayer polymer systems or hydrophilic polymer grafts. However, if the coating is too antiadhesive the bacteria will never come into contact with the AMPs. Muszanska et al. explored this with a hydrophilic polymeric brush coating made from the triblock copolymer Pluronic F-127 which acts as the antiadhesive with an AMP conjugated to

the terminal end. They found that increasing the amount of conjugated AMP increased the number of bacteria adhering to the coating surface but in most cases the degree of the adhering bacteria that were alive was also reduced (36). The results demonstrate the balancing act between the antimicrobial and antiadhesive properties of such coatings. Another challenge with these types of coatings is the grafting of the AMPs to the coating itself. Rapsch et al. investigated the grafting of several different AMPs using several different methods and found reductions in the activities based on the grafting method even if the total number of grafted peptides was increased. In addition, all grafting methods also showed a reduction in the activity compared with the free AMPs (35). However, sometimes the immobilization can also have the opposite effect, such as with an AMP (ILPWRWPWWPWRR-NH<sub>2</sub>) which showed improved efficacy specifically towards Gram-negative bacteria when immobilized compared to when in solution (36). The surface density of grafted AMPs can also influence the antimicrobial properties as shown by Paris et al. They designed a coating made from hyaluronic acid with nisin Z covalently grafted on and tested different grafting strategies. By grafting the AMP on the hyaluronic acid while still in solution a lower grafting surface density was achieved compared with grafting it on a substrate coated with hydrolysed hyaluronic acid, even if the total amount of peptides grafted was greater. The higher density grafting coating showed increased antimicrobial activity and the authors suggests that both the density and the freedom/availability of the AMPs are important factors for grafted AMPs (37).

The two design strategies have also been directly compared by Cassin et al. They designed two polyelectrolyte multilayer coatings consisting of hyaluronic acid and collagen with the AMP LL-37 either entrapped within the polymers or covalently grafted onto the polymers using carbodiimide chemistry. Comparing the two formulations they found that the coating with the immobilised peptide was slightly more efficient at reducing the coverage of live bacteria and significantly more efficient at killing an existing bacteria layer (although in both cases the difference was mainly seen at the low peptide concentration levels). However, the coating with the entrapped AMPs did also significantly reduce the number of planktonic bacteria and was less toxic to rat hepatocytes cultured on the coatings (26). Townsend et al. also compared the two strategies this time regarding a calcium phosphate coating. They

found that the coating with the covalently grafted AMP was much better at reducing the bacterial growth on the coating surface but was worse at inhibiting the planktonic growth. Interestingly, they also made coatings that combined both approaches and this coating seemed to conserve the advantages from each of the others (34).

There are both advantages and disadvantages to both design strategies and the optimal strategy must be determined on an individual design basis taking both the properties of the chosen AMP and the targeted application into account. Covalent immobilization might offer the potential for a longer period of activity and increased efficacy for direct surface based killing, but additional challenges regarding the antiadhesive properties and the grafting itself must be considered. For the elution strategy the release of antimicrobial agent to the surrounding tissue can be an advantage in many circumstances, such as for surgical implants, where the natural immune defence can be reduced post-surgery (31) and by modifying the formulation, the release profiles can be optimised towards different clinically relevant timeframes. In addition, the release also allows for the membrane non-disruptive mechanisms of actions of the AMPs to contribute.

#### 1.4 Sol-gel coatings

A very promising approach for making antimicrobial wound dressings and coatings for medical devices is to create a silica polymer network impregnated with antibiotics using sol-gel processing. These sol-gel materials are generally biocompatible, can be processed at gentle reaction conditions and allow for a high degree of customisability regarding many of the aspects relevant to drug delivery (38). The central component in a sol-gel is silica alkoxides (or other alkoxides) such as tetraethyl orthosilicate (TEOS) that serve as the precursors for the polymer network. These alkoxides can polymerise via first a hydrolysis reaction leading to a free hydroxyl group that can then react with another alkoxide molecule either via water or alcohol condensation. This leads to a covalent linkage between the two molecules and this process can be repeated creating a highly crosslinked polymer network. This process leads to a phase change of the system, from the sol phase where the silica alkoxides are in a colloidal suspension to the gel phase where the network has formed, often suspended in a liquid phase (38).

Because of the hydrolysis step the overall polymerisation will be dependent on the addition of water. In addition, the pH is also crucial as the reaction kinetics of the hydrolysis and condensation reactions each have their optimum at different pH values. This can be utilised to strongly influence the structural outcome of the network. Under acidic conditions hydrolysis is favoured, leading to an ordered mesoporous structure, while at neutral or basic pH condensation is favoured which can be used to produce silica nanoparticles or eventually a gel without a mesoporous structure (38). Following the polymerisation, further processing can be made to the bulk morphology of the sol-gel. Different deposition techniques followed by a curing step can be used to make coatings or thin film and, via drying, xerogels and aerogels can be made and moulded into specific dimensions (38). Sol-gel processing can also be performed in combination with organic polymers yielding hybrid sol-gel materials. These polymers can be added either because of their own physiochemical properties and how it affects the final product or as structure directing agents limiting the aggregation of the sol-gel precursors during the sol-gel process (38).

Sol-gel processing has been used to make several different formulations targeted towards biofilm infections such as coatings, wound dressings and implants. Much work regarding antimicrobial and biopharmaceutical loaded sol-gel materials and coatings has been performed by Ducheyne and colleges. They have investigated the effect of synthesis and formulation parameters such as drug loading (39-43), the water/silica precursor ratio (41) and pH (44). They have consistently found that increasing the drug loading increases the release rate. However, the mechanism of release seems to differ based on the sol-gel morphology, with the release from xerogels best described by diffusion, whereas for coatings erosion seems to correlate closely with the release (39-43). Increasing the water/silica precursor ratio was shown as an alternative way to increase the release rate without changing the drug loading (41). In addition, they have also investigated coating specific parameters finding that the thickness of the coating can be increased when dip-coating by increasing the withdrawal speed or by coating the sample multiple times with a conditioning step in-between (42). However, the effect of doing multiple coatings on the drug release is not completely consistent between papers. In a 2007 paper both the release rate and length increased with increasing number of layers which could suggest that the release

is facilitated by bulk erosion of the coating. However, in a 2009 paper only the length of the release seemed to increase which would indicate surface-based erosion. The two formulations are almost identical, only deviating regarding the addition of ethanol, substrate size and the number of layers (1-3 vs 3-5), and thus predicting the release mechanism of a sol-gel coating is not straightforward (43, 45).

When using sol-gel formulations for the drug delivery of biopharmaceuticals extra considerations are required compared with delivering small molecules. Radin et al. found that the release rate for macromolecules was inversely related to their size for xerogel formulations and a long lag time could sometimes be observed. This could however be modified by increasing the sol-gel pore size through changes to the synthesis method (44). Another concern is the stability of the encapsulated drugs. Mena et al. showed how increasing the bulk hydrophobicity of a sol-gel could increase the interactions between the sol-gel and proteins leading to increased thermal and structural stability (46).

Recently antimicrobial hybrid sol-gel formulations have also been used as wound dressings by Yeganeh and colleagues. Their core formulation was a hybrid silica sol-gel with silica functionalised polyurethane as the organic polymer with different antimicrobial additives added. The combination utilises elastic properties of polyurethane with increased tensile strength of the silica sol-gel. To create the wound dressing, they moulded the sol-gel into a thin membrane that then has the appropriate physical and mechanical properties for use in moist wound therapy. Silver and graphene oxide nanoparticles have been encapsulated within the wound dressing giving it antimicrobial activity, with low toxicity and improved wound healing *in vivo* (47, 48). Further development utilised covalently bound quaternary ammonium salts in combination with an external layer of dextran that reduced the cytotoxicity of the quaternary ammonium salts while still preserving their antimicrobial activity (49).

Some research has also gone into combining sol-gels with AMPs. Izquierdo-Barba et al. incorporated LL-37 into a mesoporous silica monolith with Pluronic P123 as a structure directing agent, which potentially could be formulated as a coating. They also made a parallel formulation that included 3-mercaptopropyl-trimethoxysilane as an additional silica precursor which increased the hydrophobic interactions between the sol-gel and

the peptide leading to slower release kinetics. The release profiles were fitted using the Noyes-Whitney equation (first order kinetics) showing that the release constant was almost halved for the modified sol-gel. The formulations showed low toxicity and significant antimicrobial activity even after 10 months of storage (50). Braun et al. used sol-gel processing to produce mesoporous silica nanoparticles with LL-37 adsorbed to them. A large surface area and negative charge for the nanoparticles could be used to increase the peptide adsorption but the negative surface charge reduced the particle interaction with DOPE/DOPG bilayers and thus the nanoparticles instead relied on release of the AMP to see any effect (51). Lastly, Diosa et al. created large non-uniform chitosan-silica hybrid nanoparticles using water-free sol-gel processing (using sodium silicate with the chitosan as the catalyst instead of silica alkoxides and water) with the AMP KR-12 adsorbed on the material. By varying the pH during the synthesis, the pore sizes and chitosan integration could be controlled, leading to changes in both the peptide adsorption and release. Adsorption of the peptides to the particles reduced their antimicrobial activity especially for the particles where electrostatic interactions were more important for adsorption (52).

## 1.5 Patch clamp analysis of antimicrobial peptides

Patch clamp electrophysiology is a diverse technique that can be utilised in many ways and with many different setups. This is also the case when it comes to the biophysical investigation of the pore forming abilities of AMPs. One of the most meaningful distinctions can be made based on the substrate that the current is measured across, being either a biological substrate such as cells or a synthetic substrate such as lipid bilayers or liposomes.

### 1.5.1 Live cells

Patch clamp using live cells has several advantages over synthetic bilayers. For example, giving better signal-to-noise ratios when voltages and ionic gradients closer to physiological levels are used and having a more complex and asymmetrical membrane composition (53, 54). However, the main disadvantage is that the most relevant target of the AMPs, namely bacteria, cannot be used because of their small size (55), a problem further exacerbated by the use of low access resistance patch

pipettes with enlarged tips (53, 54, 56, 57). For antimicrobial research this could be concerning since AMPs have been shown to act differently based on the membrane charge (58) and prokaryotic cells have more negatively charged membranes than eukaryotic cells (59). One approach for circumventing the size limitations of bacteria could be via the use of giant spheroplasts. In this approach, Gram-negative bacteria (typically *E. coli*) are first elongated by incubating them with the septation inhibitor cephalixin, whereafter the cell wall is enzymatically digested to yield an enlarged spherical spheroplast with a diameter of 5-10  $\mu\text{m}$ . This allows for the establishment of a Giga-Ohm seal using either traditional or planar patch clamp technique (60, 61). While spheroplasts have been used in combination with patch clamp electrophysiology to evaluate both native and foreign ion channels (61-63), their use in combination with AMPs have been limited to fluorescence microscopy methods (64, 65). Live cell patch clamp has been used to investigate both single channel events and macroscopic currents whilst in the whole cell configuration (53, 56, 57, 66-72), where the switch between the current types is performed by increasing the peptide concentration (53, 72). Using this method, single channel events for AMPs acting by the barrel-stave mechanism such as alamethicin can readily be analysed (53, 66, 70, 72) but investigation of peptides such as CM15 that form toroidal pores has been less successful as even at low concentrations the single channel events quickly evolve into macroscopic currents (53). Alternative methods for single channel investigations have been created by using different patch clamp configurations. By utilising the cell attached, outside-out or inside-out configurations while adding the membrane disruptive agent from the inside of the pipette (cell attached and inside-out) or to the external bath (outside-out) a smaller contact area between the membrane and the peptides can be achieved giving better single channel recordings (73-76).

#### 1.5.2 Synthetic bilayers

Regarding the biophysical investigation of AMPs, synthetic membrane models are more commonly used than live cell models. There are several different patch clamp setups that can be used for this purpose, ranging from traditional to more specialised equipment. Using a patch clamp pipette, measurement can either be made directly on liposomes using different configurations (66, 77-79) or by the "dip tip method" where a bilayer is formed across the tip of the pipette mimicking the out/inside-out

configuration (80-84). Another common approach is to use two Teflon chambers with a small hole connecting them which can vary in size to allow for both single channel and macroscopic investigations (14, 59, 80, 83, 85-88). More recently, a setup has been developed by Nanion which allows for planar bilayer experiments using disposable borosilicate chips (89-96). These chips have a hole-size that is much smaller than what is possible using other methods and therefore allows for more precise measurement of single channel events (97).

One of the biggest advantages of using a synthetic system is the ability to customise the composition of the bilayer. The main bilayer component is phospholipids and these can vary both in their head group and lipid chain. Generally lipid lengths between 16-18 carbons are used although the exact type can still vary, from the fully saturated C16 lipid DPP(X) (98), the partially unsaturated C18 lipid DOP(X) (59, 80, 99), POP(X) which have one chain from each of the previous types (59, 80, 84, 87) and lastly PDhP(X) which has branched C16 chains with 4 methyl substitutions on each chain (14, 80-82, 88, 90, 94-96, 100-102). The PDhP(X) type seems to be the most popular, likely due to its strong stability and high electrical resistance although it is less biologically relevant (103).

The lipid chain length can also be further utilised to increase the thickness of the bilayer. Ashrafuzzman et al. did this while investigating gramicidin S and found that the thickness had little effect on the measured signals, thus suggesting that the peptide did not form distinct pores such as via the barrel-stave or toroidal pore model, but instead likely disrupted the bilayer in accordance with the in-plane diffusion model (14).

The phospholipid head group is another key variable as these can both influence the charge and fluidity of the bilayer. Phosphatidylcholine (PC) is the most used zwitterionic phospholipid although phosphatidylethanolamine (PE) is also often used in combination with other lipids. Phosphatidylglycerol (PG) is the most common negatively charged phospholipid although phosphatidylserine (PS) can also be used. By combining these different phospholipids the membranes of different organisms can be mimicked. As such eukaryotic cell membranes are often represented using pure PC or a mixture of PC and PE producing neutrally charged bilayers whereas for bacterial membranes negatively charged bilayers are made using PG in combination with PC or PE or via the soybean product asolectin. In addition, further membrane components

such as cholesterol or ergosterol can also be added to further mimic mammalian or fungal cells respectively (59). Manzo et al. also further distinguish between bilayers mimicking Gram negative and positive bacteria by varying the ratio between DPhPE and DPhPG to 6:4 and 0:1 respectively (94-96).

The bilayer setup also makes it easier to vary the external conditions during the experiments. As such the effects of the ionic composition (77, 79, 86, 88), pH (102), temperature (80, 104) and peptide solvent (87) have all been evaluated.

Although bilayer experiments are mainly utilised for single channel evaluations, using the Teflon chamber setup, macroscopic evaluations can also be made. These experiments are mainly used to produce I/V curves using a voltage ramp protocol. Different useful information can be retrieved from I/V curves. If the curves are non-symmetrical between the positive and negative voltage range, then the peptide induced conductance is voltage dependent which is more common for peptides following the barrel-stave mechanism such as alamethicin (80). By evaluating the I/V curves at different peptide concentrations and comparing the voltage thresholds (where the curve becomes exponential) with the  $\ln$  of the peptide concentration the concentration dependency can be found. This value can be useful both for comparing the efficacy of different compounds and when divided by the voltage dependency it can give an estimation of the apparent number of monomers per conducting aggregate, although only if the mechanism of action is barrel-stave (80, 83, 87).

Single channel investigations of AMPs can be evaluated on several different levels. The lowest level is the raw recordings of the current over time relationship (current trace). The response signature can give an idea into the mechanism of action and can be characterised into different types of responses such as square-top, multilevel, flicker, spike and erratic behaviour (99, 105). Second to that is the amplitude histogram which shows the frequency that different current intervals have occurred during an experiment. The shape of the histogram can give insight into the mechanism of action and using a Gaussian fit the mean current can be determined for each conductance level. When multiple conductance states are present the histogram can also be a useful tool for distinguishing between them, as shown by Sondermann et al. finding 6 distinct conductance states for alamethicin (100).

For some AMPs I/V curves can also be made during single channel experiments, although it generally requires that there is one main conductance level. If the conductance is relatively constant it can be performed using a voltage ramp protocol (79), but otherwise it is mainly performed by comparing the average pore current at different voltages (59, 77, 79, 83, 88, 92, 93, 101). Single channel I/V curves are mainly used to investigate if the peptide pores are voltage dependent or not but can also be used to evaluate the ion selectivity. Pham et al. did this by evaluating the I-V relationship under symmetrical and asymmetrical KCl concentrations. Under the asymmetrical condition the reversal potential was shifted to a more negative voltage indicating selectivity towards potassium ions (88).

Time related parameters can also be evaluated based on the current trace. The lifetime of each pore can be measured, and the distribution can often be fitted with a single- or two-exponential function to aid comparison between compounds or bilayers (59, 77, 102). At the same time, it can also be useful to evaluate the frequency of pore openings (102).

Lastly, when a pore has multiple different but distinct conductance states, the opening and transition probabilities can also be calculated. Sondermann et al. used these probabilities to argue that alamethicin does not form pre-existing non-conducting aggregates before membrane polarisation, as the probability for the first conductance state to be the lowest level was 98% and if the aggregates were performed a larger distribution of conductance states would be expected (100).

Patch clamp using synthetic bilayers have also been widely used for the drug development and discovery of AMPs. Comparing an AMP with analogues with small modifications to the amino acid sequence can highlight the importance of structural motifs or individual amino acids (80, 81, 84, 85, 93, 95, 98), combining patch clamp with structural analysis techniques such as CD or solid state NMR can give insight into the effect of the secondary structure (81, 93, 96) and testing different segments of a larger peptide/protein can help identify the active part of the sequence for further development (85, 101).

Single channel bilayer experiments have also been used to distinguish between different mechanisms of action. Manzo et al. defined 5 parameters that can be used to indicate differences in the mechanism of action:

- The concentration required for activity to be seen.
- The latency between peptide addition and activity.
- The duration of the activity.
- The amplitude and number of each event.
- Whether the peptide causes the bilayer to break.

However, even using these parameters a clear mechanism of action could not be defined for all their tested peptides (95, 96).

The morphology of the current trace has also been widely used to indicate the mechanism of action although there is little consensus on the area.

The largest consensus is regarding the barrel-stave mechanism producing current traces corresponding to the square top or flickering behaviour (80, 86, 100). The toroidal pore mechanism has both been described with square tops and flickering (83, 89, 92) or by spikes, multilevel and erratic behaviour (87, 99). However, spikes, multilevel and erratic behaviour have also been used for describing the carpet (96) or the in-plane diffusion models (14).

## 1.6 Molecular dynamics simulations

To understand the behaviour of antimicrobial agents such as AMPs it is critical to gain insight into their properties, structure and interactions on a molecular level. Molecular dynamics (MD) simulations are one of the most powerful tools we have for exploring the molecular level behaviours of biological systems.

MD simulations are built on two fundamental concepts. Firstly, if the positions of all atoms in a biomolecular system are known, the force by which they interact with one another can be calculated based on their physiochemical properties. Secondly, if these forces are known, Newton's laws of motion can be used to predict the direction and velocity at which each atom is moving. In MD simulations these two principles are applied in an iterative stepwise approach, where the forces are calculated,

transformed to velocities and the atoms/molecules are then allowed to move for a very short time period (normally around 2 fs). Based on these movements the 3D positions of the atoms in the system are updated and the process is repeated from the beginning. These steps are repeated millions of times in order to generate a trajectory of the system which functions like a 3D movie showing the movement of the molecular components based on many individual static frames. Based on this trajectory a great deal of information can be gathered about the behaviour of the molecular components in the system (106, 107).

The most critical step in the simulation process is the calculation of the interatomic forces which is performed based on a so-called molecular mechanic's force field. Such force fields generally contain two components. Firstly, the mathematic equation used to calculate the interatomic forces based on the size of the interatomic potential energy. This equation consists of several terms used to describe the main ways in which atoms interact with each other through both bonded and nonbonded interactions. Bonded interactions contain terms related to the energetic effects of positional variation between atoms which are linked covalently such as the energy related to bond stretching, angle bending and dihedral and improper torsions. The nonbonded forces are based on Van der Waals interactions and Coulombic interactions. A critical aspect to these mathematical terms is that they are not designed to be as accurate to nature as possible, rather they are made to describe the behaviour accurately enough while still being simple enough to be evaluated quickly allowing for an efficient simulation speed. Therefore, the force field also contains a second part which is a specific set of atomic and molecular parameters. These parameters are generally formulated based on quantomechanical calculations and experimental observations in order to ensure that the overall force field yields accurate results within a given set of applications, even though simplified equations are used for the energy calculations. Consequently, many different force fields have been created by different research groups with different advantages and disadvantages and optimised towards different model types. Some force fields (such as CHARMM and AMBER) are mainly focused on the simulation of biological systems containing molecules such as proteins and lipids while others are more generalised or focus on inorganic compounds (108).

MD simulations have a large range of different uses depending on the application/topic of interest. The structural behaviour of large biological molecules such as peptides, proteins, lipids and nucleotides can be modelled and give context to experimentally derived average structures obtained with methods such as NMR or X-ray crystallography. Critical to this is that in MD simulations the dynamics of the structure are represented allowing for investigating phenomena such as the conformational changes of molecules during unfolding or ligand binding. In many ways, MD simulations can be used to give a better qualitative understanding of results obtained in wet lab experiments.

MD simulations are also widely used in connection with structure-based drug discovery. In this regard, they can both serve as a filter in the drug discovery process or as a tool used directly in the lead optimisation process. This can both be in terms of identifying key interactions between the drug candidate and its target or in *in silico* evaluations following changes made to the design/structure. Again, MD simulations have advantages over other computational methods due to the consideration of the dynamic changes in the structure of both the drug molecule and binding target. However, this does generally come at the cost of an increased computational demand (106, 107).

Several different simulation software packages exist to facilitate the simulations and analysis of MD simulation. For biological systems, Gromacs, originally developed at the University of Groningen and now maintained at Uppsala University, is one of the most popular. Critical contributors to this are likely that the program is open source and has a focus on facilitating the most efficient simulation speed possible on every system, ranging from supercomputers to home laptops (109). A key aspect in this regard is the support for GPU acceleration, which allows the simple but computationally expensive nonbonded force calculations to be offloaded from the CPU onto the GPU which excels at completing highly parallelised tasks. This facilitates that complex MD simulations that can now be completed, even on a low budget using consumer grade equipment (110).

## 1.7 Molecular dynamics simulations of antimicrobial peptides

As the main molecular target of AMPs is the highly adaptive and dynamic lipid bilayer, *in silico* investigations using methods that rely on static models for the binding are of limited use. Instead, MD simulations are the preferred computational method for investigating the behaviour of AMPs, at least for properties more complex than those that can be explored using simple structural projections. Due to the long and complex mechanism of action of AMPs, MD simulations have been used to explore several different aspects of the molecular level behaviour and interactions relevant to the antimicrobial activity of the peptides.

Several studies have utilised MD simulations to investigate the structural properties of AMPs by simulating their behaviour in different molecular environments. The simplest way to do this is to model their 3D structure while in solution. This is often done either in water or in a TFE/water mixture mimicking the conditions used in many *in vitro* structural experiments. These simulations are often used to either improve an *ab initio* predicted structure, give context to experimental investigations of only the secondary structure of the peptide or to explore the conformational space of the solution structure (111-114).

The most common use of AMP MD simulations is to simulate their interactions with lipid bilayers. The general setup for such simulations consists of a model with a central lipid bilayer spanning the entire x-y plane of the simulation box with a water layer on each side. One or multiple peptides are inserted into the water phase above the bilayer and as the simulation is executed these peptides will begin to interact with the lipids. Depending on the length of the simulation the peptides will generally either form an association with the bilayer surface or eventually fully insert into one of the leaflets of the bilayer. Some authors place extra emphasis on this process and have used MD simulations to describe a distinct mechanism for peptide insertion (115, 116). Once the peptide(s) are associated/inserted into the bilayer many different analysis methods can be utilised to describe aspects of the systems such as the position and orientation of the peptides relative to the bilayer and how the peptide(s) affect the properties of the bilayer itself (95, 96, 113, 115-127). Some authors also use the simulation trajectories to calculate the relative free binding energy of the peptide-bilayer complex (117, 123, 125-128).

Because AMP induced pore formation typically occurs on a timescale which is outside the current capabilities of MD simulations, exploration using this methodology is difficult but not impossible. Lipkin et al. reviewed different approaches used to make such investigations possible (129). The two main approaches are either to use preformed pores or to artificially pre-insert the peptide in a pore formation (124, 130-132). Some authors have reported spontaneous pore formation but that is likely due to unconventional parameter settings such as not adding counter ions or using a high temperature which could speed up the process.

In addition to purely exploratory biophysical investigations, MD simulations have also been utilised in the drug discovery process of new AMPs. While the use as a screening tool before *in vitro* evaluation of new peptides should be possible, very few examples have been published using this approach. Puentes et al. highlight the potential use of MD simulations as a secondary screening step in their review of different *in silico* and experimental approaches to design, screening and testing of AMPs, but do not refer to any actual examples of such use at the time (133). In a recent follow up paper, they evaluated different aspects of their AMP discovery pipeline including using MD simulations as a screening tool, but only evaluated 5 randomly selected candidates out of 252 candidates (134).

Much more common is the use of MD simulations to compare 2 or more peptide analogs and thereby give molecular level context to experimentally observed differences between these (95, 113, 118, 122-124, 126, 135, 136). In these cases, the MD simulations can help answer the question of why one analog might have a higher activity than another and thereby help inform the design of future modifications.

## 1.8 Aims and objectives

The general aim of this project is to work towards overcoming some of the drawbacks existing for natural AMPs highlighted in section 1.1, that currently limit the clinical viability of such peptides. Specifically, the natural AMP Smp24, first isolated from the venom of *Scorpion maurus palmatus*, will be the starting point for inhibitor development (137). This 24-residue long peptide shows a promising antimicrobial activity against both clinically relevant Gram-positive and Gram-negative bacteria but

also a significant cytotoxicity against mammalian cells (137, 138). In this project, two different approaches will be used in order to advance the development of this peptide and bring it closer to a stage where it potentially could be viable for clinical use. This gives rise to the following two aims that will be addressed in this study:

- Aim 1) Formulate Smp24 in a sol-gel coating to utilise its antimicrobial and antibiofilm properties to prevent the formation of biofilms on the surface of the coating.
- Aim 2) Improve the selectivity of Smp24 and at a reduced development cost using a rational drug design approach

Additionally in order to fully address the broader second aim, several objectives also need to be completed:

- The pre-existing knowledge related to the structure and mechanism of action of Smp24 will be further expanded using biophysical approaches, in order to establish a better structure-mechanism relationship that can be used to guide the design of novel analogs.
- Smp24 will be truncated using a structure-based computer aided design process to yield smaller, cheaper to procure, and more efficient analogs while retaining the antimicrobial properties of the parent peptide.
- The best of the truncated analogs will be further developed in order to optimise selectivity towards bacterial cells over mammalian cells, by either improving its antimicrobial properties or reducing its cytotoxic effects.

## 2. Materials and methods

### 2.1 Materials

Antimicrobial peptides were synthesized via Fmoc solid phase peptide synthesis by either Davids Biotechnologie GmbH (Regensburg, Germany) (Chapter 6) or Bioserv UK (Sheffield, UK) (Chapter 7) at a purity of >90%. Unless otherwise specified all other reagents were purchased from Sigma Aldrich (Basingstoke, UK).

### 2.2 Production of sol-gel coating

The sol-gel coatings were synthesised based Nichol et al (*139*), except using a different type of PDMS polymer. Shortly, 0.5 parts TEOS, 1 part TMOS, 1 part MTMS and 2.18 parts isopropanol were mixed while slowly adding 2.35 parts of a 1:1.15 0.07M nitric acid:isopropanol mixture. Thereafter, 0, 0.2 or 0.4 parts of PDMS-OH (Mn = 550, viscosity = 25 cSt) was added to achieve the desired PDMS-OH level. An additional 2.33 parts of the nitric acid: isopropanol mixture was slowly added and after 10 min of mixing a final 2.4 parts 0.07M nitric acid was added. The sol was allowed to age at room temperature under rigorous mixing for 3 days before coating.

After the ageing period the final coating mixture was prepared by mixing 1 part of the aged sol with 2 parts isopropanol. Depending on the peptide level, a total of 2 parts water and/or Smp24 stock was added, such that the amount of peptide in the final samples was either 0, 150 or 300 µg. To create the thin film samples, 37.5 µl of this final mixture was spread onto a 22mm round glass coverslip and allowed to dry overnight.

### 2.3 Evaluation of antimicrobial coatings

#### 2.3.1 Brightfield (BF) microscopy characterisation of coating structures

To evaluate the distribution of the PDMS-OH within the sol-gel coating, samples spiked with the hydrophobic dye Oil red O were prepared. This was done by using a saturated Oil red O in isopropanol solution instead of pure isopropanol when preparing the final coating mixture.

Macroscopic BF images of the peptide-loaded sol-gel coatings were taken using a microscope at approximately 1.25 magnification, while further magnified images of both loaded and non-loaded samples were taken using an inverted Olympus IX81 microscope.

### 2.3.2 Matrix-assisted laser desorption/ionization (MALDI) mass spectrometry imaging (MSI)

Peptide loaded samples were prepared for MALDI MSI by spray coating the sample with a MALDI matrix consisting of 2.5 mg/ml  $\alpha$ -Cyano-4-hydroxycinnamic acid ( $\alpha$ CHCA) in 70:30 Acetonitrile:0.5% TFA using a Suncollect MALDI Auto-sprayer (Sunchrom GmbH, Friedrichsdorf, Germany). A total of 25 layers of  $\alpha$ CHCA were deposited at a flow rate of 8  $\mu$ l/ml for each sample.

Imaging was performed using a Bruker autoflex speed MALDI-ToF mass spectrometer (Bruker Daltonik GmbH, Bremen, Germany) equipped with a 200 Hz SmartBeam™ laser using a 50 x 50  $\mu$ m spot size. Acquisition was carried out in the mass range of m/z 2375-3000 in positive-ion reflectron mode. Images were created using a raster size of 50  $\mu$ m<sup>2</sup>, with 25-250 shots per raster.

Data analysis was performed using the FlexImaging software (Bruker Daltonik GmbH, Bremen, Germany). The peptide signal was determined based on a mass range between m/z 2549-2629 corresponding to the signals from the [M+H]<sup>+</sup> and [M+Na]<sup>+</sup> peptide ions only.

### 2.3.3 Peptide elution from the sol-gel coating

The elution of Smp24 from the sol-gel coatings was evaluated by submersing the individual samples in 600  $\mu$ l PBS, incubated at 37°C, 100 rpm. The elution media was periodically collected and exchanged with fresh PBS throughout a 4-week period. The peptide concentration in each elution media sample was determined using the Pierce™ Quantitative Fluorometric Peptide Assay following the protocol specified by the manufacturer. Briefly, in fluorescence compatible 96 well plates, 10  $\mu$ l elution sample was mixed with 70  $\mu$ l assay buffer and 20  $\mu$ l assay reagent. After 5 min incubation at RT the peptide concentration was quantified via fluorescence measurement at  $\lambda_{exc}$  = 390 nm and  $\lambda_{em}$  = 475 nm.

#### 2.3.4 Coating mediated biofilm inhibition

The biofilm inhibitory properties of sol-gel coatings were evaluated against *S. aureus* SH1000 (140) based on a modified version of Skogman et al (141). An overnight culture of the bacteria species was diluted 1000x in Mueller Hinton broth (MHB) and incubated at 37°C, 200 rpm until an OD<sub>600</sub> 0.2-0.6 was achieved, to ensure exponential growth phase was reached. The bacteria suspension was re-diluted 100-fold in MHB to give a suspension of approximately 10<sup>6</sup> CFU/ml. Sol-gel coated coverslips were placed in a 24 well plate with the coating facing upwards and 1 ml of the bacteria suspension was added to each well. After 24h of incubation at 37°C, 100 rpm the planktonically growing bacteria were removed and the OD<sub>600</sub> determined. The biofilms grown on the sol-gel surfaces were washed twice with 1ml PBS and then resuspended into 1 ml MHB by sonicating the samples for 10 min. The CFU/ml of the resuspended biofilm was determined by spot plating on MHA plates in triplicate using factor 10 serial dilutions for each sample.

#### 2.4 *In vitro* biophysical evaluation of AMPs:

##### 2.4.1 Electro formation of GUVs

Vesicles for the patch clamp experiments were produced using the vesicle prep pro from Nanion (Munich, Germany) using Bruggeman et al as the starting protocol (142), optimised to work with the specific lipid mixtures. Shortly, 20 µl 3 mg/ml lipid in chloroform solution was placed as multiple small droplets on an ITO sheet and allowed to fully dry. A rubber O-ring was placed surrounding the lipid film held in place by a thin layer of silicon grease. The chamber formed by the O-ring was filled with 280 µl 1M sorbitol solution and a second ITO sheet was placed on top. The ensemble was placed in the vesicle prep pro and an electro formation protocol was initiated.

Electro formation protocol used for PC:PG type vesicles: An initial linear voltage increase from 0 to 3V was performed over 1h followed by a 2h period with a constant voltage of 3V. The protocol was finished by reducing the voltage back down to 0 over 10 minutes. All stages were performed at an amplitude of 5 Hz and a temperature of 37 °C.

Electro-formation protocol used for PC:PE type vesicles: An initial linear voltage increase from 0 to 3.2V was performed over 1h followed by a 50 min period with a constant voltage of 3V. These steps were performed at an amplitude of 10 Hz. The protocol was finished by a fall in the amplitude to 4 Hz over 10 minutes which was held for an additional 20 minutes. The voltage was not changed. All stages were performed at a temperature of 37 °C.

Once finished the GUV solution was retrieved using a pipette tip, which was cut to increase the size of the opening, by pipetting the solution up and down two times to release the vesicles from the slide. The GUVs were stored at 4 C° in an Eppendorf tube until use (max 5 days).

#### 2.4.2 Patch clamp

Electrophysiology experiments were performed on planar lipid bilayers using a Nanion Port-a-Patch planar patch clamp setup, based on a modified version of Bruggemann et al (142). Bilayers were formed by adding 5 µl of GUV solution to a 3-5 MOhm borosilicate chip which contained 5 µl of pH 4 buffer (200 mM KCl, 10 mM HEPES) solution on each side of the aperture. After applying 10-30 mbar of negative pressure a Giga-ohm seal would be formed and the pressure would be reverted to neutral. The bilayer was washed by exchanging 20 µl buffer solution 3 times. The gain was increased to 50 mV/pA and a 50-60 mV potential was applied across the bilayer. To ensure the quality of bilayer was satisfactory, the current across blank bilayer was recorded for 5 min before the bilayer was washed a second time, this time with 3x 20 µl pH 7 buffer (200 mM KCl, 10 mM HEPES). In later experiments using 16:0 4ME lipids the buffer solutions were adjusted with CaCl<sub>2</sub> to an additional 10 mM Ca<sup>2+</sup>. After a further 5 min, 3 µl concentrated peptide solution was mixed with 17 µl pH 7 buffer solution and added to the 10 µl buffer presents on the chip to obtain the active concentration.

The current traces were recorded using an EPC 10 USB HEKA amplifier and the setup was controlled using a combination of the Patchcontrol (Nanion) and Patchmaster (HEKA) software. Analysis of the current traces was performed using Fitmaster (HEKA).

## 2.5 *In vitro* biological evaluation of AMPs

### 2.5.1 Minimum inhibitory concentration (MIC)

The minimum inhibitory concentration of the peptides against *Staphylococcus aureus* SH1000 (140), *Escherichia coli* JM109 (143) and *Pseudomonas aeruginosa* PAO1 (144) was determined using the microdilution method (145). Factor two dilutions of the peptides (256-0.5 µg/ml) were incubated with 10<sup>5</sup> CFU/ml bacteria suspensions in MHB in a 96 well plate for 18-20h at 37C°. The MIC was evaluated via visual inspection and further confirmed by absorbance measurement at 600 nm.

### 2.5.2 Peptide only biofilm inhibition assay

The intrinsic ability of the AMPs to inhibit the formation of biofilms was evaluated against *S. aureus* SH1000 (140) and *E. coli* JM109 (143) based on a protocol from Skogman et al. (141). An overnight culture of the bacteria species was diluted 500-1000x in MHB and incubated at 37C°, 200 rpm until an OD<sub>600</sub> 0.2-0.6 was achieved, to ensure exponential growth phase was reached. The bacteria suspension was re-diluted 100-fold in MHB to give a suspension with approximately 10<sup>6</sup> CFU/ml. The bacteria suspension was added to a 96 well plate and mixed with the peptide, giving final concentrations from 2x the MIC to 1/64th MIC. The plate was incubated at 37C°, 100 rpm for 18h (*S. aureus*) or 24h (*E. coli*). The biofilms grown in the wells were washed twice with sterile PBS whereafter the biofilm cell viability was evaluated by incubating them at room temp (RT) with 20 µM Resazurin for 20 min (*S. aureus*) or 2h (*E. coli*), followed by fluorescence quantification at  $\lambda_{exc} = 560$  nm and  $\lambda_{em} = 590$  nm. The biomass of the same biofilms was evaluated following the Resazurin stain by fixing the biofilm with 96% ethanol for 15min, staining with 0.02% Crystal violet for 10 min, washing twice with water and redissolving the stain with 33% acetic acid for 1h. The biomass was quantified by absorption at 595 nm. The relative biofilm formation was evaluated at each concentration (n=8) compared to untreated bacteria controls (n=16).

### 2.5.3 Haemolysis assay

The haemolytic activity of the AMPs was evaluated based on Corzo et al (146). Defibrinated sheep's blood was washed with PBS 3-5 times in order to isolate the erythrocytes and then diluted down to a final test concentration of 10%. The erythrocytes were incubated with factor two dilutions of the peptides (512-1 µg/ml) adjusted to 290 mOsm/l in triplicate for 1h at 37C°, 100 rpm. A 10% triton-x solution was added for the positive control and PBS for negative control. After the incubation the samples were centrifuged at 10,000 x g for 5 min and the absorbance of the supernatant was measured at 570 nm. The absorbances were corrected against the negative control and the %lysis was estimated relative to the positive control. HC<sub>50</sub> values were estimated using the Hill equation.

### 2.5.4 Cell culture

The HEK293 (147) and HepG2 (148) cell lines were both grown in Dulbecco's modified Eagle's medium (DMEM) supplemented with 10% fetal bovine serum (FBS) and 1% pen-strep. The cells were incubated in T-75 flasks at 37C°, 5% CO<sub>2</sub> and the media was changed twice a week. Upon reaching a confluence of 90% the cells were washed with PBS and trypsinised using 0.25% trypsin.

### 2.5.5 Cell line toxicity

The cytotoxicity of the peptides was evaluated using the CyQUANT LDH cytotoxicity assay with methodology based on Rawson et al (149). The cells were seeded in 96 well plates at a density of 20,000 cells/well and incubated for 24h. Factor two dilutions of the peptides (465-0.9 µg/ml in water) were added to the wells and the plates were incubated for a further 24h. Following the incubation period, the LDH release was quantified in accordance with the manufacture's specification. Briefly, lysis buffer was added to the maximum LDH controls and incubated for 45 min. 50 µl sample from each well was transferred to new 96 well plates and mixed with 50 µl reaction mixture. After a 30 min incubation period, 50 µl stop solution was added to each well. The absorbance was measured at 490 nm and 680 nm. The LDH activity was determined by subtracting the 680nm absorbance from the 490 nm absorbance values. The %cytotoxicity was determined by correcting the LDH activity against the negative

control (water) and then comparing the value relative to the corrected maximum LDH control. The IC<sub>50</sub> values were estimated using the Hill equation, with the maximum response based on an average of the maximum response of the peptides.

## 2.6 *In silico* evaluation of AMPs:

### 2.6.1 Molecular dynamics simulations

All molecular dynamics simulations were performed using the Gromacs 2020.2-4 packages. All simulations were performed using the leapfrog algorithm with a 2 fs timestep, hydrogen bond constraints were performed using the Lincs algorithm, Wander Vaals and short-range electrostatic interactions cut-offs were 1.2 nm, Nose-Hoover thermostat was used for temperature control and the Parrinello-Rahman barostat for pressure control with semi-isotropic conditions for the bilayer models and isotropic conditions for the solution models.

Unless otherwise specified all production runs were performed in the NPT ensemble at 293K, 1 atm and with centre of mass correction of the system every 100 steps.

The Gromacs tutorials by Justin A. Lemkul were used as a starting point for the setup and basic simulation procedure for both the solution and bilayer simulations (150).

### 2.6.2 *Ab initio* structure generation

The starting 3D structure of all peptides used in the MD simulations were generated using the Pepfold3 server (151) following 100 simulations sorted by the sOPEP energy.

### 2.6.3 Peptide water model

The topology of the peptide was described using the amber99sb-ild all-atoms force field. In each system a peptide was placed in the centre of a 7 nm<sup>3</sup> box filled with water molecules described by the TIP3-P water model. The net charge of the model was neutralised by adding chloride ions.

An initial energy minimization was performed prior to the equilibration. The model was equilibrated in two steps, firstly a 100 ps NVT simulation was performed using the V-rescale thermostat with protein and non-protein coupling groups to equilibrate the temperature. Thereafter a 100 ps NPT simulation was performed with the addition of

the Parrinello-Rahman barostat to equilibrate the pressure. During both equilibration steps position restraints were placed on the peptide atoms.

The production runs were performed in the NPT ensemble simulated for 500 ns.

#### 2.6.4 Peptide TFE/water mixture model

The peptide topology was again described using the amber99sb-ild all-atoms force field. The peptide was placed in the centre of a 7 nm<sup>3</sup> box filled with water and TFE molecules in a ratio of approximately 2.7-2.8 water to TFE. The water and TFE mixture model was based on previous work by Gerig et al. with the TFE topology described as TFE model V (152) and the water model used was TIP5PE. The net charge of the model was neutralised by adding chloride ions. Following an energy minimization, the same equilibration procedure as for the water only models were used.

The production runs were performed in the NPT ensemble simulated for 500 ns.

#### 2.6.5 Bilayer models

Over the span of the studies several different bilayer systems were created to aid in the exploration of the structure mechanism relationship, drug design and *in silico* comparison between the AMP. All the models were based on an original base system with modifications applied in order to explore different aspects of the peptide bilayer interactions. A short description of the purpose of each model can be found in table 2.1. Further explanation for the design principles behind the different models can be found in chapter 5.

All bilayers were built using CHARMM-GUI (153), with lipid and peptide topology described using the CHARMM36m forcefield. The standard TIP3P water model was used for all bilayer simulations.

**Table 2.1 Overview of baseline bilayer models used in the different simulations.**

Bilayer simulation variant	General changes relative to base model	Purpose of simulation
Base		Basic models for evaluating the early interactions and equilibrium state between a peptide and a negatively charged phospholipid bilayer
1	Bilayer composition changed to DOPC:DOPE lipids	Models for evaluating the effects of the lipid composition
2	Larger bilayers with more peptides inserted	Models for evaluating the effect of the peptides on the properties of the bilayer
3	Single toroidal pore induced in the bilayer	Models for evaluating the interactions between a single peptide and a toroidal pore
4	Single toroidal pore induced in a larger bilayer with multiple peptides inserted	Models for evaluating the interactions between multiple peptide and a toroidal pore
5	Reduced size of bilayer and increased ionic strength	Smaller version of the base model for increased simulation efficiency

### Base model

The central component of the base model was a 7 nm<sup>2</sup> phosphor lipid bilayer, consisting of 1:1 DOPC:DOPG dual lipid mixture (72 of each lipid).

A single peptide was inserted into the model with its centre of mass about 1.5 nm above the bilayer. On each side of the bilayer an approximately 3 nm layer of water molecules were also added, to ensure the bilayer was properly hydrated. Some of the water molecules were exchanged with potassium and chloride ions to make the system overall neutrally charged. Following an energy minimization, the models were equilibrated in 3 steps. Firstly 100 ps NVT simulation was performed using the V-

rescale thermostat with protein, lipid and water+ions coupling groups to equilibrate the temperature. Thereafter two NPT simulations were performed with the addition of the Parrinello-Rahman barostat to equilibrate the pressure, the first being 100 ps and the second 900 ps. During all equilibration steps 1000 kJ/mol nm<sup>2</sup> position restraints were placed on the peptide atoms. The simulations were initially simulated for 500 ns, however in some cases the length had to be increased in order to reach an equilibrium.

#### Variant 1

Composition of the bilayer was changed to 1:1 DOPC:DOPE lipid (74 of each). Everything else was performed as with the base model.

#### Variant 2

Simulations of larger bilayers (12.62-14.21 nm) with 0-16 peptide inserted into the top leaflet was performed via several steps. Firstly, different sized DOPC:DOPG bilayers (3.3 nm<sup>2</sup>, 4.0 nm<sup>2</sup> and 7.0 nm<sup>2</sup>) were created and insertion of a single peptide was achieved in accordance with the base model. Larger models were created based on the final frame of the previous simulations using the gmx genconf command with the -nbox flag. This function multiplied the molecular components of the model in a grid like pattern along the X and Y axis several times (2x2, 3x3, 4x4), yielding a larger bilayer with multiple peptides already inserted (figure 2.1). The larger models were first simulated at 323K for 500ns to facilitate peptide diffusion/mixing in the bilayer plane followed by 250ns simulation at 293K used for the analysis. A similar approach has previously been used by Chen et al (124).

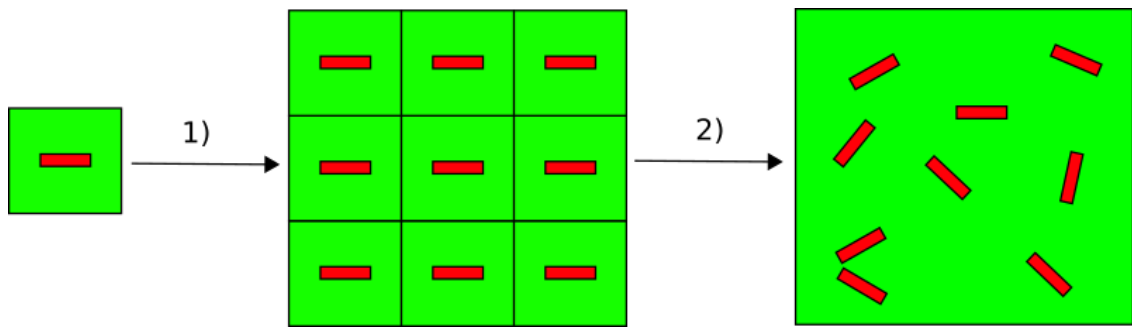


**Figure 2.1 Creation of larger bilayers with multiple peptides inserted.** 1) Small bilayer model with a single peptide inserted was multiplied in the X and Y directions in a grid-like pattern. 2) The larger bilayer was simulated at increased temperature to facilitate mixing of the peptides.

### Variant 3

Bilayer simulations with a pre-formed toroidal pore and a single peptide were created using an electroporation approach. The final frame from the base model simulations (peptide inserted into 7 nm<sup>2</sup> DOPC:DOPG bilayers) was used as a starting point for these simulations. A pore was created using electroporation by simulating a relatively large electric field (0.3 V/nm) running across the bilayer. Under these conditions a toroidal pore would form and quickly expanded leading to the complete destruction of the bilayer. Via visual inspection of the simulation trajectory, a frame was found where a small toroidal pore had been formed before the complete bilayer disruption and this configuration was extracted. The simulation parameters were changed to lower the strength of the electric field to 0.065 V/nm. Using the new parameters and the previously extracted configuration a simulation could be performed with a relatively stable toroidal pore which would remain open over the full 500 ns simulation time without leading to the complete disruption of the bilayer.

COM corrections, which modifies the directional velocities for a group of molecules to reduce the overall drift relative to the simulation box, were increased to every 10 steps for the bilayer to counteract the additional drift induced by the one-directional electrical field.

The range of possible pore associated peptide configurations were further evaluated by manually changing the position of the peptide within the pore lumen. This was done using a pull function where a constant force was applied to the centre of mass of the

peptide pulling it down and towards the pore. The pull function was applied to the peptide in two different starting positions (based on the previous set of simulations) and stopped at three different levels of insertion giving a total of 6 simulations. Thereafter the system was equilibrated for 5 nanoseconds with the peptide position locked. Finally, the system was simulated for 50 ns to see how the position of the peptide changed over time.

#### Variant 4

Simulations were performed using a similar methodology as with the variant 3 simulations except using the final frame of the variant 2 simulation with 16 peptides as the starting point.

#### Variant 5

Simulations were performed using a similar approach to the base model, except the size of the bilayer was reduced to 5 nm<sup>2</sup> (38 of each lipid). Furthermore, additional ions were added to reach a KCl concentration of 0.15 M instead of just to neutralize the system.

## 2.7 MD simulation analysis methods

### 2.7.1 3D structure visualisation

Visualisation of the 3D simulation outputs were performed using either visual molecular dynamics (VMD) or Pymol. VMD was generally used for analysis of multi-frame trajectories while Pymol was used for the evaluation of static 3D structures.

### 2.7.2 Evaluation of peptide structure

The analysis of the secondary structure of peptides based on the MD simulations was performed using two approaches:

The per residue secondary structure over time was estimated using the VMD plugin called Timeline. This yields a 2D box plot where each type of secondary structure corresponds to a specific colour. This method allows for the detection of all types of secondary structure including alpha helices, 3-10 helices, beta-sheets and random coil structures. An example of a 3D peptide structure and the corresponding secondary structure box plot can be seen in figure 2.2:



**Figure 2.2 Correlation between the 3D structure of a peptide and the corresponding secondary structure 2D box plot.** White represents random coil structure, purple represents alpha helical structure and blue represents 3-10 helix structure.

Alternatively, for peptides which were almost exclusively helical the gromacs function `gmx helix` was used. This function calculates the average degree of helicity for each residue over a given period of time. These per-residue values were again averaged with each other to estimate the overall helicity for the peptide.

The changes in the peptide structure over time were evaluated using three different methods:

The Root-mean-square deviation (RMSD) of atomic positions was calculated using the gromacs `gmx rms` function based on the backbone of the peptide. This analysis gives an indication of how much the structure changes over time relative to the starting position and can also give an indication of the moment-to-moment structural fluctuation.

The root mean square fluctuation (RMSF) was calculated using the `gmx rmsf` function and represents the per-residue standard deviation in the atomic positions. This can be used to identify which residues have larger structural fluctuations over a given time period.

The radius of gyration was calculated using the `gmx gyrate` function and can be used to estimate the maximum 3D size of the peptide at a given time point.

The formation of intermolecular salt-bridges was investigated based on the distance between charged atoms over time. Cationic atoms include the nitrogen atoms of the peptide N-terminal amine or the nitrogen atom of the lysine sidechain. Anionic atoms include the oxygen atoms of the carboxylic acid groups of the C-terminal residue and the aspartic acid sidechain. If the distance between such two atoms was less than 0.32 nm it was taken as an indication of the presence of a salt-bridge. The distance was calculated using the gromacs function `gmx distance`.

For some peptides the bending of a helical region within the peptide structure was investigated. This was done using the Bendix plugin for VMD (figure 2.3). This plugin looks at a helical structure and transforms it into a curved cylindrical structure based on shorter cylindrical sections (4 residue segments) following the local helical axis. Using these shorter sections, the bending angle of the helix can be represented/calculated for each residue to see where and how much the structure of the helix deviates from a perfect cylinder. This analysis can be done for each frame in a simulation to calculate the average bending angle for all residues over a given timeframe of a simulation.

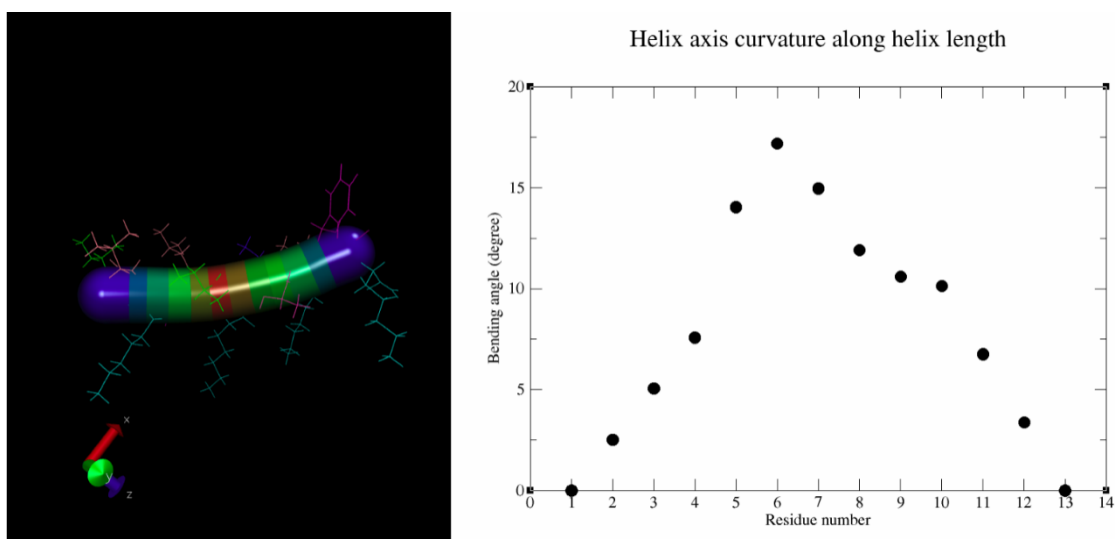


**Figure 2.3** Analysis of the helical bend of a peptide structure using the Bendix plugin. Left = 3D representation of the curve of a helical region. Right = Graphical 2D representation of the curvature.

### 2.7.3 Analysis of the position and orientation of the peptide relative to the bilayer

The position of the peptide relative to the bilayer over time was estimated by calculating the centre of mass (COM) over time of different molecular components present in the model (figure 2.4). As the bilayer spans the XY-plane of the simulation box the Z-axis coordinates of a given molecule can be used as a proxy for its position relative to the bilayer. Thus, to describe the changes in the relative position of the peptide over time the COM of the peptide and the terminal residues were calculated relative to the Z-axis. In addition, the COM of the phosphor atoms for each lipid leaflet was also calculated to represent the approximate parameters of the bilayer. The COM was calculated using the gmx traj function with the `-com` flag.

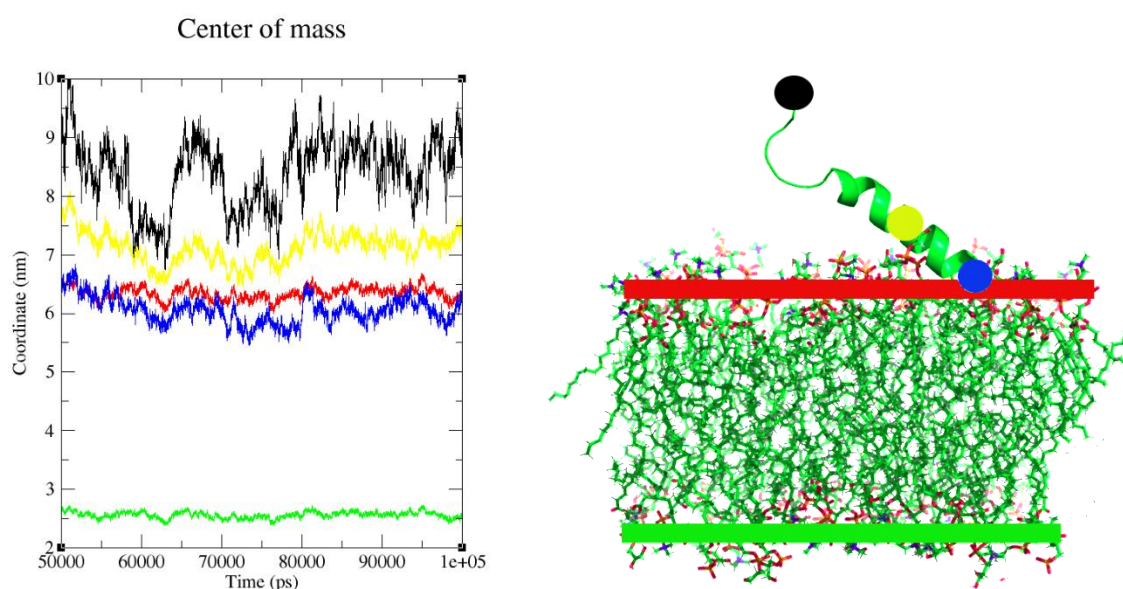


**Figure 2.4 Correlation between centre of mass (Z-axis) over time and the 3D structure of the bilayer model.** The red and green lines correlate to the lipid phosphor atoms and represent the rough outline of the lipid bilayer. Black and blue correlates to the COM of the C- and N-terminal of the peptide respectively. Yellow represents the COM of the entire peptide.

The orientation of the peptide relative to the bilayer surface was analysed using the primary helical region, which for this purpose can be represented as a ridged cylinder with a local axis running through the centre of it (figure 2.5). The angle between this helix axis and the Z-axis represents the tilt of the peptide and was calculated using the gmx bundle function with the `-z` flag. This angle was transformed to instead represent the angle between the helix and the surface of the bilayer (XY plane) to represent the peptide-bilayer angle.

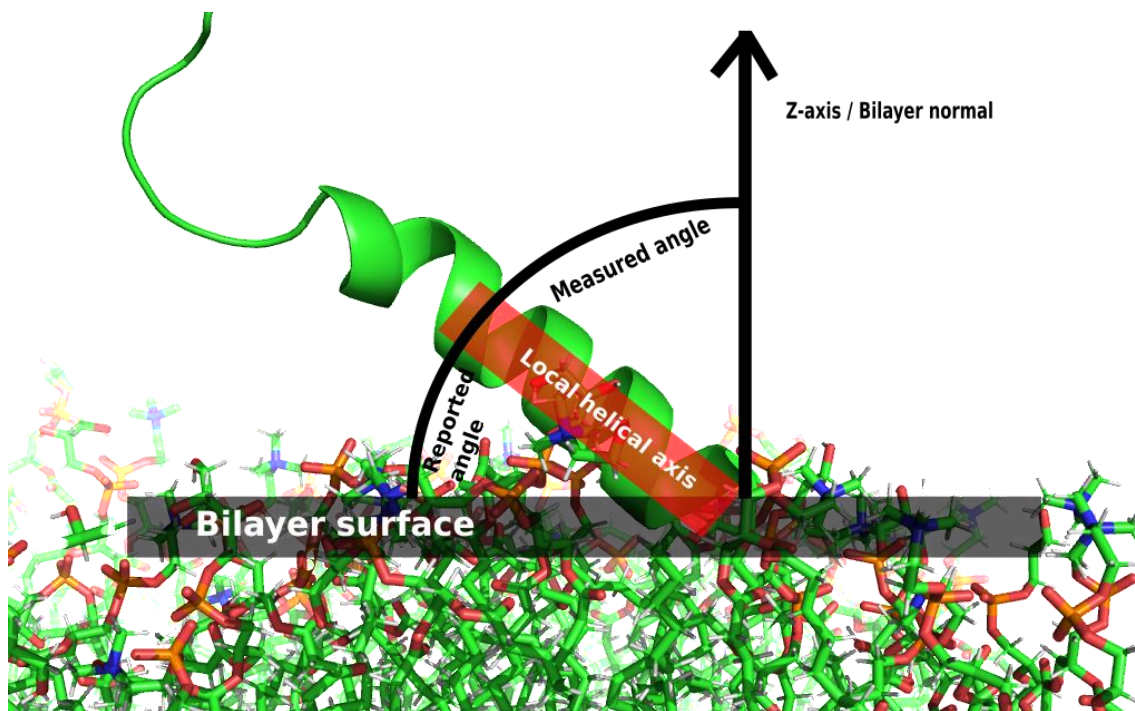


**Figure 2.5 Correlation between the 3D structure of the peptide and bilayer and the helix-bilayer angle measurements.** The angle is measured between the local helical axis and the Z-axis/bilayer normal. This angle is transformed to represent the angle between the local helical axis and the bilayer surface (XY-plane).

Changes in the helical orientation/rotation over time was estimated using the gmx helixorient function. The orientation of each residue relative to the central helical axis is estimated and the cumulative changes relative to this starting position were calculated for each time step. Thereby a line can be created showing by how many degrees the orientation of each residue has shifted over a given time period (figure 2.6).

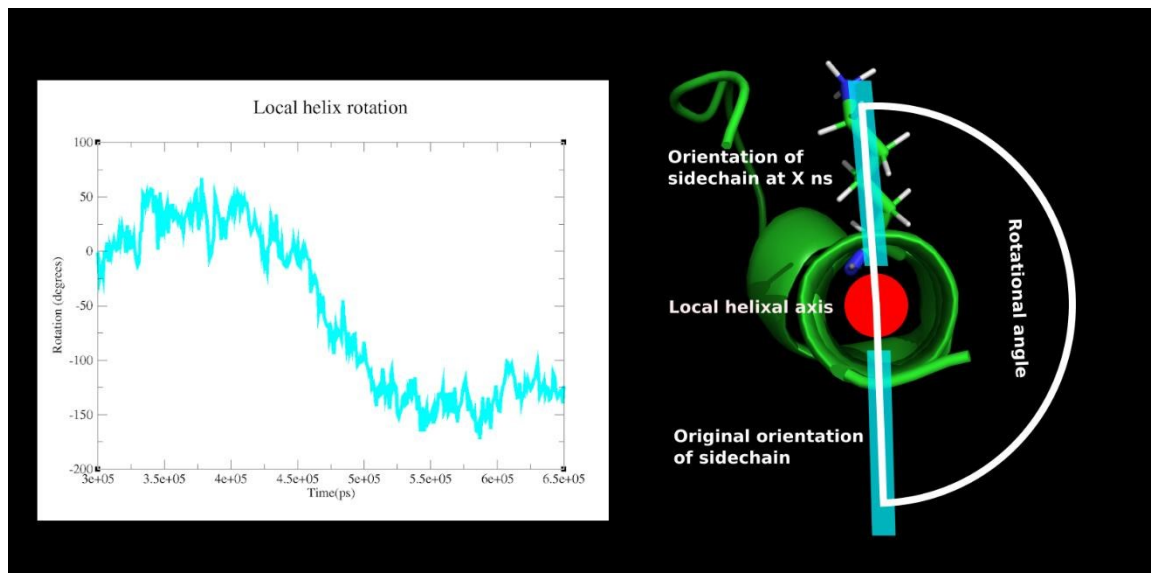


**Figure 2.6 Correlation between the 3D structure of the peptide and the helical rotation over time.**

Investigating the formation of charged interaction between the peptide and the lipids is not practical using direct distance calculations as specific residues of the peptide can interact with many different individual lipids over the time span of the simulation. Therefore, radial distribution functions (RDFs) were used instead, calculated using the `gmx rdf` function. A RDF describes how the density of a group of atoms changes relative to the distance from a single reference atom averaged over a given time period. An example of this could be between the phosphor atoms of the lipid headgroups and the positively charged amine group of a lysine residue (figure 2.7). If these motifs form any strong interactions between them, a peak will be seen in the RDF as it is more likely for a phosphate atom to be positioned at this specific distance from the amine groups at a given time point due to this distance yielding the optimal strength of the interaction. Moving further away from the reference atom the exact position of the phosphor atoms will be more variable as the interactions are weaker, leading to a flattening of the curve.

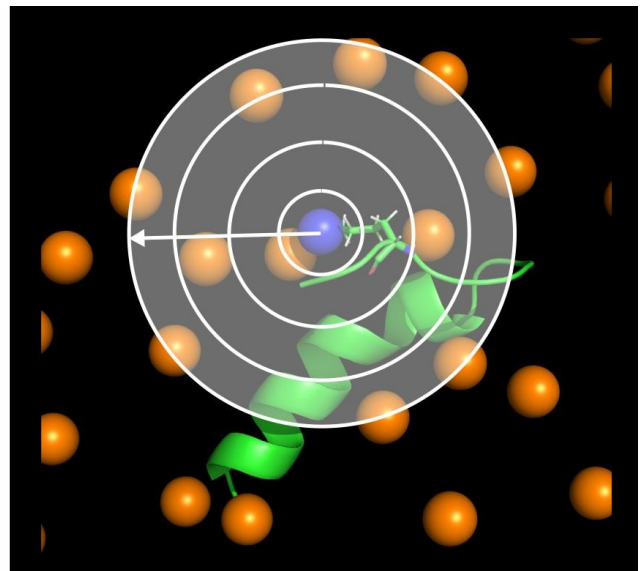
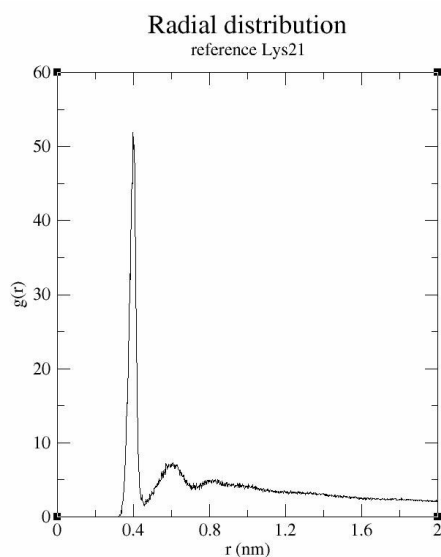


**Figure 2.7 Correlation between the 3D structure of the peptide and lipids and the radial distribution function.** The density of the lipid phosphate atoms (orange) is calculated relative to an amine group of a lysine residue sidechain (blue). The lysine is close enough to interact with one phosphate group so its position over time relative to the lysine will be constricted leading to a peak in the graph. The remaining phosphate groups are too far away for strong interactions to occur so they will move around leading to a flattening of the curve.

After a simulation had reached an equilibrium state, the Z-axis position of the peptide relative to the bilayer can be evaluated by calculating the partial density profiles of specific molecular components of the model. The partial density profile provides a clearer overview of the positional distribution of a set of atoms once an equilibrium has been reached and when multiple density profiles are combined from the same simulation it can create a 2D representation of the model (figure 2.8). The average position of each molecular group can be further quantified by fitting the data to a Gaussian distribution. The density profiles were calculated using the gmx density function, with the `-center` option which ensures that the results are calculated relative to the centre of the bilayer.

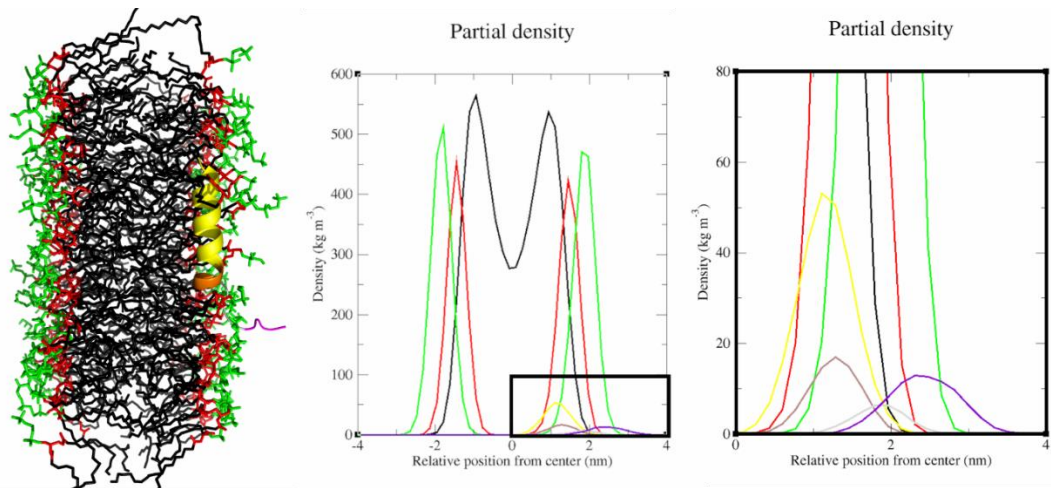


**Figure 2.8 Correlation between the 3D structure of the peptide/bilayer and the partial density profiles.** The middle graph represents the density profile of the entire system, while the right graph is zoomed in to highlight the positional distribution of the peptide. Green = lipid headgroups, red = lipid glycerol groups, black = lipid acyl chains, yellow, brown, grey and purple = different parts of the peptide structure.

Another way a peptide can interact with a bilayer is through the formation of hydrogen bonds. The average number of hydrogen bonds between a peptide and a bilayer over a specific period of time was calculated using the gmx hbond function. The hydrogen bonds were determined based on the hydrogen - donor – acceptor angle and the distance between the donor and acceptor (figure 2.9). The standard cutoff values of  $30^\circ$  (max deviation from the ideal  $180^\circ$  hydrogen-donor-acceptor angle) and 0.35 nm were used.

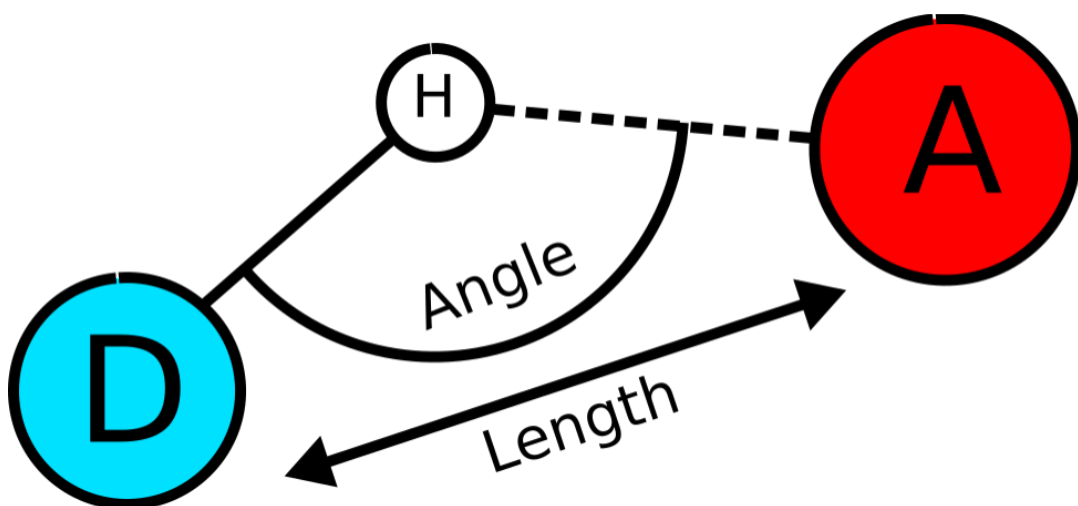


**Figure 2.9 Schematic of the geometric parameters used to determine the occurrence of a hydrogen bond.**

#### 2.7.4 Energy calculations

The key method used for evaluating the strength of the overall interactions between the peptide and the bilayer was to estimate the relative binding free energy using the MMPBSA method (154). Using this method, the difference in the Gibbs free energy between the bound complex (peptide + bilayer) and the peptide and bilayer on its own is calculated. The Gibbs free energy of each part is based on three terms, the molecular mechanics energy plus the solvation energy minus the temperature adjusted entropy. The molecular mechanics energies are based on the bonded and non-bonded (electrostatic and van der Waals) energy for the component in vacuum, calculated based on the topology parameters from the MD simulation's force field. The solvation energy is based on two terms, the polar and non-polar solvation energies. They represent the energy contributed to the system due to the solvation of the different molecular components. This is critical to consider when investigating the binding between a ligand (in this case the peptide) and its target (in this case the bilayer), as it often involves the removal of hydrogen bonds between the solvent and the ligand/target which has a relatively large energy cost associated with it. The polar solvation energy is calculated based on the Poisson–Boltzmann equation, while the non-polar solvation energy traditionally is based on the solvation accessibility surface area (SASA). However, in this study a more modern approach to calculating the non-polar solvation energy is used where it is based on two terms, the cavity and dispersion terms. The cavity term is still based on the SASA while a surface-integration method is used to calculate the dispersion term. The entropy can be estimated based on several different methods added to the MMPBSA calculations, with normal mode analysis being the most common. However, for large biological systems this is very computationally demanding and thus the entropic term is often omitted from the energy calculations (117, 123, 125-127, 135). This means that absolute binding energy values are not experimentally correct. However, when comparing two systems (such as two simulations with different bilayers) the effect of the entropic term is expected to be relatively small. As such the relative comparison between the two systems is still relatively accurate when based on only the standard MMPBSA calculation. The three components of the system (complex, peptide, bilayer) that the energy calculations are based on, can be obtained via two different approaches. In the multi-trajectory approach each component is simulated by itself, increasing the

computational demands but potentially also improving the accuracy. However, for AMPs this approach is not used as simulating the peptide by itself in water likely would lead to a highly variable unordered structure. This would introduce a high degree of variation in the energy calculations, making comparisons much less consistent. Instead, a single trajectory approach is used, where all three components are taken from the same simulation. Thereby the structure of the peptide itself is the same as in the complex so the energy differences are only based on how strong the interactions with the bilayer are.

In some cases, the energy contributions were further evaluated on a per-residue basis using a decompositional energy study of the binding energy. This allows for the investigation of the energetic influence of individual residues/regions of the peptide. However, as the solvation energies are not strictly decompositional the focus of this analysis is on the direct electrostatic and hydrophobic interactions (155).

### 3. Development of a sol-gel coating as a drug delivery system for Smp24

#### 3.1 Introduction

Previously at Sheffield Hallam University sol-gel coatings have been developed for a range of different applications such as corrosion inhibition and antifouling (156-158). Another application has also been as an antimicrobial coating for preventing biofilm related infections during hip or knee arthroplasty (139). The sol-gel was functionalised to gain antimicrobial properties via the incorporation of gentamicin, a concept which could be replicated with other antimicrobial agents such as AMPs. A unique aspect to the formulation is that it contains two polymeric components, both classic sol-gel organosilica precursors which are hydrolysed to yield a relatively hydrophilic polymer network and the more hydrophobic preformed silica polymer PDMS. This hybrid composition could provide a starting point for controlling the elution of AMPs both via physical entrapment and direct interactions between the peptide and matrix.

Another previous discovery at Sheffield Hallam University is the natural AMP Smp24, originally derived from the venom of *Scorpio maurus palmatus* (137). This peptide was chosen to be incorporated in the coating, in order to provide it with improved biofilm inhibitory properties. The peptide is cationic, adopts an amphiphilic helical structure in a membrane mimicking environment and has a broad spectrum of activity against clinically relevant, biofilm forming pathogens such as *E. coli*, *S. aureus* and *P. aeruginosa* (137, 149). The peptide also has some intrinsic antibiofilm properties below its MIC explored in chapter 6.

In order to explore the peptide-matrix interactions, the general behaviour of the coating and the parameter range within which the formulation is functional, two key components of the formulation were chosen as variables within the experimental design.

While the effect of changing the concentration of the active pharmaceutical ingredient (API) has been investigated for past sol-gel coatings (42), it is such an important formulation variable that in most circumstances it should be considered when evaluating new drug delivery systems. When developing a formulation with a new API it is critical to have some idea about what concentration of the API can be

added to the formulation while still retaining its properties with a desired range. It is also key to have knowledge about how the API concentration interacts with other formulations variables, in the case the total dose needs to be adjusted later in the development process and other formulation parameters need to be adapted in order to retain the desired behaviour of the formulation as a whole. Therefore, the amount of Smp24 in each sample was chosen as the first formulation variable.

As the investigation of the peptide-matrix interactions was one of the main objectives of the study, the choice of the second formulation variable was focused on parameters that might affect these interactions. Thus, parameters related to either the hydrophobic or hydrophilic properties of the coating were considered, with the amount of PDMS in the formulation chosen in the end. This was done as it was deemed the simplest way to affect the hydrophobic/hydrophilic balance of the sol-gel. Contrary to modifying the organosilica precursors, the PDMS is a single component, and it does not need to be included in the formulation for a coating to be formed. Therefore, variations of the formulation could also be made without any PDMS in it, making it even clearer what effect it has on the coating structure and peptide-matrix interactions.

## 3.2 Results

### 3.2.1 Method development

As a starting point for the formulation development, a previously developed sol-gel production protocol was used (139). This protocol includes the steps necessary to create a basic sol-gel without any API added, a list of components that could make up the sol-gel and a starting point for at which ratios these components should be added. However, several changes had to be made to the protocol and the formulation in order to adapt it for the use of Smp24 as the active pharmaceutical ingredient (API) in the coating.

One key problem was that Smp24 was stored in frozen stock solutions at 20 mg/ml. Previously antimicrobial compounds had been added to the basic sol-gel either directly as a solid to be dissolved in the solvent already present the sol or as a very concentrated solution such that only a small amount (5% vol/vol) of additional water would need to be added (139). However, to achieve the desired levels of Smp24 within

the final coating, the volume of Smp24 stock solution that needed to be added would exceed the volume of the basic sol-gel itself. In principle, it should not matter if additional water were to be added to the sol phase of the sol-gel shortly before the coating procedure, as at this point additional water should not affect the silica crosslinking substantially. The additional water would dilute the sol-gel leading to a thinner coating, but this could be counteracted by increasing the coating volume as most of the additional water should evaporate during the curing process. However, as the sol-gel consists of a mixture of hydrophobic and hydrophilic components the polarity of the solvent in the sol phase is important to facilitate the physical stability of the suspension. In the initial testing of the formulation, partial aggregation of the sol-gel was observed after the addition of water volumes equal to those needed of the Smp24 stock solution. A small quantity of the hydrophobic red dye Oil red O was added to the sol-gel in order to further evaluate what was happening. Depending on the amount of water present, two different phenomena were seen. Firstly, at the highest volumes of added water, the hydrophobic components of the sol-gel would aggregate in the sol phase, seen by the formation of a red aggregate at the bottom of the sample tube. The remainder of the sol phase would become clear, indicating that all hydrophobic components had been removed from solution (Figure 3.1A). Secondly, if the volume of water was reduced, the physical stability of the sol-gel in the sol phase could be retained. However, after the sol was coated onto the substrate (glass coverslip) and allowed to cure, formation of large, hydrophobic, droplet shaped aggregates were seen in the finished coating and the overall coverage of the substrate was often uneven (figure 3.1B). Both problems were only exacerbated if the proportion of PDMS was increased in the formulation, further indicating that this was due to the hydrophobicity of the sol-gel.

Both phenomena can be explained based on how the additional water changes the total polarity of the solvent phase. During the sol stage of the sol-gel production, the sol-gel consists of a silica nanoparticle network and the PDMS, suspended in a solvent phase consisting of water, 2-propanol added during the production and ethanol and methanol which are the hydrolysis products from the polymerisation reaction. The increased water concentration changes the bulk polarity of the solvent to such an extent that the PDMS can no longer stay in solution. Even if the water concentration is

kept below this point, aggregation of the PDMS can still occur during the curing process. The different solvent molecules do not have the same evaporation rate as the more hydrophobic components which evaporate much faster than water. This means that the relative proportion of water in the solvent will increase over time during the curing process (159), leading to the polarity of the solvent phase again reaching a point where aggregation of PDMS occurs.

Several solutions were considered to circumvent these problems: In principle the Smp24 could also be added as a solid directly into the sol-gel by freeze-drying the peptide first. However, with the <1mg amounts needed to be added for each sample this was not deemed a practical solution. The total volume of peptide loaded sol-gel could be scaled up to make the amounts more manageable, but due to the high cost of Smp24 this would not be an economical solution. The Smp24 could also instead be added with the nitric acid during the production of the basic sol-gel, thereby avoiding the need to add additional water afterwards. However, this would mean that before the coating could be made Smp24 would have to be in an acidic, oxidative, room temperature solution for 3 days during the aging of the sol-gel in its sol form. While it was not investigated it is likely that under such conditions a significant proportion of the peptide molecules would be degraded, reducing the antimicrobial effectiveness of the finished coating. Finally, two approaches were identified which did not have the previous downfalls. Firstly, after the aging stage but before adding the additional water to the sol-gel an equitant volume of 2-propanol was mixed into the sol-gel. This ensured that the balance between the hydrophobic and hydrophilic components of the solvent phase were not affected by the additional water. Using this approach, 2 times the sol-gel volume of water could be added without causing aggregation of the PDMS in the sol phase (figure 3.1A left). While this also did improve the aggregation problems during the curing process somewhat, it was still deemed unacceptable especially if higher PDMS concentrations were used. Therefore, a second modification was made, changing the type of PDMS used in the formulation. In the original formulation the PDMS had its polymer terminals end capped with methyl groups and therefore it would only be incorporated into the sol-gel network only by physical entrapment. In the new formulation, the PDMS type was changed to PDMS-OH which has a free hydroxyl group in each terminal end. This makes the chemistry of the

terminals similar to that of the hydrolysed silica precursors and thus the preformed PDMS-OH polymers could potentially be covalently incorporated within the sol-gel network. Incorporation of PDMS-OH in silica sol-gels has been investigated in previous studies, showing that covalent PDMS-OH incorporation in a TEOS sol-gel occurs (160). The rationale for this modification was that covalently binding the PDMS-OH to the sol-gel network could inhibit the ability of the polymer to aggregate into these large macroscopic defects seen in figure 3.1B. The modification did improve the look of the final coatings, although with the highest level of PDMS-OH in the coating some small hydrophobic aggregates were still visible to the naked eye (figure 3.4). Still, the overall macroscopic structure and homogeneity of the coatings were deemed to be at an acceptable level after the changes to the protocol/formulation.

A schematic overview of the different steps in the final sol-gel production procedure can be seen in figure 3.2 also highlighting how the polarity of the solvent and sol-gel components changes throughout the procedure.

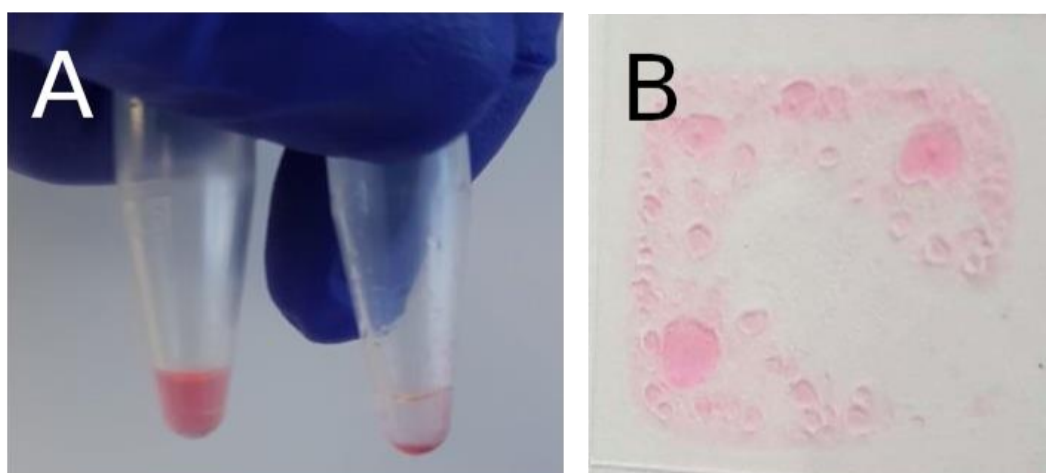


**Figure 3.1 Examples of sol-gel where the hydrophobic and hydrophilic parts have separated.**

A) Two different preparations of the sol-gel mixture before coating. In the left tube the sol-gel is well dispersed due to the addition of extra 2-propanol as indicated by the homogeneous red colour. In the right tube too much water had been added, leading to precipitation of the hydrophobic parts of the sol-gel, seen as a red precipitate. B) An example of the separation happening during the curing of the coating leading to large red droplets and uneven coating of the substrate.

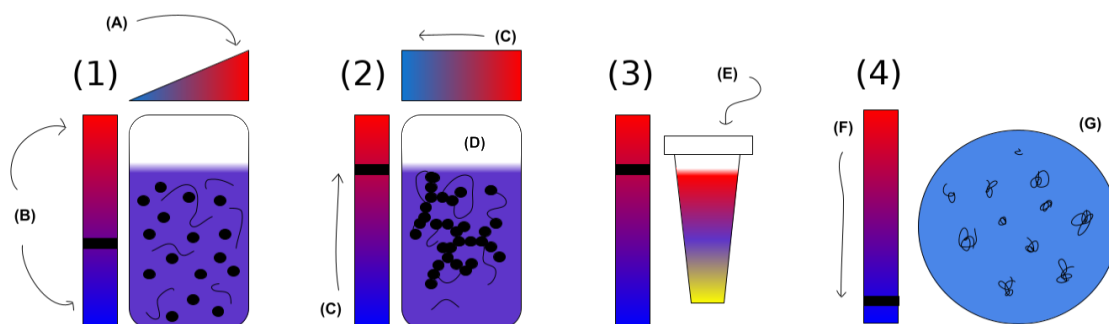


**Figure 3.2 Schematic overview of the production of the sol-gel coating. Step (1), the sol-gel precursors, PDMS and the solvent mixture are slowly mixed together.** (A) Initially all the silica compounds added to sol-gel are predominantly hydrophobic. (B) A solvent mixture made of 2-propanol and dilute nitric acid is used. The nitric acid serves as the catalyst for the polymerization reaction but is highly hydrophilic. Therefore, the more hydrophobic but still miscible solvent 2-propanol is also added to improve the suspension of the silica compounds. **Step (2), the sol-gel is aged for 3 days.** (C) The ether sidechains of the organo-silica precursors are hydrolysed making the silica compounds more hydrophilic. This also releases ethanol and methanol to the solvent, making it overall more hydrophobic. (D) The newly hydrolysed hydroxyl groups of the silica precursors condense together creating a branched polymer network. The hydroxyl terminals of the PDMS also allow these preformed chains to be covalently incorporated into the rest of the sol-gel. **Step (3), the coating mixture is prepared.** (E) One part sol-gel is mixed with either two parts 20 mg/ml Smp24 or one part 20 mg/ml Smp24 and one part water. Two parts 2-propanol are also added in order to conserve the hydrophobicity of the solvent and avoid precipitation of the sol-gel. **Step (4), the sol-gel mixture is coated onto a 13mm glass cover slide and cured at RT overnight.** (F) As the solvent starts to evaporate during the curing process, the hydrophobic solvents will evaporate at the fastest rate reducing the overall hydrophobicity of the solvent. (G) The change in the solvent composition will course the hydrophobic regions of the sol-gel (the PDMS) to precipitate the first, creating small hydrophobic domains throughout the coating.

### 3.2.2 Formulation overview

For each of the two formulation variables three different levels were chosen (table 3.1). In each case the lowest level was set as either no PDMS-OH or no Smp24 added to the formulations, allowing for the evaluation of the coatings completely without these components. The middle level of PDMS-OH was set to the same as used in the original formulation, with the highest level set as double that amount after initial testing showed that a reasonable looking coating could be made at this level.

The middle and high levels of Smp24 were chosen based on previous experience using the antimicrobial lipopeptide daptomycin as a model drug while establishing the protocols for some of the coating evaluation methodologies and some limited testing

using Smp24 at a range of concentrations. 150 µg Smp24 per sample was found to be the minimum level of peptide needed to ensure a consistently quantifiable peptide elution, with double that amount chosen as the highest level.

Based on these variables, coatings were made from a total of 9 different sol-gel formulations. Variable levels and name scheme can be seen in the table below (table 3.1).

**Table 3.1 Overview of the different formulations and formulation variable levels.**

		Smp24 per sample		
		0 µg	150 µg	300 µg
PDMS-OH per batch	0 µl	0B (no PDMS, no Smp24)	0L (no PDMS, low Smp24)	0H (no PDMS, high Smp24)
	200 µl	1B (low PDMS, no Smp24)	1L (low PDMS, low Smp24)	1H (low PDMS, high Smp24)
	400 µl	2B (high PDMS, no Smp24)	2L (high PDMS, low Smp24)	2H (high PDMS, high Smp24)

### 3.2.3 Evaluation of sol-gel only coating morphology

A key step in understanding why two coatings might behave in different ways is to investigate the microscopic structure of coatings. As some of the coatings used in this study were made from a hybrid of both more hydrophobic and more hydrophilic polymers their microscopic distribution throughout the coating was investigated. This was again done by adding the red dye Oil red O to the coating. This dye is very hydrophobic and commonly used to stain lipids in biological samples. Therefore, if the structure of the sol-gel is split into hydrophobic and hydrophilic phases most of the dye molecules would accumulate within the hydrophobic phase colouring it red. The coatings were investigated using brightfield microscopy using two different microscopes, with one allowing for capturing a slightly magnified image of the whole sample and the other allowing for higher magnification images of smaller sections. To limit the use of the expensive Smp24 these investigations were only done for the

formulations without peptide added. This would still give a baseline understanding of the effect PDMS-OH has on the microscopic structure without complicating it with the peptide-matrix interactions.

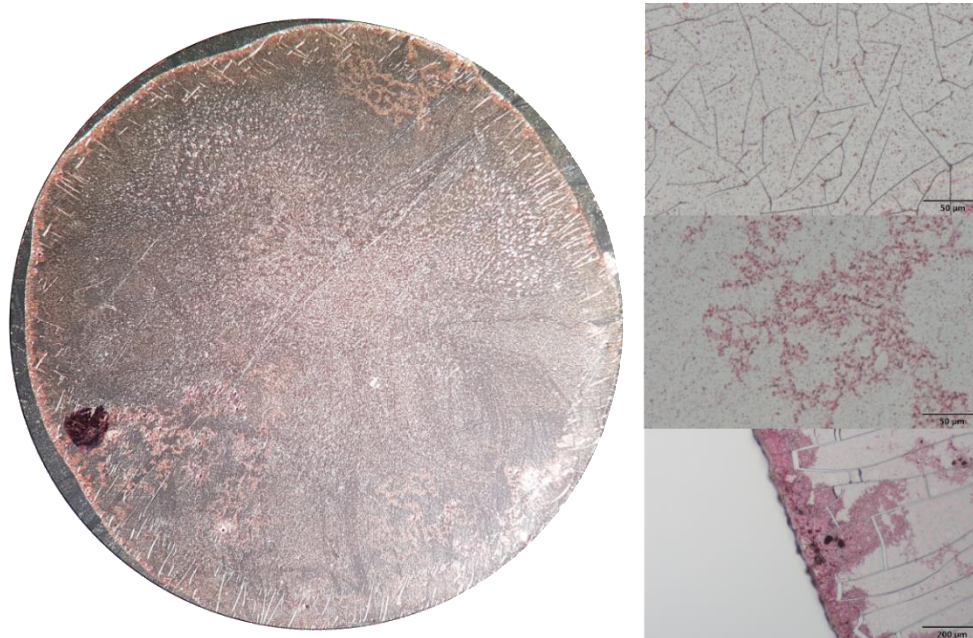


**Figure 3.3 Morphology of the 0B (no PDMS, no Smp24) formulation doped with Oil red O.** Macroscopic image taken at about 1.5x magnification. Top and bottom microscopic image showing the different morphology at the central parts of the coating at 40x magnification. Bottom microscopic image shows the morphology at the edge of the coating at 10x magnification.

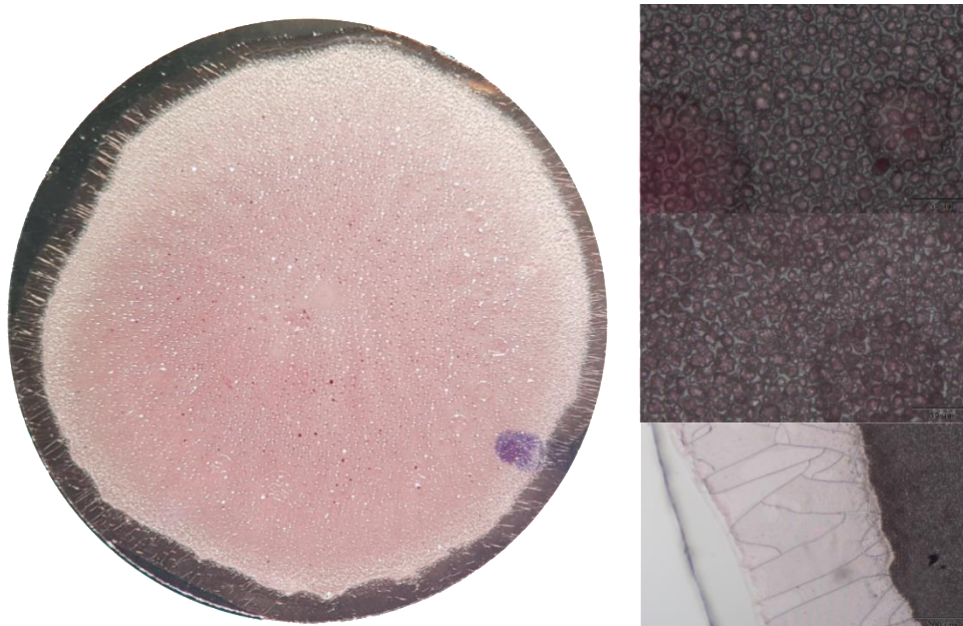


**Figure 3.4 Morphology of the 1B (low PDMS, no Smp24) formulation doped with Oil red O.** Macroscopic image taken at about 1.5x magnification. Top and bottom microscopic image showing the different morphology at the central parts of the coating at 40x magnification. Bottom microscopic image shows the morphology at the edge of the coating at 10x magnification.

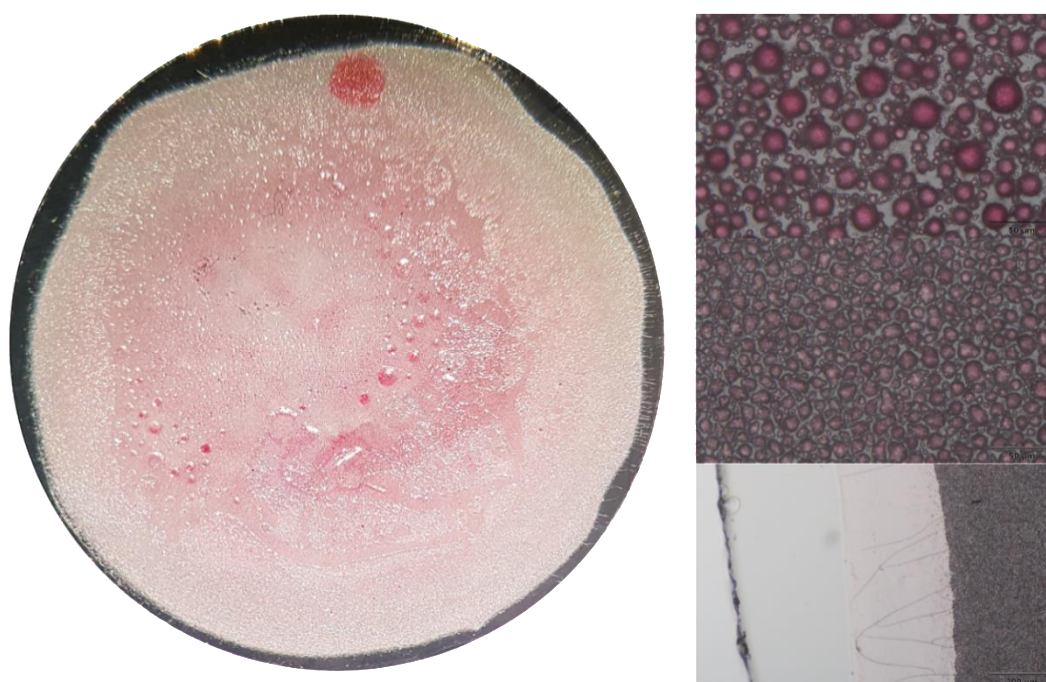


**Figure 3.5 Morphology of the 2B (high PDMS, no Smp24) formulation doped with Oil red O.** Macroscopic image taken at about 1.5x magnification. Top and bottom microscopic image showing the different morphology at the central parts of the coating at 40x magnification. Bottom microscopic image shows the morphology at the edge of the coating at 10x magnification.

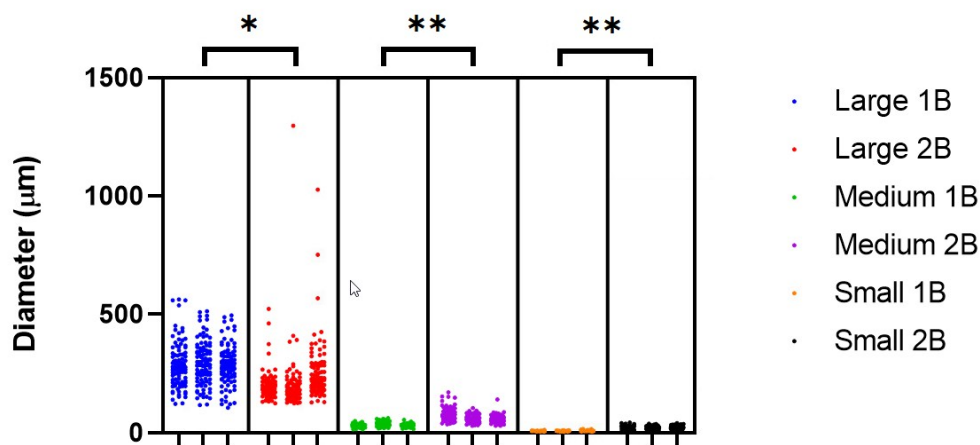


**Figure 3.6 Average diameter of three categories of hydrophobic domains in the blank formulations containing PDMS-OH.** Blue = large domains, low PDMS-OH samples, red = large domains, high PDMS-OH samples, green = medium domains, low PDMS-OH samples, purple = medium domains, high PDMS-OH samples, orange = small domains, low PDMS-OH samples, black = small domains, high PDMS-OH samples. n=100, N=3

Without PDMS-OH in the formulation the microscopic structure of coating was transparent and homogeneous with frequent cracks both independent and branched (figure 3.3). In most regions of the coating, small red dye particulates were relatively evenly distributed throughout the coating without any distinct structures of high dye accumulation. However, in some parts red fissure-like structures could be seen. Further magnification revealed that these structures were made from areas of slightly larger and more densely distributed dye particles, but no differences in the sol-gel structure itself was visible.

For the two formulations with PDMS-OH the structure changed drastically (figure 3.4 and 3.5). In both cases the structure resembled an oil in water emulsion, with droplet shaped hydrophobic domains coloured by the red dye distributed throughout a clear phase with occasional dye particulates. The microscopic cracks seen in the first coating were no longer present. The hydrophobic domains could roughly be separated into three general size groups. The largest domains had a diameter above 100 µm, were located closer to the surface of the coating and were dispersed much less consistently throughout the coating than the others. The medium and small domains were distributed much more consistently throughout the coating and make up the majority

of the microscopic structure. The sizes of these domains were estimated based on 100 domains from three samples (figure 3.6), with both the small and medium size domains being significantly larger for the coatings with the highest level of PDMS-OH. Additionally, the domains also seemed to be less densely packed at the highest PDMS-OH level.

For all three formulations the morphology of the edge of the coatings deviated somewhat from the rest of the coating. In the samples without PDMS-OH the edge had a much higher concentration of dye particles but otherwise the structure was relatively similar. For the formulations with PDMS-OH the hydrophobic domains become smaller and smaller until they reach a point where they seemingly stopped occurring. After this point the morphology changed, becoming clear with cracks, looking similar to that of the coating without PDMS-OH.

#### 3.2.4 MALDI-TOF profiling of the sol-gel Smp24 system

The heterogeneity of the hybrid hydrophobic/hydrophilic structure of the sol-gel coatings containing PDMS-OH raised concerns about how this would affect the 2D distribution of the AMPs across the 2D plane of the coating. One could imagine that in a coating with a nonuniform structure some regions of the coating surface could contain less of the API than others. If this was the case, these regions could potentially serve as hotspots where bacterial attachment and biofilm formation could be more likely. On a small scale this would not be a problem as the non-covalent encapsulation of the AMPs ensures that they can diffuse into areas above the coating where the concentration gradient is lower and thereby still cover these areas. However, if the areas of low peptide loading are large and the media exchange is limited, local variations in the peptide concentration might start to become a problem.

Therefore, to evaluate the 2D distribution of Smp24 in the loaded sol-gel coatings MALDI-ToF mass spec imaging was used. However, before imaging of the coatings could be performed, profiling of the Smp24 in the sol-gel formulations needed to be done to evaluate which components of the formulations could be detected. Profiling of a pure Smp24 stock solution was done by mixing it with the MALDI matrix  $\alpha$ CHCA which gave a clear spectrum with two main peaks located at around 2578  $m/z$

corresponding to the  $[M+H]^+$  and one at around 2600  $m/z$  corresponding to the  $[M+Na]^+$  (figure 3.7A). Several lower intensity peaks could also be seen with lower  $m/z$  ratios, which could be due to impurities, fracturing of the peptide, other peptide charge states or a combination of the three. More detailed analysis of these peaks would have required additional calibration of the mass spec method, but for imaging purposes the clear detection of the two main peaks with the highest  $m/z$  ratio was deemed sufficient.

In the next stage of the profiling, spectra were captured for peptide loaded and blank sol-gel samples, again using  $\alpha$ CHCA as the MALDI matrix (figure 3.7 C-E). Without Smp24 in the sample, signals were only seen below a  $m/z$  ratio of 1000. This was ideal as it meant that the signals corresponding to the sol-gel coating itself would not overlap with the main peptide signals. The sol-gel samples with Smp24 added all showed clear peaks responding to Smp24 independently of the PDMS-OH level. In addition, some smaller signals could also be seen in the region below a  $m/z$  of 900, which correlated to the signal observed for the unloaded sol-gel samples.

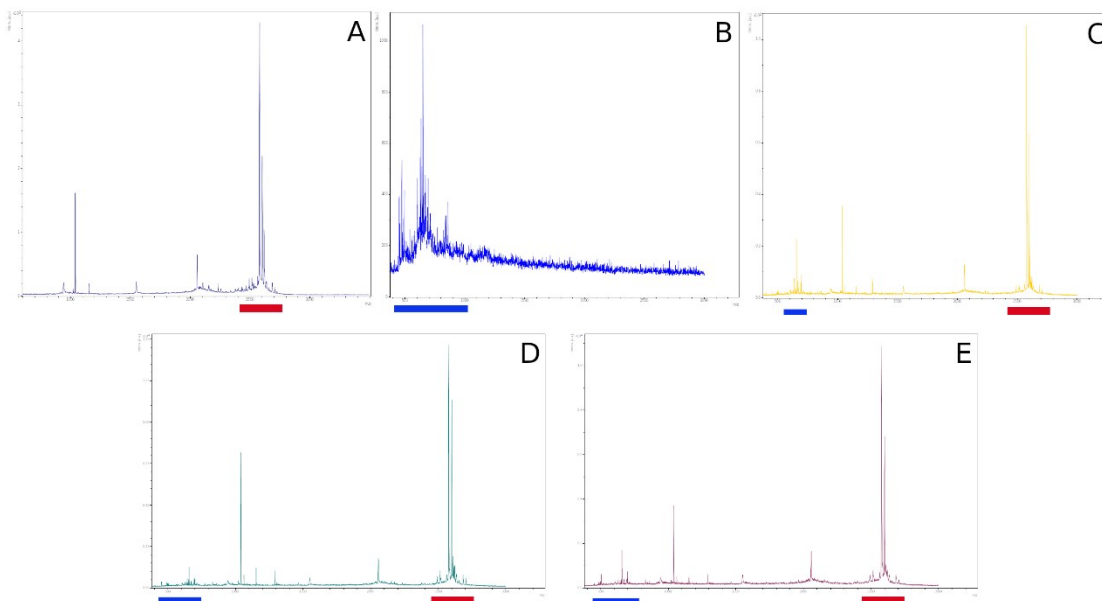


**Figure 3.7 M/z spectra from MALDI-TOF profiling of the smp24 sol-gel system using  $\alpha$ CHCA as the matrix.** A = 100  $\mu$ g/ml Smp24 without solgel, B = example of spectrum for sol-gel coating without peptide encapsulated (1B (low PDMS, no Smp24)), C = spectrum for formulation 0L (no PDMS, low Smp24), D = spectrum for formulation 1L (low PDMS, low Smp24), E = spectrum for formulation 2L (high PDMS, low Smp24). Main peptide peaks marked with red, sol-gel matrix peaks marked with blue.

Overall, these observations were taken as a strong indication that the peptide distribution would be possible to investigate using the imaging technique. However, to further understand the mechanistic behaviour of why some regions might have a higher peptide localisation than others, it would be ideal to also detect other components of the sol-gel to evaluate if they would be co-localized with the peptide. The most obvious candidate would be PDMS-OH as it is the main hydrophobic component of the coatings. While the PDMS-OH used in the formulations is a polymer its average molecular mass is 550 Da so it should in principle be detectable at the same time as Smp24 without any overlap in their signals. However, using  $\alpha$ CHCA as the MALDI matrix no discernible difference were observed for the sol-gel related peaks when comparing between the samples with and without PDMS included, both with (figure 3.7 C-E) and without Smp24 included in the coating (data not included).

To further explore if both Smp24 and PDMS-OH could be detected at the same time, two additional MALDI matrix compounds were tested. 2,5-DHB was chosen as it is a

common alternative to  $\alpha$ CHCA for the analysis of peptides (161), while dithranol was chosen as it commonly used with polymers (162). Both matrixes have also previously been used for the analysis of PDMS polymers (163).

The spectra obtained using 2,5-DHB were relatively comparable with those obtained with  $\alpha$ CHCA. Smp24 was able to be detected while in the sol-gel and produced a spectrum with high intensity peaks for the  $[M+H]^+$  and  $[M+Na]^+$  ions (figure 3.8A). However, the signals corresponding to the sol-gel itself had an even lower intensity making the detection of PDMS-OH even less possible.

Contrary to this dithranol produced a very low intensity signal for the peptide compared with the signal corresponding to the sol-gel itself (figure 3.8B). However, a clear difference between the samples with and without PDMS-OH was still not observed (data not shown).

To ensure dithranol and the method was able to ionize the PDMS-OH, a spectrum was captured with a mix of pure PDMS-OH and dithranol (figure 3.8C). As expected, a clear polymeric mass pattern was observed similar to what has been reported in the literature previously (164). While mass range for the pure PDMS-OH signals does overlap with the signal mass range for the sol-gel samples, the distinct polymeric peak pattern was not present in any of the sol-gel samples. Since 2,5-DHB and dithranol did not allow for the ionisation of both Smp24 and PDMS-OH,  $\alpha$ CHCA was chosen as the matrix for the imaging, as it produced the most intense signals for the peptide.

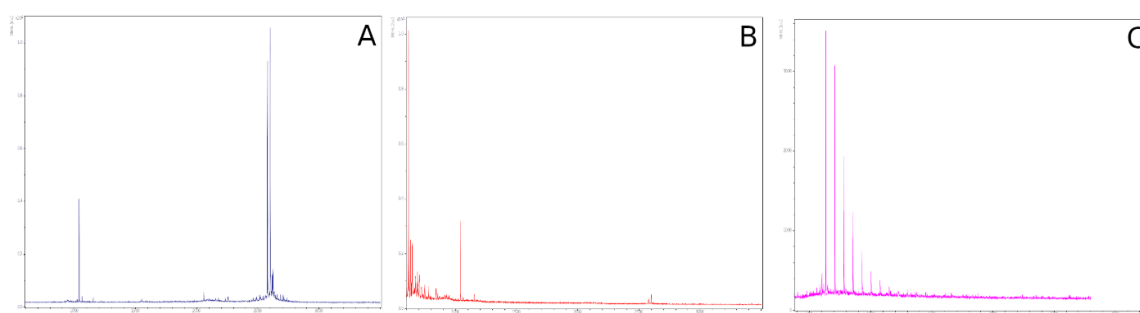


**Figure 3.8 M/z spectra from MALDI-TOF profiling using other matrixes than  $\alpha$ CHCA.** A = spectrum for the solgel with Smp24 (1L (low PDMS, low Smp24)) using 2,5-DHB as the matrix, B = spectrum for the solgel with Smp24 (1L (low PDMS, low Smp24)) using dithranol as the matrix, C = spectrum of pure PDMS-OH using dithranol as the matrix.

### 3.2.5 Evaluation of peptide distribution and integration into the sol-gel

As it would not be possible to determine the co-localisation of the peptide with the PDMS-OH, the peptide distribution was instead compared with the overall morphology of the coatings. Firstly, the coating morphology was evaluated for all the samples using brightfield microscopy. The relationship between the PDMS-OH level and the morphology follows the general trends observed for the samples without peptides. Without PDMS-OH the coatings were transparent and relatively homogeneous but with a high number of microscopic cracks (figure 3.9 and 3.10). However, with the addition of PDMS-OH the coatings become more opaque and with fewer cracks but also much less homogenous both on the macroscopic and microscopic level (figure 3.11-14). The 1L (low PDMS, low Smp24) sample was the most homogeneous on the macroscopic level (figure 3.11). In the microscopic images, a droplet structure like that for the blank samples could be observed especially near the centre of the sample. The macroscopic morphology changes significantly with the higher peptide concentration of the 1H (low PDMS, high Smp24) sample which could be separated into 3 zones (figure 3.12). The outer zone was relatively transparent but black specs and droplet like structures could be observed. The middle zone was completely clear with a microscopic morphology very much like the samples without PDMS-OH. The central zone seemed to be very densely populated with droplet like structures. The morphology of both the 2L (high PDMS, low Smp24) and 2H (high PDMS, high Smp24) formulations were relatively similar (figure 3.13). Most of the coatings' surfaces had a relatively dense and uniform morphology with some larger fissure-like structure seen most clearly in the 2H (high PDMS, high Smp24) sample (figure 3.14). However, both samples also contained a large droplet like spot with a completely different morphology. These spots were not completely unlike the central zone of the 1H (low PDMS, high Smp24) sample but did deviate in that they (especially 2H) had a less clear microscopic droplet structure, had a glossy sheen on the macroscopic images, and seemed to easily crack/delaminate.

The MALDI MSIs revealed several trends regarding the distribution of the peptide signals that were consistent throughout the different samples. For all samples the areas with the highest peptide signals could be found around the outer edge of the

coating. The morphology of the edge of the coating could differ slightly from the bulk of the sample, such as with the 1L (low PDMS, low Smp24) sample where the very edge of the coating was less opaque than the rest of the sample (figure 3.11).

However, the correlation between the high peptide signal and the coating morphology was not consistent throughout the images. Within a single coating such as the 1H (low PDMS, high Smp24) sample, the areas of the edge with a high peptide signal did not seem to have a clear morphological difference from areas with a much lower signal (figure 3.12).

Another trend was that the overall peptide intensity of the bulk region of the coating increased with an increasing level of PDMS-OH in the formulation. The samples without PDMS-OH in the formulation both had a detectable peptide signal throughout the bulk of the sample, but higher laser intensity and longer imaging time was required in order to obtain the images. This was inconsistent with the initial profiling studies where the signal intensity for these formulations was equivalent to the rest. For the formulations with a low level of PDMS-OH the peptide signal was much easier to detect, but still relatively low compared to the hot spots around the edge. At the highest PDMS-OH level this difference between the bulk coating and the hotspots was further diminished.

Lastly, some morphologically distinct regions of the coating did correlate with the peptide signal. The large spots seen for the samples with the highest level of PDMS-OH both had a lower peptide intensity than the bulk of the sample. This was also the case for the centremost region of the 1H (low PDMS, high Smp24) sample although no large difference could be seen between the two other regions (figure 3.12).

Other large morphological features of the coatings were also visible in the MALDI images. In the 0H (no PDMS, high Smp24) sample some flakes of the coating had detached during the matrix deposition (figure 3.10). These were visible as black areas with sharp edges along the top of the MALDI image. The 2H (high PDMS, high Smp24) sample has some regions with a fissure-like pattern which has a slightly darker shade than the bulk coating when observed at high magnification, especially near the centre of the sample (figure 3.14). These patterns could also be seen on the MALDI image, indicated by a slightly higher peptide signal than the bulk coating.

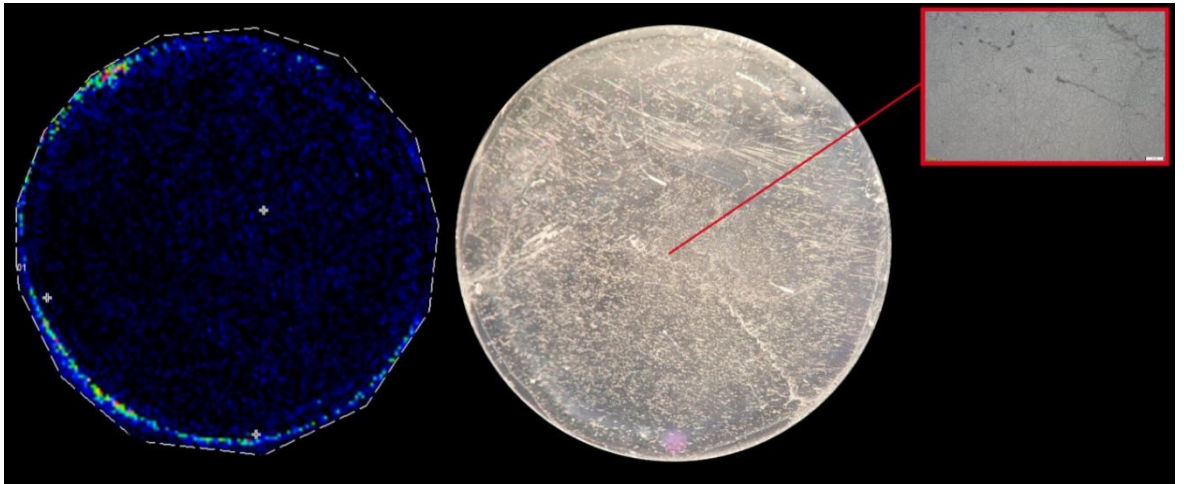


**Figure 3.9 MALDI imaging and brightfield microscopy of 0L (no PDMS, low Smp24) coating.** Left) MALDI image highlighting the local signal corresponding to Smp24. Middle) Macroscopic brightfield image of the sample. Right) Brightfield image at 10x magnification.

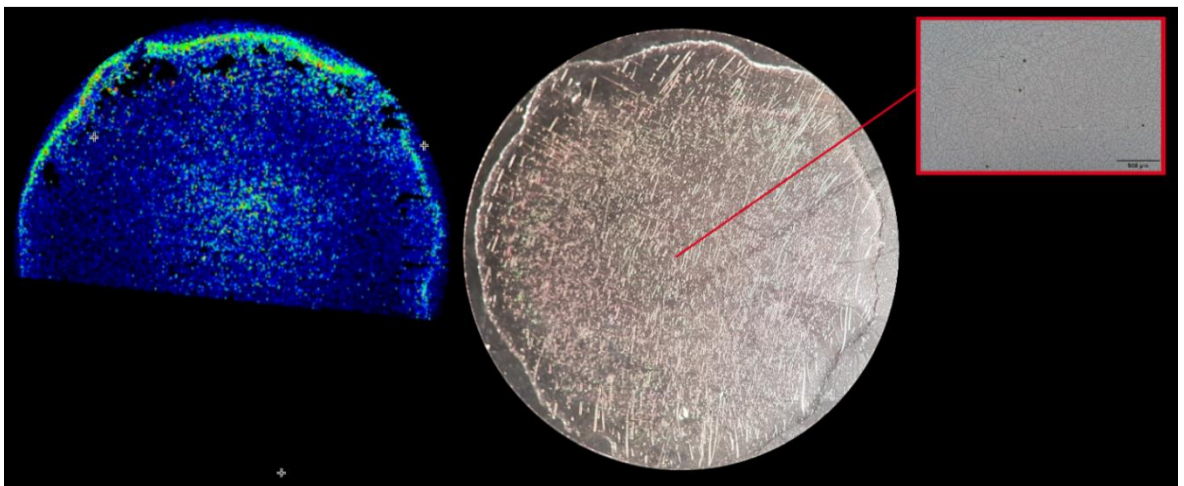


**Figure 3.10 MALDI imaging and brightfield microscopy of 0H (no PDMS, high Smp24) coating.** Left) MALDI image highlighting the local signal corresponding to Smp24. Middle) Macroscopic brightfield image of the sample. Right) Brightfield image at 10x magnification.

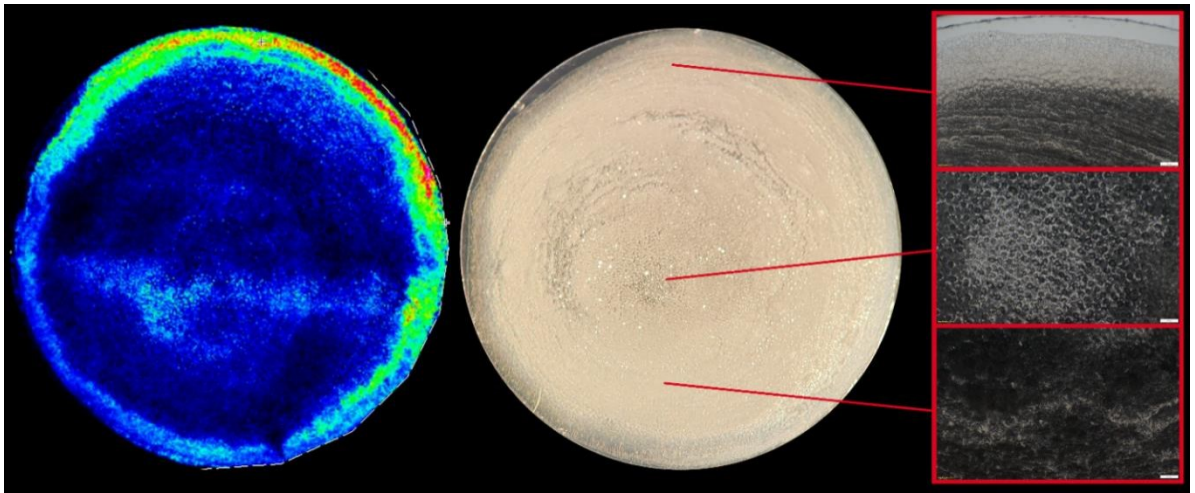


**Figure 3.11 MALDI imaging and brightfield microscopy of 1L (low PDMS, low Smp24) coating.** Left) MALDI image highlighting the local signal corresponding to Smp24. Middle) Macroscopic brightfield image of the sample. Right) Brightfield images at 10x magnification.

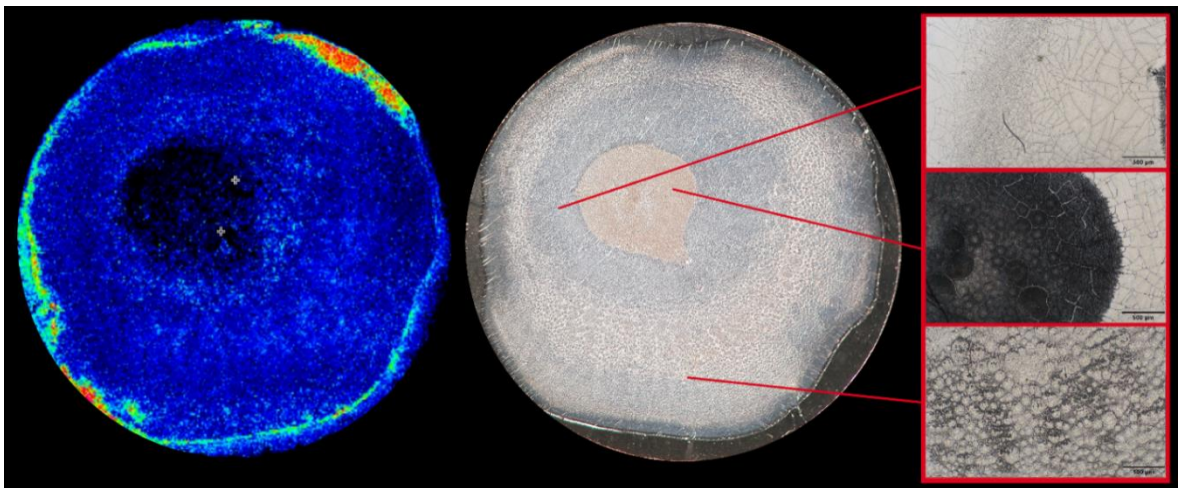


**Figure 3.12 MALDI imaging and brightfield microscopy of 1H (low PDMS, high Smp24) coating.** Left) MALDI image highlighting the local signal corresponding to Smp24. Middle) Macroscopic brightfield image of the sample. Right) Brightfield images at 10x magnification.

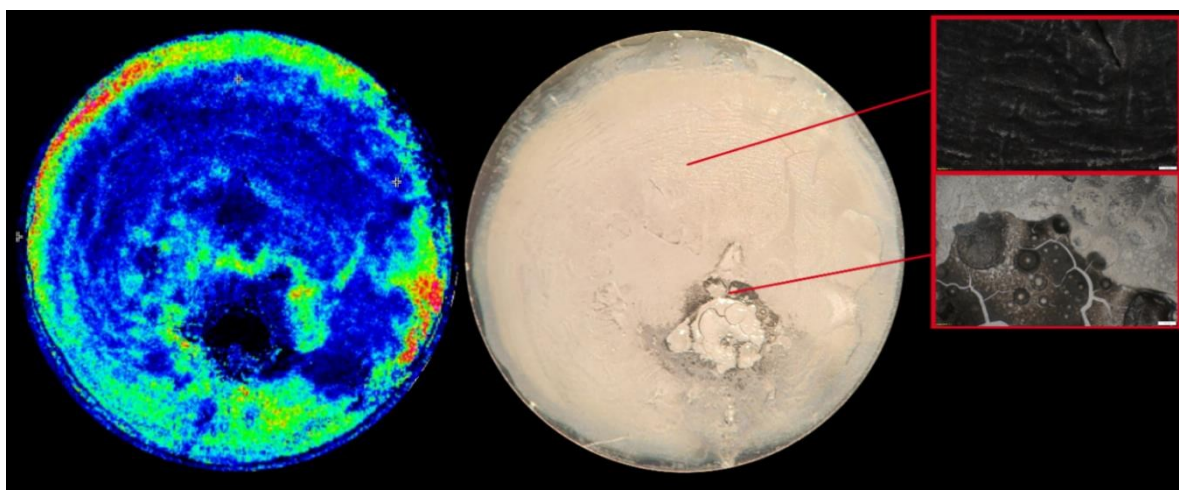


**Figure 3.13 MALDI imaging and brightfield microscopy of 2L (high PDMS, low Smp24) coating.** Left) MALDI image highlighting the local signal corresponding to Smp24. Middle) Macroscopic brightfield image of the sample. Right) Brightfield images at 10x magnification.

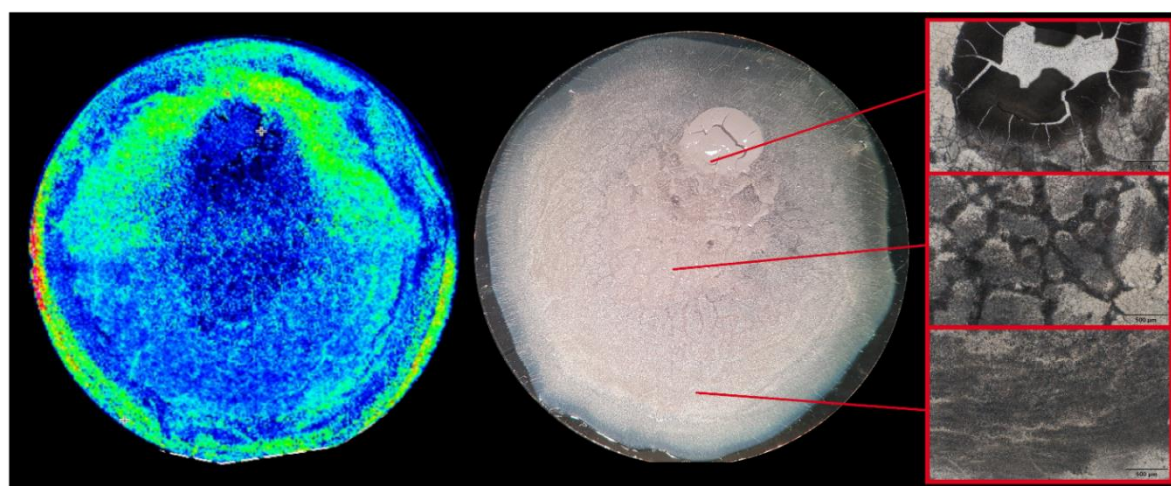


**Figure 3.14 MALDI imaging and brightfield microscopy of 2H (high PDMS, high Smp24) coating.** Left) MALDI image highlighting the local signal corresponding to Smp24. Middle) Macroscopic brightfield image of the sample. Right) Brightfield images at 10x magnification.

### 3.2.6 Evaluation of peptide elution from the sol-gel coatings

The elution of Smp24 over time was evaluated for the 6 formulations containing the antimicrobial peptide over a 4-week period (figure 3.15).

The inclusion of PDMS-OH was the main factor determining the shape of the elution profiles. All formulations with PDMS-OH had an initial burst release of Smp24 over the first 24h, with the degree of initial release increasing with both high PDMS-OH and peptide levels. Both formulations with the highest level of PDMS-OH had released more than 40% of the encapsulated peptide within the first 6h, while the burst was

slightly more gradual at the lower PDMS-OH level. After the initial burst, the peptide elution rate slowed down greatly, giving a relatively steady release rate over the next 4 weeks. At the end of the experiment the high PDMS-OH formulations had released about 75% of the encapsulated peptide, while the low PDMS-OH, low and high peptide samples had released 49% and 62% respectively.

The behaviour of the formulations without PDMS-OH differed greatly. Instead of an initial burst release, the elution rate was relatively slow during the first 24-48h. However, after this point the elution rate increased causing the cumulative release to match or surpass that for the PDMS-OH formulations within the first week of the experiment. After the full 4 weeks of elution more than 94% of the encapsulated peptide had been released from the coating.

The peptide level had a smaller but expected effect on the elution profiles. In all cases the higher peptide level pushes the relative release to occur faster in the beginning of the curve. The peptide level only affected the relative maximum release for the low PDMS-OH level formulations, where the 1H (low PDMS, high Smp24) samples still retained a significantly higher release after the full 4 weeks.

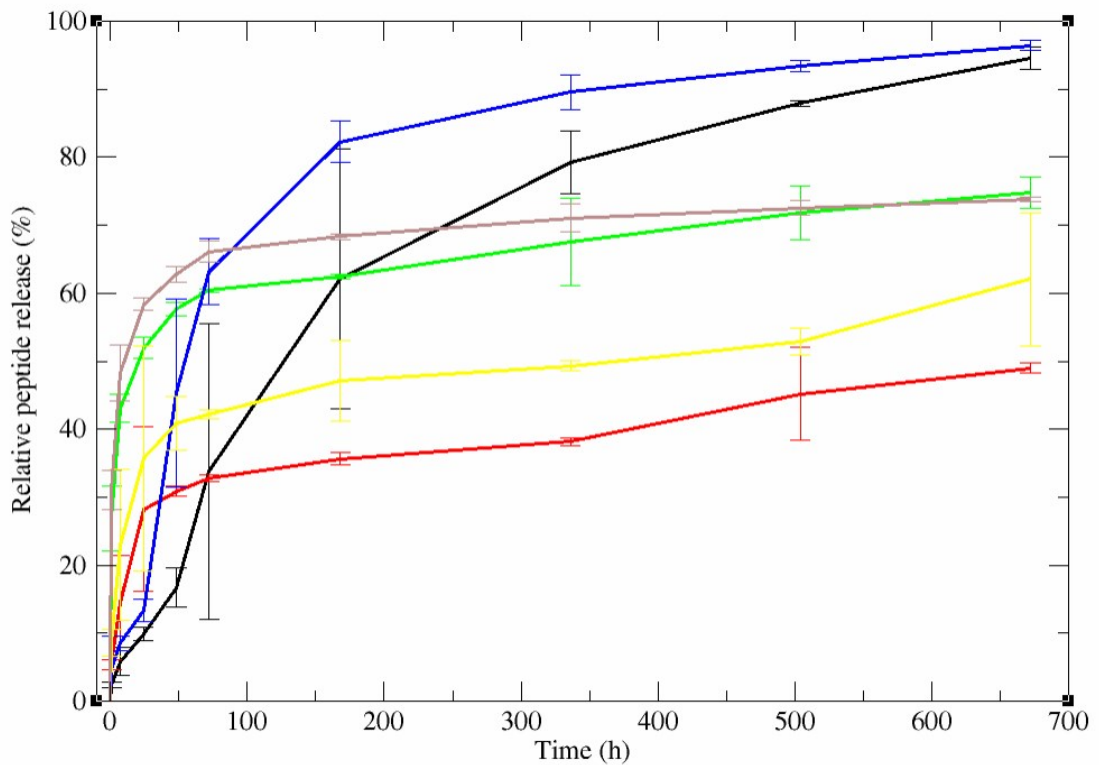


**Figure 3.15. Relative cumulative peptide elution profiles for each formulation type.** Black = 0L (no PDMS, low Smp24), red = 1L (low PDMS, low Smp24), green = 2L (high PDMS, low Smp24), blue = 0H (no PDMS, high Smp24), yellow = 1H (low PDMS, high Smp24), brown = 2H (high PDMS, high Smp24), n=3.

### 3.2.7 Evaluation of the biofilm inhibitory properties of the coatings

To investigate the antimicrobial properties of the different formulations, the reduction in biofilm growth on the coating surfaces was evaluated relative to the biofilm formation on substrate only samples. The evaluation was done for both coatings with and without Smp24 so the intrinsic properties of the sol-gel itself also could be considered. The biofilm inhibition was evaluated against *S. aureus* SH1000 for several reasons. Firstly, *S. aureus* is a clinically relevant pathogen, with Gram-positive staphylococci being the leading cause for medical device related infections and *S. aureus* often leading to particularly serious infections (165). Secondly, Smp24 has previously been shown to have a strong antimicrobial activity against this species with an MIC between 8-16  $\mu\text{g/ml}$  (149). Lastly, *S. aureus* has a low motility meaning that the biofilm growth mainly occurs at the bottom of the well and not in the water air interface (166). Therefore, the same sample types (sol-gel spread on glass coverslips) as used in the other experiments could also reasonably be used for the biofilm

inhibition experiments as the coverslip covers most of the well bottom in a 24 well plate. Some biofilm might still grow around the bottom edge of the well, but if effective, most growth should be inhibited by the presence of the sol-gel sample.

Again, the PDMS-OH level had a major effect on the properties of the formulation (figure 3.16). As expected, the OB (no PDMS, no Smp24) formulation performed similarly to the substrate samples but surprisingly the peptide incorporation in the OL (no PDMS, low Smp24) and OH (no PDMS, high Smp24) formulations did not facilitate a significant improvement in the biofilm inhibition. Even at the highest peptide level the biofilm growth was not significantly lower than on the substrate only samples ( $P=0.376$ ).

With PDMS-OH in the formulation, the biofilm growth was increased on the coatings without peptide, but if peptide was encapsulated, a concentration dependent reduction was seen. Even for the 1L (low PDMS, low Smp24) sample which had the lowest reduction, the biofilm growth was still significantly lower than the control ( $P<0.0046$ ). The biofilm inhibitory effect was greatest for the formulations with the highest level of PDMS-OH, reducing the biofilm growth by approximately 98% at the highest peptide level and 92% at the lowest peptide level. Only peptide loaded coatings with the highest level of PDMS-OH significantly reduced the planktonic bacteria growth.

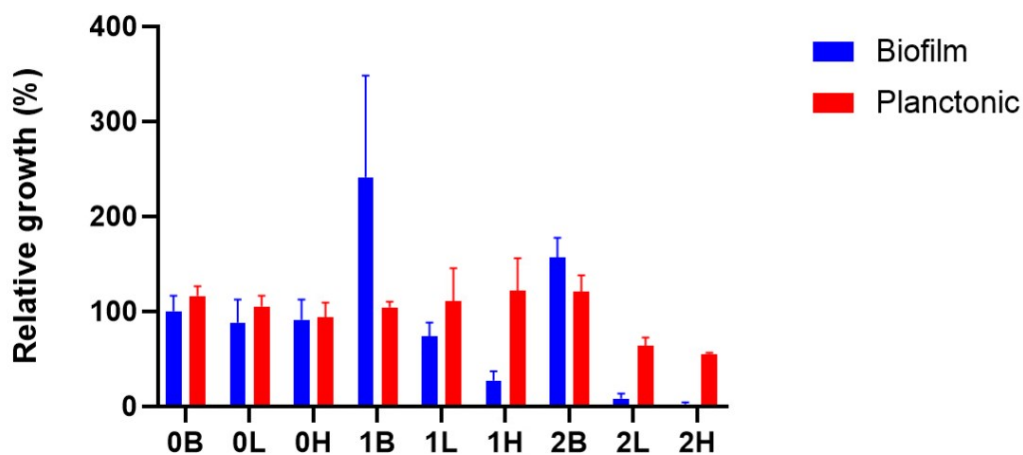


**Figure 3.16 Antibacterial effects of the different formulations against *S. aureus*, relative to substrate only samples.** 0-2 corresponds to the PDMS-OH level, B,L,H corresponds to blank, low and high level of Smp24. Blue = Relative biofilm growth on the surface of the different coatings after 24h, red = relative planktonic growth in the media above the different coatings after 24h. n=3

### 3.3 Discussion

#### 3.3.1 Evaluation of the peptide distribution using MALDI MSI

While MALDI has been used in combination with silica sol-gels before, the focus has not been on analysis of sol-gel based formulations. Instead, it has been used in the methodology called sol-gel assisted laser desorption/ionization mass spectroscopy, where the sol-gel and 2,5-DHB or  $\alpha$ CHCA are mixed to form a hybrid structure/matrix. These hybrid matrixes act like the traditional MALDI matrix but can reduce some of the background signals, which is especially useful when analysing small molecules (167-169). In these cases, the matrix chemical is mixed into the sol directly, something that cannot be done when analysing a standalone formulation/coating without changing its structure. Instead, the matrix chemical must be deposited on/in the coating after the fact which can complicate the interpretation of the final image. Ideally the intensity of the peptide signal at a given point would only be dependent on the local peptide concentration at that point, however for the sol-gel coatings this was likely not the case. The total peptide concentration was the same for all the low peptide samples,

but the signal intensity was very different with the PDMS-OH concentration having a huge impact on the overall intensity of the peptide signal. Therefore, two other factors must also be considered, namely the matrix deposition methodology and the interaction between the coating structure and the peptide desorption/ionization efficiency.

During the optimisation of the MALDI imaging and matrix deposition methodology it was observed that the matrix flow rate had a much greater impact on the peptide signal intensity than the amount of matrix deposited on the sample. Using a low spray speed (2  $\mu\text{l}/\text{min}$ ) the  $\alpha\text{CHCA}$  matrix was mainly deposited on surface of the sample, which did not allow for consistent detection of the peptide. With these parameters the matrix did not come into close contact with most of the peptide population located within coating itself and as such only the small fraction of peptides nearest the surface were effectively ionized. To counteract this, a matrix deposition flow rate (8  $\mu\text{l}/\text{min}$ ) and a lower  $\alpha\text{CHCA}$  concentration was used. This allows the solvent with the matrix to penetrate into sol-gel for a short period of time before it evaporates and thus the MALDI matrix became more evenly distributed throughout the depth of the coating. This greatly improved the intensity and consistency of the peptide signal and thus allowing for higher resolution images to be obtained.

However, a concern in relation to using these parameters might be that the penetrating solvent could either disrupt the structure of the sol-gel or affect the local distribution of peptide. While this might happen on a microscopic level, the macroscopic morphology of the coatings seems to be relatively unaffected by the matrix deposition with macroscopic structures being detectable for both the MALDI and BF images for most of the samples.

One area of the coatings that might be more affected by the high matrix flow rate could be the edge of the sample. The high peptide signal intensity areas could be explained by the thinnest regions of the sol-gel being disrupted by the solvent to a much greater degree. Closer inspection of the images reveals that many of the highest intensity peptide signals originate from the substrate surface outside of the boundaries of the coating itself. These regions could represent an artifact of the matrix disposition and sample disruption rather than an actual high local concentration of

peptide. This could also explain why there did not seem to be a direct correlation between where around the edge these high intensity areas were and the specific morphology of the coating at those points. If the high intensity areas instead are related to coating disruption it is more understandable that one side of the edge might have a higher signal than the other, as there could be differences in the thickness or slight damage during sample handling.

In order to explain the difference in the overall peptide signal related to the level PDMS-OH another factor must be considered. The signal intensity of the different formulations correlates well with the initial burst or lag phase observed in the elution study. This indicates that the signal intensity is also related to how easily the peptide can be physically removed from the formulation. Park *et al.* has previously shown that even weak interactions such as hydrogen bonding between the analyte and the surrounding matrix can significantly reduce desorption/ionization efficiency (170). This effect will likely be even greater if the analyte is strongly physically entrapped within the matrix as is the case with the formulations without PDMS-OH. The greatly reduced desorption/ionization efficiency will thus give the illusion that the peptide concentration is lower than it is. This also lends further credence to the theory that the high signal around the edge could be due to breakdown of the thinner sol-gel during the matrix deposition, as this would result in peptide being released from the polymeric network of the sol-gel improving the desorption/ionization efficiency in that area.

The effect of the formulation composition on the peptide intensity was not observed during the profile study. However, this can be explained by the differences in the way the matrix was deposited onto the coating. During the profiling stage the matrix was added as a single drop onto a small sample of sol-gel which had been directly coated on a metal MALDI sample plate. This single application of a relatively high volume of matrix relative to the coating size/thickness would likely completely disrupt the structure of the coating, releasing the peptide for easy desorption/ionization independently on the formulation composition.

The relationship between peptide signal and the sol-gels effect on the desorption/ionization efficiency can also give additional insight into the interpretation

of each individual image. The central low signal spots on the 1H (low PDMS, high Smp24), 2L (high PDMS, low Smp24) and 2H (high PDMS, high Smp24) could potentially all be as a result of a lower desorption/ionization efficiency. The microscopy image of the central region of the 1H (low PDMS, high Smp24) sample indicates that this zone consists mainly of densely packed PDMS-OH droplets. Thus, this could be an indication that in this formulation the peptides are more strongly entrapped within the coating while associated with the droplets rather than the bulk sol-gel. This could also be the case for the low signal spots on the high PDMS samples which looks relatively similar to the 1H (low PDMS, high Smp24) sample when comparing the MALDI images. However, based on the microscopy images the morphology of these areas do differ greatly. The central spots on the high PDMS-OH samples are smaller, have a completely different gloss/texture, much higher degree of cracking/detachment and especially for the 2H (high PDMS, high Smp24) have a more uniform microscopic structure. This could indicate that these regions are more akin to pure PDMS-OH deposits rather than a PDMS-OH/sol-gel mixture. As such it might be that in these cases the lower peptide signal is actually due to a lower peptide concentration.

While MALDI-MSI could be a powerful method for evaluating API distributions in complex drug delivery systems such as the sol-gel coating used in this study, the many complexities in the method procedure and ambiguity in the image interpretation suggest that more method development is still needed.

One way to improve the consistency of the images and reduce the number of artifacts could be to change the coating methodology used when preparing the sol-gel samples. While the spread coating used in this study produces samples with a very consistent and predictable total API content, the method is not well suited for producing coatings with a consistent thickness throughout the individual sample. Alternative coating methods such as controlled dip-coating or spin-coating could improve the quality of the MSI where the API distribution and sample uniformity is more important than the overall API quantity. Additionally, if the thickness of the sample were more consistent, the spray flow rate used in the matrix deposition could also more easily be optimised to ensure that the necessary matrix penetration is achieved with minimal disruption to the coating structure.

Lastly, for cases such as with the samples without PDMS-OH, further pre-treatment of

the sample might be necessary in order to obtain a better signal. With the current methodology quality images investigating the 2D peptide distribution cannot be obtained as the peptide signal for each spot of the laser is simply too low. However, if the coating was treated with a volatile acid such as TFA before the MALDI matrix, some breakdown of the silica polymer network could occur. If so, this might lead to an improved desorption/ionization efficiency allowing for the capturing of a higher quality image.

### 3.3.2 Peptide-matrix interactions and microscopic structure of sol-gel coatings

All experiments in the study indicate that the inclusion and level of PDMS-OH in the formulation greatly affects the properties of the corresponding coatings. These large-scale behavioural differences seen in the elution rates or biofilm inhibitions are likely downstream effects of how the PDMS-OH affects the microscopic structure of the sol-gel and how the peptides interact with this structure. Based on the evaluation of the different coatings, three microscopic sol-gel structures are proposed (figure 3.17):

Without the addition of PDMS-OH it is clear from the different microscopy images that the sol-gel structure does not contain distinct hydrophobic domains. Instead, the sol-gel only consists of a tight, homogenous silica polymer network with the peptides physically entrapped within. The low initial release rate, desorption/ionization efficacy and biofilm inhibition all indicate that peptides initially are strongly encapsulated within the coating reducing their ability to encounter the bacteria on the surface of the sample. This is due to the relatively large size of the peptides limiting their ability to diffuse through the initially small pores in the sol-gel network. Previous studies have shown that the pore size of silica sol-gels increases over time after immersion in water due to hydrolysis of the silica network (171), with the elution profiles indicating that the pore size reaches a point that allows for rapid diffusion of the peptide out of the coating after 24-48h. This initial lag-period in the peptide release is likely also the reason why the coatings without PDMS-OH show no significant biofilm inhibition, as the experiment is only done over a 24h period. However, after the lag-period the peptides are no longer strongly entrapped within the sol-gel network and the interactions between the peptides and the sol-gel are mostly limited electrostatic

interactions with the hydroxy groups. Therefore, almost all of the peptides eventually will be eluted from the system, indicated by the high maximum release after the 4-week period.

The addition of PDMS-OH to the sol-gel drastically changes the microscopic structure of the sol-gel. As previously described, the addition of PDMS-OH to the formulation facilitates the formation of hydrophobic domains during the curing process as the more hydrophobic solvents evaporate leading to the aggregation of the PDMS-OH polymers. These domains can to some extent mimic the physicochemical properties of a phospholipid vesicle/micelle with a hydrophobic core and a more hydrophilic surface in the interface with sol-gel network. Due to the amphiphilic structure of AMPs, their interactions with hydrophobic/hydrophilic interfaces are highly favourable as both the hydrophobic and the hydrophilic/charged residues can form thermodynamically favourable interactions with the surrounding environment at the same time (172). It is thus likely that if AMPs are added to the formulation, a large proportion of them will accumulate around the surface of the hydrophobic domains. Such principles have previously been demonstrated for other hydrophobic/hydrophilic AMP formulations, showing a change in the secondary structure of the peptide upon encapsulation indicating direct interactions between the peptide and the hydrophobic moieties (173). Due to the increased interactions between the peptides and the hydrophobic domains compared with the bulk sol-gel it is likely that these peptides will be more strongly encapsulated. This provides a possible explanation for why the central region in the 1H (low PDMS, high Smp24) sample has a lower peptide signal compared with the rest of the coating and why the formulations with PDMS-OH have a lower maximum peptide release after the 4 weeks.

However, the formation of the hydrophobic domains is likely not the only way the addition of PDMS-OH affects the sol-gel structure. Several studies have previously shown that the addition of PDMS-OH to silica sol-gels increases the pore-size of the silica network, although length of the PDMS-OH polymers used in these studies are much longer than the one used in this project (160, 174, 175). Still, if this is the case it could facilitate a more rapid elution of the peptides not associated with the hydrophobic domains compared with the coatings without PDMS-OH. This could be the explanation for the burst release seen for these formulations which also facilitates

the increases antibiofilm properties within the 24h timeframe. Another example of this can also be seen with the MALDI image of the 1H (low PDMS, high Smp24) coating. While the central morphological zone is densely populated with hydrophobic domains, the next zone out has barely any in it and its overall look is much more akin to the coatings without PDMS-OH. Thus, based on looks alone one would expect the peptide desorption/ionization efficiency to be very low. However, the desorption/ionization efficiency does not differ greatly from the efficiency of the outermost zone which consists of a mixture of hydrophobic domains and sol-gel network. This indicates that the PDMS-OH also affects the properties of the sol-gel network itself and that this effect does not depend on the local presence of hydrophobic domains after the coating is cured.

Based on the samples without peptide added, the main effect of increasing the level of PDMS-OH on the coating structure is that the size of the hydrophobic domains increases while the frequency potentially slightly decreases. Due to the droplet-like shape of the domains this would result in a reduction in their combined surface area, limiting the proportion of the peptide population that can bind to the interface. This would in theory result in an increased burst release (and thereby increased biofilm inhibition and desorption/ionization efficiency) while also having a lower proportion of peptides encapsulated after the end of the elution study. All these observations are consistent with the experimental results for the samples with the highest level of PDMS-OH.

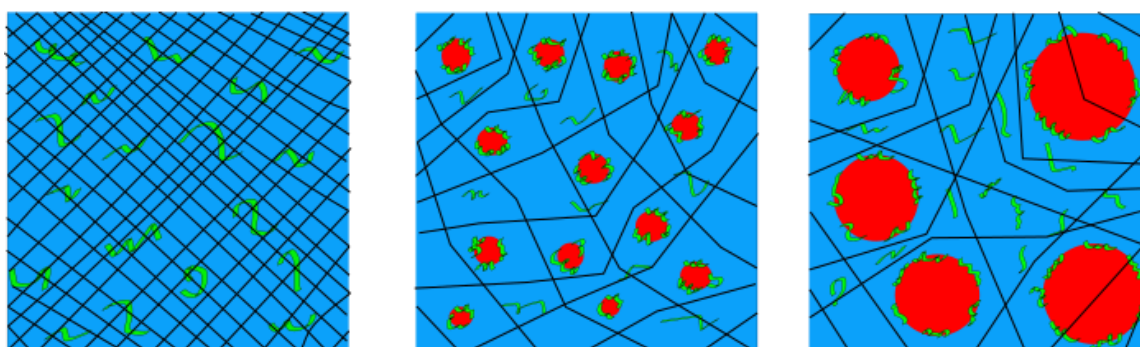


**Figure 3.17 Proposed microscopic structures of the different sol-gel formulations.** Left = no PDMS-OH, middle = low level of PDMS-OH, right = high level of PDMS-OH.

### 3.3.3 Effect of the peptide concentration on the coating behaviour

During the initial stages of the formulation development it can be difficult to predict what level of peptide loading is necessary to obtain the optimal clinical properties *in vivo*. Therefore, it is an advantage if the peptide loading can be changed, and the formulation still behaves in a predictable way. This is the case for both the formulations with no PDMS-OH and with PDMS-OH at the highest level. The peptide level has a minimal effect on the sample morphology and the expected effect on the elution profile, increasing the relative peptide release rate slightly during the start of the experiment (42). The formulations without PDMS-OH did not show the expected concentration dependent biofilm inhibition, but this can be explained by the lag-period in the peptide release not being overcome within the timeframe of the biofilm inhibition assay.

However, with the large changes in the coating morphology and differences in the maximum release the low level PDMS-OH formulations act in the least predictable way when the peptide loading is varied. The large differences in the morphology between 1L (low PDMS, low Smp24) and 1H (low PDMS, high Smp24) samples could indicate that the coating was oversaturated with peptide compared to the amount of PDMS-OH at the highest peptide level. The different zones in the heterogeneous morphology of the 1H (low PDMS, high Smp24) sample follow the curing rate of the coating, with the edge drying the fastest and the centre the slowest. Thus, the different morphology zones could be related to interactions between the peptides and PDMS-OH changing as the composition of the solvent evolves.

The outer zone seems to consist of a mixture of sol-gel, PDMS-OH domains and peptide like expected. However, in the middle zone the deposition of the PDMS-OH domains seems to stop. This could be due to an interaction between the high ratio of peptide relative to the PDMS amount in combination with the change of the solvent composition, with the peptides acting as surfactants and thereby allowing the PDMS-OH to stay in solution. At some point the solution becomes oversaturated with PDMS-OH and the central zone is formed.

In the other formulations containing PDMS-OH, the PDMS-OH deposition rate seems to either be consistent throughout (1L) or consistent until the solution becomes oversaturated with PDMS-OH and a relatively pure deposit is formed (2L and 2H).

#### 3.3.4 Optimal formulation parameters for the antimicrobial coating

Based on the formulations evaluated in the study the inclusion of PDMS-OH in the AMP loaded sol-gel coating seems to provide general improvements to the formulation. The PDMS-OH reduces cracking of the coating surface which could contribute to a less controlled elution via an increased surface area and greater coating detachment, facilitates a relatively homogeneous 2D distribution of peptide despite the heterogenous microscopic structure, changes the elution profile to a more desirable burst followed by slow-release profile and significantly improves the anti-biofilm properties.

The formulations without PDMS-OH might be significantly improved by increasing the pore size of the sol-gel network such as by increasing the water/silica precursor ratio. However, this might also significantly reduce the time it takes to reach the effective maximum release and thereby limit the timespan over which the formulation is active. The optimal PDMS-OH level for the current formulation is likely somewhere between the two levels tested, low enough to avoid the PDMS-OH spot defects seen for the high PDMS-OH samples while still providing a predictable behaviour at different peptide levels.

The study also highlights the interesting properties the coating acquires when having a hybrid hydrophobic/hydrophilic microscopic structure. Without PDMS-OH the only variable that can be used to control the peptide elution rate from the coating is the pore size of the sol-gel network. This limits the extent to which the behaviour of the coating can be customized for different clinical applications. However, with the addition of the hydrophobic domains the peptide can be controlled in two stages. The rate of the burst release can be modified by changing the sol-gel network pore size, while the long-term release can be affected by modifying the properties of the hydrophobic domains. Thus, if an application required a burst release required a burst release over 12 hours followed by a gradual release over 6 weeks, the PDMS-OH containing formulation should provide more options to optimise its behaviour to fit these specific parameters.

### 3.4 Conclusions

The antimicrobial peptide Smp24 can be utilized to provide biofilm inhibitory properties to thin film sol-gel coatings. However, the effectiveness of these properties are not only dependent on the concentration of the peptide in the formulation, but also the presence of the excipient PDMS-OH. Without PDMS-OH in the formulation the pore size of the sol-gel polymer network is initially too small allow for rapid peptide elution hindering the antibiofilm efficacy. However, if PDMS-OH is added, the microscopic structure of the coating changes, facilitating both an initial burst release of peptides and a slower long-term release. Such properties would allow for greater control of the coatings behaviour and would likely be more desirable in most clinical applications.

## 4. Investigation of the structure and mechanism of action of Smp24

### 4.1 Introduction

Compared to many other pharmacologically active compounds, both the structure and mechanism of action of AMPs is very complex. While most compounds act by binding to a molecular target such as a receptor, either facilitating or inhibiting its activation, the antimicrobial activity of AMPs occurs downstream of multiple biophysical processes, including membrane binding, membrane insertion and membrane disruption. Understanding how the structure of the peptide relates to the individual aspects of the mechanism of action can help guide the rational design of new AMPs. The fundamentals of establishing a structure mechanism relationship (SMR) for AMPs is to somehow build a bridge between some experimentally observed mechanistic effects and the structure of the peptide. This can be relatively difficult as the mechanistic information is often observed on a scale many orders of magnitude greater than total size of the individual peptide. In the next chapter (chapter 5) molecular dynamics (MD) simulations will be used to connect the structure and mechanism on a molecular scale and provide additional insight to a range of experimental observations for Smp24. However, to do so effectively, key mechanistic and structural features of Smp24 must first be defined and critical gaps in the knowledge must be identified and filled prior to connecting them. In this chapter, the prior published biophysical observations related to Smp24 are reviewed and built upon using both *in silico* and *in vitro* approaches.

### 4.2 Results and discussion

#### 4.2.1 Structure of Smp24

The ability of AMPs to inhibit the growth of microbes is not just due to their overall physiochemical properties. The structure of the peptides is a central component of their activity, as shown clearly by the loss of activity seen if their sequence is scrambled (176). The higher order structure of AMPs can range greatly (177), however for scorpion venom derived peptides most are helical in their active configuration (178). These peptides often have the ability to change their structure depending on the

surrounding environment, going from a disordered state in aqueous solution to the active helical configuration when interacting with a membrane like environment. When in their helical configuration the structure is amphiphilic with the charged and polar residues on one side of the helix and the hydrophobic residues on the other, allowing the peptide to interact with the hydrophobic/hydrophilic interface of a phospholipid bilayer.

Based on previous results, these general observations are also true for Smp24. The previous structural information comes from two sources.

Firstly, the peptide has been investigated using circular dichroism (CD) spectroscopy, which has given information about the secondary structure of the peptide and how this structure is affected by the surrounding environment. CD spectroscopy is a standard experimental method for exploring the structure of peptides in a specific solution. For AMPs two different solvents are often used together, water and trifluoroethanol (TFE). TFE is a relatively hydrophobic solvent but still miscible in water and thus a mixed solution of those solvents can somewhat mimic the hydrophobic/hydrophilic environment of a membrane/lipid bilayer. The CD experiments show that Smp24 is disordered in an aqueous solution but gradually adopts a more helical structure as the proportion of TFE is increased until 60% v/v. The experiments also indicate that the peptide has two regions of helical content consisting of about 59% and 22% of the peptide based on comparison to 29 reference proteins (137, 149). This is still lower total helical content than its closest related peptide Pandinin 2 which is indicated to have a total helicity of 99% (146). Smp24 likely consists of a large helical region, a smaller helical region (about a third of the size of the large one) and a/some unstructured region(s), but the CD spectra does not indicate where these regions are located along the primary structure.

The second approach was to try to predict the 3D structure of the peptide using *ab initio* computational modelling (149). This model indicates that the peptide is alpha-helical from the N-terminal to residue 20 with the final 4 residues forming a non-ideal helix (figure 4.1A). However, several factors call into question the validity of the predicted structure based on this model. Firstly, the presence of the different regions of secondary structure indicated by the CD analysis cannot clearly be observed in the predicted structure. The long alpha helical region in the predicted structure could fit as

being the combined helical regions (approximately 80% of the peptide) from the CD analysis but no clear separation between them can be observed. This would also indicate that the C-terminal region should count as unstructured while the predicted structure suggests it to be helical. Further questions about the structure of the C-terminal regions come from the 3D charge distribution which indicates that the negative charges from Asp23 and Ser24 are located on the same side of the helix as most of the hydrophobic residues (figure 4.1B). This might be possible for the structure while the peptide is in solution but is unlikely when the peptide is interacting with a bilayer/membrane as the negative charges would likely not be orientated in the same direction as the hydrophobic residues. Lastly, the model cannot show the change in the structure based on the environment as seen with the CD spectra. Since the structure of the peptide is so dependent on the surrounding environment, modelling/simulation that does not use an explicit solvent model would likely not be able to predict an accurate 3D structure. For the purposes of creating the SMR a more reliable predicted 3D structure of Smp24 is needed, and such structure needs to agree with the experimental observation from the CD data.

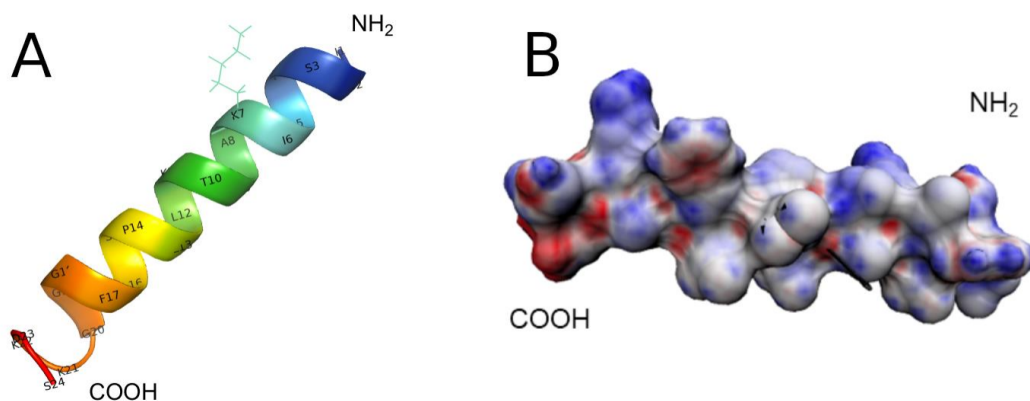


**Figure 4.1 Previous attempts at predicting the 3D structure of Smp24 using in silico modelling.** A = Predicted 3D structure of Smp24, B = 3D charge density distribution of Smp24. Figures adapted from Rawson et al. (149).

#### 4.2.2 More accurate *In silico* modelling of the solution behaviour of Smp24

One aspect of MD simulations that makes them the preferred method for predicting the structure of biological molecules is their use of explicit solvent models. In this case, it is not only the biological molecule of interest that is simulated but also each solvent molecule surrounding it, allowing for much more accurate predictions of the solvent's effect on the structure. Since biological molecules such as peptides are large and very flexible, their interaction with the surrounding solvent is key for understanding how they fold into their optimal 3D structure. The most important solvent molecule in a biological context is water, and therefore MD simulations can utilize several different models for water, which range in complexity to obtain the most accurate or efficient simulations. These water models generally differ based on how many distinct sites each molecule consists of, with more sites giving a more accurate model, but at a much higher computational cost. 3-site water models such as SPC or TIP3P are the most used for MD simulation of biological molecules as they provide a reasonable degree of accuracy at a high computational efficiency. The structure of the 3-site water model is very intuitive as the 3 sites in the model match the actual atomic structure of the water molecule (179). One of the more complex water models often used is the 5-site water model TIP5P-E. This model has two extra so-called "dummy" atoms representing the lone pair of atoms of the oxygen atom. This gives the water molecule a more experimentally accurate tetrahedral structure, especially important for correct mixing behaviour with other solvents (179). In addition to water, other solvent molecules can also be utilized in MD simulation to completely customize the environment surrounding a biological molecule.

In order to gain increased insight into the structural results obtained for Smp24 in the CD experiments, the two most extreme conditions (0% TFE, 60% TFE) were replicated *in silico* using MD simulations. To mimic the 60% v/v solution a molar ratio of approximately 2.73 water molecules per TFE molecule was used. The simulations in pure water were done using the AMBER99SB-ildn force field using the recommended water model, TIP3P. The TFE/water mixture simulations were based on work by Gerig (180), also using the AMBER99SB-ildn force field. A key finding of Gerig's was that the use of the 5-site water model TIP5P-E significantly improved the mixing behaviour between the two solvent molecules compared with using the standard TIP3P model

which produced much larger water clusters. Therefore, TIP5PE was used as the water model for these simulations. The topology used for the TFE molecules were adopted from the same paper (called TFE model V), which was shown to produce the most accurate results.

MD simulations require a 3D structure for the peptide/protein of interest to be used as the starting configuration for the simulation. Ideally an experimentally derived structure would be used, but as none exists for Smp24 another approach must be used. Similarly to the previously described study an *ab initio* structure was generated, although a different server was used (151). Again, the predicted structure does not correspond with what would be expected for the structure in water. A large portion is helical although a larger portion of the peptide around the C-terminal is unstructured than previously predicted. However, even if it is not a realistic configuration for the peptide in water, having a more ordered starting structure could be an advantage for the simulations. It is easier to simulate the loss of secondary structure rather than the modelling the folding from an unstructured configuration to a helical structure, as semi stable intermediary 3D structures can be formed during the simulation delaying the formation of the most ideal configuration. The two Smp24 solution simulations were thus designed to show whether the helical starting structure was lost in pure water and retained in the 60% TFE solution, as would be expected based on the experimental results.

An overview of the completed simulations can be seen in table 4.1

**Table 4.1 Overview of solution-based Smp24 models.**

	Number of simulations	Length	Names
Simulation of Smp24 in water	3	500 ns	sw24_(1-3)
Simulation of Smp24 in 60% v/v TFE	3	500 ns	st24_(1-3)

### 4.2.3 Solution structure of Smp24

A key indication if the simulations produce accurate predictions of the structure of the peptide, is the evolution of the secondary structure over time in the different solvent environments (figure 4.2).

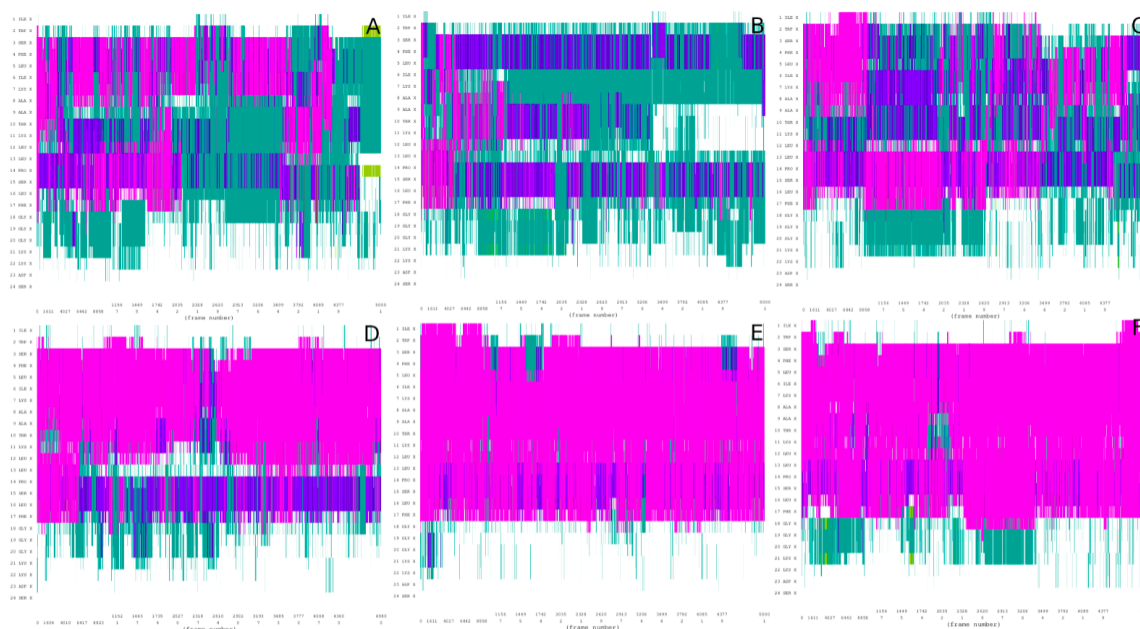


**Figure 4.2 Secondary structure of Smp24 in water or 60% TFE over time, determined using the VMD plugin “Timeline”. (A,B,C) 3 500 ns simulations in water, A = sw24\_1, B = sw24\_2, C = sw24\_3. (D,E,F) 3 500 ns simulations in 60% TFE, D = st24\_1, E = st24\_2, F = st24\_3. Pink indicates alpha-helix, blue indicates 3-10 helix, green indicates turn, yellow indicates isolated bridge and white indicates random coil.**

In the water simulations Smp24 quickly loses the contiguous alpha-helix that is present in the starting structure. Shorter alpha helical regions of 4 to 6 residues in length and 3 residue length 3-10 helices takes over between residue 1 and 17. However, there does not seem to be any consistency regarding the placement of these helical regions between the repeat simulations. Over time the proportion of helical content gradually declines, reaching no helical content in sw24\_1. The region between residue 18-24 adopts almost exclusively either a coil or turn structure.

Smp24 behaves significantly differently in 60% TFE. In st24\_2 and st24\_3 the peptide retains a continuous alpha helical region between residue 3 and 17. In st24\_1 an alpha helical region can be seen between residue 3 and 12, with a smaller 3-10 helix between residue 14 and 17. However, sporadic transitions between alpha helix and 3-10 helix can also be seen in the latter part of the helix in the other simulations. In all

three simulations, residues 1-2 and 18-24 adopted a coil structure throughout the majority of the simulation period.

Due to the overall unstructured nature of the peptide in pure water a representative static 3D structure cannot be produced. However, in 60% TFE the structure is stable and relatively consistent so in this case determining a representative structure is possible (figure 4.3).

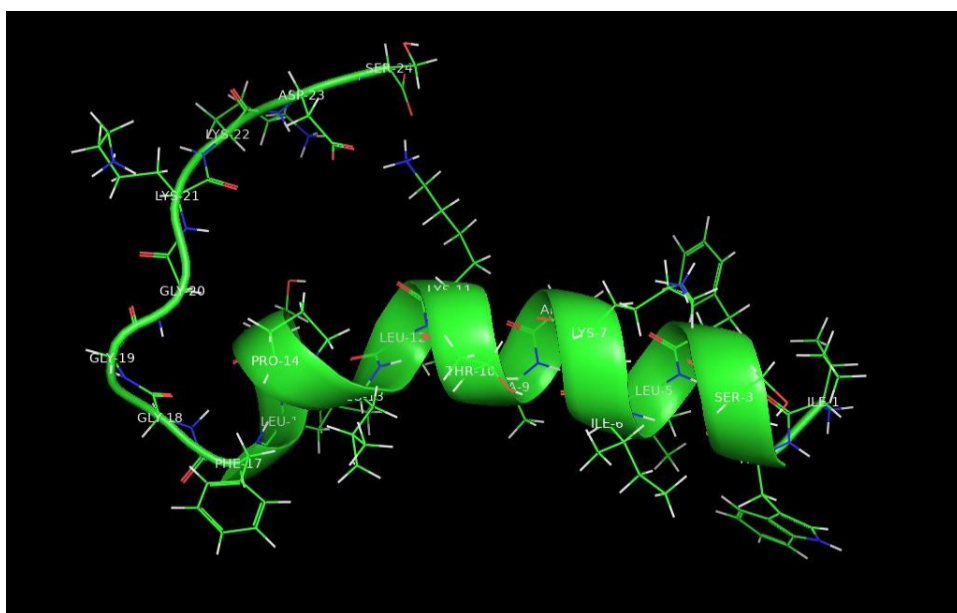


**Figure 4.3 Representative 3D structure of Smp24 in a 60% TFE solution.**

The main observation that can be made from the 3D structure is that the helical region has a kink around residue 13 due to the proline residue present at position 14. This could explain why the end of the helix is more variable between the replica simulations, with the higher flexibility of the kink influencing the type of helicity of the last part of the helix. Based on visual inspection of the simulations it seems the angle of the kink can vary significantly based on the position of the unstructured region, with the kink being less dramatic in simulation st24\_2. To ensure the possible presence of the kink was accounted for in the structural analysis, the representative structure (figure 4.3) was taken from simulation st24\_3 where the kink is clearly present. It can also be seen that while the N-terminal end does not form an ideal alpha helix it can still be thought of as mostly helical. As seen in the secondary structure analysis the

regions near the C-terminal are unstructured and in this specific configuration it is bent around the back end of the helical region.

To further evaluate the average structural stability of the peptide the relative mean square fluctuations (RMSF) were calculated (figure 4.4). Most of the structural fluctuation is associated with the terminals and the two central lysine residues (Lys7 and Lys11), independent of the solvent. The RMSF are generally lower in the 60% TFE simulations except for the terminals which reach similar levels as those seen in water.

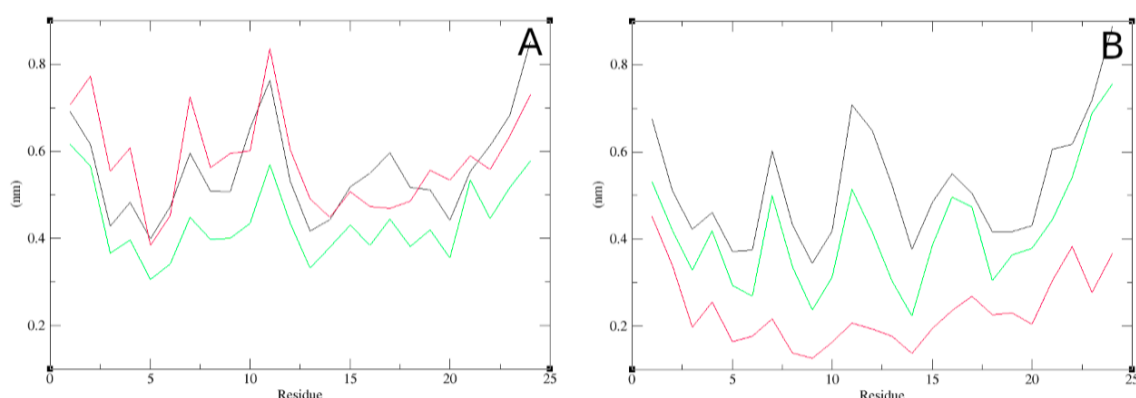


**Figure 4.4** The root mean square fluctuations of the peptide per residues. (A) Smp24 in water, black = sw24\_1, red = sw24\_2, green = sw24\_3. (B) Smp24 in 60% TFE, black = st24\_1, red = st24\_2, green = st24\_3.

All these observations clearly indicate that, as expected, the stability of the helical structure is highly dependent on the composition of the surrounding solvent. The hydrophobic/membrane mimicking properties of the TFE molecules stabilized the hydrophobic residues in the helical region from around residue 1 to 17, allowing this region to broadly retain its starting helical structure and lowering the structural fluctuations over the simulation period. However, the region near the C-terminal is unaffected by the solvent, remaining unstructured in both environments.

Consistent with what was observed for the experimental approach, the helical part of the peptide can be separated into two distinct regions. The MD simulations reveal that this separation happens around residue 13. Depending on which helix residue 13 is counted as belonging to, the larger helix is about 2.4-3.3 times the size of the smaller helix, which correlates well with the experimental result of a 2.7 times size difference. Overall, the MD simulations indicate a total helical content of 71% (residue 1-17) which

is slightly lower than the experimental result of 81% (137). However, as previously mentioned the value obtained from the CD spectrum is not due to a direct measurement of the helical content but based on a comparison with a protein library which could lead to a slight overestimation. This was the case for Panindin 2 which when investigated using the more accurate structural NMR technique showed a lower total helicity than the CD spectra initially indicated (146).

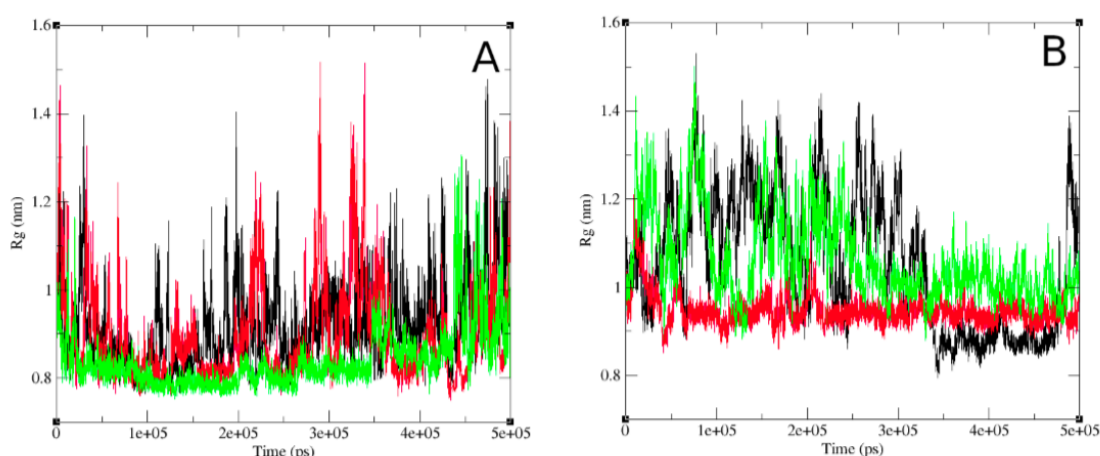


**Figure 4.5 Radius of gyration of Smp24 in water or 60% TFE over time.** (A) Smp24 in water, black = sw24\_1, red = sw24\_2, green = sw24\_3. (B) Smp24 in 60% TFE, black = st24\_1, red = st24\_2, green = st24\_3.

To gain further insight into how the 3D structure and the size of the peptide is affected by the solvent the radius of gyration was calculated (figure 4.5). The size of the peptide in water varies significantly throughout the simulations. Many short spikes can be seen in the radius of gyration where the peptide extends to a more stretched out 3D structure before returning to a more compacted structure for varying amounts of time. Sw24\_2 seems to adopt a stable compacted structure for the longest time, between 30-350ns, but towards the end of the simulation it also presents similar spikes in the size like the other two simulations. However overall, the average radius of gyration in all 3 simulations is smaller than that of the starting peptide structure.

In 60% TFE all simulations show an initial increase in the peptide size. Following that, st24\_1 and st24\_3 enter a longer period where the size varies significantly with the Rg ranging between 0.9 and 1.4 nm. Eventually the peptide in both simulations adopts a

more stable size, that being  $0.88 \pm 0.03$  nm for st24\_1 and  $1.01 \pm 0.04$  nm for st24\_3. Contrary to the rest, st24\_2 adopts a stable size much sooner than the other simulations with a Rg of  $0.94 \pm 0.03$  nm.

Based on the secondary and 3D structure it seemed most likely that that the variations in the Rg would be due to the unstructured region near the C-terminal, as it has a much greater flexibility than the helical region. The sudden reduction in the size variation could indicate that intermolecular interactions were being formed, restricting the position of the unstructured region. Smp24 has an interesting distribution of charged residues, with two lysine residues present in the main helical domain (lys7 and lys11) and 4 charged residues near the C-terminal (Lys21, Lys22, Asp23 and Ser24). Ionic interactions between the two lysine residues of the helical region and Asp23/Ser24 could restrict the movement of the more flexible random coil end of the peptide giving increased structural stability.

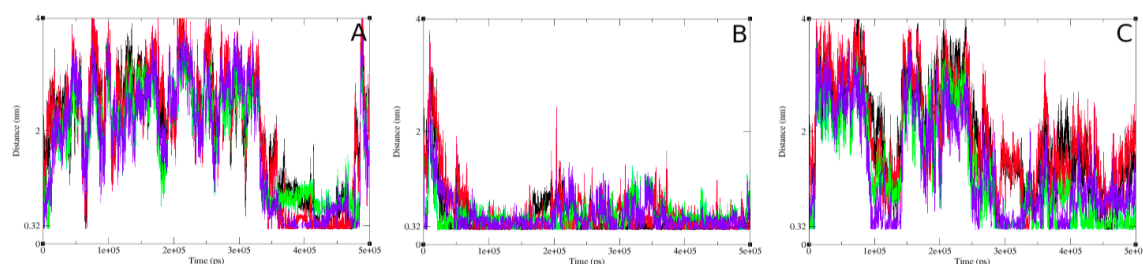


**Figure 4.6 Distance between charged atoms of select residues of Smp24 in 60% TFE simulations over time. A = st24\_1, B = st24\_2, C = st24\_3. Black = Lys7 to Asp23, Red = Lys7 to Ser24, Green = Lys11 to Asp23, Blue = Lys11 to Ser24.**

Investigating the distance between these 4 residues in the 60% TFE shows that the distance between the charged atoms reaches levels below  $3.2 \text{ \AA}$  indicating the formation of salt bridges (figure 4.6). The timepoints where the shortest distances are reached also correlates well with the smaller and more stable periods of the radius of gyration. All 4 residue combinations can seem to occur, although for st24\_1 Lys7 to Ser24 is dominant, for st24\_3 Lys11 to Asp23 or Ser24 is dominant and for st24\_2 a combination of all the interactions occurs, but Lys 7 to Asp23 is the most dominant. An example of one of these salt bridges can be seen in figure 4.3 where lys11 interacts with both the C-terminal and the Asp23 side chain.

The presence of these salt bridges and their potential impact on the stability of the peptide's structure while in solution, calls into question the robustness of a TFE/water mixture as a membrane mimicking environment. While the TFE does seem to mimic the hydrophobic characteristics of a membrane, the charged characteristics of the lipid headgroups are not well represented. Due to this, the peptide forms structure stabilizing charged interactions with itself which in a true membrane environment could instead occur with the external environment. This could over emphasize the importance of anionic residues, when evaluating the ability of the peptide to adopt its helical structure in TFE. Removal or modification of Asp23 and Ser24 could potentially increase the % of TFE needed for the peptide to adopt its maximum helical structure but might not affect the willingness for the structural transition in a true membrane environment.

There are other AMPs that could potentially also be affected by this phenomenon such as Magainin 2 and Panindin 2. Magainin 2 has a similar structural motif as Smp24 with lysine residues positioned in the central helical region and a negatively charged glutamic acid next to the C-terminal which potentially could form cross peptide salt bridges. The peptide's structure has been investigated with NMR while inserted into SDS vesicles. Here magainin 2 adopts a predominantly helical structure but no salt bridge formation is seen, with the cationic residues instead being able to interact with the anionic SDS molecules (181). Structural NMR studies of Panidinin 2 show that it is disordered in water but adopts a majority helical structure in both TFE and when inserted in DPC vesicles. Similarly, to what is seen in the Smp24 in TFE simulations Pandinin 2 also has an unstructured region near the C-terminal starting at about residue 19-20 (146). The anionic C-terminal and the flexibility of unstructured region could facilitate the formation of salt bridges in TFE which does not seem to be present when the peptide is interacting with the vesicles.

A key process in the structural investigation of peptides and proteins is to break their overall structure into smaller regions or motifs. The distinguishing features between different regions can be based on several factors such as secondary structure, 3D orientation and residue composition.

Smp24 can be separated into 4 different regions (figure 4.7, table 4.2). First is the primary helical region consisting of the long, strait helix starting at the N-terminal and

spanning till around residue 13. Following that is the smaller secondary helix from residue 14-17, characterized by having a different spacial orientation than the primary helix. Residue 13 could arguably belong to either of the helical regions depending on how dramatic the kink is in the specific configuration. However, as it is the proline residue at position 14 that facilitates the distinction between the helices, this residue seems like a good starting point for the secondary helical region. The next region consists of three glycine residues in a row which facilitates a link between the helical regions and the remaining unstructured residues. The glycine linker region can be separated from the rest of the unstructured part of the peptide due to the large difference in the physicochemical properties between it and the remaining 4 residues. The last 4 residues of the peptide are all charged, either via their side chain or via the C-terminal itself and form the final region called the tail region. The fully charged nature of this region makes it unique from the other major regions of the peptide as these consists of a mixture of hydrophilic and hydrophobic residues.

The separation of the peptide into these 4 regions can help in the construction of the SMR by allowing for analysis of the peptide-bilayer interactions in a segmented way without needing to do it in a per residue manner.

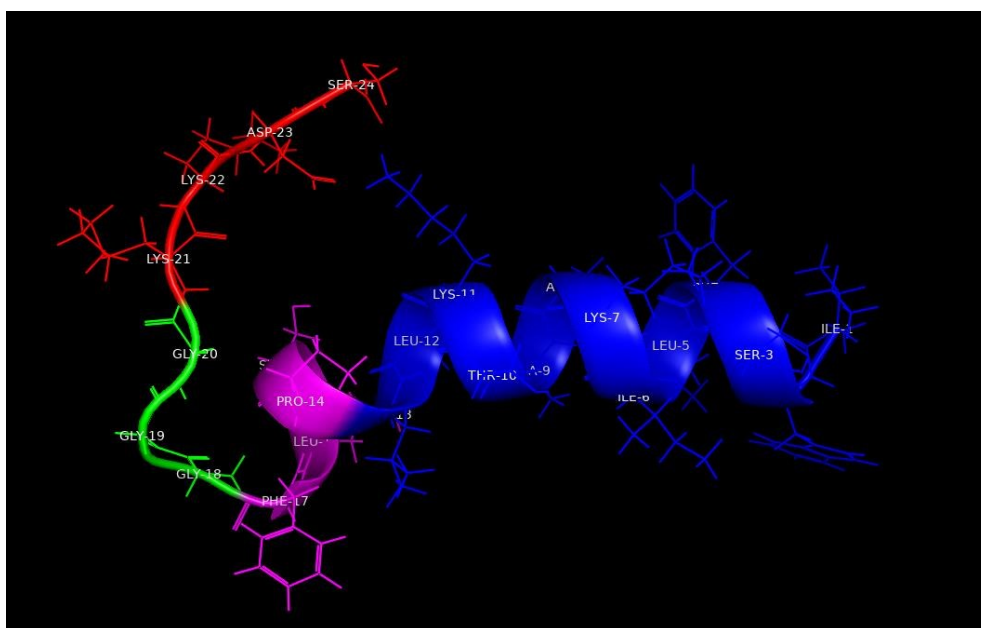


**Figure 4.7 Regional structural breakdown of Smp24.**

**Table 4.2 Overview of structural regions of Smp24.**

Residues	Colour	Structural region
1-13	Blue	Primary helix
14-17	Magenta	Secondary helix
18-20	Green	Glycine linker
21-24	Red	Tail

#### 4.2.4 Mechanism of action of Smp24

As is the case for most AMPs, the mechanism of action of Smp24 is complex. Its primary activity relates to how the peptide can disrupt the bacterial membrane(s), causing leakage of intercellular components leading to cell death. Due to the heterogenic and dynamic nature of cell membranes, interactions with the peptide will be complex and change over time. Therefore, the use of multiple biophysical methods is necessary, in order to obtain a relatively complete picture of the interactions. Smp24 has previously been investigated with a range of methods, allowing for the formulation of three overarching mechanistic statements.

##### Smp24 shows selectivity based on the lipid headgroup composition

While the lipid selectivity of Smp24 has been demonstrated using several techniques, the clearest example is via liposomal leakage assays (figure 4.8). Liposomes of different lipid compositions loaded with carboxyfluorescein were exposed to Smp24 at two different concentrations and the vesicle lysis was estimated. The key observations from this experiment were that the peptide induced lysis was greater for the overall negatively charged PCPG vesicles when compared with the neutral PCPE vesicles. However, this difference was dramatically reduced once the ionic strength of the surrounding solution was increased, shielding electrostatic interaction. From this, two mechanistic conclusions can be drawn. Electrostatic interactions between the positively charged peptide and the negatively charged lipids play a key role in the selectivity and the selectivity occurs early in the mechanism of action as changes in the solution can affect the final lysis level (58).

Smp24 contains several cationic lysine residues and a charged N-terminal which all could play a role in the initial interactions between the peptide and the phospholipid headgroups, however it is not clear how exactly these initial interactions are formed and if all the cationic residues have a similar contribution and function during this process.

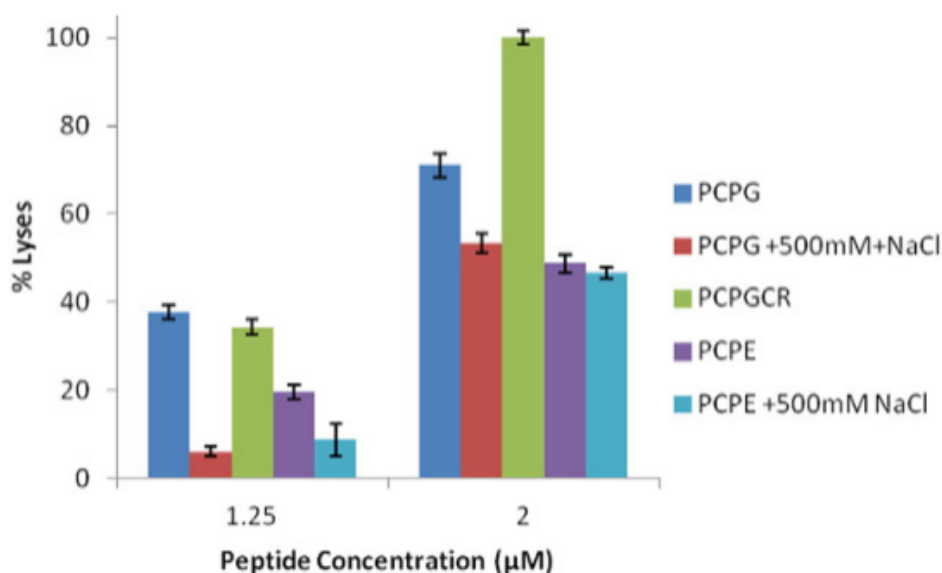


**Figure 4.8 Smp24 induced lysis of liposomes with different lipid compositions.** Adapted from (58).

#### Smp24 can insert into lipid bilayers

Quartz crystal microbalance with dissipation monitoring (QCM-D) can be used to measure structural changes and increase in the mass of a bilayer due to the addition of membrane active peptides. Smp24 was added to a DOPC:DOPG bilayer at different concentrations and the changes in the dissipation and frequency were measured. At low concentrations the frequency decreases with increasing dissipation indicating that the peptide is accumulating on the bilayer. At increasing peptide concentrations, a threshold is reached where a “swing back” in the dissipation is seen, indicating a change in the membrane structure (figure 4.9).

These results indicate that the peptide first accumulates on the surface of the bilayer likely due to electrostatic interaction between the peptide at the lipid headgroups. The eventual “swing back” in the dissipation could indicate the peptides inserting to the

bilayer, resulting in a reduced interaction with the aqueous phase. Thus, the peptide interacts with the bilayer in a stepwise process of first electrostatic attraction, followed by accumulation and insertion (58).

This raises the question of how these accumulation and insertion processes happen on a molecular level. The stepwise process indicates that three intermediary equilibrium peptide configurations exist, a solution structure, a structure where the peptide is accumulated on the surface of the bilayer and lastly a structure where the peptide is inserted within the bilayer. Gaining insight into how the structure, orientation and position of the peptide relative to the bilayer changes throughout these different configurations would be a key step in establishing the SMR.

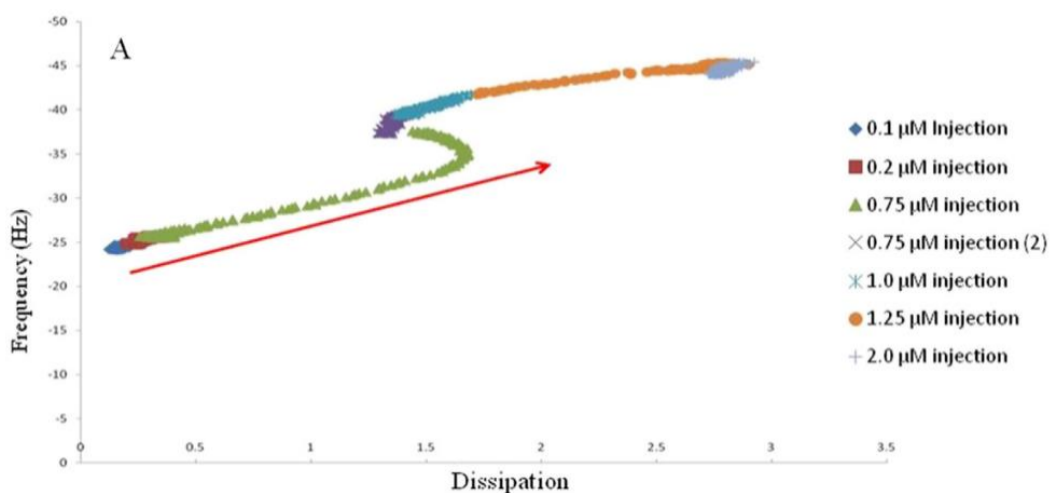


**Figure 4.9** QCM-D analysis of Smp24 at increasing concentrations against a DOPC:DOPG bilayer. Adapted from (58).

#### Smp24 can disrupt lipid bilayers via pore formation

The most detailed mechanistic information in relation to the structure of membrane pores induced by Smp24 comes from atomic force microscopy (AFM). This methodology allows for the visualization of peptide induced pores in lipid bilayers by measuring the change in the thickness of the bilayer. Negatively charged DOPC:DOPG planar bilayers were exposed to 1.25 μM Smp24. Before peptide addition the bilayer had a smooth appearance without any visual defects (figure 4.10A). However, after 30

min incubation with the peptide the formation of differently sized stable pores is seen (figure 4.10B). These pores have a depth of 2-4 nm and an average diameter of  $80 \pm 40$  nm. The presence of distinct pores of greatly varying size indicates that at least under these conditions the pore structure is toroidal in nature. Higher peptide concentrations ( $2.0 \mu\text{M}$ ) lead to the complete destruction of the bilayer (58).

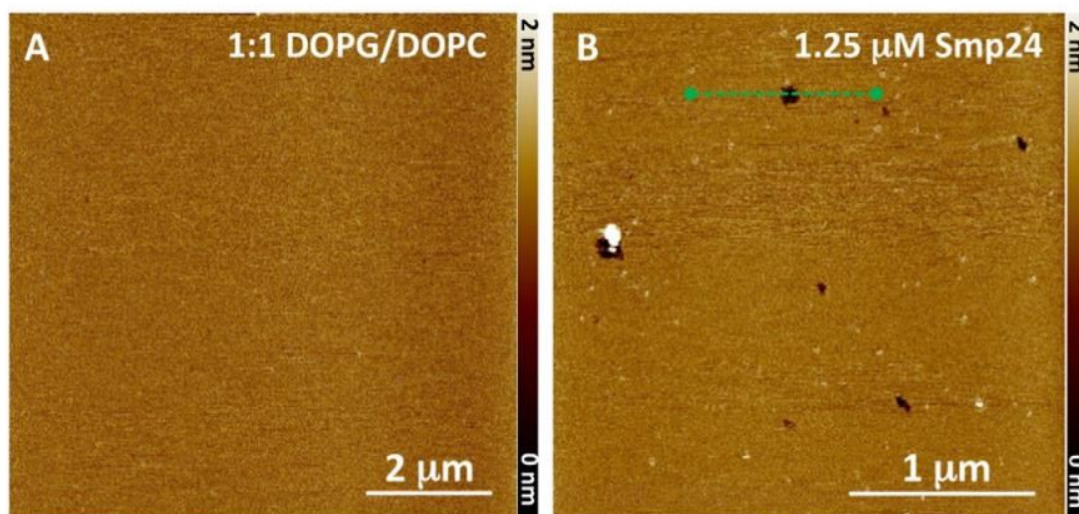


**Figure 4.10 AFM image of Smp24 induced pore formation.** A = Bilayer before peptide addition, B = bilayer after peptide addition. Adapted from (58).

For the purposes of this study using only the AFM images as the experimental basis for the SMR would be challenging. The pores seen in the AFM image could be said to represent mature Smp24 induced pores as the image is taken 30 min after peptide addition once the growing pores have stabilized in size. At this point the average pore diameter is  $80 \pm 40$  nm which is 40 times the approximate length of the peptide itself. At such dimensions the lumen of the pore would have a surface area of hundreds to thousands of  $\text{nm}^2$  and there would be as a minimum hundreds of individual peptides associated with it. These conditions cannot easily be emulated using MD simulations. Both in terms of the timescale and model size simulating a bilayer with such a pore would not be feasible using an all-atoms methodology. Modelling of one of the smaller pores over a limited time period could potentially be done using a lower resolution coarse grained MD simulation, where the molecules are made up of larger simplified subunits rather than individual atoms. However, this limits the amount of detail that

can be determined for the interactions between the pore and the individual peptide, which is the most important aspect for better understanding the SMR.

Instead, experimental information related to the earlier stages of the pore's lifespan would be better suited to be used in combination with MD simulations. The main factor for this is that pores start out much smaller in overall size relative to at their mature state. Therefore, the necessary dimensions of the model containing the pore would be much less computationally demanding and fewer individual peptides would participate in the pore-peptide assembly. This both simplifies the overall analysis and represents a more direct correlation between the structure of the individual peptide and the pore compared to a mature pore where the macroscopic behaviour based on many peptides is dominant.

#### 4.2.5 Investigation of Smp24 induced pore formation using planar patch clamp electrophysiology

While AFM provides direct visual information about the structure of the fully formed peptide induced pores, other methodologies can provide such information earlier in the process via indirect ways. One such approach is to measure the change in the current running across a bilayer due to a disruption of the bilayer's structure. The effect of a membrane disruptive agent such as AMPs on the bilayers structure can be explored on both a macroscopic and microscopic (commonly called "single channel") level depending on the size of the bilayer that the disruptive agent is exposed to. The molecular level changes to the membrane structure can be difficult to determine based on the interpretation of macroscopic current changes, as the overall signal can stem from a multitude of individual events happening at the same time. However, if the size of the bilayer is sufficiently reduced individual events can be isolated, giving a much more direct correlation between the current spike and the nature of the pore. Factors such as the shape, size, length and repeatability of the conductance events can be used to gain insight into the underlying size, structure and stability of the membrane pore. Furthermore, some information in relation to the kinetics of the pore formation and membrane disruption can also be obtained. However, compared with the kinetic information that can be obtained in experiments on the macroscopic scale, the variance in the kinetic data obtained at the single channel level is much greater as

it is generally based on single stochastic events rather than the average response of many events.

In this study the membrane disruption induced by Smp24 was investigated via planar patch clamp electrophysiology with synthetic bilayers using the Nanion port-a-patch. The port-a-patch is a portable patch clamp system that utilizes disposable borosilicate microchips containing a small aperture instead of a traditional patch clamp pipette. The size of the chip aperture determines how large of an area of bilayer the measurement occurs on and thus allows for measurement of singular pores or channels using an aperture with a diameter of approximately 1  $\mu\text{m}$  (142). In the experiments a bilayer is formed across this aperture using giant unilamellar vesicles (GUVs) as an intermediary vehicle for the lipids. These vesicles are added to the external solution atop the chip and negative pressure is applied through the bottom of the chip to move the vesicles towards the opening. Once a vesicle hits the surface of the chip near the aperture the vesicle bursts creating an open lipid bilayer that is then sucked into place atop the aperture. After a tight seal between the bilayer and the chip is achieved the pressure can be neutralized as the bilayer is kept in place via hydrophilic interactions between the bilayer and the boro-silicate glass substrate of the chip surface, which are improved by forming the bilayer at pH 4. In this state the bilayer creates a high resistance giga-ohm barrier between the outer and inner compartments of the chip, separating the two silver electrodes used to measure and control the current or voltage going across the bilayer.

Due to the use of synthetic bilayers the composition of the membrane can be highly customised. In this set of experiments a 1:1 mix of DOPC and DOPG lipids were used, which was chosen for several reasons. Firstly, these lipids are partially unsaturated containing a cis double bond at the 9<sup>th</sup> carbon atom of the lipid chain. This impacts the packing of the lipid chains, lowering the phase transition temperature below room temperature and thereby ensuring that the bilayer is in the disordered liquid crystalline phase during the experiments. The inclusion of the DOPG lipids also ensures that the bilayer has an overall negative charge which mimics the charged state of the bacterial inner membrane, the main target of Smp24. Lastly, the 1:1 DOPC:DOPG mixture is the same bilayer composition used in the previous biophysical

characterizations of Smp24, so keeping the composition consistent allows for a more direct comparison between the different experiments.

After the formation of the bilayer a holding potential is applied across it to ensure a high resistant seal between the bilayer and the chip has been achieved. The external solution is exchanged, washing the bilayer in two rounds. The first round is done to remove the remaining vesicles thereby limiting peptide binding to lipids not associated with the main bilayer and secondly to increase the pH of the solution to 7, after ensuring the bilayer is stable. At pH 7 the protonation state of both the peptide and the lipids will be the physiologically relevant states, but formation of the bilayer is much more difficult. After adjusting the amplifier gain and starting the recording of the current trace, the Smp24 was added to the external chip solution at different concentrations, denoting the starting point for each experimental run.

The general trajectory of an experimental run is that after an initial lag period where the current is at the baseline level, short periods with an increased current running across the bilayer start to occur denoted as a conductance event. To begin with, these events will often be reversible with the current returning to the baseline level shortly after the disturbance begins. Each of these conductance events represents a molecular level disruption of the bilayer structure leading to increased ability for water and ions to penetrate the bilayer. The holding potential placed across the bilayer drives the translocation of chloride ions, producing the measured change in the current. Based on the shape of the current trace, corresponding to the conductance event, they can be separated into different categories and in addition the length and current distribution of the event can be analysed. In most cases, these individual reversible events will eventually escalate in intensity and frequency eventually leading to the irreversible disruption/destruction of the bilayer. This will lead to a large drop in the membrane resistance and thus the current will exceed level which can be measured at the amplifier gain level and the experiment/measurement is ended. If the gain level is dropped the membrane resistance is often returned to a level close to that of the chip alone, indicating the complete destruction of the section of bilayer spanning aperture.

The membrane disruptive effect of the peptide was evaluated at 5 different concentrations with 5 independent repeats at each level.

#### 4.2.6 Kinetics of membrane disruption

In general, the lag time between the peptide addition and the occurrence of the first conductance event was very short, with the first event happening within 20 s in more than half of the runs (figure 4.11B). However, at peptide concentrations below 4.85  $\mu\text{M}$  some runs starts to have a much longer lag period, although it is not consistent for all repeats.

Similar observations can be made for the lag time between the peptide addition and the complete destruction of the bilayers (figure 4.11A). At high concentrations the bilayers were often destroyed within the first 5 min of the peptide addition, though greater variation was seen compared with the lag time to the initial event. However, at concentrations below 3.9  $\mu\text{M}$  a large increase in the variation was again seen, and the average is shifted drastically. In addition, for some of the runs at the two lowest concentrations the bilayer was still intact after 30 min, with 2 examples where no conductance events were seen at all.

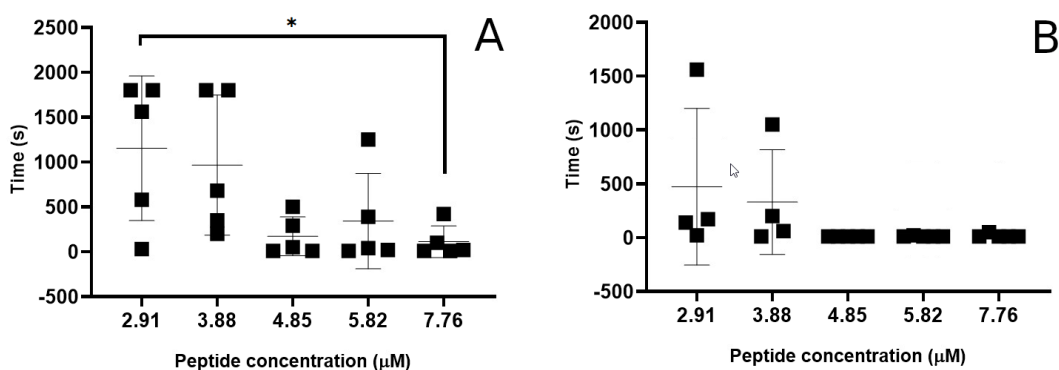


**Figure 4.11 Kinetics of pore formation observed for Smp24 during the patch clamp experiments.** A = Time between addition of peptide to the bilayer and the occurrence of an irreversible disruption of the bilayer resistance. B = Time between the addition of peptide to the bilayer and the observation of the first conductance event. \* Significant difference based on unpaired t-test ( $P < 0.05$ ).

The short delay between peptide addition and the first events indicates that the initial interaction between the peptide and the bilayer occurs at a rapid rate. However, the

buildup in membrane disruption leading up to the total membrane destruction is the much slower process.

The concentration dependency of the responses seems to be threshold based rather than a linear dose dependency, with much greater variation at the two lowest concentrations. Such threshold-based behaviour is consistent with what was observed previously in the QCM-D experiments (58). The large variations between the individual experimental repeats at the lower concentrations is due to multiple factors. Firstly, the stochastic nature of individual molecular level events such as the formation of membrane pores will intrinsically have an increasing variability in the time to occur as the concentration decreases. Secondly, the kinetics would likely be more affected by variation in the external experimental factors at these conditions. Due to the use of a single bilayer per experiment, small sample volumes and a limited ability to ensure consistent mixing of the peptide with the external solution buffer, the experimental setup was relatively susceptible to run to run variations, especially impactful at a low peptide concentration.

The mechanism of action behind the membrane disruption cannot be determined based purely on the kinetics data, however it can potentially be narrowed down. In the traditional carpet model of AMP induced membrane disruption, the disruption happens as an irreversible event once a specific number of peptides are bound to the surface of the bilayer (95). If Smp24 acted primarily through this mechanism, we would not expect the high frequency of reversible conductance events before the complete membrane destruction. In addition, variation in the kinetics between individual runs at the same concentration would be expected to be relatively low as a large number of peptides would be needed in order to form the carpet on the bilayer before the membrane disruption is triggered. The kinetic observations do not correlate well with these expectations and thus the results suggest that at least under the tested conditions the mechanism of action is not well described using only the carpet model. The complete and irreversible disruption of the bilayer at the end of the experiments could still occur via a mechanism related to the carpet model, but other mechanisms of membrane disruption are also occurring prior to that point.

#### 4.2.7 Qualitative analysis of conductance events

In addition to the kinetic measurements a qualitative analysis of the current traces was also done in order to evaluate the individual membrane disruptive events induced by the peptide. Multiple different types of event signatures were found throughout most runs, which could broadly be categorized into 3 distinct event types based on Chui et al. (105).

Multilevel events (figure 4.12A) were the type of signal that most closely represents what would be expected for a distinct pore. The start and end of the signal are both sharp transitions from the baseline. During the event a consistent but highly variable increase in conductance could be observed, lasting between a 100 ms to a few seconds. Depending on the length of the event an average conductance level could be estimated using amplitude histograms fitted with a Gaussian distribution function. However as seen in figure 4.12A the spread of the current distribution corresponding to the multilevel event is much greater than the baseline. Comparing the average current measured between different multilevel events also shows a large distribution of values ranging from 2.8 to 18.3 pA.

Like multilevel events, spike events (figure 4.12B) also have a clear transition to and from the baseline albeit the length of the event is much shorter (<50ms). Again, no consistent average/maximum current level can be found when comparing different individual events, even within a singular run. Spike events were both observed as lone events or coming in multiples with a short time gap between them.

Erratic events (figure 4.12C) were long (often multiple seconds) but with a relatively low and very variable conductance level. Unlike the other event types, they did not have a very clear beginning or end, but rather gradually increased or decreased the conductance. Over the lifetime of the event the conductance level could shift multiple times and often return to a partial baseline with increased noise and conductance in between. Due to the more gradual conductance evolution, the amplitude histograms did not show an independent conductance level for the event, but rather a broadening of the baseline peak.

All the different event types were found at all peptide concentrations, however like for the kinetic data a large variation in the number of events were seen within the same

peptide concentration. Therefore, no significant relationship between the peptide concentration and the likelihood of a specific event type occurring could be found. However, for the entire data set spike events were the most likely to occur followed by erratic events and lastly multilevel events.

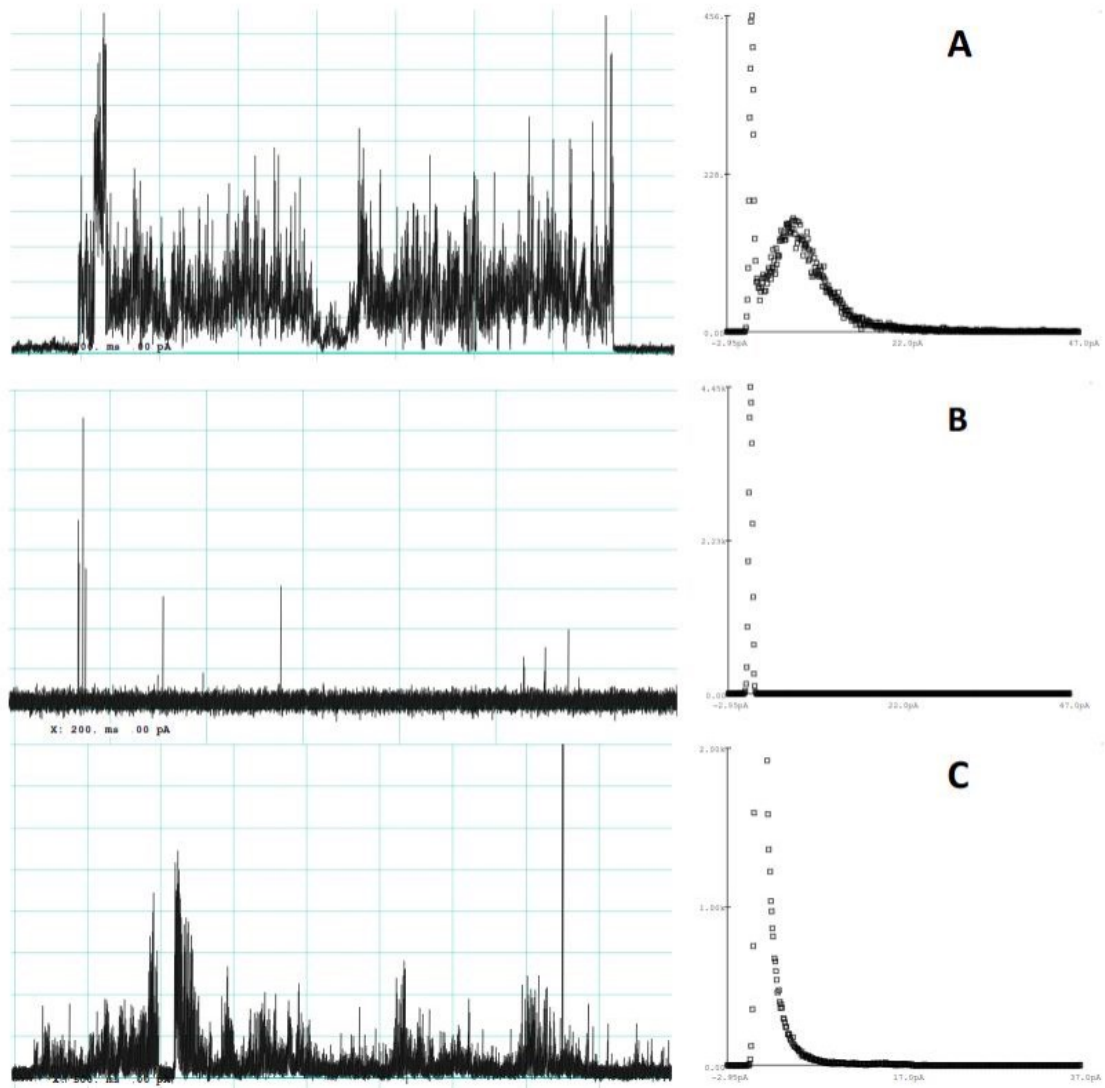


**Figure 4.12 Representative examples of the current trace and amplitude histograms for the three different event types observed in the patch clamp experiments. A = multilevel event, B = spike events, C = erratic event.**

There is no well-established singular approach for interpreting the current traces induced by AMPs. Some authors take an approach that is similar to how one would analyse the single channel activity of protein ion channels, which works for peptides

creating very ordered pore structures such as via the barrel stave mechanism (100). Manzo et al. Investigated peptides with less defined channel activity and focused more on the morphology of larger periods of current trace rather than isolating the individual conductance events (182). However, with the main objective of this chapter being to gain insight into the molecular level structures responsible for the pore disruption, the best approach would be to look at the morphology of the individual conductance events. Since hundreds of conductance events were counted across the experimental runs, the events were grouped in to three categories to simplify the analysis. However, the interpolation of the conductance event categories is still highly theoretical so the mechanism of action and pore structure cannot be decidedly determined using only this biophysical method.

The structural characteristic of the peptide induced pores that the current trace analysis can give the most direct information about is if the pores are ordered or disordered in nature. The archetypal example of an AMP forming ordered pores is alamethicin, which forms the basis for the barrel-stave model of pore formation. This peptide produces conductance events which can be categorized as clear “square top” events. These events show repeatable distinct conductance states strongly indicating the formation of different ordered molecular level structures with different opening levels based on the number of peptides the pore assembly consists of (100). Peptides thought to act through the toroidal pore model such as pleurocidin can also show “square top” and “flickering” conductance events indicating that the type of toroidal pores that this peptide induces are of a relatively ordered nature (83). However, none of these event morphologies were observed to be induced by Smp24. Repeating events of all types have different conductance event levels within the same trace and the conductance level of individual events varies much more than what is seen in the literature for ordered pores. The patch clamp experiments are thus a strong indication that at least under these conditions the mechanism of membrane disruption and the pore structures are disordered in nature.

The multitude of different event types observed is consistent throughout all the experimental runs at all the different concentrations indicating that the peptide induced membrane disruption occurs via several different competing mechanisms. In the traditional view of the mechanism of action of AMPs, each peptide is thought to

intrinsically act via one of the three models of membrane disruption (barrel-stave, toroidal pore or carpet) due to the specific structure of the peptide. However, newer alternative models such as the SMART model put a greater emphasis on the mechanism of action being not only dependent on the structure of the peptide but also the other conditions of the specific system such as the peptide concentration and the properties of the bilayer (15). Such models better account for the peptide acting via multiple competing mechanisms of action at the same time, as observed in this study. The observation that a variety of different event types is seen for a single peptide is not uncommon for AMPs. While some examples of pore formation result in consistent and distinct conductance levels following the square-top or flickering signature can be found (83, 183), they are not always consistent between different studies (184). Many AMPs show either erratic behaviour or a combination of different event types like Smp24 (87, 96, 99, 182, 184). One particularly interesting example is cyclic beta sheet AMP Gramicidin S. While having very little in common with Smp24 both structurally and origin wise, the conductance behaviour of the two peptides is remarkably similar (14). Due to the structural dissimilarity between the two peptides, this again indicates that the disruption occurs in a more generalized and disordered manner rather than by the formation of distinct structural assemblies.

The disordered nature of the conductance events makes it more difficult to establish a direct theoretical correlation between the increased current running across the bilayer and the change in the molecular level structure of the bilayer. However, some general characteristics can still be proposed to explain the underlying biophysical differences between the event types.

Both the spike and multilevel events share a key characteristic in that they both have a distinct and clear beginning and end to the signal. This mimics the behaviour that can be observed for more ordered ion channels in which the channel can have either an open or closed state depending on the configuration of the protein membrane assembly. While the spike and multilevel events do not have any specific well defined open states, the open/closed dichotomy still seems to be present. Therefore, the structural change of the bilayer must be at least somewhat akin to what happens during the opening and closing of an ion channel. Based on these observations it is likely that the spike and multilevel events represent the formation of some type of

toroidal pore, with the inside of the pore lumen consisting of mixture of the phospholipid headgroups and peptides. The main difference between the two event types seems to be that in the case of the multilevel events the open state of the toroidal pore is better stabilized, greatly increasing the lifetime of the pore. Since not all spike events transition into multilevel events, it seems that the conditions for stabilizing a pore do not always follow the conditions necessary for forming one. Furthermore, the higher frequency of occurrence of spike events also seems to indicate that it is easier for the peptide to induce the conditions necessary for pore formation rather than pore stabilisation.

It is well known that AMPs at lower concentrations can induce non-disruptive changes to the biophysical properties of the bilayer such as membrane thinning, lipid de-mixing and line tension reduction (118, 185, 186). In the lateral diffusion model for low concentration AMP induced membrane disruption, these changes to the bilayer happen as the peptides insert into the top bilayer leaflet and then affect the bilayer in a small area around each peptide. The peptides can diffuse in the lateral plane of the bilayer leading to overlaps in the area of the bilayer they affect, which can potentiate their disruptive effect and thereby lead to the conditions necessary for the formation of a pore (187). Thus, the pore formation could be induced even without the peptides directly taking place in the pore structure, with the pores thereby missing out on the stabilizing effect the inclusion of the peptides in the structure likely would have. Such a mechanism could be responsible for the spike events (figure 4.13A). By contrast, in the case of multilevel events the local conditions at the pore formation could include more peptides in the proximity, allowing for the peptides to be incorporated into the toroidal pore structure itself, greatly increasing the lifespan of the pore (figure 4.13B).

Proposing an underlying molecular structure corresponding to the erratic event type is more challenging. The lack of a distinct start and endpoint makes it less likely that the “pore” structure is similar to a water channel in the traditional sense. Instead, the event type could represent a more general form of disruption of the membrane structure increasing the “leakiness” of the bilayer, allowing for water and ions to sporadically cross the bilayer at an increased rate. Changes to the structure of the bilayer such as membrane thinning, increased lipid chain disorder, a higher portion of membrane defects or lipid removal via micelle formation could all be factors lowering

the intrinsic resistance of the bilayer and thereby lead to periods of increased conductance (figure 4.13C).

Another option could be the formation of less well-defined peptide-lipid aggregates. It has previously been proposed that micellar like peptide-lipid aggregates could form within the bilayer creating structures that somewhat functions as a pore but without the toroidal or channel like shape (187). This would produce a much less defined path for the water and ions to penetrate the bilayer which could explain the more gradual shifts in the conductance seen for these events (figure 4.13D).

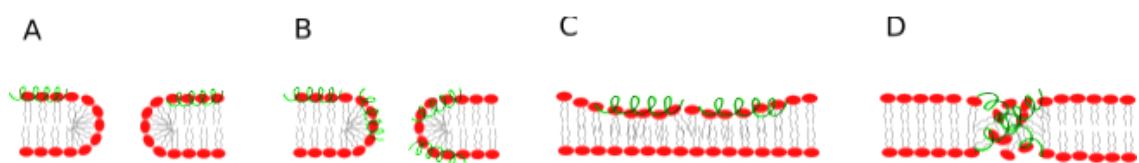


**Figure 4.13 Proposed molecular level structures corresponding to the conductance events observed in the patch clamp study.** A = The short-lived spike events are caused by unsupported toroidal pores without peptides in the pore lumen, B = The longer-lived multilevel events are caused by supported toroidal pores with peptides taking part in the pore structure, C = General disruptions to the bilayer structure such as membrane thinning could be the reason for the erratic events, D = Micellar like aggregates within the bilayer could be the reason for erratic events.

Overall, the results of the patch clamp study show that Smp24's mechanism of pore formation is complex. The AFM results do not show the same range of disruptive events but that is to be expected. The pores investigated using the patch clamp methodology represent pores existing early in the membrane disruption process and are thus both smaller in size and much shorter lived than what is likely to be observed using AFM. On the contrary, the larger, more stable and mature pores observed using AFM would likely not be observable using the patch clamp setup, as the small unsupported bilayer would not be able to sustain such pores without it leading to its complete disruption. Still, both experiments suggest that a significant part of the membrane disruption is due to the formation of toroidal pores and these pore structures also exist on a smaller scale than what was observed with AFM. To formulate the SMR it would thus be key to better understand how the structure of the peptide relates to the stabilisation of these small toroidal pores. It is likely that the

peptide structure would need to adopt a specific configuration that would allow it to be positioned within the pore lumen, while retaining its favourable interactions with the bilayer. Specific residues or regions could potentially be more important than others for making any conformational change possible and thereby the peptide-lipid pore assembly more favourable.

#### 4.3 Conclusions

Like many other amphiphilic AMPs the secondary and tertiary structure of Smp24 is highly dependent on the environment surrounding the peptide. Therefore, the structural prediction could be improved using MD simulations which allows for the explicit simulation and customisation of the solvent as well. The new predicted 3D structures based on the TFE simulations correlated well with previous experimental investigations of the peptide structure, based CD spectroscopy. Both approaches indicated the presence of two helical and one unstructured region with the MD simulations providing additional insight into where along the sequence these regions are likely located.

Investigation of the early stages of the Smp24 induced membrane disruption in synthetic bilayers indicated that the mechanism of action might be more complex than can be explained by the traditional models for AMP pore formation. Three distinct conductance event types were observed which likely corresponds to at least three different pore structures, however they all show signs of being disordered in nature. The spike and multilevel events could be correlated to the early stages of toroidal pore formation, which correlates to the mature pore structures observed previously in AFM experiments.

## 5. Structure mechanism relationship of Smp24

### 5.1 Introduction

MD simulations have the relatively rare ability to investigate both the structural and functional properties of a system at the same time, such as the structure of a ligand and strength of its interactions with a target. Furthermore, this information can be gained at an atomic level resolution, which allows for the influence of individual residues or regions of a peptide/protein to be evaluated. This makes this approach uniquely suited to be utilized in the construction of the SMR, where the structure and function of the drug molecule needs to be connected.

Another advantage of MD simulations is that they can investigate a system going towards an equilibrium state. Thereby details of processes happening on a femto- to micro-seconds scale can be investigated, something much more difficult to do using *in vitro* biophysical techniques.

However, in the case of simulations there are always several factors that need to be considered to ensure efficient and accurate use. Complex simulations are always going to be limited in scope compared to the real-world phenomenon that they are mimicking, whether that is in the complexity of the components and interactions, or in the scale of time and size of the system. Therefore, simplifications and assumptions must be made in the model design to ensure a reasonable level of simulation efficiency and lower the simulation-to-simulation variability. To ensure that the simplified model is still relevant to the real world, whenever possible the outcomes of the model/simulations should be checked against experimental results. In some cases, outcome values can be directly compared between the simulation and an experiment, however often this is not possible. If not, general trends observed in the simulations should at least be consistent with the experimental observations, giving an indication of a consistency in the behaviour.

### 5.2 Results and discussion

#### 5.2.1 Design of MD simulations

As the main target of Smp24 is the (inner) bacterial cell membrane, the central objective in exploring the SMR would be to gain insight into the interplay between the

peptide and the membrane. As shown previously the membrane can reasonably be replaced with a simplified synthetic bilayer without the peptide losing its activity (58). Therefore, the obvious approach would be to design a simulation modelling the interactions between the peptide and a synthetic bilayer. However, to fully model all the different aspects of the interplay between Smp24 and the bilayer a single simulation would not be sufficient. Therefore, an approach was chosen in which a base model was designed which could then be further modified into supplementary variant simulations expanding the scope of the investigations.

The base model was designed to investigate the basic interactions between Smp24 and a negatively charged bilayer. The central component of the model is a 7 nm<sup>2</sup> phospholipid bilayer, which both allows for efficient simulation and is large enough to avoid artifacts due to the peptide interacting with itself. A dual lipid mixture was chosen for bilayer consisting of 1:1 DOPC:DOPG lipids. This bilayer composition is much simpler than for real biological membranes but allows for a high degree of consistency at molecular scale while still representing some of the heterogeneity present in the real membrane. In addition, it also mimics the conditions previously used in *in vitro* synthetic models allowing for easy comparisons (58). The bilayer composition serves as a rough approximation for the surface charge profile present for prokaryotic membranes.

The Smp24 peptide was inserted into the model with its centre of mass about 1.5 nm above the bilayer, allowing for a very short delay before the peptide-bilayer interactions start. As previously shown, the vast majority of Smp24 molecules will adopt a random coil structure in the water phase which will gradually change to a helical structure during the interactions with the bilayer. However, simulation-wise this introduces two major problems. Firstly, starting with the peptide in a random structural configuration will introduce a large amount of variation between simulations, which is concerning due to the low number of replicate simulations that are feasible to do using MD simulations compared with other techniques. Secondly, having the peptide needing to undergo major structural changes would likely require a significant increase in simulation time per model, further limiting the overall number of simulations possible to run. Therefore, an already helical peptide configuration from the pepfold3 server (figure 5.1) was chosen as the starting structure used in the

simulation.

On each side of the bilayer an approximately 3 nm layer of water molecules were also added, to ensure the bilayer was properly hydrated. Some of the water molecules were exchanged with potassium and chloride ions to make the system overall neutrally charged. The simulations were, as a starting point, initially simulated for 500 ns, however in some cases the length had to be increased in order to reach an equilibrium.

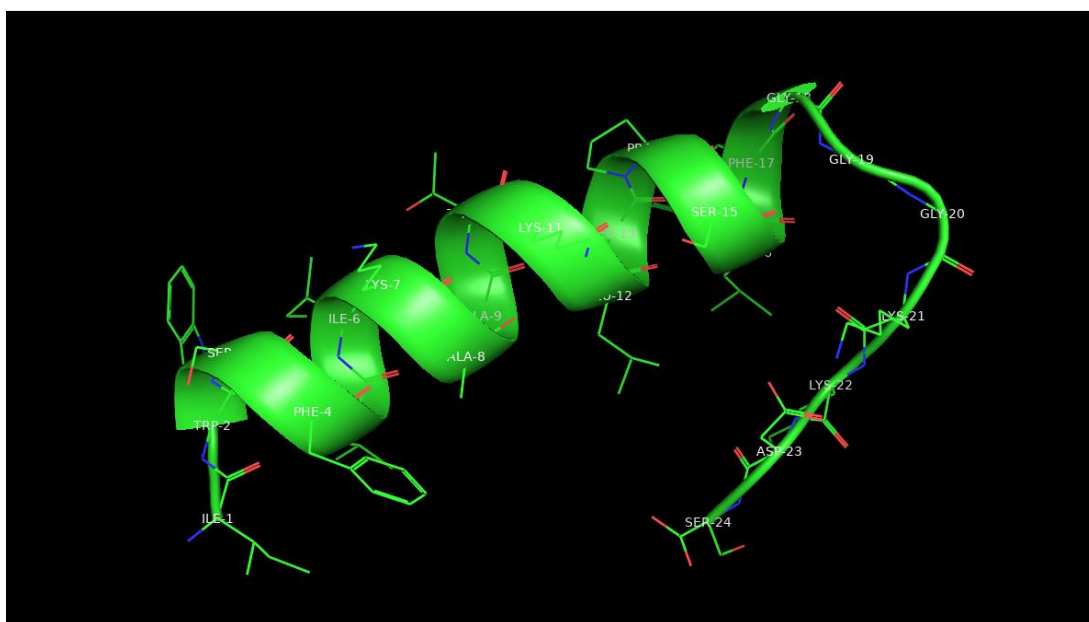


**Figure 5.1 Starting structure of Smp24 used in the MD simulations.** Generated via the PEPFOLD3 server (151).

The first simulation variant was designed to evaluate the effect of the bilayer's lipid composition. The only change made compared with the base model was changing the DOPG lipids to DOPE lipids. This gives the bilayer an overall neutral charge, mimicking that of the outer leaflet of a eukaryotic membrane. Again, this bilayer composition is also consistent with what has previously been used in *in vitro* experiments (58).

The second set of simulation variants were created to explore the effect of increasing the peptide to lipid ratio. This was done by having larger bilayers with multiple peptides inserted in each. However, to improve the efficiency of the simulation setup, the larger models were built in several steps. Firstly, simulations were run using the same conditions as the base model except with smaller bilayers. This ensures the

peptide insertion can be completed in an efficient manner. Once the simulations have reached an equilibrium they were multiplied in a grid like pattern along the X and Y axis several times (2x2, 3x3, 4x4), yielding a larger bilayer with multiple peptides already inserted. The larger models were simulated for some time to allow the bilayer to equilibrate and the peptides mix, before the final simulation run was executed. A similar approach has previously been used by Chen et al (124).

The third set of simulation variants builds onto the base model in order to investigate the peptide's role in membrane disruption. Based on biophysical experimental approaches, the formation of toroidal pores seems to be the most consistent way the peptide induces membrane disruptions. Therefore, models were designed to investigate how the peptide can interact with the toroidal pore and be incorporated into the pore structure. Under normal simulation conditions it is very unlikely that peptide induced pores can form, due to the limited timeframe of a simulation (129). Therefore, an approach was chosen where the pore is manually induced. With this type of approach, the role of the peptide in inducing the nucleation event creating the pore is not explored. Instead, investigating the way the peptide is incorporated into the pore structure is the main objective. The pore was created using electroporation by simulating a relatively large electric field (0.3 V/nm) running across the bilayer. Pore creation can also be done via other methods (129), but electroporation was chosen as it mimics the conditions present in the patch clamp experiments. The starting points for the simulations were the endpoint from the base simulations as this way the peptide was already inserted into the bilayer. Once the electric field had induced a small but consistent pore, the strength of the electric field was lowered to 0.065 V/nm which allowed for the pore to remain open over the full 500ns simulation time.

The range of possible pore associated peptide configurations were further evaluated by manually changing the position of the peptide within the pore lumen. This was done using a pull function where a constant force was applied to the centre of mass of the peptide pulling it down and towards the pore. This changed the position of the peptide relative to the pore such that it mimicked a deeper/more extreme inserted orientation. The pull function was applied to the peptide in two different starting positions and stopped at three different levels of insertion giving a total of 6 simulations. Thereafter the system was equilibrated for a few nanoseconds with the

peptide position locked. Finally, the system was simulated for 50 ns to see how the position of the peptide changed over time.

The fourth and final simulation variant explored if the peptide-pore interactions changed at a higher peptide to lipid ratio. The design/setup was done as with the previous variants except the starting point was the endpoint of one of the second variant simulations (mbcg\_16). Thereby the pore is formed in a larger bilayer with several peptides inserted, such that a pore structure which included multiple peptides could be explored.

**Table 5.1 Overview of Smp24 bilayer models.**

Simulation name	Simulation variant	Bilayer composition	Number of peptides	Bilayer size (nm <sup>2</sup> )	Peptide to lipid ratio	Simulation length (ns)	Number of repeats
bpg24_(1-3)	Base	DOPC:DOPG	1	7.03	1:144	500-970	3
bpe24_(1-3)	1	DOPC:DOPG	1	7.02	1:148	500-980	3
mbcg_0	2	DOPC:DOPG	0	13.64	na	100	1
mbcg_4	2	DOPC:DOPG	4	14.21	1:144	500	1
mbcg_9	2	DOPC:DOPG	9	12.62	1:48	250	1
mbcg_16	2	DOPC:DOPG	16	14.20	1:32	250	1
Long_pbcg_1-3	3	DOPC:DOPG	1	7.1	1:144	500	3
Pull_N_pbcg_1-3	3	DOPC:DOPG	1	7.1	1:144	50	3
Pull_C_pbcg_1-3	3	DOPC:DOPG	1	7.1	1:144	50	3
Multi_pbcg_1-5	4	DOPC:DOPG	16	14.20	1:32	100	5

### 5.2.2 Initial interactions and insertion of the peptide into the bilayer

Before the mechanism of insertion of Smp24 into the DOPC:DOPG bilayer can be explored, the evolution of the secondary structure must first be investigated. If the secondary structure changes over time, it must be considered during the insertion analysis making it much more complicated. The secondary structure of Smp24 over time in the simulations is comparable to what was found in the 60% TFE models and remains relatively stable throughout the insertion process in all three DOPC:DOPG simulations (figure 5.2). The peptide is helical starting at around residue 1 until residue 16-17. The rest of the peptide is unstructured. The consistent structure allows for the treatment of the primary helical region as a static geometric structure which can be used to easily evaluate the orientation relative to the bilayer.

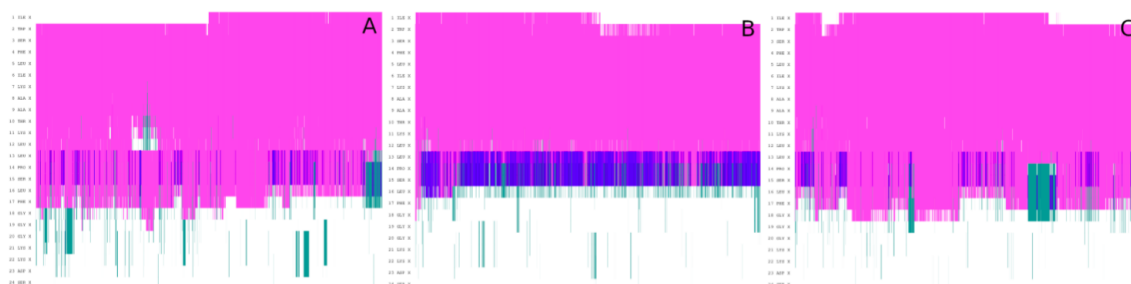


**Figure 5.2 Secondary structure of Smp24 over time in the DOPC:DOPG simulation.** Pink indicates alpha-helix, blue indicates 3-10 helix, green indicates turn, yellow indicates isolated bridge and white indicates random coil.

In all simulations, the peptide followed a consistent mechanism of insertion into the negatively charged bilayer that can be separated into multiple distinct steps.

Following an initial lag period with some sporadic electrostatic interactions between the peptide and the bilayer, the first consistent step seen in all the simulations is the anchoring of the N-terminal region to the bilayer (figure 5.3A & 5.4A). This interaction is, initially, driven by electrostatic interactions between the N-terminal amine and the lipid phosphate groups then, following a short delay supported by further electrostatic interactions between the bilayer and the two lysine residues (lys7 and lys11), positioned in the helical part of the peptide (figure 5.4B). In this position/orientation

most of the hydrophobic residues were orientated facing away from the bilayer except for the sidechains of the N-terminal ile1 and phe4, so hydrophobic interactions were limited to those residues. Due to the position of the helical lysine residues, the helical region of the peptides was orientated with a tilted angle relative to the bilayer normal of 125-140 degrees which inhibits interactions between the latter half of the peptide and the bilayer (figure 5.3B). The length of this stage of the insertion varied from a few ns to hundreds of ns, likely dependent on how consistent the lysine-phosphate interactions were.

The next stage of the insertion is defined by a major rotation of the helical region of the peptide, changing the orientation of the hydrophobic residues to facing down towards the core of the bilayer (figure 5.3C & 5.4C). This rotation also drove further changes to the peptide orientation, such as a reduction in the tilt angle and a change in the overall position of the peptide's centre of mass, bringing it closer to the core of the bilayer. These processes were not instant, taking around 50 ns or more from the beginning of the rotation until the peptide reached a stable orientation and insertion depth (figure 5.4D).

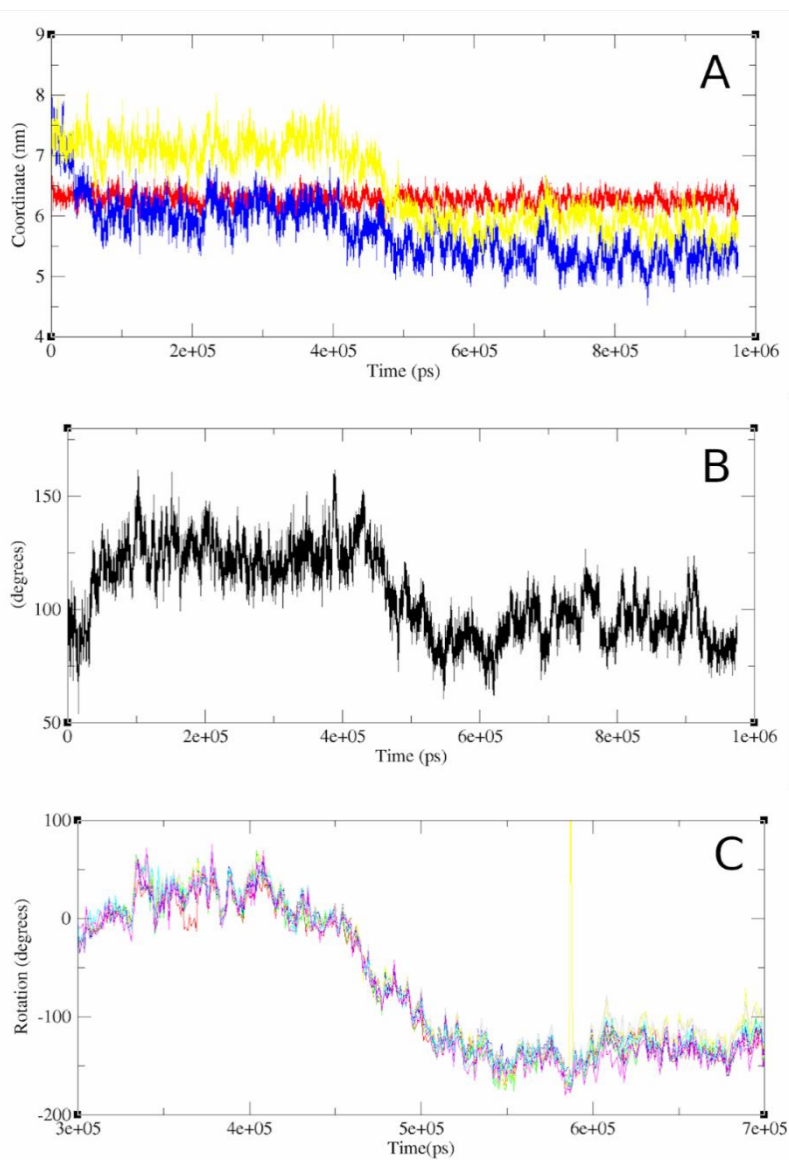


**Figure 5.3 Characteristics of the insertion of Smp24 into the negative bilayer** A: Changes over time in the Z-axis centre of mass of peptide (yellow) and N-terminal (blue) relative to the phosphor atoms of the top leaflet (red). B: Changes over time in the tilt angle relative to the bilayer norm of the helical region from residue 1-12. C: Cumulative changes in the local helical rotation of residue 2-10 during the rotational stage of the insertion process. Figures shown are based on one simulation (bcg24\_1).

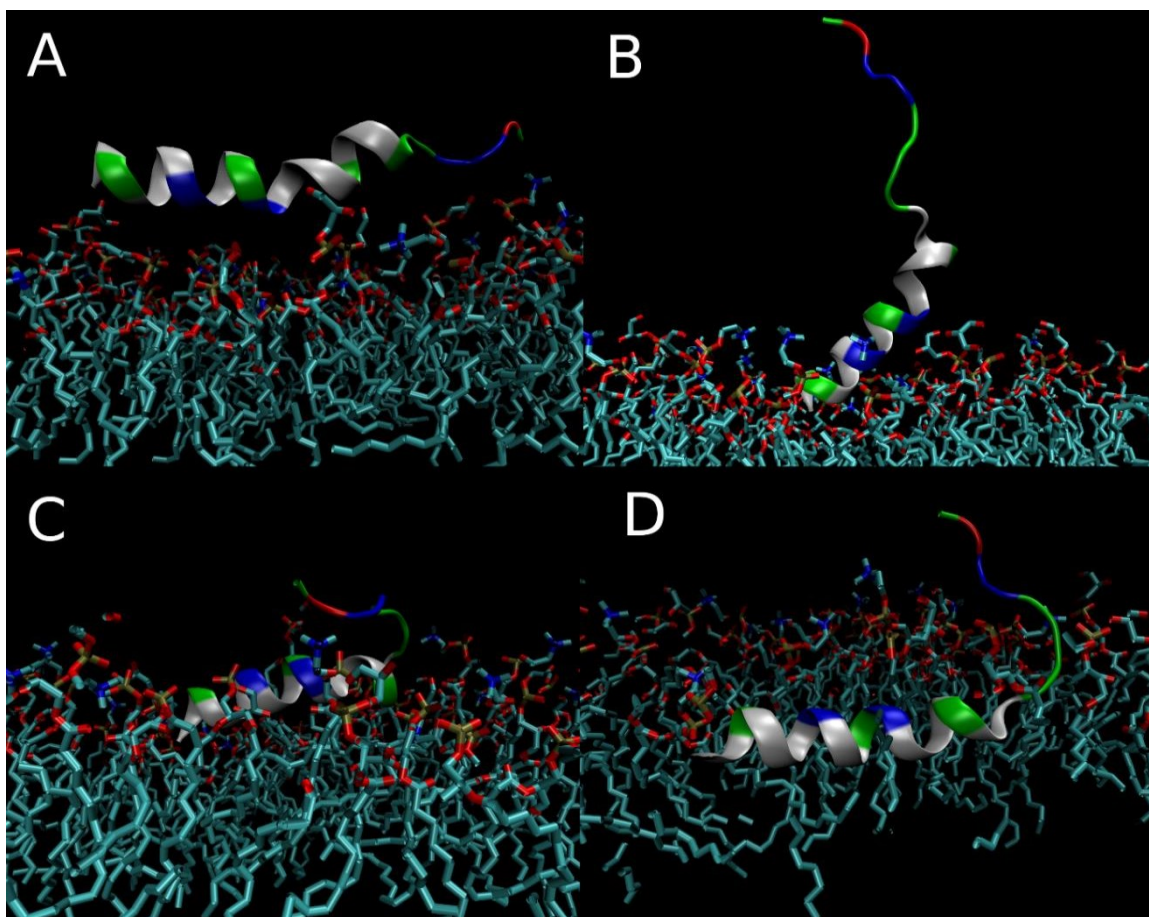


**Figure 5.4 Representative 3D structures of Smp24 during the different stages of the insertion process.** A = Initial lag period, B = N-terminal inserted stage, C = Helical rotational stage, D = Fully inserted peptide.

Due to the dynamic nature of the bilayer there is a relatively large variation in the kinetics for some of the transitions between the stages in the insertion process when comparing between the repeat simulations (table 5.2). However, similar changes in the peptide position and orientation could be found in all repeats.

**Table 5.2 Breakdown of insertion stages for Smp24 DOPC:DOPG bilayer models.**

Simulation name	Initial lag period	N-terminal inserted	Helical rotation	Fully inserted
bcg24_1	0-32ns	32-450ns	450-500	500-970
bcg24_2	0-2.2ns	2-6ns	6-80	80-500
bcg24_3	0-7.7ns	8-60ns	60-110	110-500

### 5.2.3 Mechanism of insertion

The ability to separate the insertion process into distinct phases based on a set of consistent and repeatable observations strongly suggests that the peptide has a specific mechanism of insertion.

The first stage is named the initial lag period and it is a necessary inclusion as the peptide starts the simulation in solution and is thereby not directly associated with the bilayer. However, due to the low starting distance between the peptide and bilayer, interactions happen almost instantaneously, driven by electrostatic interactions between positively charged lysine residues and the negative phosphate groups. Contrary to the observations in the other stages, the specifics of these interactions are not consistent between the different simulations. Therefore, even though interactions occur they are still counted as part of the lag period until consistent behaviour can be overserved.

Another aspect in which the initial lag period is inconsistent between the different simulations is in the length of the stage. An example of this is the *bcg24\_1* simulation in which the initial lag period is over 4 times longer than in the other simulations. This could be explained by consistent interaction between the bilayer and both lys7 and lys11 in this simulation. As both lysine residues are part of the primary helix they would lock the orientation of the helix in parallel with the bilayer surface, inhibiting the downwards movement of the N-terminal necessary for the transition to the next stage. In the other simulations these interactions were less consistent so the helix could more easily adopt the tilted orientation and thus the transition happens faster.

The process of the N-terminal moving from solution to the same level at the phosphate groups could have been designated as its own distinct stage of the insertion process. However, this process happens over a couple of hundred ps and is therefore on a completely different timescale than the other parts of the insertion process.

Instead, the next stage is called the N-terminal inserted stage. During the duration of this stage no active change in either the peptide position or orientation occurs, the stage instead describes an intermediary equilibrium which is facilitated by a couple of specific salt bridges. Consistent interactions were seen between the lipid phosphate groups and the N-terminal, lys7 and to a lesser extent lys11, as the polar part of the

primary helix is positioned down towards the bilayer. All these residues have an inflexible relative orientation, all being part of the primary helix which induces an angle between the helix and the bilayer surface of around 30-50 degrees. Further indications of how these electrostatic interactions affect the peptide orientation can be seen in the *bcg24\_1* simulation. Here the interaction between lys11 and the bilayer was much more consistent, providing a third contact point between the peptide and the bilayer further away from the N-terminal. This induced a slightly narrower angle between the helix and the bilayer compared with the other simulations where the lys11 interaction was less dominant. Other authors have similarly found that lysine residues closer to the N-terminal play a key role during the early part of the insertion process (115). Again, large variations can be seen in the length of this stage. The consistency of the different electrostatic interactions again likely plays a role but the adaptability of the bilayer must also be considered. The local environment surrounding the peptide can vary regarding both the lipid composition and their positioning and this is likely to affect when the transition to the next stage is possible.

A key observation of this part of the insertion process is that not all parts of the peptide seem to contribute to the interactions between the peptide and the bilayer. The tilted orientation of the primary helical region makes it such that the secondary helix and tail region are oriented away from the bilayer. As such, the interaction is mainly facilitated by a set of 5 key residues located on the primary helix (figure 5.5). As previously mentioned, the cat-ionic residues (N-terminal, lys7 and lys11) likely play the most significant role but in addition some other residues near the N-terminal are also positioned in such a way that they can contribute. The hydrophobic sidechains of the N-terminal Ile1 and phe4 are both positioned relatively low and oriented down towards the core of the bilayer. Thus, unlike the rest of the hydrophobic residues, these two residues could still be contributing to the binding at this stage of the insertion and potentially help anchoring the N-terminal to the bilayer. Substitution of the phe4 residue in *Smp24* to a smaller less hydrophobic alanine residue leads to a consistent reduction in activity both against prokaryotic (2x reduction) and eukaryotic cells (about 1.5X reduction) with especially the haemolytic activity being affected (5.5x reduction) (149). The specificity in the activity loss toward the erythrocytes could indicate that the residue specifically plays a role in the binding/insertion, which would

be consistent with the observations made in the simulation. The smaller alanine residue would not be able to contribute to the anchoring of the N-terminal to the same extent as the larger phenylalanine, leading to a reduced insertion efficiency. Finally, the sidechain of the Ser3 residue is also positioned to allow for the formation of hydrogen bonds with the lipid headgroups. While such polar interactions would be less energetically significant than the salt bridges, it would still contribute to the overall stability of the peptide-bilayer surface assembly.

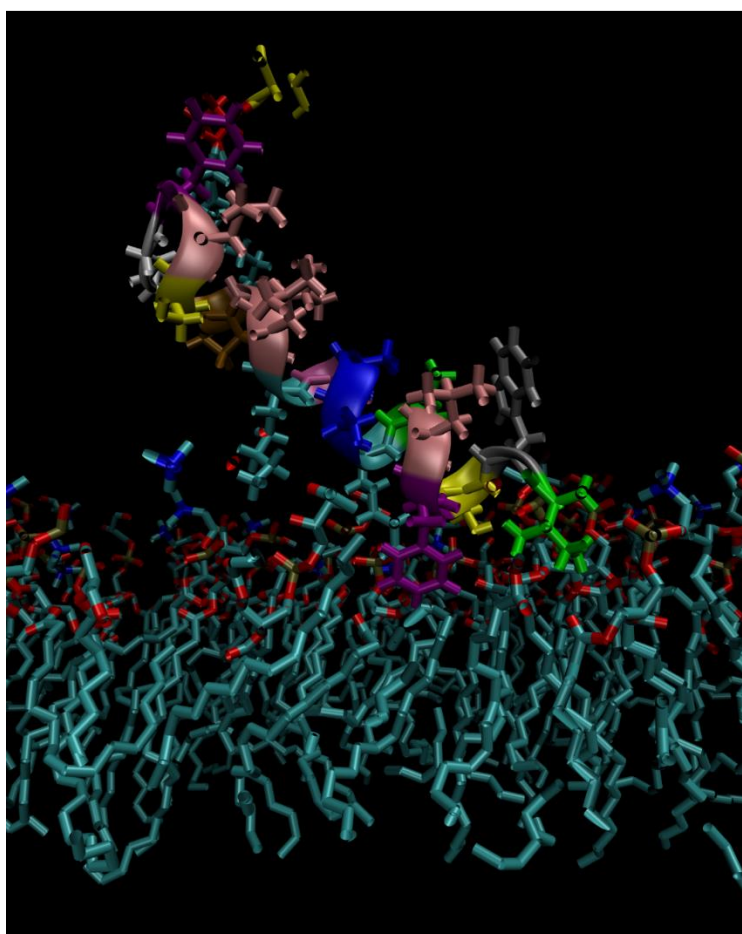


**Figure 5.5 Bilayer surface associated configuration of Smp24 representing the N-terminal inserted stage of the insertion process.** Interactions between the peptide and bilayer occur through the two lysine residues (light blue), N-terminal isoleucine residue (green), phenylalanine residue (purple) and serine residue (yellow).

The importance of the N-terminal region has been observed in MD simulations for other AMPs as well, with multiple examples of the N-terminal forming the initial interactions with the bilayer and serving as an anchor during the start of the insertion

process (115, 123, 125, 126, 182). However, *in vitro* studies indicate that the importance of the N-terminal amine in driving the insertion process might be dependent on the membrane composition. A few authors have investigated the effect of acetylating the N-terminal and thereby removing its positive charge. As expected, this seems to strongly reduce the antimicrobial efficacy against fungus and Gram-negative bacteria however against Gram-positive species the efficacy is conserved or even increased (188, 189). This effect could be explained by the acetylation allowing the N-terminal to insert deeper into the bilayer improving the membrane disruption (188). It is thus still possible that the acetylation reduces the initial interactions with the Gram-positive bacteria, but improved membrane disruption still leads to an overall increase in the antimicrobial efficacy.

The intermediary equilibrium configuration between the peptide and the bilayer surface could be a reasonable representation of the proposed surface attached state of the peptide. It is seen consistently throughout all the repeats, supported by several highly favourable electrostatic interactions and at least in one simulation has a relatively long lifetime. Counting against this theory is the fact that a large part of the peptide does not interact with the bilayer. This might be due to the more ordered starting configuration of the peptide used in the simulations. In a more realistic scenario where the peptide starts its interactions with the bilayer in a less ordered state, increased structural flexibility could potentially also allow the tail region to contribute to the binding/association. Since the secondary helix does not seem to actively contribute to the interaction with the bilayer, there should not be a strong driving force for it to fold into its helical state at this point. Therefore, one could imagine a more energetically favourable surface associated configuration where this region is unstructured allowing the tail region more freedom to interact with the bilayer. However, in any case the tilted configuration of the primary helix would likely still be the most fundamental part of the surface association.

The next stage of the insertion process is where the greatest change in both the positioning and orientation of the peptide happens. The major event characterising this is a rotation of the helical part of the peptide relative to the surface of the bilayer. Previously most of the hydrophobic residues were pointing away from the bilayer to facilitate the initial electrostatic interaction from the lysine residues on the other side

of the helix. However, after the rotation the hydrophobic residues are now positioned towards the bilayer core allowing for hydrophobic as well as electrostatic interactions between the peptide and bilayer. The bcg24\_1 simulation shows this rotation the clearest as it had a longer time to equilibrate the helical rotational orientation in the N-terminal inserted stage, showing a very clear rotation of around 180 degrees over around 90ns. As the rotation happens much earlier in the two other simulations, the peptide structure does not reach full equilibration before the rotation starts making it more difficult to evaluate the exact degree of the rotation.

The rotation is accompanied by both a large reduction of the angle between the peptide helix and the bilayer and a large change in the position of the COM of the whole peptide. In depth comparison of the timings between these different changes shows that the helical rotation starts slightly earlier than the change in angle or COM, which indicates that it is the rotation that drives the other changes. The electrostatic interactions that facilitated the orientation and position relative to the bilayer in the previous stage are still present during the rotation. However, the contact points shift from being below the peptide to on the side and above the helix as it is rotating. This is what allows for the initial reduction in the angle between the peptide and bilayer which also brings the COM of the whole peptide down. As the helix rotates further full hydrophobic interaction between the hydrophobic residues and the lipid acyl chains can be realized, leading to the fully inserted positioning of the peptide.

Recently, other authors have shown similar stepwise insertions mechanisms using MD simulations for other AMPs.

Ramos-Martin et al. (2020) describes a 3-4 step insertion mechanism for the AMP K11 with bilayers containing negatively charged lipids. Similarly, to Smp24 the first step is anchoring of the N-terminal facilitated mainly by electrostatic interactions. This is followed by step 2 and 3 where the peptide first twists causing a deformation of the bilayer that allows for the insertion of two aromatic residues, one near the N-terminal and one near the C-terminal. While residues near the C-terminal do not take part in the insertion process for Smp24, phe4 is inserted during the N-terminal inserted stage like the trp2 residue in the K11 peptide. Lastly, for some bilayers a 4th step is seen, where the helix rotates and full internalisation into the upper leaflet of the bilayer is seen. Thus, the two insertion mechanisms are very similar excluding the twisting step,

which is associated with a change to the area per lipid not observed for Smp24. However, this step is likely only possible due to the large amount of lysine residues present in K11 pulling on the bilayer, whereas Smp24 only interacts through the N-terminal amine, lys7 and lys11 (115).

Annaval et al. (2021) have found an insertion mechanism for the peptide BLP-3 that is very similar to Smp24. Initial interactions were established through the N-terminal amine, which then allowed for further salt-bridge formation of the more central lysine residues. Further into the simulations the helical region rotates allowing for full insertion into the top leaflet (116).

While some differences are present in the insertion mechanisms depending on the specific structure of each AMP, these observations could indicate that the 2 main steps being N-terminal anchoring followed by a helical rotation represents a consistent mechanism across this class of AMPs.

#### 5.2.4 Evaluation of the system equilibrium

After the rotational stage of the insertion process is completed, the peptide is assumed to be in its fully inserted state. While smaller changes can still be seen in the time dependent properties analysed during the insertion process, none are comparable in proportions or repeatability to the changes that were previously described. Therefore, the system is assumed to have reached an equilibrium with further changes in the peptide position and orientation being dynamic variation.

##### 5.2.4.1 Structure, orientation and positioning of the fully inserted peptide:

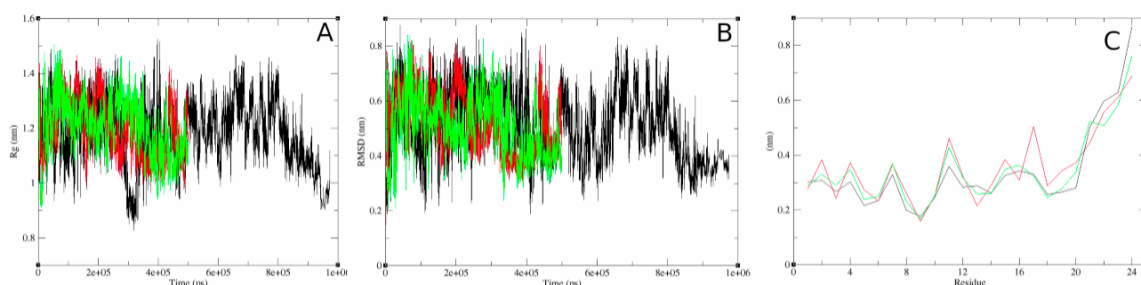


**Figure 5.6 Figures related to the structure of Smp24 in the DOPC:DOPG simulations.** A = The radius of gyration of the peptides over time. B = The root mean square deviation of the peptide backbone over time. C = The root mean square fluctuations of the peptides after full inserted into the bilayer. Black = bcg24\_1, Red = bcg24\_2, Green = bcg24\_3.

It could be expected that upon insertion into the DOPC:DOPG bilayer Smp24 would have a relatively stable 3D structure. However, in all simulations a high level of variation in both the backbone RMSD and peptide radius of gyration can be seen throughout most of the run time, suggesting constant changes in the structure (figure 5.6 A&B).

The bcg24\_1 simulation, which runs for the longest time with the peptide in the fully inserted state, does reach a point towards the very end of the simulation where both the RMSD and radius of gyration is lower and less variable. This could suggest that with more equilibration time in the inserted state a stable structure could be found.

The RMSF highlights that the structural fluctuations are much greater around the last 4 residues, reaching similar levels to what was seen in the solution models (figure 5.6C). The remaining residues show much lower structural fluctuations, generally even lower than what was observed in the 60% TFE models. In addition, the variation between the 3 simulations is also much lower than what was observed in the solution models.

These observations indicate that the tail region is still very flexible after the peptide is inserted into the bilayer. This is unlike what was observed in the 60% TFE solution simulations where the flexibility eventually was diminished due to the formation of intramolecular salt bridges. The simulations were checked for the formation of such salt bridges, however over a total of 1300ns of simulation in the inserted state only a single 20ns period could be found where the C-terminal or Asp23 were close enough to the helical lysine residues for salt-bridge formation to be possible. This happened right at the end of the bcg24\_1 simulation where the variation in the size and structural deviations are greatly reduced similarly to what was seen in the solvent models. Instead, the tail residues interact with the phosphor lipids which will be further explored in later sections.

The structural flexibility of the tail region is further highlighted in the representative 3D structures of the insertion peptide (figure 5.7). While the position of the tail region relative to the bilayer is relatively consistent in the two representative examples, the orientation of them deviates significantly. In one case, the tail is pointed away from the bilayer while in the other it lies almost in parallel with the primary helical region.

This is thus a direct example of the range of configurations the tail region can adapt. The orientation of the rest of the peptide is less variable. The structure and orientation of the primary helix is relatively consistent in the inserted state, lying almost in parallel with the bilayer surface. The kink between the primary and secondary helical regions is clearly present however the relative direction of the secondary helix varies throughout the trajectories. The glycine linker region is consistently oriented away from the bilayer core although the exact shape and direction depends on both the secondary helix and the tail region.

Overall, the secondary structure of the peptide is consistent with what was found in the 60% TFE simulation and the 4 structural regions are still clearly identifiable and relevant to the 3D structure.

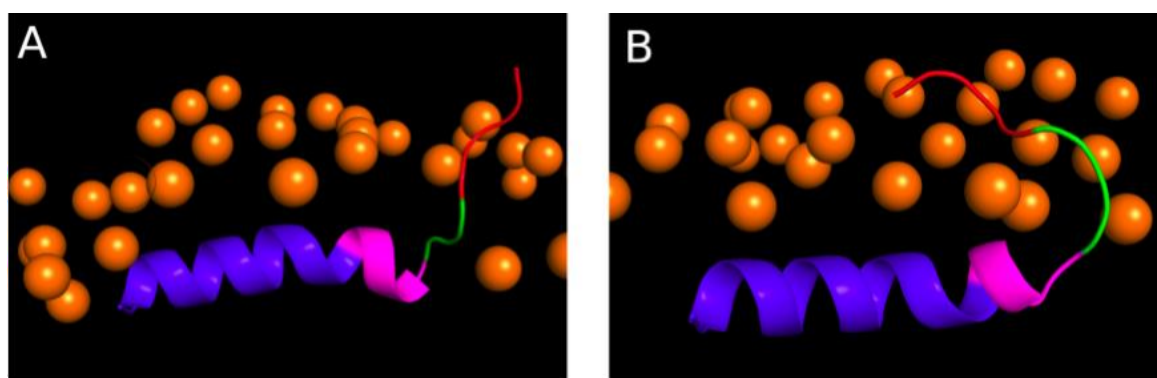


**Figure 5.7 3D structure of Smp24 inserted into a DOPC:DOPG bilayer.** taken from bcg24\_1 at A = 640 ns and B = 890 ns. Blue = primary helix, magenta = secondary helix, green = glycine hinge, red = tail, orange = lipid phosphor atoms.

While some information about the position of the different peptide regions relative to the bilayer can be obtained based on the 3D structures, a better overview of the positional distributions can be obtained by looking at the partial density profiles (figure 5.8). The partial density relative to the z-axis was calculated for the different peptide regions and compared to the lipid headgroups, glycerol esters and acyl chains. The density profiles show that the primary helical region is inserted at the deepest level, overlapping in position with the lipid glycerol esters and the top of the acyl chains. Next follows the secondary helical region which is still located in the same region of the bilayer although on average is slightly higher than the primary helix as it is depicted in figure 5.7B. The glycine hinge is located further up in the bilayer, overlapping mainly

with the lipid headgroups. Located the furthest from the bilayer centre is the peptide tail region, which partially overlaps with the lipid headgroups but is also partially above the bilayer in the water phase. The peptide positions are relatively consistent between all 3 simulations although for bcg24\_2 the helical regions are located slightly higher in the bilayer compared with the other.

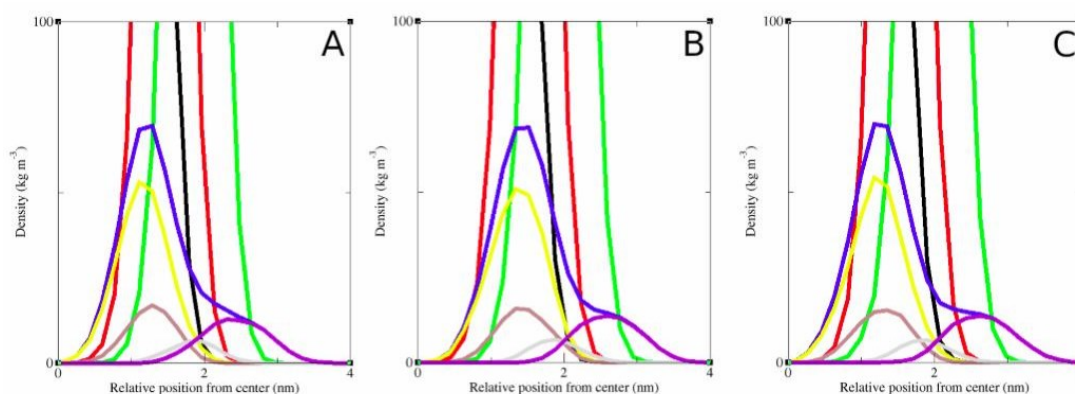


**Figure 5.8 Partial density profiles of Smp24 inserted into DOPC:DOPG bilayers, with positions relative to the z-axes.** A = bcg24\_1, B = bcg24\_2, C = bcg24\_3. Black = Lipid acyl chains, Red = Lipid glycerol esters, Green = lipid headgroups with phosphates, Blue = whole peptide, Yellow = primary helix, brown = secondary helix, Grey = glycine hinge and purple = polar tail region.

High resolutions structures of AMPs inserted into bilayers or vesicles can also be derived via experimental methods such as solid state or solution based structural NMR. While this has not been done for Smp24 yet, experimentally derived structures for other similar sized AMPs have been found and can be compared with the structure of Smp24 predicted by the simulations.

Piscidin 1 and 3 (both 22 residues) both adopt an almost fully helical structure with the alpha helical region spanning from residue 3-20, when inserted into either 1:1 PE/PG or 3:1 PC/PG bilayers. As with Smp24 the C-terminal region is positioned slightly higher than the rest of the peptide, but further evaluation using MD simulations shows it is still inserted well below the lipid headgroups unlike the tail region of Smp24 (190). The key structural difference in this case is that the piscidin peptides do not have nearly as large of an unstructured region at the C-terminal.

Magainin 2 (23 residues) has been shown to have a majority helical structure when inserted into a 9:1 POPC/POPG bilayer, with some unravelling of the helix near the C-

terminal observed from residue 20. However, in a 3:1 DMPC/DMPG bilayer the C-terminal region was observed to better retain the helical structure (191). Thus, like piscidin this peptide also lacks the consistent large unstructured regions near the C-terminal.

Pandinin 2 (24 residues) is the natural peptide with the highest sequence homology to Smp24, which includes a similar residue sequence near its C-terminal (KKDS vs SKKD). However, a key difference is that it lacks the glycine linker region before the polar tail. The tail instead comes directly after a secondary helix ending with an unstructured phenylalanine residue similarly to what precedes the glycine linker in Smp24. Like for Smp24 the tail region is unstructured while the rest of the peptide is helical, however no information about the position of the regions relative to a bilayer exists (146).

Consequently, it is not unheard of for AMPs to have an unstructured region near the C-terminal positioned slightly higher in the bilayer, but neither is it consistent. However, for Smp24 the large size and completely distinct position of the C-terminal tail region do represent a unique structural motif compared with most similar sized AMPs. The uniqueness is further facilitated by the inclusion of the glycine linker region which even Pandinin 2 lacks. However, searching AMP databases for the triple glycine motif reveals that one other peptide might also have a similar overall structure as Smp24. The AMP Con10 (FWSFLVKAASKILPSLIGGGDDNKSSS) found in the venom of the scorpion species *O. cayaporum* also containing 3 glycine residues followed by a range of only polar and charged amino acids. Simple *in silico* structure prediction indicates that this part of the peptide would be non-helical but more advanced *in silico* or NMR studies would be needed to confirm the structural similarities (192, 193).

The inclusion and position of the tail region could potentially offer a unique opportunity to influence the selectivity of the peptide after it is inserted into the membrane. As one of the major differences between the prokaryotic and eukaryotic membranes are the lipid headgroup compositions, having part of the peptide being positioned there could present an opportunity to optimise the structure for interactions with only one type of membrane. Other peptides might only interact with the variable part of the lipid headgroups during the insertion process and thereby selectivity based on the headgroups cannot be efficiently exploited after the peptide is fully inserted.

Another aspect that the tail region provides to Smp24 is that the peptide not only has an amphiphilic separation along the helical region but also along the primary sequence with the C-terminal end being much more polar than the rest of the peptide. Such a structural motif could be involved in binding Smp24 to other targets than the membrane. It has previously been hypothesised that the C-terminal region could be involved in binding of Smp24 to siderophores as sub-lethal concentrations leading to changes in regulation of several genes related to siderophore uptake and synthesis (194).

The unique orientation of the polar tail region also affects the 3D hydrophobic moment vector of the peptide. Previously the vector has been estimated for Smp24 to be at an angle of 127 degrees relative to the Z-axis, pointing towards the N-terminal of the peptide (149). However, this estimation was based on a fully helical structure of Smp24 which is not supported by the observations of the MD simulations or the prior CD spectra data (137, 149). Taking the position of the tail region from the MD simulations into account, the hydrophobic moment vector will not be shifted to the same extent towards the N-terminal. The increased flexibility of the tail region would also facilitate a greater variability in the hydrophobic moment, and it could potentially shift during pore formation. However, a clear relationship between the 3D hydrophobic moment and antimicrobial efficacy is yet to be established.

One structural motif present in the inserted structure of Smp24 which is also conserved in many other similar sized AMPs is the kink between the helical regions often facilitated by a proline or a glycine residue. Melittin (195), Magainin 2 (196), Brevinin-1EMa (197), Piscidin 1+3 (190) and Gaegurin P14 (198) all have a kink somewhere around the central part of their helical region. Multiple studies have compared the effect of removing the kink, most indicating that the kink influences pore formation however the exact effect is not clear. Computational studies indicates that inclusion of a helical kink improves the thermodynamics for formation of toroidal pores but inhibits barrel-stave pores (199), while another study indicates that kinks can reduce pore formation but increase membrane translocation and secondary targeting (200).

The kink could therefore have an important role in the mechanism of action of Smp24. However, while the position of the proline residue in Smp24 at position 14 is

consistent with the previously mentioned peptides, the large unstructured region of Smp24 necessitates that the secondary helical region of smp24 is much smaller than for other comparable AMPs. This reduced size of the secondary helix could impact the effect of the kink for Smp24. An indication for this can be found in a previous study where the proline residue was substituted with a more flexible GVG motif, which reduced the toxicity for Pin2 but had no effect on the toxicity of Smp24 while reducing the antimicrobial efficacy (137).

After the full insertion of Smp24 the primary helix is oriented almost in parallel to the bilayer surface. Using solid state NMR with oriented bilayers and N15 labelled peptides the orientation of many antimicrobial peptides in bilayers have previously been investigated. There is a broad consensus that for amphiphilic peptides such as Smp24, the peptide helix will be oriented in parallel with the bilayer at low peptide to lipid ratios. Some peptides such as PGLa have been shown to change into a more tilted state when the peptide to lipid ratio is increased, but as the base simulations were done at a very low peptide to lipid ratio, the observation of the in-plane orientation is expected (13, 190, 191, 201-203).

Some helical tilt can come from helical kinks such as with the peptide CAMA which has two helical regions separated by a GIG hinge. Both helical domains are tilted at about 20 degrees from the bilayer plane but if taken together, the overall orientation of the peptide is in parallel to the bilayer (204). This effect can also be seen for Smp24 in figure 5.7A and can explain some of the variation seen in the helix-bilayer angle as only the primary helical region is considered for these calculations.

Reißer et al have directly compared peptide bilayer orientation obtained by solid state NMR and MD simulations for 3 different helical AMPs. While they did find systematic differences in the rotation angle of the helix, the tilt angle between the peptide and bilayer were almost identical, all being about 6-11 degrees from the bilayer plane (205). Other authors have also found good consistency between the tilt angles from MD simulations and experimental methods (190, 202).

Thus, the orientation of the helical region of smp24 found in the DOPC:DOPG simulation is in good agreement with what has been observed for similar peptides both experimentally and *in silico*.

Overall, the predicted inserted structure of Smp24 based on the MD simulations has both some aspects that are consistent with most similar sized AMPs and some that are more unique. The unique parts of the structure could potentially be avenues for improving the properties of Smp24 compared to other peptides, but the lack of homology with other peptides could also indicate that they are not critical for the antimicrobial activity.

#### 5.2.4.2 Interactions between Smp24 and the bilayer:

The second aspect in which the equilibrium state was analysed was regarding the interactions between the peptide and the bilayer. It is the strength of these interactions that thermodynamically pushes the equilibrium towards the inserted state, a key step in the process towards the membrane disruption. Therefore, it is crucial to understand which underlying forces drive the interactions and which parts of the peptide are involved.

**Table 5.3 Breakdown of the free binding energies for the Smp24 PC:PG bilayer complexes.** All values are in kcal/mol.

Simulation name	Van der Waals energy	Electrostatic energy	Polar solvation energy	Non-polar solvation energy (Cavity)	Non-polar solvation energy (Dispersion)	Delta G total
bcg24_1	-158.379 ± 11.984	-406.273 ± 19.321	373.265 ± 16.237	-126.257 ± 8.806	230.808 ± 13.591	-86.835 ± 10.343
bcg24_2	-158.159 ± 13.887	-416.964 ± 19.799	383.224 ± 16.380	-127.211 ± 10.513	230.030 ± 15.905	-89.080 ± 10.958
bcg24_3	-156.655 ± 15.107	-407.661 ± 20.622	374.050 ± 17.427	-124.739 ± 10.915	229.112 ± 17.501	-85.893 ± 11.465
Average negative bilayers	-157.731 ± 0.766	-410.299 ± 4.747	376.846 ± 4.521	-126.069 ± 1.018	229.983 ± 0.693	-87.269 ± 1.337

The free binding energy of the peptide-bilayer complex was estimated using the MMPBSA method (table 5.3). As mentioned previously the MMPBSA method is best suited for analysing the relative binding energies when comparing between two systems, however some trends can still be analysed from a single system.

The calculations reveal that the overall binding energy is relatively consistent between the repeated simulations. This supports the idea that a consistent equilibrium exists and is reached in the simulations. The total binding energy is negative, so the formation of complex is energetically favourable as would be expected. The electrostatic energy contribution is by far the largest, however this is somewhat balanced by a relatively high cost in the polar solvation energy. The hydrophobic interactions are lower than the electrostatic ones but still significant even when correcting for the non-polar solvation terms. These general observations are consistent with what has been found for other AMPs, with electrostatic interactions consistently being shown to play a greater role than hydrophobic interactions for the overall binding energy (119, 125, 126, 172).

Since the electrostatic interactions were the main energy contribution, the formation of salt bridges between the cationic residues and phosphate groups were again analysed using RDFs (figure 5.9). The functions show that after insertion all the positively charged residues are involved in electrostatic interactions with the phosphate groups, which explains the high electrostatic energy contribution. This is contrary to what was observed during the insertion process where the two lysine residues near the C-terminal did not form consistent interactions. The interactions based on the N-terminal amine are still the most consistent of all the electrostatic interactions. The position 7 lysine now seems to form the least consistent interactions out of all the lysine residues, while it was one of the most consistent in the previous stages of the insertion.

These shifts in the RDF profiles indicate that the importance of the location of the lysine residue is not the same during the insertion process and the fully inserted stage. While the positioning of the lysine residues on the correct side of the helix is important in both stages, during the insertion positioning nearer the N-terminal seems to be

facilitate more consistent interactions. However, after the full insertion this is no longer the case. At this stage the increased positional flexibility of the lysine residues on the tail region might allow for the formation of more consistent interactions relative to the more inflexible positions of the lysine residues on the helix. The orientation of the inserted helix is based on what is optimal for all the helical residues as a total, which might make it such that the lys7 residue is not positioned optimally to consistently form interactions.

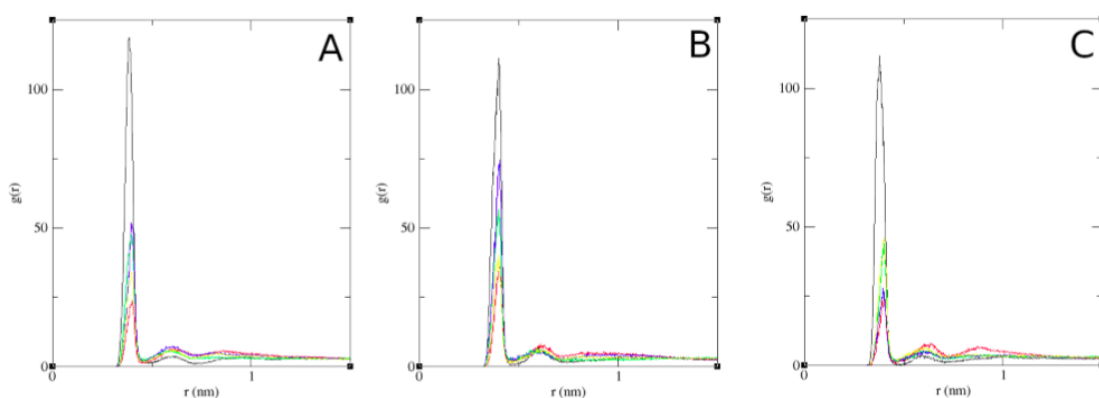


**Figure 5.9 Radial distribution functions between the positively charged amine groups of Smp24 and the phosphate groups of the leaflet of the bilayer that the peptide is interacting with, while the peptide is fully inserted into the bilayer (see table 5.2).** A = bcg24\_1, B = bcg24\_2, C = bcg24\_3. Black = N-terminal, red = Lys7, green = Lys11, blue = Lys21 and yellow = Lys22.

If, as proposed, the peptide's mechanism of action follows a stagewise mechanism (initial interaction, surface accumulation, insertion and membrane disruption) a key indication would be that the fully inserted state is more energetically favourable than the surface associated state. If the energy saved upon the peptide-bilayer complexes are fully inserted > surface accumulated > initial interaction the cascade would be driven towards the membrane disruption. Based on the MD simulations this seems to be the case. Firstly, in all three simulations full insertion is eventually achieved, demonstrating the feasibility of the cascade at low peptide conditions. Secondly, hydrophobic interactions have a significant impact on the binding energy of the fully inserted complex, interactions which must have been much smaller in the earlier stages of the peptide-bilayer association due to the different orientation and position

of the peptide. Lastly, even though electrostatic interactions seem to be the main driving force in the earlier stages, at least for the configurations observed in the MD simulations more residues can contribute to the electrostatic interaction after the full insertion of the peptide.

#### 5.2.5 Influence of membrane composition on insertion, structure and selectivity

In order to understand the SMR for AMPs it is not only important to understand which forces drive the mechanism but also which can inhibit it. As the target for activity and toxicity in both cases is the cell membrane, understanding the mechanisms behind the selectivity is necessary for improving the properties of the peptide. Therefore, the insertion process and equilibrium state were also investigated with a neutral bilayer mimicking the eukaryotic membrane, to highlight where differences are observed relative to the base model.

##### 5.2.5.1 Insertion of Smp24 in DOPC:DOPE bilayers:

The insertion of Smp24 into the neutral DOPC:DOPE bilayers share some similarities with the DOPC:DOPG bilayers, but also some major differences. The relevant time frames for the insertion process are summarized in table 5.4.

**Table 5.4 Breakdown of Smp24 DOPC:DOPE bilayer models.**

Simulation name	Overall Insertion level	Initial lag period	N-terminal inserted	Full insertion/rotation	Inserted
bce24_1	Full	0-101	101-424	424-490	490-980
bce24_2	Partial	0-389	389-465	460-475	475-500
bce24_3	Full	0-93	93-100	100-190	190-500

In general, the initial lag period was somewhat longer compared with in negative bilayer, which is likely due to the extra layer of positively charged lipid headgroups which inhibited the insertion of the cationic N-terminal. This increased lag time before

significant structure stabilizing interactions between the peptide and the bilayer could be established also lead to some degradation of the helical structure of the peptide in some of the simulations (data not shown). Only in simulation bce24\_1 did the peptide achieve a structure/configuration completely equivalent to the structures observed with the negative bilayer. Contrary, in the bce24\_2 the peptide did not achieve a full insertion below the phosphate lipid groups.

#### 5.2.5.2 Position of Smp24 inserted into the neutral bilayer

A much greater variation in the density profiles is seen with the DOPC:DOPE bilayers compared with the base models (figure 5.10). However, this is to be expected when taking the differences in secondary structure into account.

The bce24\_2 simulation only achieved a partial insertion and that is clearly reflected in the density profile. The peptide is mainly located around the lipid headgroups, and a large part of the peptide is still above the bilayer. The residues normally making up the primary helical region span the entire peptide profile, clearly indicating the lack of structure.

Bce24\_1 and bce24\_3 have more comparable density profiles. The position of the primary helical regions is slightly higher than in the DOPC:DOPG bilayers, but still in the same overall region. The secondary helical region and tail region in bce24\_1 both seem to be somewhat lower than in the DOPC:DOPG bilayer models, but this observation is not consistent with the bce24\_3 simulation. However, in all the DOPC:DOPE simulations the tail region seems to adopt a narrower distribution compared with the other bilayer and in the bce24\_1 simulation the tail does not extrude into the water phase.

Compared to the DOPC:DOPG bilayer simulations, the structural variation of Smp24 inserted in the DOPC:DOPE bilayers is much greater. It is possible that further equilibration of the inserted state could lead to a more consistent outcome if one specific configuration is more energetically favourable, but this would require a much longer simulation time. However, for direct comparison with the DOPC:DOPG structures only bce24\_1 will be used as the secondary structure of the inserted peptide is stable and the structural regions are consistent with what is observed in the DOPC:DOPG bilayer simulations.

Regarding the peptide positioning in the DOPC:DOPE bilayer there are two important things to note. Firstly, the primary helical region is not as deeply inserted as in the DOPC:DOPG bilayer. Secondly, although the position of the tail region is not consistent between the simulations, in all cases the density distributions are tighter than for the DOPC:DOPG bilayers. This is an indication that the tail region also behaves differently depending on the lipid headgroups, potentially due to an increased ability of the last two anionic residues to interact with the lipid headgroups. If such interactions occur, they would somewhat limit the flexibility of the of these residues which otherwise have the highest flexibility in the entire peptide. This could also explain the lower moment to moment variation seen in both the peptide size and RMSD. Thereby there are two aspects in which the position of the peptide in the neutral bilayer deviates from that in the negative bilayer, both of which could play a role in the selectivity of the peptide.

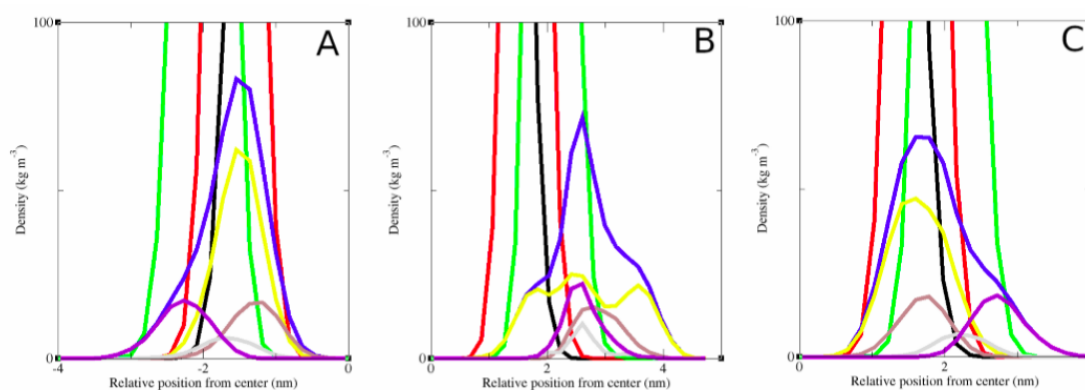


**Figure 5.10 Partial density profiles of Smp24 inserted into DOPC:DOPE bilayers, with positions relative to the z-axes. A = bce24\_1, B = bce24\_2, C= bce24\_3. Black = Lipid acyl chains, Red = Lipid glycerol esters, Green = lipid headgroups with phosphates, Blue = whole peptide, Yellow = primary helix, brown = secondary helix, Grey = glycine hinge and purple = polar tail region.**

### 5.2.5.3 Effect of membrane composition on peptide-bilayer interactions

A clear difference in the relative binding energies can be seen between the two types of bilayers. The average binding energy between Smp24 and the neutral bilayer is significantly lower than with the negative bilayer (table 5.5). Even the most favourable Smp24 DOPC:DOPE bilayer complex (bce24\_1) is still around 40% lower than with DOPC:DOPG bilayers.

A closer look reveals that the major difference is related to the electrostatic component of the binding energy which is more than 4 times smaller in the DOPC:DOPE bilayers. However, the large differences in the electrostatic energy are somewhat balanced by a correlated change in the polar solvation energy. The hydrophobic interactions are also on average slightly reduced in the DOPC:DOPE bilayers, but the difference is minor compared with the electrostatic energy and overall not significant. The bce24\_2 simulation deviates by far the most from the rest, but this can be explained by the peptide only achieving a partial insertion in this simulation. The superficial association of the peptide with the bilayer significantly reduces the hydrophobic interactions but the electrostatic energy is similar to the other DOPC:DOPE simulations.

Taking together the differences in the electrostatic interaction energy + polar solvation energy vs the Wan der Vaals interaction energy + non-polar solvation energy for the DOPC:DOPG models compared with bce24\_1, the polar effects contribution to the overall binding energy difference is still almost 5 times greater than the non-polar effects.

The small difference in the Wan der Vaals energies between the two bilayer models could be explained by the slight reduction in insertion depth of the primary helix observed in the DOPC:DOPE bilayer, limiting the interactions between the hydrophobic residues and the bilayer acyl chain. However, bce24\_2 also shows a slightly reduced insertion depth compared with the other DOPC:DOPG models, but no reduction in the Wan der Vaals energy is observed. Thus, no clear correlation between insertion depth and Wan der Vaals energy can be seen. Thereby the MMPBSA calculations overall strongly indicate that the selectivity at this stage is based on electrostatic interactions.

**Table 5.5 Breakdown of the free binding energies for the Smp24 bilayer complexes.** All values are in kcal/mol. \* Significant difference ( $P < 0.05$ ) between the two bilayer types based on a one-sided two sample independent t-test.

Simulation name	Van der Waals energy	Electrostatic energy	Polar solvation energy	Non-polar solvation energy	Energy dispersion	Delta G total
bce24_1	-152.837 ± 12.721	-86.366 ± 21.471	82.472 ± 17.064	-124.948 ± 11.186	229.429 ± 16.910	-52.250 ± 9.977
bce24_2	-61.716 ± 18.101	-60.134 ± 15.607	55.703 ± 13.422	-56.719 ± 15.606	108.958 ± 25.807	-13.908 ± 9.982
bce24_3	-148.569 ± 16.724	-56.942 ± 16.943	59.131 ± 14.956	-117.596 ± 12.839	218.056 ± 20.356	-45.920 ± 11.552
Average neutral bilayers	-121.041 ± 41.985	-67.814 ± 13.183 *	65.769 ± 11.894 *	-99.754 ± 30.578	185.481 ± 54.309	-37.359 ± 16.783 *

To further investigate the differences in the interactions a per-residue decompositional energy analysis was done, comparing the average values for all the DOPC:DOPG simulations with the bce24\_1 simulation. With this method the energy contribution of individual residues can be compared to identify if specific individual residues have a greater contribution to the selectivity than others (figure 5.11).

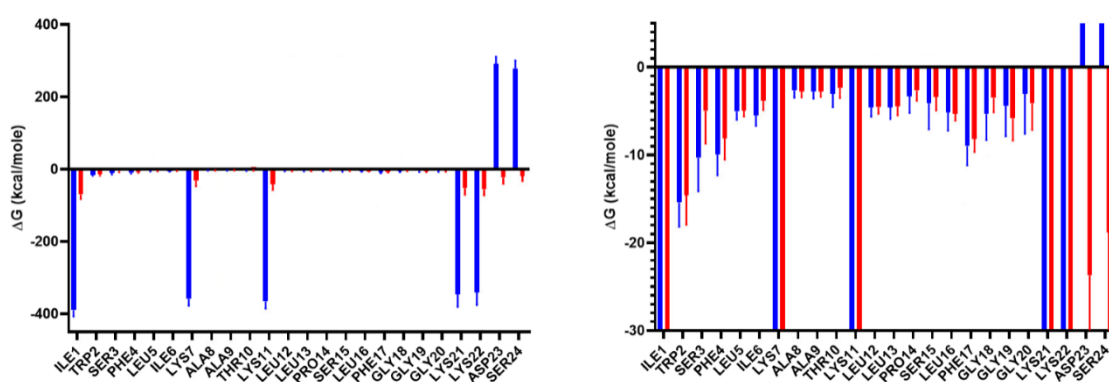


**Figure 5.11 Per-residue decompositional energy analysis comparing the average of three negative bilayer simulations with the bce24\_1 simulation.** Blue = negative bilayer, red = neutral bilayer. The difference between the two figures is only the y-axis scale.

This breakdown again highlights that the main driving force for the interactions between the peptide and both bilayers come from the positively charged residues. However, multiple clear differences can still be seen between the two bilayer types. While the positively charged residues still form strong interactions with the neutral bilayer, they are much smaller than with the negative bilayer as was expected based on the overall MMPBSA calculations. The interactions facilitated by the more hydrophobic residues are much closer between the bilayers, with some residues like leu16 even showing slightly higher interactions with the neutral bilayer but this could also be due to variation.

The most significant difference relates to the negatively charged residues Asp23 and Ser24. While these residues are relatively large contributors to the binding with the neutral bilayer, they seem to inhibit the interactions with the negative bilayer. The tail region overall seems to have a much greater relative contribution to the interaction with the neutral bilayer, likely due to the negatively charged residues being able to interact with the PE headgroups. In addition, the positively charged lysine residues on the tail region also seems to have relatively increased energy contribution compared with the other lysine residues when interacting with the neutral bilayer. This difference in how effective the tail lysine residues are based on the lipid composition could be a downstream effect of the increased interaction between the bilayer and the anionic residues. In the case of the negative bilayer the anionic residues cannot form consistent interactions with the lipids so instead they might form intermittent interactions with the cationic residues of the tail region. Such intermittent interactions could on average lead to the reduced relative energy contribution.

Based on these observations, the tail region seems to have a negative impact on the selectivity at this stage. However, this is likely very dependent on the specific composition of the bilayer/membrane. In the simulations the key differentiating factor seems to be the inclusion of the PE lipids in the neutral bilayer. However, this lipid type is not unique to eukaryotic cells. Many Gram-negative species such as *E. coli* contain a significant amount of PE lipids (206), so in these cases the tail region might also be important for the antimicrobial activity.

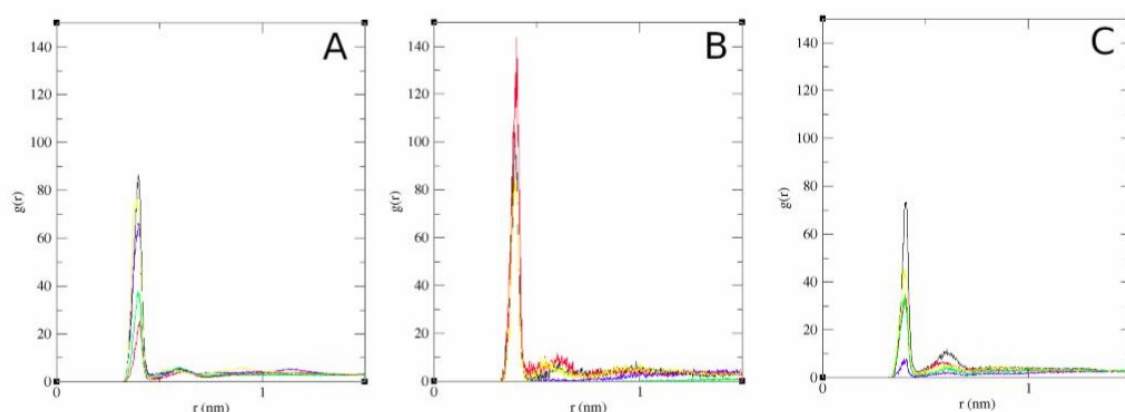


**Figure 5.12 Radial distribution functions between the positively charged amine groups of Smp24 and the phosphate groups of the leaflet of the bilayer that the peptide is interacting with, while the peptide is fully inserted into the DOPC:DOPE bilayer. A = bce24\_1, B = bce24\_2, C= bce24\_3. Black = N-terminal, red = Lys7, green = Lys11, blue = Lys21 and yellow = Lys22.**

The consistency of the salt-bridge formation was also investigated using RDFs (figure 5.12). For bce24\_1 and bce24\_3 the RDFs are comparable with DOPC:DOPG models and in both cases mainly deviate by greatly reduced interactions at the N-terminal. Otherwise, most of the lysine residues still form relatively consistent interactions except for lys21 in bce24\_3.

The bce24\_2 simulation deviates greatly from the others showing interactions only for the N-terminal, lys7 and lys22 but this can be explained by the lack of secondary structure and reduced insertion depth.

In addition to evaluating the difference in the electrostatic interactions based on the salt bridge formation, the average number of hydrogen bonds formed during the equilibrium state were also calculated (table 5.6). In most of the simulations a lower average number of hydrogen bonds is achieved between the peptide and the neutral bilayer, although overall the difference is not significant. The exception is bce24\_1 which reaches a similar level as the DOPC:DOPG bilayers but with a much greater degree of variation.

Taken together with the per-residue MMPBSA analysis it seems that the difference in the electrostatic energy component is more related to the strength of the charged interactions rather than an overall reduction in polar interactions.

**Table 5.6 The average number of hydrogen bonds once Smp24 peptide were fully inserted into the bilayers.** \* Significant difference ( $P < 0.05$ ) between the two bilayer types based on a one-sided two sample independent t-test.

Simulation name	Average number of hydrogen bonds (inserted)
bcg24_1	$8.855 \pm 2.418$
bcg24_2	$10.049 \pm 2.431$
bcg24_3	$8.585 \pm 2.234$
Average negative bilayers	$9.163 \pm 0.636$
bce24_1	$9.746 \pm 3.841$
bce24_2	$6.861 \pm 2.501$
bce24_3	$7.619 \pm 2.689$
Average neutral bilayers	$8.075 \pm 1.222$

When comparing the totality of the simulations, a clear trend can be seen that the selectivity occurs throughout the entirety of the peptide-bilayer interactions, and it is mainly driven by differences in the electrostatic interactions. These observations are consistent with experimental results from several different methodologies, showing lipid dependency both during binding (liposomal leakage assays) and during pore formation (AFM) (58). The selectivity is both expressed on a molecular level where important binding points are shielded from the peptide and on a broader thermodynamic level where the interactions are less energetically favourable. While lipid dependent differences in the membrane disruption have previously been shown (58), the early stages of the mechanism of action before the membrane disruption also seems to be crucial for the endpoint selectivity.

### 5.2.6 Concentration dependent effects on the bilayer biophysical properties

The previous sections of the simulations have mainly focused on how the peptide is affected by the bilayer. However, bilayers are dynamic macromolecular structures which can readily respond to changes in their environment. The insertion of the peptide into the leaflet of the bilayer will to some extent affect both the local and macroscopic structure of the bilayer as the peptide takes up space between the lipids. Any macroscopic changes to the bilayer's properties could be difficult to identify based on the base model only, since the peptide to lipid ratio is relatively low. A clearer indication of any effects would be if concentration dependent changes to the properties could be observed by increasing the peptide to lipid ratio.

Simulations were done at three different peptide to lipid ratios in addition to one simulation of only the bilayer and several bilayer related properties were explored.

The area per lipid (APL) and membrane thickness are two measurements related to the macroscopic structure of the bilayer. Both of which were affected by the insertion of the peptides in a concentration dependent manner (table 5.7). The increasing peptide to lipid ratio led to a reduction in the bilayer thickness and an increase in the APL.

The increase in the APL can be somewhat counterintuitive. While the average area each lipid takes up is greater after the peptide insertion, it does not necessarily mean that all the lipids are more spread out. In the top bilayer leaflet where the peptides are inserted space between the lipids will be taken up by the peptide causing the total size of the bilayer to expand. The bottom bilayer leaflet will at least to some extent match this expansion to ensure the integrity of the bilayer core is retained, causing a relatively straight forward increase in the APL for that leaflet.

The behaviour of the lipids in the top bilayer leaflet is more complex. Some of the lipids will be pushed together while others will have a large direct distance between them due to being separated by the inserted peptides. However, this amounts to an increased APL for the leaflet and the bilayer as a whole.

The macroscopic changes to the top leaflet of the bilayer can also have indirect effects on the properties of the peptides. One such property could be the ability for the peptides to move around in the lateral plane of the bilayer. The lateral diffusion constant for the peptides were estimated for the different bilayer systems showing a concentration dependent decrease as the peptide to lipid ratio is increased (table 5.7).

This suggests that as more peptides are inserted into the bilayer their ability to move around becomes highly restricted.

**Table 5.7 Area per lipid, membrane thickness and lateral peptide diffusion constants of the DOPC:DOPG bilayers after insertion of Smp24 relative to the peptide:lipid ratio.**

Simulation name	Peptide:lipid ratio	Area per lipid (nm <sup>2</sup> )	Bilayer thickness (nm)	Lateral peptide diffusion constant (10 <sup>-7</sup> cm <sup>2</sup> /s)
mbcg_0	na	0.696 ± 0.006	3.797 ± 0.029	na
mbcg_4	1:144	0.707 ± 0.006	3.789 ± 0.030	1.52 ± 0.52
mbcg_9	1:48	0.736 ± 0.007	3.752 ± 0.030	0.99 ± 0.37
mbcg_16	1:32	0.758 ± 0.006	3.711 ± 0.029	0.32 ± 0.26

Another key indicator for if the structure of the bilayer is changing due to the peptide insertion is the lipid acyl chain order parameters (figure 5.13). These order parameters are calculated for each carbon atom in the lipid's acyl chains based on the orientation of the C-H bond relative to the bilayer normal. If the structure or order of the lipid chains changes the lipid acyl chain order parameters will also shift for the affected parts of the chains.

No differences could be seen between the bilayer only simulation and the lowest peptide to lipid ratio, however as more peptides are added the lipid order starts to be affected. A small increase in the order parameters could be seen for the top of the lipid chains but the main effect is a concentration dependent reduction in the order for the lower half of the lipid chains, indicating the orientations of the lower part of the lipid chains shifts due to the presence of the peptides.

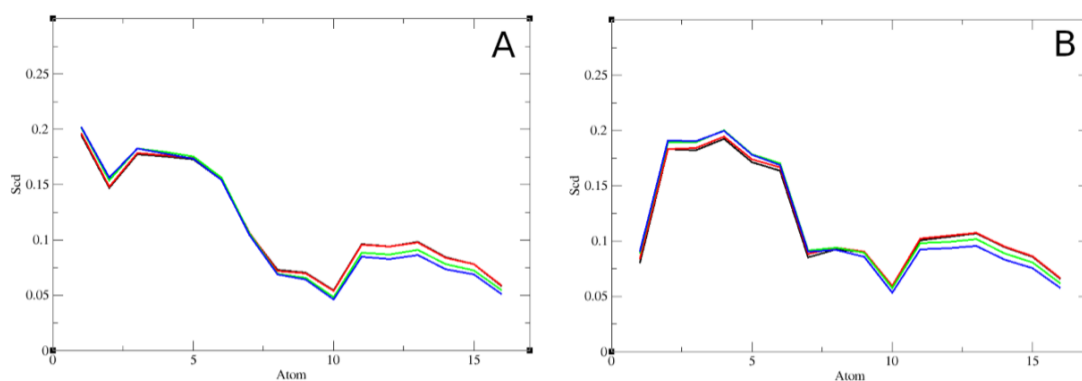


**Figure 5.13 Deuterium order parameters of the multi-peptide simulations.** A = sn1 chain, B = sn2 chain. Black = mbcg\_0, red = mbcg\_4, green = mbcg\_9, blue = mbcg\_16.

All the different macroscopic effects on the bilayer are likely linked to the molecular level changes to the lipid structure that they need to make in order to adapt to the inserted peptides. When the peptides are inserted into the leaflet, the lipids are pushed apart leading to the increase in the APL. To retain the integrity of the hydrophobic lipid core, some of the lipid chains need to bend underneath the peptides as the peptide does not extrude all the way to the centre of the bilayer. This causes the change in the order parameters of the lower half of the acyl chains. Lastly, with some of the lipid chains adapting a less straight configuration, the overall thickness of the bilayer will be reduced.

Changes to the properties of the bilayer/membrane such as thinning have been shown for other AMPs before and been linked to membrane disruption.

Grage et al. found that amphiphilic AMPs such as Magainin 2 and BP100 caused concentration dependent changes to the deuterium order parameters, increased the APL and reduced the membrane thickness of DMPC bilayers when investigated using solid state NMR (207).

Chen et al. have investigated the relationship between membrane thinning and the transition of the AMPs from a surface parallel to a transmembrane like state. They hypothesise that the peptide induced membrane thinning could make it more favourable for the peptide to transition to an orientation indicative of toroidal pore formation (208).

### 5.2.7 Modelling of pore associated configurations of Smp24

As the experimental results indicate that the formation of toroidal pores is one of the most consistent ways that the peptide induces membrane disruption, understanding how the structure of the peptide adapts to the pore could give insight into how the peptide stabilises the pore structure. Simulations were first done at a low peptide to lipid ratio to investigate how an individual peptide could interact with a preformed pore in an unrestricted way.

Throughout the three simulations two different pore-associated peptide configurations were observed, where in both cases the peptide positioned itself at the interface between the pore and the rest of the bilayer. In the first configuration (figure 5.14A) the peptide is oriented with the N-terminal towards the centre of the pore. The primary helical region is positioned along the top of the pore lumen and thus to follow the higher curvature of the bilayer in this region it adopts a higher tilt angle (30 degrees relative to the bilayer surface) compared with the normal orientation of the helix in the non-pore bilayer. The secondary helix is positioned further away from the pore where the bilayer curvature is less extreme and thus adopts a lesser tilt angle (10 degrees relative to the bilayer surface), more in line with the normal orientation. The trp2 residue is inserted the deepest within the pore, with an average position around 0.6 nm above the bilayer centre. In the second configuration (figure 5.14B) the helical regions of the peptide are positioned in reverse. As such the secondary helical region is now the one oriented towards the centre of the pore. Therefore, it is the secondary helix that adopts the higher tilt state (-25 degrees relative to the bilayer surface), while the primary helix is only tilted slightly (-6 degrees) compared with the normal orientation. In this configuration the leu16 residue was inserted the deepest at an average position of around 0.85 nm above the bilayer centre.

In both cases the tail region seems to behave relatively independently from the membrane pore, while the helical regions facilitate the positioning and orientation between the peptide and the pore. As such, due to the difference in the position of the secondary helix in the two configurations the tail region is also positioned very differently. In the A configuration the tail region is positioned the furthest from the pore itself and therefore likely has very little influence on the pore structure. In the B configuration the transition from the helical to unstructured regions starts almost in

the centre of the pore giving the tail region a much better opportunity to impact the pore. However, the interactions still seem to be relatively minimal. In the configuration shown in figure 5.14B the tail is positioned in the solvent phase above the pore, while in other examples it is positioned above the peptide's helices. The overall inconsistency in the position and orientation of the tail indicates that its role in the peptide-pore assembly structure is minimal compared to the helical regions.

Throughout the 3 simulations (combined 1.5  $\mu$ s simulation time) the peptide spent approximately 150 ns in the A configuration, 720 ns in the B configuration and 630 ns in configurations not associated with the pore. The A configuration only occurred in one simulation where the pore nucleation site was close to the N-terminal of the peptide whereas the peptide transitioned to the B configuration at some point in all three simulations.

Two key observations can be made from the peptide-pore configurations. Firstly, a key property of the configurations that peptides adopt is that they allow the helical regions to align with the increased curvature of the pore interface. This ability is to a large extent driven by the inclusion of the kink between the two regions allowing the overall shape of the helix to be bent. However, with the singular flexible point the alignment is not perfect. This might explain why the B configuration is more commonly found. In the A configuration the larger inflexible primary helix is positioned further within the pore lumen where the curvature is the greatest, with the kink itself being positioned right at the interface between the pore and the rest of the bilayer. However, in the B configuration the lumen position is taken up by the secondary helix and thus the kink is also positioned within the high curvature region itself. This allows the helical regions to adapt and have an overall curve that better aligns with the pore and is likely slightly more favourable.

The second key observation was that at no point does the peptide adopt a fully transmembrane configuration where it is oriented tangentially to the bilayer surface or is positioned with parts of the peptide going through both sides of the pore. The peptide seems limited to being positioned at the top half of the pore lumen, which is also consistent with previous experimental observations using AFM (58). This might again be related to the shape of the helical regions. The long-helix short-helix motif

seems to be better suited to align with the upper or lower half of the pore lumen where the curvature is uneven at each side of the kink. If instead the kink was positioned more centrally within the overall helical region an orientation more central in the lumen might be more plausible.

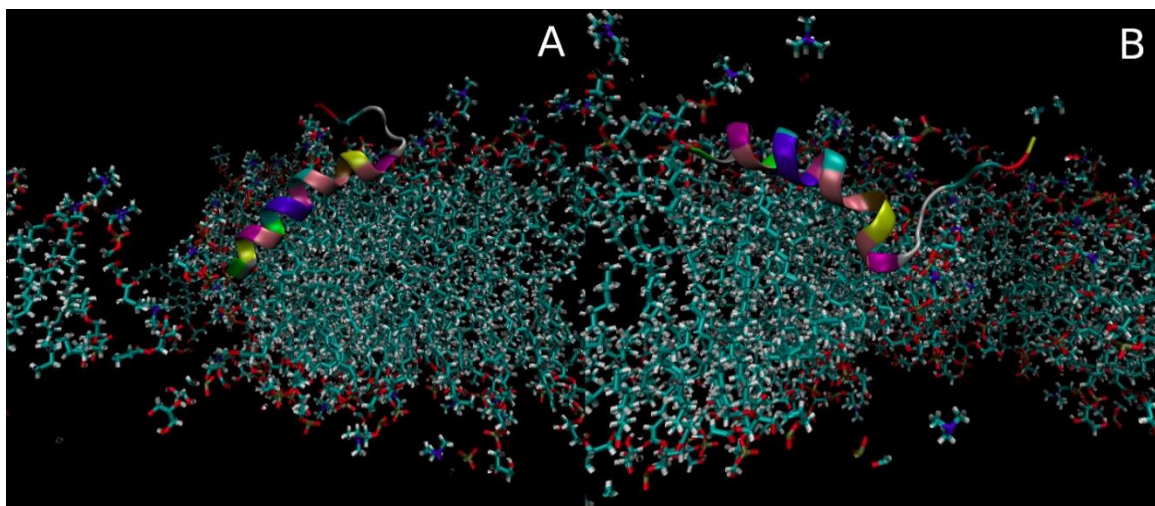


**Figure 5.14 3D models of the two pore associated configurations seen for Smp24 in the long\_pbcg\_1-3 simulations.** A) The helical regions of Smp24 are aligned with the curvature of the pore interface with the secondary helix positioned within the top of the pore. B) The helical regions are aligned in reverse such that the primary helix is positioned within the top half of the pore.

To further evaluate whether the lack of a transmembrane peptide configuration was due to it being unfavourable or due to kinetic limitations of the simulation timeframe, several more extreme insertion configurations were induced. The peptide was pulled down deeper into the pore lumen at three different levels, starting from either of the previously described configurations. The centre of mass relative to the Z-axis was evaluated over a 50 ns period to investigate if the peptide would stay in the more extreme positions or transition back to the original configurations (figure 5.15).

At the lowest level of pull (figure 5.15 A and D), the positions were more or less the same as they were in the unrestricted simulations. While the 3D positions of the peptides were locked during the equilibration step after the pull, the position of the bilayers were not. It seems that the bilayer/pore itself quickly adapted to the slightly deeper insertion peptide insertion level and as such when the unrestricted simulation

started the peptide was basically already posited as previously observed. Both starting positions were relatively stable, although for the configuration with the primary helix positioned towards the pore the peptide did eventually move away from the pore after about 30 ns.

In all the remaining cases where the peptides were pulled further down the pore lumen, the peptide relatively quickly moved away from the extreme starting position. For the configurations where the primary helix was inserted the deepest within the pore (figure 5.15 E and F), the peptide ended up reaching a state where both the primary and secondary helix were positioned in same plane indicating that the peptide was no longer associated with the pore. In the cases where the peptide started with the secondary helix positioned the deepest within the pore (figure 5.15 B and C), the peptide either transitioned to the previously described pore associated configuration or to an unassociated configuration.

These observations indicate that the lack of a true transmembrane peptide configuration in the unrestricted simulations was not just due to the limited simulation time. The deeply inserted configurations did not seem to be very stable supporting the previous observations related to the peptide's shape. Other factors such as the pore size could also impact the stability of the deeply inserted configurations, but a larger pore would be difficult to induce without completely disrupting a bilayer of the size used.

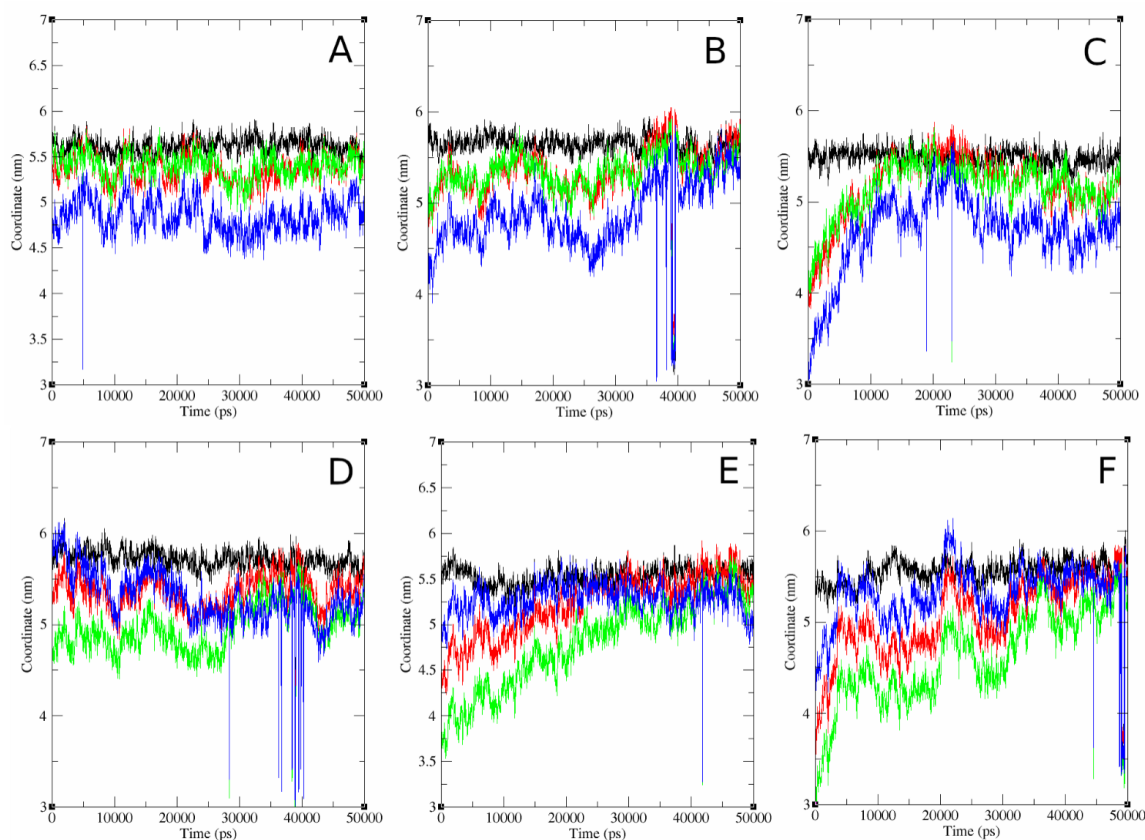


**Figure 5.15 Center of mass over time for Smp24 after being pulled into more extreme positions within the pore.** A-C) Peptide pulled from a starting position with the secondary helix oriented towards the pore opening. D-F) Peptide pulled from a starting position with the primary helix oriented towards the pore opening. Black = COM of the phosphate group of the top leaflet, red = COM of the whole peptide, green = COM of the primary helix, blue = COM of the secondary helix.

As previous experimental results have indicated that the Smp24 induced membrane disruption follows a threshold-based behaviour, the peptide-pore assembly structure was also investigated at a higher peptide to lipid ratio. To achieve this, a pore was induced into the endpoint of the mbcg\_16 simulation containing 16 inserted peptides in a 14.2 nm<sup>2</sup> bilayer. This allows for the visualization of a slightly larger pore with multiple peptides associated with it and it occurs at a much higher peptide to lipid ratio (1:32 vs 1:144). This ratio is within the level needed to observe pore creation *in vitro* for other AMPs such as melittin (209). As the simulation of the larger system is much more computationally expensive, the simulations were only done over 100ns but instead 5 repeats were done with independent pore formation.

As in the single peptide simulations most of the peptides adopted either a configuration associated with the top of the pore lumen or one completely

independent of the pore. The number of peptides associated with the pore at the endpoint of each simulation ranged from 4 to 5, with 33% being in the A configuration, 58% in the B configuration and 8% adopting a more sideways facing configuration. However, while the peptide configurations in the multi-peptide setup broadly align with what was observed with the single peptide, in some cases the position and orientation of individual peptides were more extreme. In all the simulations, 1-3 of the peptides adopted a deeper inserted position with part of the peptide reaching below the centre of the bilayer at some point in the simulation (figure 5.16). In addition, to accommodate the new positions of the peptides within the pore more tilted orientations of the helical regions were also observed. Both types of the previously described pore-associated configurations were observed to be able to transition to this greater inserted state, although the specific 3D structure, position and orientation of the peptide was more variable between different instances of this new state.

The A configuration (figure 5.16A) was not too dissimilar to the single peptide configuration with the tilt of the primary helix just increasing by up to a further 20-30 degrees. The secondary helix was still mostly positioned at the interface between the pore and the rest of the bilayer.

However, for the B configuration (figure 5.16B) the deeper insertion meant that the primary helix now also was placed within the pore lumen and thus had to adopt a much steeper tilt angle in order to align with the bilayer curvature, varying greatly depending on the specific position.

The relatively similar position and orientation of the primary helix might explain why both configurations can transition to the more deeply inserted states. With its large size and central position in the pore the inflexible primary helix is in both cases the main contributor to the peptide-pore structure. This is further supported by the behaviour of the secondary helix. In the cases where the primary helix is in an extreme orientation the kink between the secondary helix is often much less pronounced, especially when the secondary helix is positioned the deepest within the pore lumen. Thus, in these cases the behaviour of the two helical regions is closer to how a single contiguous helical region would act, placing less importance on which end is inserted the deepest.

This is also in agreement with the previous observation that the position of the kink

within the helical region seem more suited to allow the peptide to align with the curvature at the top of the pore lumen rather than the middle of the pore.

The investigation of peptide-pore structures of AMPs using MD simulation has been done for several different peptides using different approaches. The most similar overall peptide-pore structures were found by Marrink and colleagues investigating the pore formation of both the Magainin analog MG-2H and melittin. Spontaneous pore formation was achieved due to the use of a high temperature, short chained lipids, a high peptide to lipid ratio, close positioning of the peptides and potentially aided by a lack of counter ions in the system. The observed peptide-pore structures are consistent with what was found for Smp24, with one or two peptides located near the centre of the pore lumen while the rest remains bound close to the mouth of the pore. A high degree of variation was seen between the different pore associated peptide configurations in terms of their position and orientations. The authors suggest that this behaviour is not well described by the traditional toroidal pore model where it is assumed that the pore is cylindrical with the peptides positioned between the lipid headgroups in a transmembrane/perpendicular orientation. Instead, a disordered toroidal pore model is more accurate where the shape of the pore and position/orientation of the peptides is more variable with only a fraction of the peptides being positioned deeply within the pore lumen (209, 210).

However, other studies indicate that the behaviour of melittin is different. Sun et al. found that unconstrained melittin peptides gradually moved down into the pore lumen of a preformed pore, created via induced lipid flip-flop. The peptides adopted transmembrane/perpendicular configurations within the centre of the pore lumen as would be expected by the traditional toroidal pore model. Removal of the peptides from the pore lumen led to a rapid closure of the pore indicating that the peptide-pore assembly had a strong stabilising effect (132). Like for Smp24 the inclusion of a proline residue in the helical region of the peptide allowed it to better align with the pore curvature. However, unlike Smp24, melittin's proline residue is located at the centre of its helical region which could explain the difference in the preferred pore associated orientation.

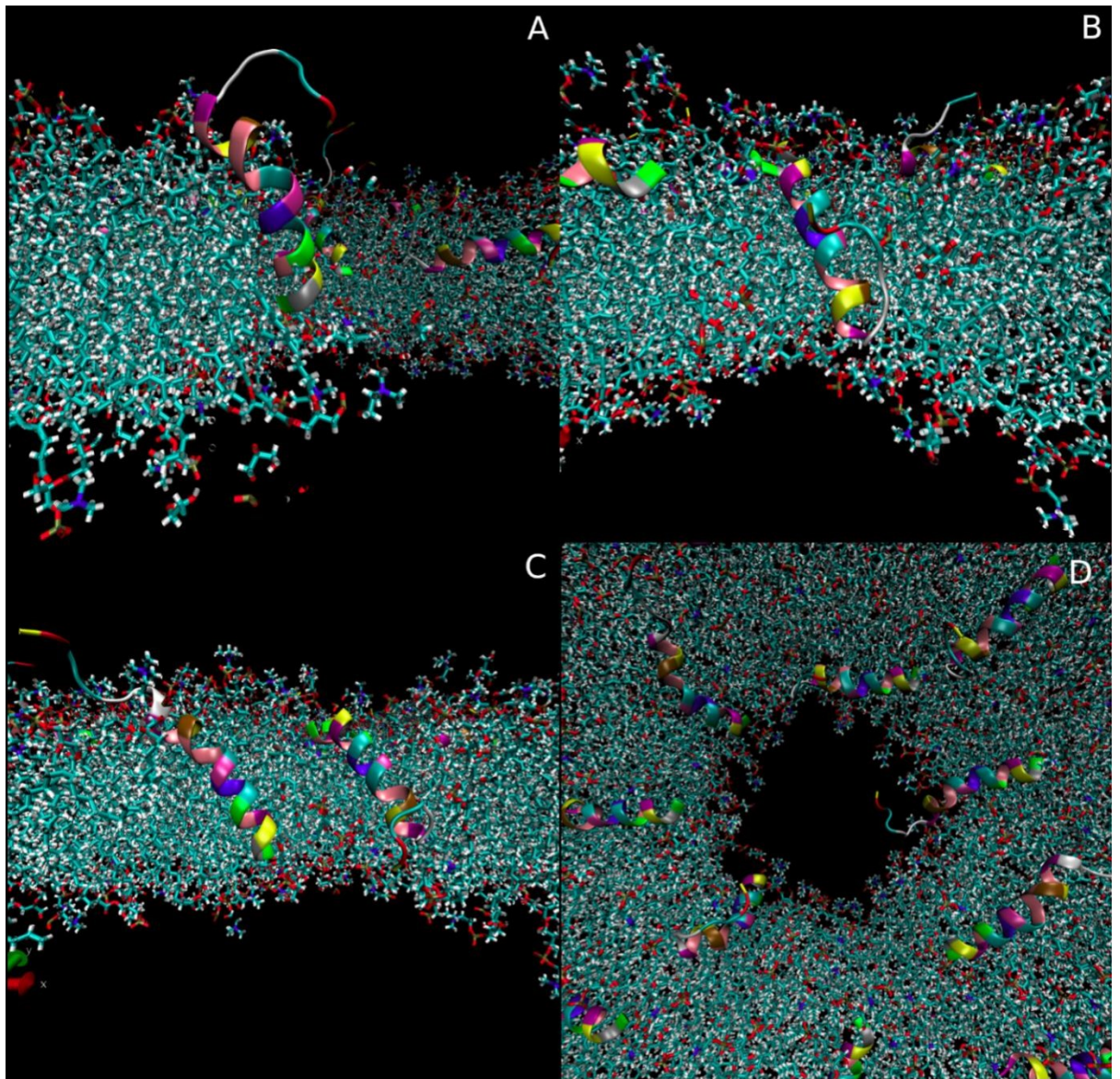


**Figure 5.16** Examples of transmembrane peptide configurations in the multi peptide pore simulations. A = Example of peptide with the primary helical region positioned the deepest in the pore lumen, B = example of peptide with the secondary helix positioned the deepest in the pore lumen, C = two peptides in transmembrane configurations in the same pore, D = example of a top-down view of a pore with multiple peptides associated with the pore interface.

A key question raised by the pore simulations is what causes the peptide to be able to transition to the more extreme inserted configurations as the peptide to lipid ratio is increased. If the peptides had formed an ordered peptide-pore assemblies one might have expected that a certain number of peptides would be needed to form the structure, however the disordered nature of Smp24's peptide-pore structures suggest that this is not the case. Some AMPs like Magainin 2 and PGLa have been shown to synergistically interact with each other through specific charged interactions between the two peptides. These interactions help PGLa to transition into a more consistent

configuration positioned deeply within the pore lumen and are, as such, an example of how peptide-peptide interaction can change the peptide-pore structure (191, 203). However, no consistent direct interactions could be seen between the Smp24 peptides and even when the peptide adopts one of the more extreme configurations the surrounding peptides are not positioned within the range needed for the formation of strong interactions between them.

However, one aspect that the increase in the peptide to lipid ratio would affect is the general properties of the bilayer. As mentioned previously, the insertion of the peptides changes the structure of the bilayer leading to macroscopic effects such as an increase in the APL. While the macroscopic changes affect the bilayer as a whole, on a molecular level the direct effect occurs in the top leaflet where the peptides are inserted. The effect on the bottom leaflet is more secondary as the changes are due to it adapting to the structure of the top leaflet. Thus, a mismatch occurs between the ideal macroscopic properties of the two leaflets, with the top leaflet, for example, ideally wanting to take up a larger overall area to accommodate for the inserted peptides, while the bottom leaflet still wants to retain the original dimensions. The addition of a pore in the bilayer represents a bridge between the two leaflets changing the dynamics of the system. Lipids can transition from one leaflet to the other by moving through the pore lumen at a much lower energy cost than through lipid flip-flop that would be required in the intact bilayer. Thus, the difference in the properties between the two leaflets can relatively easily be equilibrated over the duration of the pore simulations.

The movement of lipids between the two leaflets over time was investigated by calculating the density of each lipid species in the bottom leaflet over 1 ns time intervals (figure 5.17). Two key trends can be observed. Firstly, de-mixing of the DOPC and DOPG lipid occurs. The negatively charged DOPG lipids were affected by the electric field running across the bilayer, leading to them consistently moving from the top leaflet to the bottom. To retain the integrity of the bilayer the neutral DOPC lipids that are less affected by the electric field move across the leaflets in the opposite direction. For the simulations with a single peptide the lipid movements result in an overall wash where the combined lipid density in the bottom leaflet stays relatively stable throughout the entire simulation. However, this is not the case for the

simulations at a higher peptide to lipid ratio. The general DOPC, DOPG de-mixing behaviour is still present although it seems to occur at a much slower rate. This is likely an artifact of the evaluation method as with the larger bilayer more lipids would need to transition in order to produce the same change in the density. The key observation is that the combined lipid density of the bottom leaflet does not stay stable through the simulation but instead gradually increases especially during the first 30 ns of the simulation. Until around 90 ns of simulation time have passed, the density of the DOPC lipid is even increased in the bottom leaflet. Thus, in these simulations a net movement of lipids from the top leaflet to the bottom leaflet occurs.

The different behaviour of the two systems can be explained by the increased number of peptides inserted into the top leaflet. These peptides affect the properties of this leaflet and cause the need for some lipids to transition to the bottom leaflet in order to establish an equilibrium between them. This behaviour of the lipids could be part of the explanation for why the peptides can transition into the more extremely inserted configurations at the higher peptide to lipid ratio. Combined with the previous observation that the ability for the peptide to move throughout the bilayer is inhibited at a higher peptide to lipid ratio, the peptides interacting with the moving DOPG lipids could be forcing or pulling them down further into the pore lumen. Thereby deeper peptide insertion would be expected even if the new peptide-pore structures themselves are not intrinsically more favourable. The lower peptide diffusion rate and physical interference from other nearby peptides adapting more favourable peptide-pore configurations could greatly inhibit the ability of the inserted peptide to move out of the pore lumen, forcing the pore to stay open for longer.

Other authors have also found indications that the asymmetric effect the peptides have on the bilayer leaflets plays a key role in the pore formation such as by inducing tension leading to a difference in the equilibrium area for each leaflet also leading to redistribution of lipids away from the leaflet with the peptides inserted after the pore is formed (210).

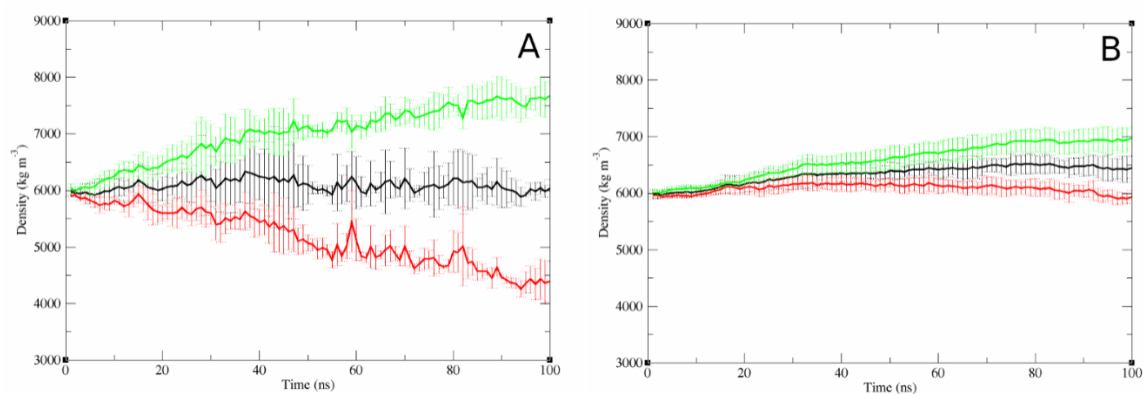


**Figure 5.17 Average lipid density in the bottom leaflet over time for the pore simulations. A =** Single peptide pore models (n=3), B = Multi peptide pore models (n=5). Black = Combined density for both DOPC and DOPG lipids divided by 2, Red = Density of DOPC lipids, Green = Density of DOPG lipids.

The peptide-pore structures and behaviour observed in the MD simulations correlates well with the toroidal pore associated results from the patch clamp experiments. The lack of a consistent favourable transmembrane peptide configuration explains why not all pore openings lead to a transition from the unsupported spike events to the longer multilevel events. Instead, the peptide prefers to be positioned around the top of the pore lumen only providing limited stability to the pore structure and therefore leading to rapid closer seen as spike events.

The simulations also suggest that the transition to peptide configurations which likely provides improved pore stability is very dependent on the local bilayer environment. As the deeply inserted peptide configurations are not based around one single highly favourable configuration a great deal of variation and disorder dominates even the stabilised pore structures. This leads to the large variation in the conductance levels and life spans of the multilevel events.

On a molecular level the transition from the unsupported to supported pore is random, likely needing the peptides to be positioned in such a way that multiple of them achieves a deeper insertion level and others around them restrict them from moving out of the pore lumen. However, the chances of this occurring should increase with the local peptide concentration as imbalance between the properties of the top and bottom leaflet would be greater and more peptides could be incorporated in the disordered assembly and interface area.

#### 5.2.8 Use of MD simulations to investigate the mechanism of action of AMPs

The complexity of the mechanism of action of AMPs makes it difficult to study how they work directly during the disruption of the bacterial membranes. This challenge is further exacerbated due to the small size of bacterial cells, limiting the use of techniques that potentially could directly measure live cell membrane disruptions such as patch clamp electrophysiology (63). Therefore, synthetic phospholipid bilayers are often used as a model instead, as they can mimic the properties of cell membranes, bacterial or otherwise. Synthetic bilayers have been used with many experimental techniques such as electrophysiological measurements (184), liposomal release (58) and binding assays (211), Q-CMD (58), solid state NMR (212) and more. Synthetic bilayers can be used as they represent some of the most important key features of cell membranes such as their amphiphilic structure and ability to form a barrier which is mostly impenetrable to ions. However, compared to actual membranes their compositions are much simpler, with cell membranes having much greater diversity in terms of the lipid composition (206) and also contains a roughly equal proportion of membrane proteins (213). Therefore, the use of synthetic bilayer models relies on the assumption that even though the models are much simpler than real membranes, they still represent the aspects of cell membranes that are the most critical for the activity of the antimicrobial peptides. Some indications that this is the case could be the ability of AMPs to lyse both synthetic liposomes and simple cells such as hemocytes (137) or the similarity seen in single channel conductance events between cell derived and synthetic patches (72, 100).

For investigations using MD simulations the reliance on several assumptions is even more apt as one also needs to assume that the simulation of the synthetic system is accurate to reality. The limited scale of the simulations also introduces the potential for more faulty assumptions as shortcuts needs to be taken in the model setup such as stating the peptide in an already helical configuration. Therefore, it is unlikely that MD simulation will ever be able to by themselves predict the more complex behaviors of AMPs such as the overall mechanism of action. Instead, the strength of the simulations lies in the contextualization of experimental observations. The output of biophysical experiments often requires a lot of data interpretation to understand how the

measurements relate to changes in the system on a molecular level. By mimicking the conditions expected based on the experimental observations in the MD simulations setup, predictions can be made regarding some of the more minute details allowing the researcher to create a more complete interpretation of the original data. In the case of this chapter, the patch clamp observations only provided information related to the overall structure/shape of the peptide induced pore. However, given the toroidal pore shape, the MD simulations allowed us to make some predictions as to where the peptides might be positioned under different conditions, increasing the detail of our models for the different pore/event types.

### 5.3 Conclusions

A critical aspect in the process of designing AMPs with improved properties, is bettering the understanding of how their mechanism of action relates to the structure of the peptide. MD simulations such as those performed in this chapter could play an important role in this process as they allow for simultaneous prediction of both the peptide structure and bilayer interactions on an atomic level. Simulations replicating the conditions of mechanistic biophysical experiments could thus allow for contextualization of such mechanistic observations with structural predictions as well.

Simulations of the interactions between Smp24 and lipid bilayers showed that the peptide insertion potentially occurs in a stepwise fashion, driven mainly by the N-terminal and primary helical region of the peptide. Following the full insertion, the unique structure and physiochemical properties of the different regions of Smp24 likely both affects how deeply each region inserts within the top membrane leaflet and how strong their interactions with the surround lipids are. Furthermore, the interactions between the inserted peptide and the lipids also affects the overall properties of the bilayer, with concentration dependent effects on aspects such as the bilayer thickness, lipid chain order and the ability of the peptide to diffuse around in the bilayer plane.

The simulations of the interactions between Smp24 and pre-formed toroidal pores predicted that the kink motif between the helical regions of the peptide plays a key role in the ability for the peptide structure to align with the curvature of the pore.

However, at low peptide to lipid ratios the peptide seems to prefer to adopt configurations near the pore interface rather than position itself deeply within the pore lumen. The simulations indicated that this could potentially change if the local peptide to lipid ratio around the pore is increased, as the high peptide concentration induces a difference in the ideal properties of the top and bottom lipid leaflets causing a net migration of lipids towards the bottom leaflet. The movement of lipids could help pull the peptides deeper within the pore lumen while restricted peptide movement could inhibit the ability of the peptide to leave this configuration, facilitating the formation of a pore with an overall improved stability. Such predictions of the peptide pore interactions could help explain why the short-lived toroidal pores observed in the patch clamp experiments not always evolved into more stable pores.

## 6. Rational design of truncated Smp24 variants

### 6.1 Introduction

Naturally occurring peptides such as Smp24 could form the basis for the development of new antimicrobial molecules. These compounds can be some of the most potent pharmacological molecules in the world due to natural optimization through millions of years of evolution. However, the original properties of such molecules might not be ideal for medical use. Components from natural sources such as venom are adapted towards specific functions relevant to the animal of origin. Thus, the potency of a venom derived molecule might therefore be stronger against cellular targets not related to humans.

Invertebrates such as scorpions lack an adaptive immune system and therefore rely completely on the innate immune system for protection against infections. Their venom gland is especially at risk as it is in direct contact with the environment and therefore can fall victim to infections from soil or prey related pathogens. Therefore, AMPs in the venom are thought to play a dual function. Firstly, they serve to protect the scorpion from infections via their antimicrobial properties and secondly, they assist in the venomous action against the scorpion's prey by inducing paralysis and digestion. In addition, the composition of scorpion venom can be very complex containing multiple peptides, proteins, nucleotides, lipids and more. Therefore, the functions of the AMPs can also be mediated in combination with other compounds (178).

The dual function of venom derived AMPs such as Smp24 means that their native structure is likely not optimal for clinical use. The microbial species that the scorpion's venom gland is commonly exposed to are likely not the same as are clinically relevant to humans, their venomous activity against eukaryotic prey is undesirable and their potential ability to interact with other components of the venom is not necessary in a medicinal formulation. As such, not all residues or regions are necessarily critical for their clinically relevant antimicrobial activity, and some might confer unfavourable properties to the peptide.

With a more extensive grasp on the SMR of Smp24 achieved in the previous chapter, the next logical step would be to try and apply the newly gained knowledge to improve the properties of the peptide. This can be done by utilising rational drug design

principles to develop novel analogs using the structure of Smp24 as the baseline framework. With the SMR in mind, the peptide structure can be modified in a rational manner by making specific changes which would be expected to improve the properties of the peptide, either in relation to the mechanism of action or in general terms related to the drug-like properties of the molecule. It would be expected that the success rate of such analogs designed according to the SMR would be better than analogs based on random modifications, leading to a more effective development process.

A second logical step would also be to start expanding the SMR into a proper structure activity relationship (SAR). This means starting to move away from simplified, synthetic *in silico* and *in vitro* biophysical models, towards the utilisation of more physiologically relevant *in vitro* models. This makes the construction of the SAR more challenging for several reasons.

Firstly, cells (bacteria and eukaryotes) are a much more complex target than synthetic bilayers. Both on a molecular level with a much more diverse membrane composition containing a range of different lipid types, membrane proteins, leaflet asymmetry, multiple membranes in the case of Gram-negative bacteria and many unique membrane components such as cholesterol or lipopolysaccharides. All of which could potentially greatly affect how the peptide interacts with the membrane in all stages of the mechanism of action. Furthermore, live cells are also a much more dynamic system than bilayers, with them growing, multiplying and responding dynamically to their environment including the addition of drug molecules.

Secondly, the concept of the activity of the peptide is a much more difficult response to relate to the structure. The activity is the accumulation of all the different mechanistic processes, all of which might have completely different relationships with the structure of the peptide. Therefore, it is impossible to directly interpret the relationship between the structure and the activity of a peptide without comparing different analogs with distinct structural modifications. Still, using this approach the SAR would be very simplistic if it was not paired with mechanistic data to contextualise the structure related changes in the activity.

The specific approach used under the guidelines rational drug design can vary depending on the main objective of the development step. For AMPs, improvement of

antimicrobial activity, antibiofilm activity, stability and selectivity could all be objectives of the design of a new peptide variant. However, if the development is done in an iterative fashion some objectives should be a higher priority earlier in the development process. For naturally derived AMPs such as Smp24, truncation of the structure could be an ideal first step for multiple reasons.

Firstly, shortening the size of the peptide sequence could significantly reduce the cost of synthesising new analogs during the development process. Linear AMPs are often produced via solid phase peptide synthesis during the development process, as it is relatively easy and allows for seamless inclusion of different modifications. However, as the length of the peptide increases each additional residue will reduce the yield, increase the synthesis time and likely complicate the purification process (214). Thus, on a limited budget a smaller peptide scaffold could mean that a larger number of structural modifications could be explored.

Secondly, during the early stages of the drug discovery process new analogs also play a key role in the continued process of expanding the understanding of the SMR and SAR. The removal of residues can be a very useful tool for this purpose. Cutting out a residue can in some instances give results that are easier to interpret compared with a residue substitution where the residue still exists but has its properties are changed. However, the effect of a truncation is also dependent on the position of the residue within the sequence, so the approach must be used carefully. If truncations are utilised both carefully and efficiently, they can allow for the evaluation of the importance/function of an entire structural region at once, providing mechanistic or activity-based information more closely related to the higher order structure of the peptide.

Lastly, for the later stages of development in an iterative design process it can also be an advantage to have a smaller more efficient peptide scaffold. Having fewer possible modification sites can speed up the development process and further reduce the number of new analogs that need to be designed, synthesised and evaluated. For a larger peptide there is a greater risk of time and effort being spent on modifying residues or regions of the peptide which in the end do not have that large of an impact on the activity of the peptide.

Furthermore, truncating the peptide during development can also improve the properties of the final drug candidate. A smaller peptide agent could potentially be

improved in terms of production costs, formulation ease and in relation to its pharmacokinetic properties.

While the primary objective of any drug design process is to improve the properties of the drug lead in some regards, a secondary objective is also to do it as efficiently as possible. This can primarily be done by trying to increase the success rate of the newly designed analogs. Thereby, the total number of analogs needed to complete the development process can be reduced, also leading to reduced synthesis cost and less time spent on the *in vitro* evaluation. One of the most effective approaches for achieving this is via computer aided drug design, leading to two key advantages. Firstly, using computational methods potential drug candidates and analogs can be screened against a target. This can be used to predict whether a specific molecule would likely be active or not and thereby the number of potential drug molecules can be narrowed down to a more manageable number for the *in vitro* evaluation stage. Secondly, computer models can also be used directly in the design process. Visualization of the 3D structure of the base molecule and analogs can help the researcher envision the special effects of modifying the structure of a molecule. With a rational approach to the drug design, a large degree of the process is a creative endeavour trying to solve a complex 3D puzzle in the most efficient way possible. Having tools to aid in this process is critical to achieving an efficient drug design process and for exploring the large range of possibilities.

Therefore, a secondary objective of this chapter is to explore whether the MD simulations developed in the previous chapter could be used in the computer aided drug design of new AMPs. While the base simulation does not convey any direct predictions related to the peptide induced pore formation, it should still be able to produce consistent and quantifiable results related to the inserted state of the peptides. These two factors are a critical prerequisite for the ability to use the models to compare and evaluate different designs. In addition, several response variables such as the insertion depth (215) and the degree of helical structure (216) could still be potential predictors of the pore formation properties even though a direct relationship is not established within the model itself. Lastly, it is well established that pore formation is a concentration dependent process and therefore by optimising the relative binding energy between the peptide and the bilayer the thermodynamic

equilibrium could be shifted towards a greater degree of inserted peptides, indirectly reducing the peptide concentration needed to induce pore formation.

## 6.2 Results and discussion

### 6.2.1 Selection of truncation targets

The first step of the truncation process is to identify which residues/regions of the peptide could be a potential target for truncation or which most likely needs to be conserved in order to retain the activity of the peptide. The most optimal approach would be if the truncations could be performed based on the previously described structural regions. Adopting a regional rather than a residue-based view of the peptide would better allow for the truncation of multiple residues at a time and thus it would take fewer steps to reach the minimum peptide size. To do this, a select set of results from the previous chapter was reanalysed with the purpose of comparing each of the structural regions (table 6.1). All the results were based on the period where the peptides were fully inserted within the bilayer. The average helicity for each residue was calculated and again averaged for the residues within each region. The mean distance of each region to the centre of the bilayer was calculated by fitting the density profiles using Gaussian distribution. The relative contributions to the total binding energy were calculated based on the per-residue decomposition analysis.

**Table 6.1 Overview of key properties of the different structural regions of Smp24 based on the simulations from chapter 5.**

	Average helicity (%)	Mean distance from bilayer centre (nm)	Relative contribution to total binding energy with the negative bilayer (%)	Relative contribution to total binding energy with the neutral bilayer (%)
Primary helix	83.84 ± 1.12	1.251 ± 0.089	88.62 ± 0.32	51.63
Secondary helix	29.33 ± 14.38	1.340 ± 0.072	1.62 ± 0.14	5.12
Glycine linker	1.26 ± 0.75	1.856 ± 0.009	0.96 ± 0.19	3.53
Tail	1.40 ± 0.29	2.544 ± 0.089	8.80 ± 0.16	39.72

Based on broadly recognized trends related to the SAR of AMPs one would expect regions with a high helicity, deep insertion level, high energy contribution and a selectivity towards the negative bilayer to be the most critical for the peptide's activity. The primary helical region facilitates all these demands and is also consistently better than all the other regions in every category, often by a large amount. This is a clear indication that this region should as a starting point be conserved in any truncated designs.

While the secondary helix is overall helical it is to a much lesser degree than the primary helix. Some of this is due to the greater variability in the type of helical structure, switching between alpha helical and 3-10 helix throughout the simulations. Another reason is the phe17 residue which often adopts a random coil structure. The region is positioned slightly further from the bilayer centre than the primary helix but has a much lower energy contribution due to its smaller size and lack of any cationic residues. The selectivity of the region is towards the neutral bilayer type as most of its energy contribution comes from hydrophobic interactions which have a larger relative impact on the binding with the neutral eukaryotic mimicking membrane.

The tail region is both non-helical and positioned over 1 nm further away from the bilayer centre than both helical regions. However, it does have a greater impact on the binding energy than the secondary helix. Based on the chosen lipid compositions of the two bilayer models the selectivity is strongly towards the neutral bilayer, however as mentioned previously membranes for bacteria such as *E. coli* also contain a large amount of PE lipids so in reality the tail regions effect on the selectivity might be more complex.

Based on the previous observations, the main role of the glycine linker region seems to be as a spacer between the highly polar tail and the amphiphilic helical regions which need to be positioned differently in the bilayer. Therefore, values such as its helicity and binding energy contribution are probably less important for this region. Still, it has a low helicity, high distance from the bilayer centre, low energy contribution and low selectivity towards the negative bilayer.

In addition to the region-based analysis from table 6.1, some general observations from the last chapter's MD simulations were also considered when choosing the truncation targets. The primary helical region seemed to play the most significant role during the insertion process, with residues as far as lys11 taking part in the initial stages, while the other regions did not consistently contribute. The relative position of the residues within the region is critical, so truncating any of them could either interfere with the initial anchoring of the N-terminal or shift the relative helical position of the lysine residues supporting the N-terminal inserted configuration. In addition, other residues near the N-terminal such as phe4 and ser3 also seemed to aid in the anchoring of the N-terminal, a further indication that truncation could inhibit insertion. The other regions of the peptide could likely be either fully or partially truncation without affecting the insertion process greatly.

The concentration dependent effects of the peptide on the macroscopic properties of the bilayer stemmed from the bending of the lipid acyl tails to accommodate the helical regions of the peptide. Thus, truncating the tail and glycine linker regions not positioned near the lipid chains would likely have a minimal influence on these effects. In addition, due to the smaller size and reduced insertion depth the effect of the secondary helix would probably also be smaller than that of the primary helix.

During the stabilisation of the toroidal pores by the peptide, the primary and secondary helical regions again seem to have the most critical role. It is these regions that can adapt to the curvature of the pore lumen/interface providing stability to the structure and ensuring that it stays open for a longer time. The kink between the two regions seems important for the peptides ability to adopt its favourable pore associated configurations at a low peptide to lipid ratio. However, at higher peptide to lipid ratios where deeper insertion of the peptide into the pore lumen can be achieved, the shape of the peptide indicates that the kink might be less critical. Thus, it is not clear if the secondary helix is necessary for pore formation or not.

Based on the totality of these observations the following guidelines for the truncation process were made:

- Full or partial truncation of the primary helix between residue 1-11 should be avoided
- Full truncation of the secondary helix could be done
- Full or partial truncation of the tail region could be done
- Full truncation of the glycine linker region could be done if its role as a spacer region is no longer necessary

#### 6.2.2 Truncation design

Since multiple different truncation targets had been identified, an iterative approach was adopted with the objective of designing the smallest active analog possible. As such, the truncation was done in a stepwise fashion, with *in silico* evaluation of each new analog before the next truncation step was applied.

Traditionally truncations would be done at one of the terminal ends of a peptide as this does not affect the relative order of the individual residues in the primary sequence. Truncating a region in the middle of a peptide would generally be more complicated as it has a greater chance of impacting the properties and behaviour of the rest of the peptide. However, truncation of the central secondary helical region was still chosen as the first step in the truncation process. This was mainly done to aid in the validation of the MD simulations as a drug discovery tool. If a difficult design challenge such as the truncation of a central region can be done successfully it would

provide greater confidence in the output of the simulations as they relate to solving more simple challenges such as single residue substitutions.

One of the challenging aspects of this truncation was that this region represents the transition point between the helical and unstructured parts of the peptide. Therefore, there is a risk that removing this region could significantly affect the structure, orientation and position of the rest of the peptide. It is therefore important that the secondary structure and orientation of the primary helix is not disrupted by moving the transition point. Furthermore, the position of the tail region among the lipid headgroups should also be conserved, which again is very dependent on retaining a correct transition between the two types of secondary structure.

To try and achieve this the truncated region of the secondary helix was shifted slightly, removing residues 13-16 rather than residues 14-17 (residues previously designated as the secondary helix). Cutting 4 residues removes approximately one helical rotation which is the size of the secondary helix. The region of truncated residues was shifted by one residue to allow for the conservation of the phenylalanine residue at the end of the secondary helix (previous position 17, now 13).

Another key part of this truncation step was the removal of the proline residue and thereby the kink in the overall helical region. This was done as without the secondary helix there is no longer any need for a residue inducing a kink, at least not at the 14<sup>th</sup> residue position.

As such the 20-residue long peptide Smp20 was created (table 6.2).

The second iteration of the truncation process focused on the tail region of the peptide. A partial truncation of the tail region was done to eliminate the last two residues in the sequence, the aspartic acid and the C-terminal serine. This truncation thereby removed the two residues responsible for the unfavourable energy contribution when binding to the negative bilayer. However, the two lysine residues responsible for strong electrostatic interactions with the bilayer were still conserved. This led to the creation of the 18 residue long peptide Smp18, which has an overall charge increase from +3 to +4 compared to the previous peptides (table 6.2).

Lastly, in the final iteration the glycine linker region was truncated, cutting the peptide down to almost just the primary helix. The tail region was also further truncated by one of the lysine residues, with it thereby being so small that it was deemed that the

glycine linker region would no longer be necessary. The new position of the final tail lysine residues would now be similar to the lysine residues of the primary helix instead. In addition, as the position of the anionic charge of the C-terminal would now be moved much deeper within the bilayer, it was amidated to eliminate the negative charge. This also retains the total charge of the peptide at +4 similar to the last iteration.

Thus, the smallest truncated peptide Smp14a was designed, which is 42% smaller than the original parent peptide Smp24.

In addition, before the truncation strategy was fully developed one peptide (Smp21) was created and modelled which helped in the process of creating the full set of truncation guidelines.

**Table 6.2. Overview of truncated peptides.** \* C-terminal amidation not accounted for in calculations.

Name	Sequence	Number of residues	Mw (g/mol)	Charge at pH 7
Smp24	IWSFLIKAATKLLPSLFGGGK KDS	24	2578.06	3
Smp21	IWSFLIKAATKLLPSGGGKK S	21	2202.64	4
Smp20	IWSFLIKAATKLFGGGKKDS	20	2167.55	3
Smp18	IWSFLIKAATKLFGGGKK	18	1965.38	4
Smp14a	IWSFLIKAATKLFK-NH <sub>2</sub>	14	1665.07	4

### 6.2.3 In silico modelling

The primary simulations used to aid the design process were the base bilayer simulations (DOPC:DOPG) and it was based on the evaluation of each of these simulations that the iterative design process was implicated. A base simulation time of 500ns was used as in all cases this was long enough to ensure full insertion of the

peptide into the bilayer. In one simulation (bpg14a\_1) an additional 100ns were added to the simulation as the time to full insertion happened relatively late.

Following the DOPC:DOPG simulations, models were also performed using the DOPC:DOPE bilayer to give a possible indication of the toxicity of the novel peptides. The simulations were analysed using the same methods as in the previous chapter.

**Table 6.3. Overview of simulations with the truncated peptides.**

	Number of simulations	Length (ns)	Names
<b>Smp21</b> with DOPC:DOPG bilayer	1	248	bpg21_1
<b>Smp20</b> with DOPC:DOPG bilayer	3	500	bpg20_(1-3)
<b>Smp20</b> with DOPC:DOPE bilayer	3	500	bpe20_(1-3)
<b>Smp18</b> with DOPC:DOPG bilayer	3	500	bpg18_(1-3)
<b>Smp18</b> with DOPC:DOPE bilayer	3	500	bpe18_(1-3)
<b>Smp14a</b> with DOPC:DOPG bilayer	3	500-600	bpg14a_(1-3)
<b>Smp14a</b> with DOPC:DOPE bilayer	3	500	bpe14a_(1-3)

#### 6.2.3.1 Smp21 - An example of a failed truncation effort

As mentioned previously, Smp21 was designed before a concrete truncation strategy had been fully formulated, although it can serve as an example of what a failed truncation attempt could look like. Three residues were truncated relative to the parent peptide, Leu16 and Phe17 from the secondary helix and Asp23 from the tail region. Asp23 was a clear target for truncation due to its negative charge and the removal of Leu16 and Phe17 was an attempt at truncating the secondary helix without

removing the proline residue, as its purpose in shaping the direction of the unstructured region of the peptide was not clear yet.

The truncated peptide was simulated with a DOPC:DOPG bilayer for 248 ns and the following observations were made.

While the starting structure of the peptide included an alpha helical region from r1-12 the end close to the truncation (r9-12) loses much of the helical structure over time (figure 6.1A). Like the other unstructured regions of the peptide this previously helical region does not fully insert into the bilayer but rather lies on the surface, shifting the partial density profile of the peptides away from the core of the bilayer (figure 6.1B&C). While the helical part of the peptide is still inserted, it is not as deep and at a steeper angle ( $20.18 \pm 11.05$  degrees) compared with the primary helical region of Smp24.

All the observations are clear indicators that the truncation effort was unsuccessful and deliberate changes in the further truncations were made to ensure helical stability and complete insertion.

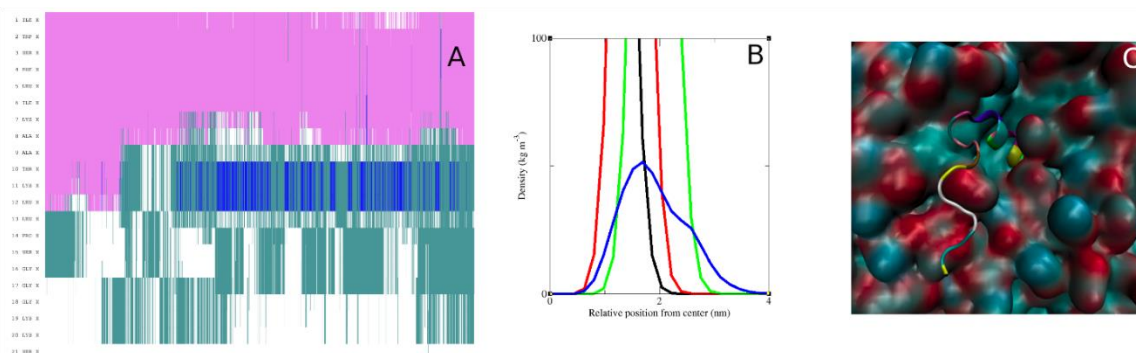


**Figure 6.1 Overview of the Smp21 DOPC:DOPG simulation.** A = secondary structure over time, B = Partial density after insertion, C = 3D structure of the inserted peptide.

### 6.3.2.3 Bilayer insertion of the truncated peptides

The insertion mechanism of the truncated peptides generally follows the mechanism outlined for Smp24. In most cases the insertion process could be separated into the previously defined stages, based on the peptide position and orientation as seen in table 6.4.

In the simulations with the DOPC:DOPG bilayer full insertion was achieved for all the peptides except for the bcg20\_2 simulation, where only partial insertion was achieved.

This was due to loss of the helical structure between residue 11-13, causing these three residues to adopt a less inserted configuration.

Greater variability can be seen for the insertion into the DOPC:DOPE bilayer. In 5 of the simulations the peptides only achieve superficial interactions with the bilayer surface and in 2 of those the interactions are only intermittent with the peptide ending the simulation period in solution rather than being associated with the bilayer. However, for all the truncated peptides full insertion into a DOPC:DOPE bilayer was achieved at least once.

**Table 6.4 Overview of the insertion process for the different simulations with the truncated peptides.**

Simulation name	Overall Insertion level	Initial lag period	N-terminal inserted / superficial interactions	Rotation	Inserted
bcg20_1	Full	0-5	5-11	11-95	95-500
bcg20_2	Partial	0-21	21-155	155-220	220-500
bcg20_3	Full	0-10	10-160	160-240	240-500
bce20_1	Full	0-20	20-365	365-440	440-500
bce20_2	Superficial interactions	0-120	120-500	na	na
bce20_3	Full	0-8	8-13	13-105	105-500
bcg18_1	Full	0-26	26-85	85-180	180-500
bcg18_2	Full	0-8	8-30	30-150	150-500
bcg18_3	Full	0-15	15-255	255-330	330-500
bce18_1	Superficial interactions	0-270	270-500	na	na
bce18_2	Full	0-35	35-85	85-140	140-500
bce18_3	Superficial interactions	0-340	340-500	na	na
bcg14a_1	Full	0-2	2-415	415-470	470-600
bcg14a_2	Full	0-5	5-17	17-100	100-500
bcg14a_3	Full	0-45	45-195	195-250	250-500
bce14a_1	Intermittent superficial interactions	Na	na	na	na
bce14a_2	Intermittent superficial interactions	Na	na	na	na
bce14a_3	Full	0-120	120-270	270-320	320-500

#### 6.3.2.4 Structure, orientation and positioning in the DOPC:DOPG bilayer

The secondary structure of the truncated peptides is relatively consistent when inserted into the DOPC:DOPG bilayers (figure 6.5). A contiguous alpha helix spanning from residue 1-13 can be seen for all the peptides with some variable loss of structure near either the beginning or the end of the helix in individual simulations. The variable region after residue 13 has a consistent random coil structure throughout all the simulations.

The 3D structures of the fully inserted configurations are also consistent, with representative examples shown in figure 6.6. In all simulations the helical region is oriented very close to parallel with the bilayer, with the average angle relative to the bilayer surface in most cases being less than 5 degrees (table 6.5). Only in bcg20\_2 is the average angle above 10 degrees, however this is also the only simulation where insertion is only partially achieved. The helical region is in all cases inserted the deepest into the bilayer, in a similar position to the primary helical region of the parent peptide. Some variation in the relative position is seen between the replica simulations but no overall consistent difference can be seen between the different peptides (figure 6.7).

For Smp20 and Smp18 the position and orientation of the glycine linker and polar tail regions are also as expected. In both cases the polar tail region is mainly positioned among the lipid headgroups, with no discernible difference in the positioning between Smp20 and the parent peptide. The truncation of Asp19 and Ser20 in Smp18 only affects the part of positional distribution furthest from the bilayer core, with the tail region no longer being positioned partly in the solution phase.

The glycine linker region has a consistent position between the tail region and the helical region, both when comparing the truncated peptides and the parent peptide. The 3D structures reveal that the transition between the helix and random coil happens when the local helical rotation points away from the bilayer core allowing the glycine linker and tail region to be oriented tangentially to the bilayer surface. While the final residue of Smp14a does not adopt a helical structure and thus could be characterized as the remainder of the tail region, its small size necessitates that it follows the curvature of the helix and thus do not have much positional or

orientational freedom.

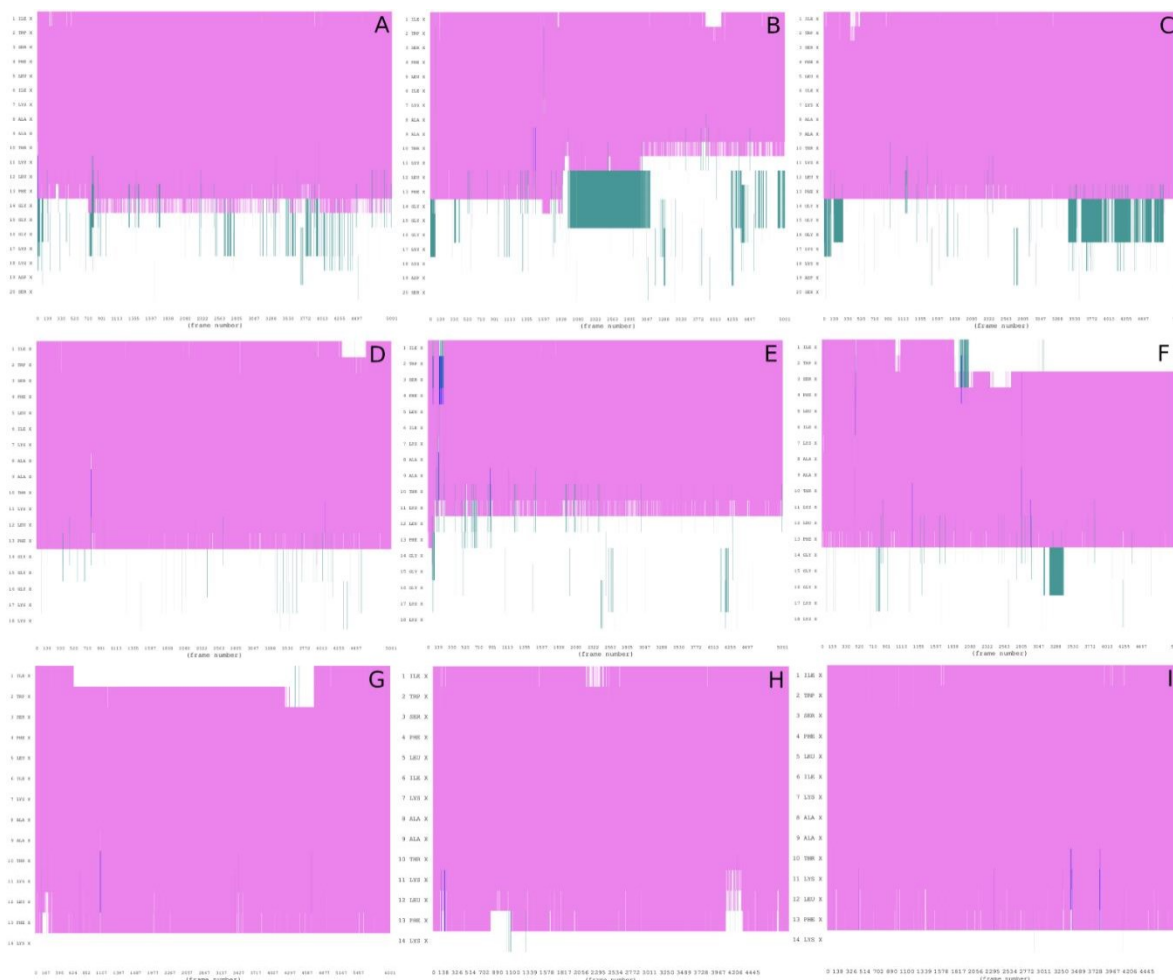


**Figure 6.5** Secondary structure of the truncated peptides over time in the DOPC:DOPG simulations. A-C = Smp20, D-F = Smp18, G-I = Smp14a. Pink indicates alpha-helix, blue indicates 3-10 helix, green indicates turn, yellow indicates isolated bridge and white indicates random coil.

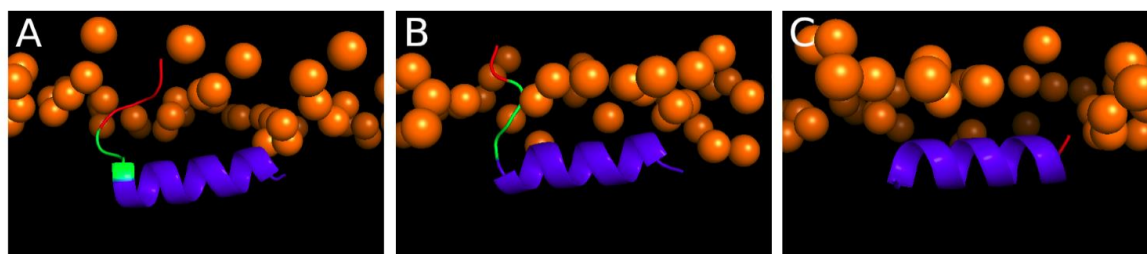


**Figure 6.6** 3D structure of truncated peptides inserted into a DOPC:DOPG bilayer. Blue = helical region, green = glycine hinge, red = tail, orange = lipid phosphor atoms. A = Smp20, B = Smp18, C = Smp14a.

**Table 6.5 Average angle between the primary helix (residue 1-12) and the bilayer (x-y plane), for the truncated peptides during different periods of the simulations. \* Residue 1-10.**

Simulation name	Helix bilayer angle during n-terminal insertion	Helix bilayer angle after full insertion
bcg20_1	33.70 ± 10.86	2.59 ± 7.76
bcg20_2*	39.24 ± 16.46	11.39 ± 12.70
bcg20_3	50.83 ± 11.56	3.20 ± 8.22
bcg18_1	47.89 ± 11.71	-2.23 ± 9.78
bcg18_2	23.16 ± 7.51	4.89 ± 9.69
bcg18_3	34.05 ± 17.94	-6.93 ± 9.07
bcg14a_1	25.70 ± 8.98	-1.68 ± 8.50
bcg14a_2	-50.70 ± 12.40	3.29 ± 8.53
bcg14a_3	27.07 ± 11.07	0.83 ± 9.31

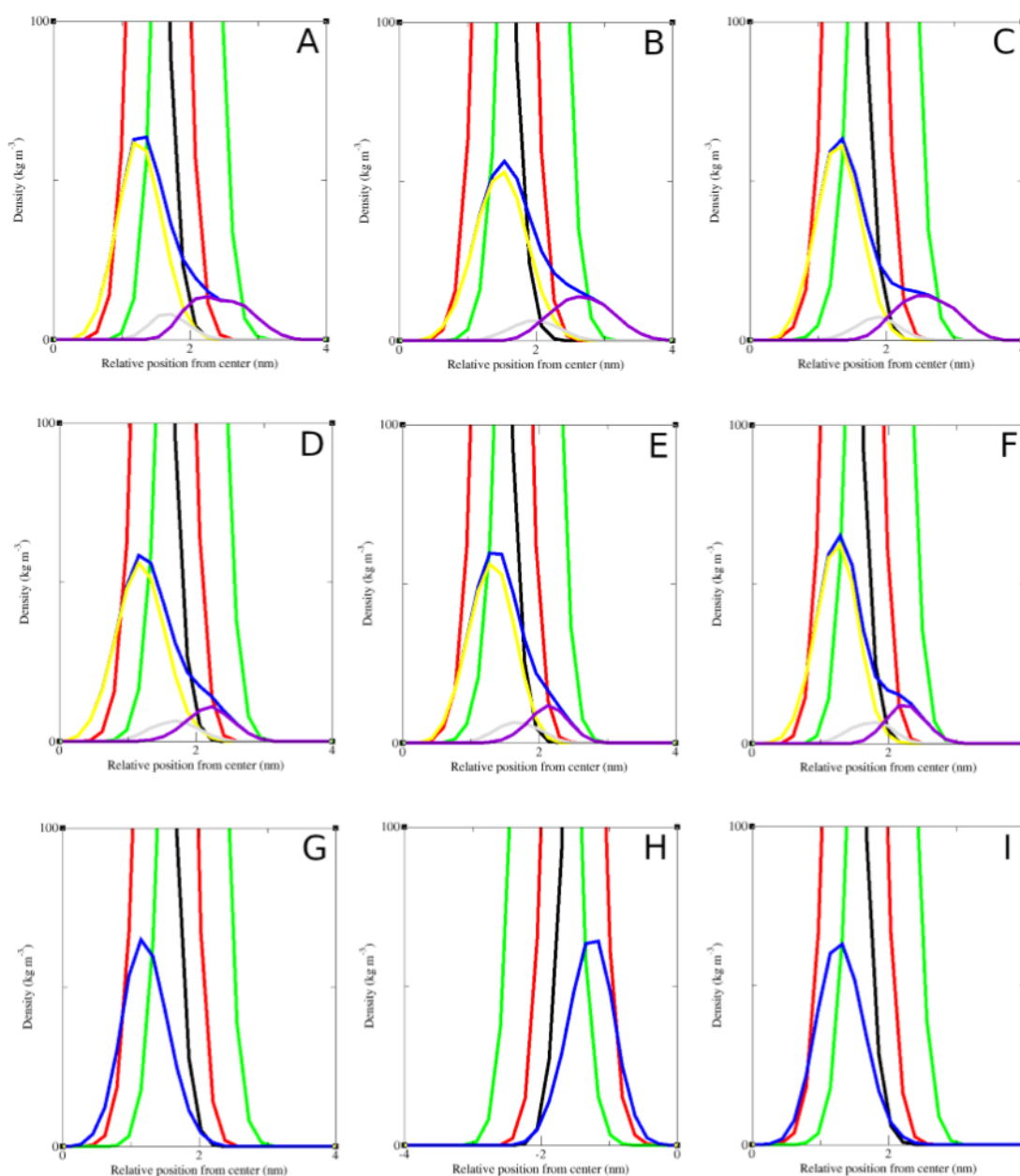


**Figure 6.7 Partial density profiles of the truncated peptides inserted into DOPC:DOPG bilayers, with positions relative to the z-axes.** A-C = Smp20, D-F = Smp18, G-I = Smp14a. Black = Lipid acyl chains, Red = Lipid glycerol esters, Green = lipid headgroups with phosphates, Blue = whole peptide, Yellow = helical region, Grey = glycine hinge and purple = polar tail region.

#### 6.3.2.5 Interactions with the DOPC:DOPG bilayer

To evaluate the interactions between the truncated peptides and the bilayer the relative binding energies were calculated (table 6.6).

Overall, the average total binding energy is relatively similar for all the truncated peptides, being slightly lower than the average of -87.27 kcal/mol for the parent peptide. However, the energies do vary significantly for both Smp20 and Smp18, with the median values indicating that the difference between the peptides could be

greater than the averages show. The outlier for Smp18 (bcg18\_3) is likely due to the loss of helical structure near the N-terminal for this simulation.

Looking further into the individual energy components a couple of trends can be identified. Compared with the parent peptide the Van der Waals interactions are significantly reduced for all the peptides, with a further reduction between Smp14a and the other truncated peptides. Both the cavity and dispersion terms follow a similar trend. The electrostatic interactions are slightly increased for Smp20 compared with the parent peptide but a much larger increase of around 100 kcal/mol can be seen for Smp18 and Smp14a. However, these increases are somewhat balanced by increases to the polar solvation energy as well.

**Table 6.6 Breakdown of the free binding energies for the truncated peptides and DOPC:DOPG bilayer complexes.** All values are in kcal/mol. \* Value is significantly different from Smp24 based on one-sided two-sample independent t-test (P<0.05).

Simulation name	Van der Waals energy	Electrostatic energy	Polar solvation energy	Cavity	Dispersion	Delta G total
bcg20_1	-140.81 ± 12.25	-436.77 ± 26.69	396.00 ± 22.04	-113.71 ± 8.35	203.84 ± 12.21	-91.44 ± 11.70
bcg20_2	-124.42 ± 11.81	-418.77 ± 29.03	382.64 ± 24.96	-99.57 ± 10.40	182.29 ± 15.75	-77.83 ± 9.88
bcg20_3	-126.72 ± 11.31	-428.80 ± 20.16	391.25 ± 16.49	-103.50 ± 8.90	188.62 ± 13.49	-79.15 ± 9.61
Smp20 average	-130.65 ± 7.25 *	-428.11 ± 7.36 *	389.96 ± 5.53*	-105.59 ± 5.96 *	191.58 ± 9.04 *	-82.81 ± 6.13
bcg18_1	-133.67 ± 10.55	-523.47 ± 20.01	478.18 ± 16.22	-106.48 ± 7.40	194.05 ± 10.63	-91.40 ± 10.23
bcg18_2	-124.14 ± 11.38	-517.89 ± 17.68	471.33 ± 14.50	-102.59 ± 8.06	185.59 ± 12.11	-87.70 ± 9.69
bcg18_3	-118.32 ± 10.66	-501.21 ± 18.95	459.18 ± 16.01	-95.21 ± 8.26	177.42 ± 13.08	-78.14 ± 8.78
Smp18 average	-125.38 ± 6.33 *	-514.19 ± 9.46 *	469.56 ± 7.86 *	-101.43 ± 4.67 *	185.69 ± 6.79 *	-85.75 ± 5.59
bcg14a_1	-115.22 ± 9.02	-490.44 ± 14.63	448.80 ± 12.52	-93.74 ± 6.32	170.34 ± 9.33	-80.26 ± 8.33
bcg14a_2	-118.16 ± 8.96	-506.11 ± 14.78	461.78 ± 12.09	-95.87 ± 5.61	174.25 ± 8.15	-84.11 ± 8.26
bcg14a_3	-116.79 ± 8.35	-509.78 ± 14.81	464.32 ± 12.30	-94.05 ± 5.35	170.86 ± 7.78	-85.45 ± 7.94
Smp14a average	-116.72 ± 1.20 *	-502.11 ± 8.39 *	458.30 ± 6.80 *	-94.55 ± 0.94 *	171.82 ± 1.73 *	-83.27 ± 2.20

The per-residue decomposition binding energies were estimated in order to investigate to what extent the differences in the binding energies for the overall peptides were due to the removal of specific residues versus the truncations affecting the behaviour of the conserved residues (figure 6.8).

All the conserved cationic residues of the truncation peptides (Ile1, lys7, lys11 and lys21) have a small but consistent energy increase relative to the residues of Smp24 (figure 6.8A). Individually none of these increases are statistically significant, however together they could explain the overall significant increase in the electrostatic energy for the Smp20 peptide which has the same overall charge as Smp24. The positive  $\Delta G$  of the anionic residues (Asp23 and Ser24) was again slightly increased for Smp20 but of course completely eliminated when the residues are truncated in Smp18 and Smp14a, explaining the large increase in the overall electrostatic energy for these peptides.

Another key observation relates to the effect of amidating the C-terminal. For Smp18 the C-terminal residue is moved to one of the tail lysine residues which corresponds to lys22 of Smp24. The effect of the move is a large reduction in the  $\Delta G$  compared to what would be expected for a standard lysine residue. The  $\Delta G$  is still negative due to the cationic charge of the side chain but the unfavourable anionic charge of the terminal carboxylic acid strongly diminishes the strength of the overall interaction. For Smp14a the C-terminal is located on the neighbouring lysine residue corresponding to lys21 of Smp24. The effect of the amidation completely eliminates the energetically unfavourable interactions of the charged C-terminal as no reduction in the  $\Delta G$  occurs for this terminal lysine residue compared with the other lysine residues.

For the non-charged residues, no significant difference between the truncated peptides and Smp24 were observed. Ile6 is the only residue with a consistent change in the  $\Delta G$  for the residue on the truncated peptides being slightly lower than for Smp24, although the difference is not statistically significant.

Comparing the total  $\Delta G$  sum of the different structural regions, the binding energy of the primary helical region was consistently slightly increased for the truncated peptide. Based on  $\Delta G$  of the individual residues this increase was mainly due to the difference between the cationic residues. No difference was seen between the glycine linker regions, except for with Smp14a where the region is fully truncated. The largest difference between the peptides was in their tail regions. For Smp20 where the region

is conserved the  $\Delta G$  was consistent with Smp24, however for Smp18 and Smp14a where the overall charge of the region is increased to +1 the  $\Delta G$  is significantly increased. The slightly larger  $\Delta G$  for Smp18 could be due to the contribution from the extra C-terminal lysine residue.

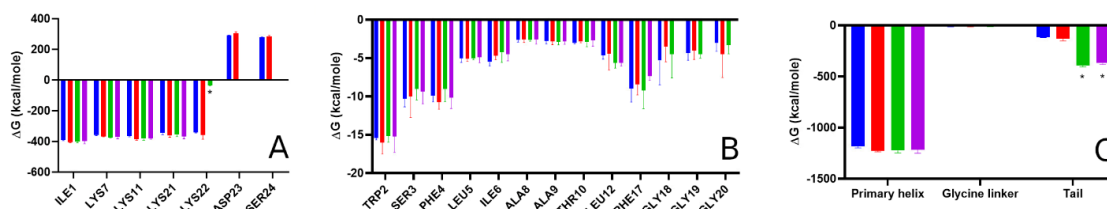


**Figure 6.8 Per residue energy contribution to the total binding energy for Smp24 and the truncated peptides based on the negative bilayer simulations.** A = Charged residues, B = neutral residues, C = sum of structural regions. \* \* Value is significantly different from Smp24 based on one-sided two-sample independent t-test ( $P < 0.05$ ).

To further elaborate on the electrostatic interactions between the peptides and the bilayer the average number of hydrogen bonds and the RDF between the polar sidechains and the phosphate groups were calculated.

While the absolute number of hydrogen bonds decreases with the number of residues truncated, if adjusted to a per residue basis the number of hydrogen bonds are relatively stable and larger than for Smp24 (table 6.7). However, only the values for Smp14a are significantly different from the parent peptide, with the total number being lower ( $P = 0.018$ ) but the per residue number being higher ( $P = 0.043$ ).

The RDFs show that for all the peptides, all lysine residues are positioned to allow them to form strong electrostatic interaction with the negatively charged phosphate groups (figure 6.9). For the polar sidechain residues, Thr10 shows very little interaction, while Ser3 shows a peak at a similar distance to the charged groups but often also a secondary peak a little further from the phosphate groups. While the first peak indicates direct interactions between the serine sidechain and the phosphate groups the second peak is most likely an artifact caused by the interaction between the N-terminal and the phosphate groups. The secondary peak is not present for bcg18\_3 (figure 6.9F) which corresponds to a change in the relative position between Ser3 and the N-terminal due to loss of the helical structure.

**Table 6.7 The average number of hydrogen bonds once the truncated peptides were fully inserted into the DOPC:DOPG bilayers in absolute and per residue numbers. \* Value is significantly different from Smp24 based on two-sided two-sample independent t-test (P<0.05).**

Simulation name	Hydrogen bonds	Hydrogen bonds per residue
bcg20_1	11.183 ± 2.735	0.559
bcg20_2	8.772 ± 2.299	0.439
bcg20_3	8.387 ± 2.549	0.419
Smp20 average	9.447 ± 1.237	0.472 ± 0.062
bcg18_1	7.956 ± 2.356	0.442
bcg18_2	9.576 ± 2.204	0.532
bcg18_3	6.959 ± 2.156	0.387
Smp18 average	8.164 ± 1.078	0.454 ± 0.060
bcg14a_1	6.053 ± 2.124	0.432
bcg14a_2	7.023 ± 1.936	0.502
bcg14a_3	7.362 ± 1.988	0.526
Smp14a average	6.813 ± 0.555 *	0.487 ± 0.040*

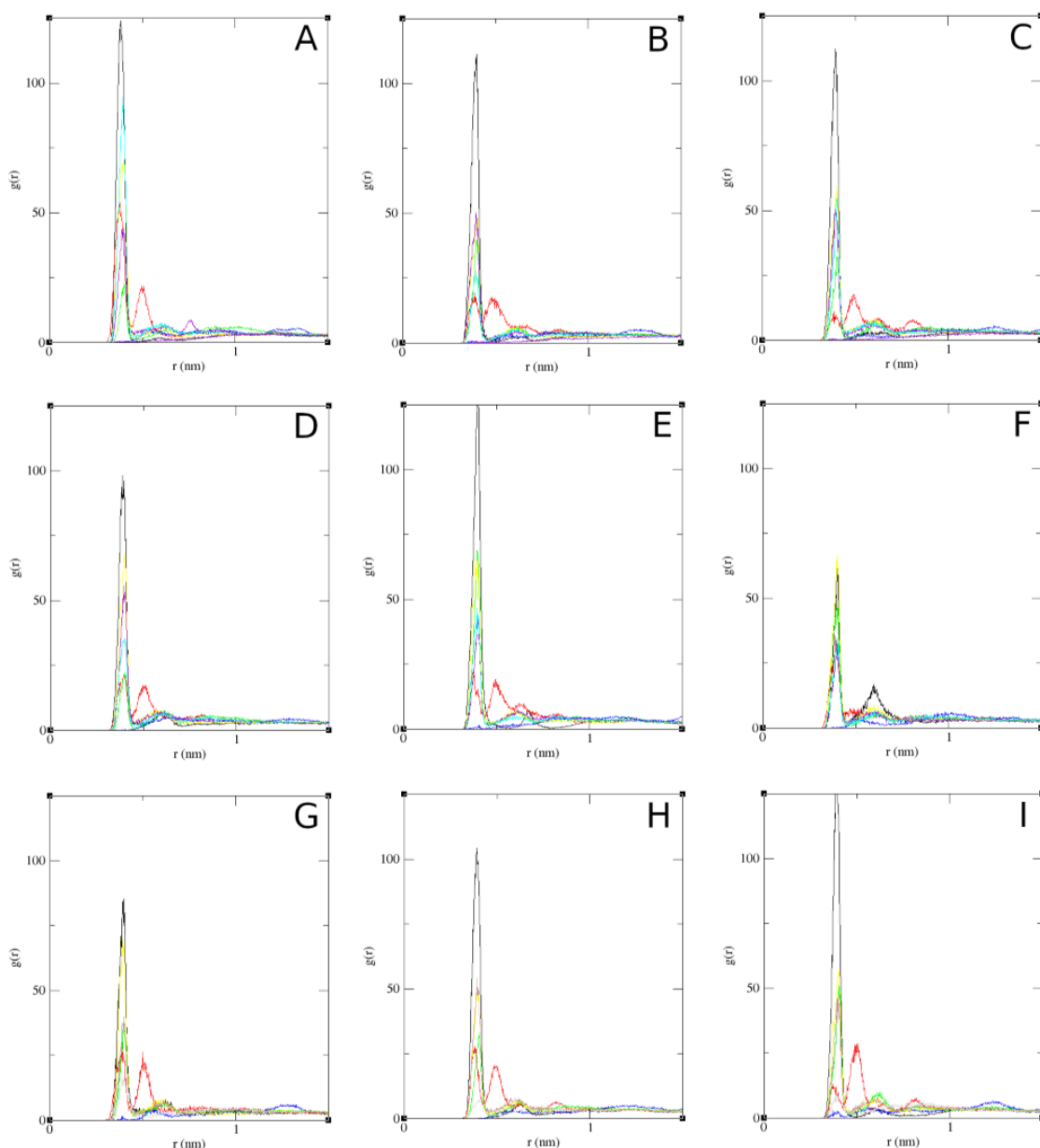


**Figure 6.9 Radial distribution functions between select polar sidechain atoms of the truncated peptides and the phosphate groups of the leaflet of the bilayer that the peptide is interacting with, while the peptide is fully inserted into the bilayer. A = bcg24\_1, B = bcg24\_2, C = bcg24\_3. Black = N-terminal, red = Ser3, green = Lys7, blue = Thr10 and yellow = Lys11, violet = Lys17 (Smp18 and Smp20), cyan = Lys 18 (Smp18 and Smp20), brown = Lys14 (Smp14a) and grey = C-terminal amide (Smp14a).**

### 6.3.2.6 Structure, orientation and positions in the DOPC:DOPE bilayer

As mentioned earlier, the insertion of the truncated peptides into the DOPC:DOPE bilayers was much less consistent. For Smp20 and Smp18 there is a clear correlation between the simulations where a significant loss of the helical structure occurred and only superficial interactions with the bilayer were achieved (figure 6.10). Interestingly, this correlation is not as clear for Smp14a where loss of the secondary structure is only

seen towards the very end of the simulations. The retention of the helical structure might be the reason why in these simulations the superficial interactions were only intermittent.

In the cases where full insertion was achieved the secondary structure was similar to that of the peptides inserted in the DOPC:DOPG bilayers, except for the bce14a\_3 simulation where some loss of helical structure was seen near the C-terminal.

However, taking the observations from the other insertions into account this is likely just some structural variation in this specific simulation rather than a repeatable structural difference based on the bilayer type.

For further evaluation and comparison between the insertion structures in the different bilayers only the simulations where full insertion was achieved were used. As seen in figure 6.11 the 3D structures of the truncated peptides inserted into the DOPC:DOPE bilayers are very similar to in the DOPC:DOPG bilayers. The helical regions are oriented in parallel with the bilayer surface with an angle of below 10 degrees (table 6.8). The angle is slightly higher for Smp14a than the others, however this is likely due to the extra random coil structure near the C-terminal. However, in most cases the position of the helical region is further from the core of the bilayer than in the DOPC:DOPG bilayers (figure 6.12). Observations related to the glycine linker and polar tail regions are in general similar as to with the DOPC:DOPG bilayers. However, like for the parent peptide the main difference between the two bilayer types seems to be that the positional distribution of the tail region, that is much tighter in the DOPC:DOPE bilayer although this is only the case with the full-size tail region. For the truncated tail region of Smp18 the positional distribution is slightly broader in the DOPC:DOPE bilayer.

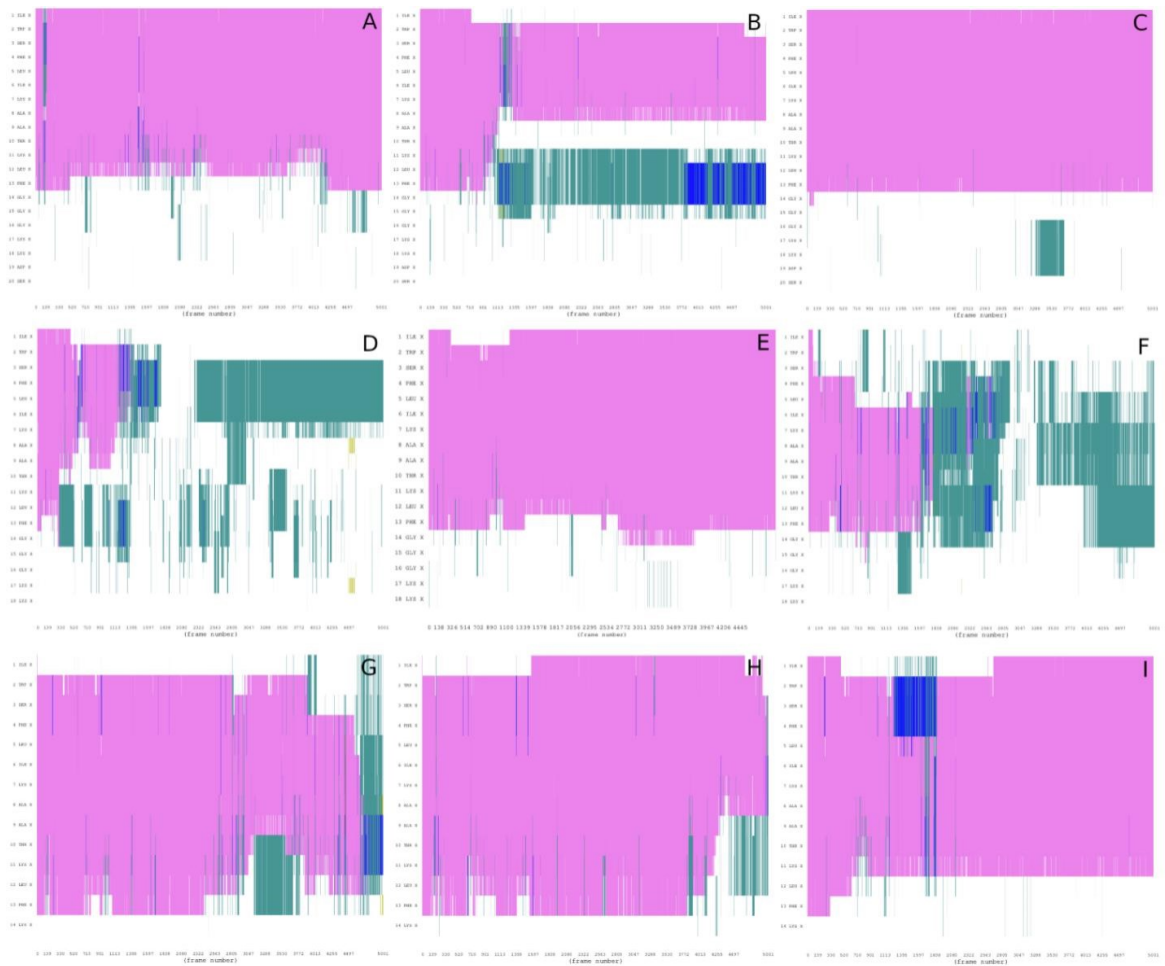


**Figure 6.10 Secondary structure of the truncated peptides over time in the DOPC:DOPE simulations.** A-C = Smp20, D-F = Smp18, G-I = Smp14a. Pink indicates alpha-helix, blue indicates 3-10 helix, green indicates turn, yellow indicates isolated bridge and white indicates random coil.

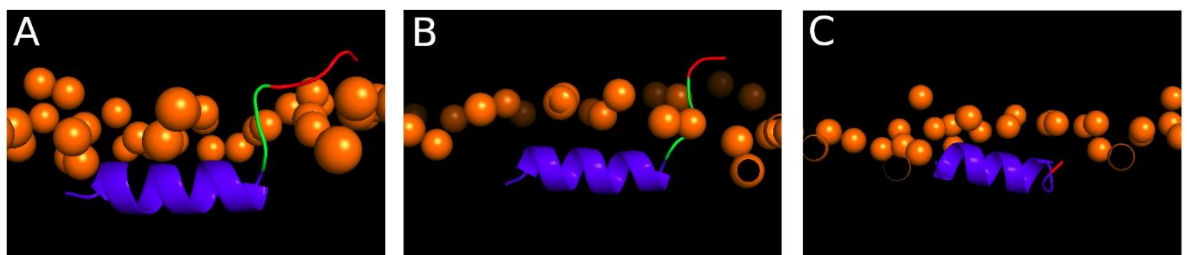


**Figure 6.11 3D structure of truncated peptides inserted into a DOPC:DOPE bilayer.** Blue = helical region, green = glycine hinge, red = tail, orange = lipid phosphor atoms. A = Smp20, B = Smp18, C = Smp14a.

**Table 6.8 Average angle between the primary helix (residue 1-12) and the DOPC:DOPE bilayer (x-y plane), for the truncated peptides after insertion.**

Simulation name	Helix bilayer angle after full insertion
Bce20_1	$-0.36 \pm 7.50$
Bce20_3	$1.07 \pm 8.10$
Bce18_2	$3.10 \pm 8.26$
Bce14a_3	$9.78 \pm 11.59$

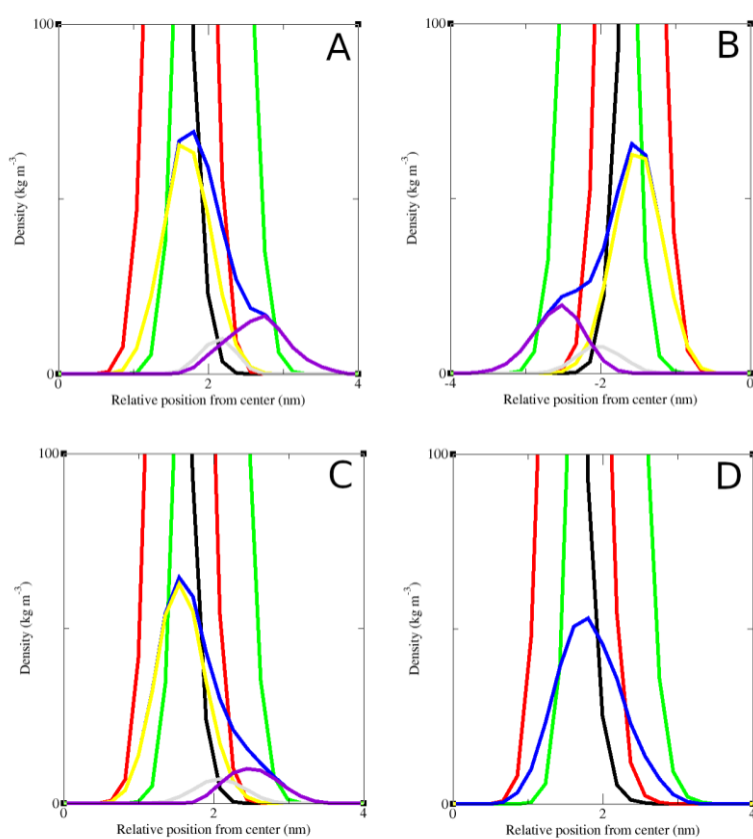


**Figure 6.12 Partial density profiles of the truncated peptides inserted into DOPC:DOPG bilayers, with positions relative to the z-axes. A = bce20\_1 B = bce20\_3, C= bce18\_2, D = bce14a\_3. Black = Lipid acyl chains, Red = Lipid glycerol esters, Green = lipid headgroups with phosphates, Blue = whole peptide, Yellow = helical region, Grey = glycine hinge and purple = polar tail region.**

### 6.3.2.7 Interactions with the DOPC:DOPE bilayer

The total relative binding energy is relatively similar for the truncated peptides in the DOPC:DOPE bilayer as well (table 6.9). Smp14a deviates somewhat from the others, but the slight misfolding might have influenced this. Overall, the relative binding energies are in all cases less than half of what was found for the DOPC:DOPG bilayers.

The Van der Waals energies and both non-polar solvation terms all follow similar trends as was observed for the DOPC:DOPG bilayer models. However, the electrostatic and polar solvation energies are both relatively similar for all the truncated peptides, unlike what was observed with the other bilayer.

The number of hydrogen-bonds between the peptides and the bilayer follow the same trends in the DOPC:DOPE bilayer as for the DOPC:DOPG bilayer, with a stepwise reduction in the absolute number but a relatively stable number of hydrogen bonds per residue (table 6.10). However, both numbers are in general lower compared with the DOPC:DOPG bilayer models.

The RDFs show that all the positively charged amine groups are still involved in interaction with the lipid phosphate groups although in general the peaks associated with the lysine sidechains are smaller than for the corresponding DOPC:DOPG simulations (figure 6.13). The N-terminal amine still seems to form the most consistent interactions, while the uncharged polar sidechains have the lowest interactions.

**Table 6.9 Breakdown of the free binding energies for the truncated peptides and DOPC:DOPE bilayer complexes.** All values are in kcal/mol.

Simulation name	Van der Waals energy	Electrostatic energy	Polar solvation energy	Non-polar solvation energy	Energy dispersion	Delta G total
bce20_1	-117.26 ± 10.56	-68.50 ± 18.10	66.09 ± 15.35	-96.48 ± 8.50	177.12 ± 11.88	-39.02 ± 9.19
bce20_3	-120.25 ± 10.54	-72.39 ± 19.96	68.53 ± 16.77	-97.32 ± 9.01	180.11 ± 14.42	-41.31 ± 8.28
bce18_2	-114.71 ± 11.46	-65.65 ± 15.49	62.73 ± 12.66	-91.47 ± 8.70	168.48 ± 13.54	-40.62 ± 9.29
bce14a_3	-97.57 ± 10.12	-62.26 ± 12.48	58.83 ± 9.96	-79.63 ± 7.00	146.19 ± 12.07	-34.43 ± 7.34

**Table 6.10 The average number of hydrogen bonds once the truncated peptides were fully inserted into the DOPC:DOPE bilayers in absolute and per residue numbers.**

Simulation name	Hydrogen bonds	Hydrogen bonds per residue
bce20_1	7.807 ± 2.599	0.390
bce20_3	8.095 ± 3.100	0.405
bce18_2	6.412 ± 2.548	0.356
bce14a_3	5.640 ± 2.161	0.403

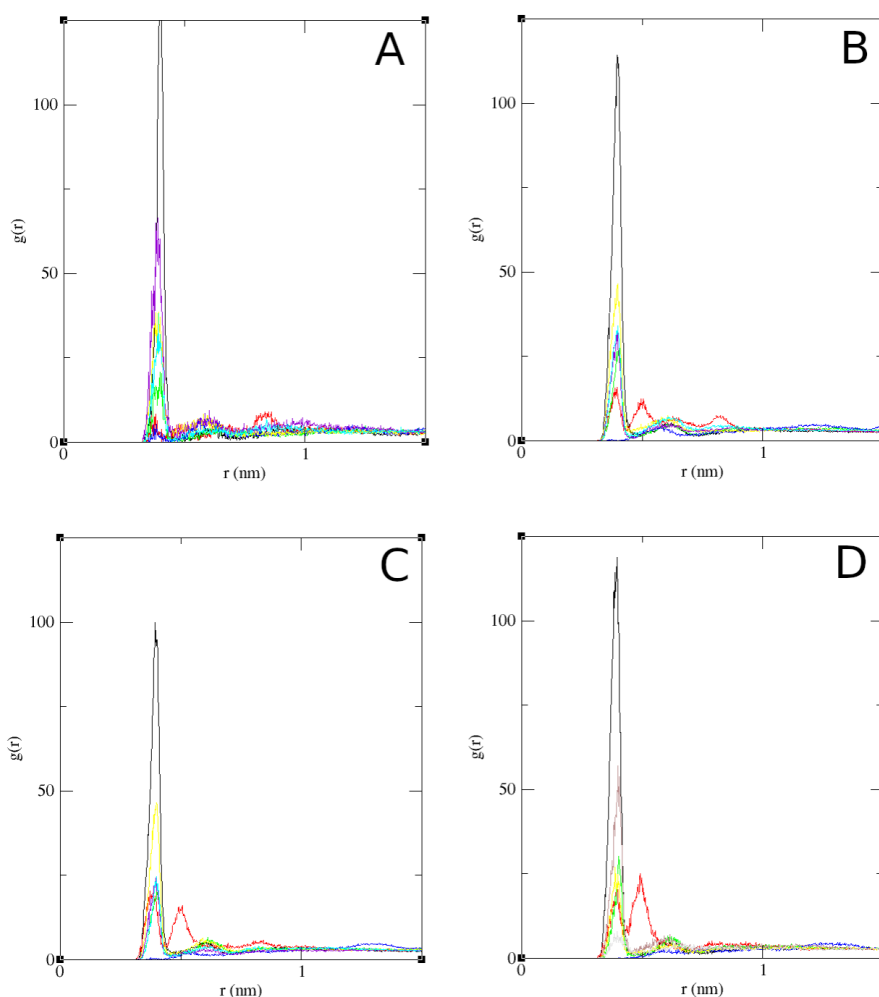


**Figure 6.13 Radial distribution functions between select polar sidechain atoms of the truncated peptides and the phosphate groups of the leaflet of the bilayer that the peptide is interacting with, while the peptide is fully inserted into the bilayer. A = bce20\_1, B = bce20\_3, C= bce18\_2 D = bce14a\_3. Black = N-terminal, red = Ser3, green = Lys7, blue = Thr10 and yellow = Lys11, violet = Lys17 (Smp18 and Smp20), cyan = Lys 18 (Smp18 and Smp20), brown = Lys14 (Smp14a) and grey = C-terminal amide (Smp14a).**

### 6.3.3 Computer aided drug design of the truncated Smp24 variants

The first line of concern when truncating a peptide is to not to lose the activity of the parent peptide. Due to the understanding gained regarding the behaviour of Smp24 in the previous chapter comparisons could be made between it and the truncated variants. The properties of the conserved regions in each design iteration could be compared with those of the parent peptide to ensure aspects such as helicity, insertion depth, interactions and binding energy did not change for the new designs. If these properties did not change, it was taken as an indication that the truncated peptides would likely also inherit the antimicrobial properties of the parent peptide *in vitro*.

This computational evaluation of the new peptides could be done during the design process, allowing for partial validation of the different design iterations without synthesis and *in vitro* evaluation. Thus, all three analogs and parent peptide could be synthesized and evaluated *in vitro* at the same time, saving months compared to a true step by step iterative approach.

The first iteration in the truncation process was the design of Smp20, which focused on truncating the secondary helix. As mentioned in the design section, the position of the secondary helical region in the centre of the peptide introduced some additional concerns during the design process, as without the presence of the secondary helix the transition from helical to random coil structure is shifted. This could potentially greatly affect the behaviour of the conserved regions of the peptide, on both sides of the truncation. An example of this is the failed initial attempt at truncating the peptide, Smp21. In this case the transition did not occur correctly, which led to a disruption of the back part of the primary helix causing it to partially unfold and no longer be oriented correctly relative to the bilayer.

2 key observations were learned from this failed truncation attempt:

Firstly, when truncating the secondary helix, the proline residue needed to be removed. The inclusion of a proline residue in an AMP must be very deliberate due to its intrinsic ability to disrupt the helical structures. The kink it induces in the peptide backbone can be utilized to control the relative orientation between different regions of a peptide. This can be done within a helical region without completely changing the secondary structure, as the helical structures on each side of the proline limit how large the structural fluctuation induced by the flexibility of the kink can be. However, if the proline is present between a helical and unstructured region the disruption of the helix is likely only going to be exacerbated. The high flexibility of the unstructured region is already going to stress the back end of the helical structure, with the proline residue further limiting the number of structure stabilizing hydrogen bonds that can be formed between the peptide backbone. Therefore, alternative approaches should be used to ensure the correct orientation between helical and random coil regions.

Secondly, anchoring of the ends of the helical region seemed key for retaining the correct orientation while inserted in the bilayer. With the tail region being both unstructured and positioned further away from the core of the bilayer it can to some

extent pull on the back end of the helical region causing it to adopt a tilted/partially inserted orientation event if it is less favourable for the helical region by itself. The truncation of the secondary helix changes the endpoint of the helical region which can disrupt the anchoring, with the problem potentially being even further exacerbated by the tail region making up an even larger proportion of the total number of residues.

Based on these design observations the successfulness of the truncation of Smp20 was evaluated based on three criteria.

Firstly, the transition between the helical region and unstructured tail must be efficient with the correct relative orientation between them. To do so a schematic of the structure of Smp24 while inserted into the bilayer was drawn and it was imagined how it would look without the secondary helix (figure 6.14). In both cases, the primary helix forms a consistent structure lying flat at the bottom of the drawings. Both schematics also have a similar position of the tail region in the top right of the structures. The tail regions are shown with a colour gradient to represent their more dynamic position among the lipid headgroups contrary to the more static position of the primary helix. Smp24 also contains the secondary helix that can adapt a range of orientations relative to the primary helix depending on the angle of the kink. The glycine linker region connects the end of the secondary helix with the tail region but as the length of the linker region is static, the shape must be variable in order to accommodate the different orientations of the secondary helix. When the secondary helix is tilted upwards the linker region is not very efficient, however it still needs to be long enough to ensure that the link can occur correctly when the helix is tilted down. For the truncated peptide the dynamic nature of the linker region is no longer necessary. The structure could instead be designed around a single orientation of the linker region and as the horizontal position of the tail region is not critical, the most efficient orientation of the linker region would be tangential to the bilayer creating a direct link between the helix and tail regions.

To achieve this orientation of the glycine linker region the helical rotation of the endpoint residue in the helical region was used. Due to the amphiphilic separation of the residues in the helical region, the rotational orientation of the helix relative to the bilayer surface is restricted once the peptide is fully inserted with a specific side of the helix always facing away from the bilayer core. This means that depending on at which

residue the transition to the linker region occurs the orientation of this transition point relative to the bilayer can vary greatly. The 13<sup>th</sup> residue was deliberately chosen to be the endpoint of the helical region in the truncated peptides as this led the end of the backbone to be oriented directly facing away from the core of the bilayer. Therefore, if the linker region was to start here and adopt a relatively straight configuration it would be oriented tangentially to the bilayer surface. The 13<sup>th</sup> residue position ended up being the last residue designated to be part of the primary helix in Smp24, however if that was not the case the truncation would still have been completed at this position as it was accounted for in the truncation guidelines that a partial truncation could be done of the primary helix after the last lysine in the 11<sup>th</sup> position. The 3D structures from the simulations of Smp20 (and Smp18) show that this criterium was met (figure 6.6). Due to the more variable orientation of the tail region the orientation of the glycine linker region is not always straight and thereby not completely tangential with the bilayer surface, which might suggest that the length of the linker itself also could be reduced without affecting its function. However, looking only at the first of the glycine residues its orientation is consistently pointing away from the bilayer centre which was the core aspect of the design objective.

The second criterium was that the behaviour of the primary helix should not be disrupted by the truncation. A key aspect in achieving this was to ensure that the orientation of the fully inserted region was conserved. This was done by shifting the truncation window by one residue such that the final residue of the secondary helix (position 17) replaced the final residue of the primary helix (position 13). The 17<sup>th</sup> residue of Smp24 is the large hydrophobic residue phenylalanine which could serve the function of helping to anchor the end of the helix within the bilayer via downwards pulling hydrophobic interactions with the core of the bilayer. In Smp24 large, aromatic, hydrophobic residues such as phenylalanine and tryptophan are only present near the end and beginning of the helical regions which could speak to them having this function. This is the same for the structurally related peptides Pandinin 2 and Con10 and thus could further suggest a common anchoring motif. In addition, the per-residue decompositional analysis of the binding energy suggests that the energy contribution of a phenylalanine residue is about twice that of a leucine residue, showing how it would be more suited for the anchoring role. Based on the orientation of the inserted helical region of Smp20 (and Smp18) the anchoring was mostly successful. In most

simulations the helix was oriented in parallel with the bilayer surface and positioned with a similar partial density profile as with Smp24. The only simulation where this is not the case is in bcg20\_2. In this simulation the end of the helical region is both partially unfolded and not fully inserted into the bilayer. It is more likely that the lack of insertion is due to the partial unfolding rather than a lack of anchoring, but it still highlights that the transition region is still susceptible to structural disruption even without the proline residue. This problem could potentially be somewhat diminished by truncating the tail such as done with Smp18, but otherwise it is difficult to imagine how it could be solved without doing any amino acid substitutions. The analysis of the interactions between the primary helix and the bilayer also indicates that the behaviour is conserved from Smp24. The RDFs show that all the charged interactions with the lipid phosphate groups still occur which is supported by the binding energy calculations. Interestingly, the per-residue decompositional energy analysis indicates that the interactions stemming from the cationic residues of the primary helix are slightly stronger for the truncated peptides compared with Smp24. This could be a downstream effect of removing the secondary helix allowing the primary helix to adopt a slightly more favourable position/orientation in the bilayer. For Smp24 the exact position/orientation is likely dependent on what is the most optimal for both helical regions at the same time, whereas in the truncated peptides there is more freedom to optimize it for the primary helix leading to the consistent improvement in the electrostatic interactions. A slight shift in the orientation of the primary helix is further indicated by a consistent reduction in the energy contribution of Ile6 in all the truncated peptides. This is the hydrophobic residue that is positioned the furthest up the side of the helix towards the lipid headgroups and thus would likely be the first residue affected by a realignment of the helix's rotational orientation. Overall, the simulations indicate that the truncation could potentially disrupt the back end of the primary helix somewhat but under ideal conditions the interaction might actually be slightly improved.

Finally, the last criterium was that the truncation should not disrupt the behaviour of the tail region. Due to this region's random coil structure and relatively large positional flexibility (especially in the negative bilayer) this was less of a concern, so no additional design decisions were implemented in order to achieve it. The partial density profiles

and energy contributions of the tail region is consistent with what was previously observed for Smp24, so this criterium was also deemed to have been achieved.

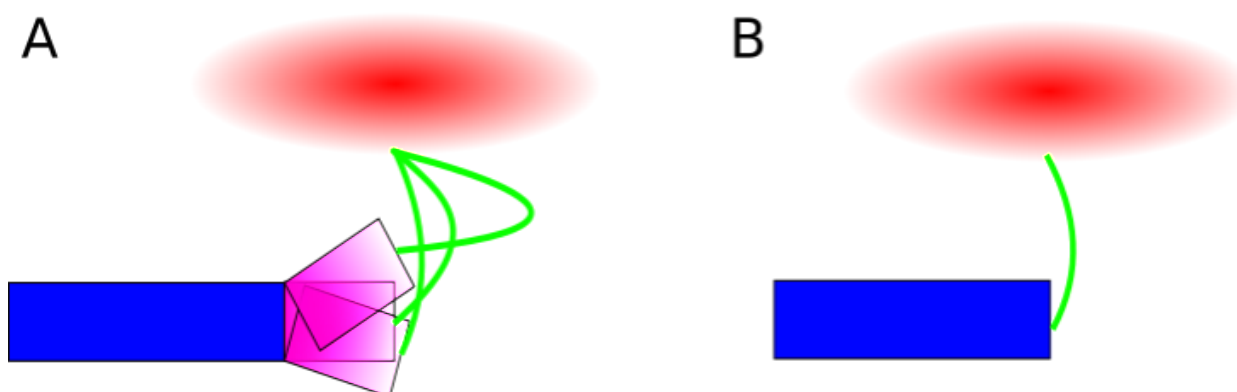


**Figure 6.14 Schematic comparing the structural design of Smp24 and Smp20. A = Schematic of the structure of Smp24 while fully inserted in the bilayer. B = Proposed schematic of what the structure would look like for Smp20. Blue = primary helix, purple = secondary helix, green = glycine linker, red = tail region.**

Compared with Smp20 the design of the next truncation iteration was much simpler. The focus was on removing the potentially unfavourable residues from the tail region which happened to be positioned as the two last residues of the peptide sequence making the design of Smp18 very straight forward. Still, two criteria for a successful truncation could be formulated.

Firstly, the position of the tail region should become more efficient. The partial density profiles for the tail region of both Smp24 and Smp20 inserted in the negative bilayer indicated that part of the tail region was positioned above the bilayer in the water phase. This part of the tail region is not likely to form strong interactions with the bilayer headgroups and is not an efficient part of the overall peptide structure.

Truncating the aspartic acid and serine residues completely removed this section from the density profiles of Smp18 while the position of the remaining part of the tail was still conserved.

Secondly, the removal of the two residues previously indicated to negatively affect the binding energy should yield an overall improvement in the energy contribution of the tail region. This criterium was only partially achieved. While a significant increase in

the energy contribution of the tail region as a whole was seen, moving the C-terminal to the lysine residue strongly reduced the energy contribution of this residue. Based on the known properties of Smp24 and the position/orientation of the C-terminal in Smp18 among the very top of the lipid headgroups, the negative charge of the carboxylic acid is likely not completely detrimental to the activity of the peptide even if it negatively affects the binding energy. However, if the tail region was to be moved to a different position it might start to become a problem.

The design of Smp14a was more of a balancing act than Smp18. As the size of the tail region is further reduced the rationale for including the three-residue linker region which by itself does not seem to play a large role in the peptide-bilayer interactions becomes less justifiable. However, if both the glycine linker region and the tail region were to be fully removed, the newly improved binding energy contribution of the truncated tail region would be lost. Therefore, the objective of the design was to truncate the regions in such a way that the desirable properties of the tail region could be retained without the presence of the glycine linker. This was achieved in two steps. Firstly, the three glycine residues from the linker region and one lysine residue from the tail region were truncated. This would drastically change the position of the last remaining lysine residue of the tail region. However, due to the orientation of the backbone following the final residue of helical region, the new position and orientation of the C-terminal lysine residue would be relatively similar to that of the lysine residues present in the primary helix and therefore likely not unfavourable. The RDF for this residue showed that the lysine side chain was still able to form strong interactions with the surrounding lipid phosphate groups indicating that moving the position of the residue did not inhibit its function.

However, the truncation also meant that the position of the negatively charged C-terminal carboxylic acid changed. While in its previous position the C-terminal might just have had a negative impact on the binding energy, but the new position would be like that of the primary helix around the glycerol esters and lower parts of the lipid headgroups. This is directly overlapping with the position of the negatively charged lipid phosphate groups which would repel the negatively charged C-terminal, risking that the full insertion into the bilayer would be inhibited. To tackle this, the negative charge was neutralized by amidating the C-terminal. Such a post-translational C-

terminal modification is not uncommon for AMPs, even in nature where peptides which do not have significant unstructured regions near the C-terminal such as melittin and mastoparan have their C-terminal amidated (212, 217). The simulations indicated that this approach was successful, with the primary helix of Smp14a behaving similarly to those of Smp24 and the other truncated peptides in terms of structure, orientation, position and interactions. In addition, the amidation also completely eliminated the negative impact of the C-terminal on the binding energy and thus the design objective was fully achieved.

During the use of the MD simulations in the design process, the choice of truncation targets based on the Smp24 simulations were also further validated. The truncation of the back half of the peptide did not seem to impact the insertion mechanism to a great extent, with the same stepwise changes in the position and orientation occurring for the truncated peptides as with Smp24. N-terminal insertion followed by a helical rotation leading to a full insertion was observed for all simulations with the negative bilayer, except for one where the insertion was only partial due to some loss of the helical structure. The timeframes for the insertion process were also in line with the previous observations for Smp24. As for Smp24, the insertion into the neutral bilayer was much less consistent, something potentially exacerbated by the partial truncation of the tail region with both Smp18 and Smp14a only achieving insertion in 1/3 simulations. Furthermore, in two simulations Smp14a only achieved intermittent interactions with the bilayer surface indicating that the negatively charged residues/terminal could play a role in surface attachment and thereby could affect the selectivity of the peptides.

The solution behaviour of the truncated peptides was also consistent with Smp24. The main difference was that the truncations of the tail region did start to inhibit the formation of intermolecular salt-bridges (partially for Smp18 and fully for Smp14a). This did lead to an increase in the structural fluctuations for Smp18 in the 60% TFE solution compared to Smp20, especially in the tail region of the peptides. However, all truncated peptides still retained their helical structure in 60% TFE even without the consistent cross peptide interactions.

The very limited reduction in the overall binding energy for the truncated peptides relative to Smp24 also confirms that the primary helix was the main contributor to the binding energy. As expected, a slight shift towards hydrophilic interactions being even more dominant for the peptide-bilayer interaction was observed for all the truncated peptides, driven by removal of mainly hydrophobic residues, elimination of unfavourable electrostatic interactions and the slight improvement of the electrostatic interactions of the cationic residues of the helix. This shift translates into a relatively large reduction in the binding energy with the neutral bilayer for all three truncated peptides of 21-34% compared with the bce24\_1 Smp24 simulation, potentially indicating an improvement of the selectivity of the peptides. In addition to the changes to the balance between the direct hydrophobic and electrostatic interactions, a size dependent shift in the non-polar solvation terms was also seen for all the truncated peptides, favouring a smaller overall size. Initially one could expect that the non-polar solvation energy would be more favourable for a larger peptide as binding could facilitate a greater reduction in the solvent accessible surface area, but due to the dynamic nature of the bilayer the size of the binding pocket will also change with the peptide size. A more accurate estimation of this effect could potentially be done by using a multiple trajectory MMPBSA approach but factors such as the energy cost of dispersing lipids upon peptide binding still complicates the binding energy estimations for peptide truncations.

#### 6.2.4 Antimicrobial and cytotoxic properties of the truncated peptides

The antimicrobial properties of the truncated peptides were characterised by evaluating their MIC against a range of clinically relevant bacteria (table 6.11).

Truncation of only the secondary helical region seems to facilitate a general reduction in the antimicrobial efficacy with Smp20 showing a twofold increase in the MIC against both a Gram-positive and Gram-negative pathogen compared with the parent peptide. However, with further truncation of the polar tail region general reductions in the MICs were seen for both Smp18 and Smp14a. In total for smp14a, a two-fold reduction in the MICs was seen for both Gram-negative pathogens and a 2-4 times reduction was seen against *S. aureus*, based on the  $\mu\text{g/ml}$  values.

All the peptides showed a higher selectivity towards *S. aureus*, except for Smp20 which has similar selectivity towards both *S. aureus* and *E. coli*.

**Table 6.11 MIC of the truncated peptides and smp24.** Values are in µg/ml with the values in parentheses being the equivalent in µM.

Peptide	<i>S. aureus</i>	<i>E. coli</i>	<i>P. aeruginosa</i>
Smp24	16 (6.2)	32 (12.4)	32 (12.4)
Smp20	32 (14.8)	32 (14.8)	64 (29.5)
Smp18	8 (4.1)	16 (8.1)	32 (16.3)
Smp14a	4-8 (2.4-4.9)	16 (9.8)	16 (9.8)

As the primary mechanism of action of AMPs like Smp24 is against the cell membrane, erythrocytes can serve as a decent model for investigating the toxicity of AMPs against eukaryotic cells. Sheep erythrocytes were incubated with Smp24 and the truncated peptides at a range of concentrations to investigate their haemolytic activity, based on the haemoglobin release (table 6.12). Clear differences can be seen in the haemolytic activity of the different peptides. Smp24 has the highest haemolytic activity followed by Smp14a, Smp18 and Smp20. The HC<sub>50</sub> values for all the truncated peptides are significantly higher than for Smp24, showing a consistent reduced haemolytic activity. Between the truncated peptides they follow a similar trend as observed with their antimicrobial activity, with Smp20 having by far the lowest activity while Smp14a is slightly more active than Smp18. These differences are still observable when correcting for the molecular mass change.

**Table 6.12 HC<sub>50</sub> values for Smp24 and the truncated peptide based on the haemolysis of sheep erythrocytes.** \* Value is significantly different from Smp24 based on one-sided two-sample independent t-test (P<0.05).

Peptide	HC <sub>50</sub> (µg/ml)	HC <sub>50</sub> (µM)
Smp24	88.33 ± 1.82	34.26 ± 0.71
Smp20	245.47 ± 59.38*	113.25 ± 27.39*
Smp18	156.35 ± 21.19*	79.55 ± 10.78*
Smp14a	120.61 ± 2.28*	72.44 ± 1.37*

To further evaluate the cytotoxicity of the truncated peptides against a more complex cellular target, two secondary human cell-lines representing toxicologically relevant tissues were exposed to the peptides at different concentrations. The cell survival rates were estimated using the LDH release which is a marker for membrane damage (table 6.13). The cell-line cytotoxicity for all the peptides follows the same trends against both the kidney cell-line (HEK293) and the liver cell-line (HepG2), although based on the EC<sub>50</sub> values the peptides are slightly more toxic against the HEK293 cells. Smp20 is consistently significantly less toxic than Smp24 and the other truncated variants. However, unlike against erythrocytes the activity of both Smp18 and Smp14a is not significantly different from Smp24, at least within a certain concentration range. At concentrations above 58 µg/ml the response for Smp14a starts to deviate from the other peptides, giving this peptide an overall lower maximum cytotoxic response.

**Table 6.13 EC<sub>50</sub> values for Smp24 and the truncated peptide based on the LDH release from the secondary cell lines.** The EC<sub>50</sub> values for all peptides are calculated against the average maximum LDH release rate for Smp24, Smp20 and Smp18 relative to the positive control. Average maximum LDH release was 52.2 ± 5.71% and 52.2 ± 2.78 % against HEK293 and HepG2 cell lines respectively. \* Value is significantly different from Smp24 based on one-sided two-sample independent t-test (P<0.05).

Peptide	HEK293 (µg/ml)	HEK293 (µM)	HepG2 (µg/ml)	HepG2 (µM)
Smp24	35.66 ± 7.59	13.83 ± 2.94	42.52 ± 8.25	16.49 ± 3.20
Smp20	54.38 ± 7.10*	25.09 ± 3.28*	58.86 ± 4.87*	27.16 ± 2.25*
Smp18	38.41 ± 6.56	19.54 ± 3.34	40.86 ± 5.62	20.79 ± 2.86
Smp14a	37.01 ± 4.61	22.23 ± 2.77*	42.92 ± 5.80	25.77 ± 3.48*

#### 6.2.5 The truncations effect on the antimicrobial activity and selectivity

From a molecular viewpoint truncation can often be thought of as a balancing act, between how much of the peptide structure can be removed without significantly impacting the biophysical processes leading to the biological activity. However, as seen with the truncated Smp24 variants, in some cases the activity can be improved. Such improvements could occur via several different mechanisms. Firstly, the truncated regions could have had an overall negative impact on the activity of the parent

peptide. Thereby, removing them from the structure (without disrupting the remaining regions) would facilitate a direct improvement of the activity on a per molecule basis. The activity could also be improved in an indirect way by removing residues or regions that had no impact on the overall activity. This would not change the activity of an individual molecule, however in microbiology the activity of an antimicrobial agent is commonly evaluated based on its mass and thus reducing the size of the peptide would increase the number of molecules per gram leading to an indirect improvement of the activity.

The biological evaluation of Smp24 and the truncated peptides indicates that both types of improvements and a direct decrease of the activity occur following the different truncation iterations. While MICs do not produce the most detailed output for comparing relatively small differences in activity between antimicrobial agents, they are the gold standard methodology and can still provide insight into the trends related to the activity. The first truncation iteration (Smp20) has a slight but consistent reduction in its antimicrobial activity compared with the parent peptide. This is not completely unexpected based on the observations from the MD simulations where this peptide has the lowest overall binding energy and potentially some challenges related to the structural stability of the end of the helical region. Furthermore, there is also the removal of the helical kink which was indicated to potentially play an important role in stabilizing the peptide induced pore structures. While the reduced antimicrobial activity of Smp20 could indicate that truncation somewhat inhibited the membrane disruptive properties, the changes are not so great that the secondary helix should be deemed critical for the antimicrobial activity.

The 27-residue alpha helical AMP Fowlicidin-3, unlike Smp24, does not contain a proline kink in its helical region. Instead, it contains a larger –AGIN- hinge region which also provides flexibility to the helical backbone due to the glycine residue (218). Truncation of the parts of the peptide before and after this region eliminated the antimicrobial activity but truncation of only the hinge region only affected it slightly. However, the truncations significantly reduced the haemolytic activity of the peptide (219). These observations correlate well with the results for Smp20, further indicating that kink/hinge regions might not be necessary for the antimicrobial activity of AMPs.

The partial loss in activity due to the truncation of the secondary helix in Smp20 can be compensated for by increasing the overall charge of the peptide as is done with Smp18 and Smp14a. Both show consistent improvements in their antimicrobial activity compared with Smp20 and in most cases also compared with Smp24. Some of these improvements might be indirect due to the size reduction with the molecular weight of Smp14a being around 35% lower than Smp24. However, based on the  $\mu\text{M}$  MIC values some direct improvements of the activity are also likely, with the MIC of Smp14a against *S. aureus* being between 2.4-4.9  $\mu\text{M}$  meaning that the MIC of Smp24 (6.2  $\mu\text{M}$ ) should have been one level lower if the molecular activity was the same.

These results are comparable with observations from the simulations where Smp18 and Smp14a behaved very similarly to Smp24 on a molecular level. Furthermore, as indicated by the non-polar solvation terms, the smaller size of the peptide could also facilitate some energetic advantages independent of the direct interactions, such as by reducing the energy cost of creating the binding pocket in the lipid leaflet. Other factors related to the overall charge of the peptides might play a larger role *in vitro* than indicated purely based on the simulations. Due to the peptides starting already in their helical configuration very close to the bilayer in the simulations, the importance of the overall charge in the very early stages of the mechanism of action is not well modelled. The increased charge could ensure that the peptides get adsorbed to the membrane surface faster and at higher concentrations *in vitro* and stronger electrostatic interactions could make the folding into the helical structure more favourable. All in all, this could facilitate that more peptides, in their active configuration, get inserted into the bacterial membranes at a lower overall concentration yielding an increase in the activity.

Increasing the overall charge of an AMPs is one of the most consistent ways of improving its antimicrobial activity. The activity of Smp24 was previously broadly improved by substituting any of the three serine residues for lysine residues, although the improvement was the greatest for the position 3 serine (149). Jiang et al systematically investigated the effect of changing the net charge of the AMP V13K by substituting in either cat- or anionic residues, showing a good correlation between net charge and MIC although the specific position and net number of the cationic residues also played a role (220). Truncations of unstructured C-terminal regions have also

previously been shown to improve the properties of AMPs. Nine residues from the unstructured tail region of the AMP GV30 were truncated and the C-terminal amidated which did not inhibit the overall antimicrobial properties of the peptide but improved its killing kinetics and reduced its haemolytic activity. Further truncation of the helical region eliminated the antimicrobial activity (221).

For AMPs especially, improved activity is not always a purely desirable property. As the primary target for the peptide against both bacteria and eukaryotic cells is the cell membrane, higher activity could also lead to increased cytotoxicity. Therefore, evaluation of new peptides cytotoxic properties is also necessary during an iterative design process. The activity of AMPs against eukaryotic cells is downstream from both the membrane disruptive activity and selectivity of the peptides so both must be considered when evaluating the results.

The cytotoxicity of the peptides against eukaryotic cells were evaluated against both sheep erythrocytes and secondary human cell-lines. Haemolysis assays are the most universally used way of evaluating the toxicity of AMPs due to the simplicity and ease of use of the method. The relatively simple cellular structure of erythrocytes and their encapsulation of haemoglobin which can serve as a natural dye, means that erythrocytes can serve as a natural version of a dye filled liposome. Therefore, the membrane disruptive activity of AMPs can easily be evaluated against a cell membrane with a lipid composition representing eukaryotic cells. The secondary cell lines represent a more complex cellular model, with the cells potentially being able to respond to the peptides in more dynamic ways. These assays also allow for selection of cells from specific tissues which might be more at risk for a toxic response *in vivo*, giving further context to the cytotoxic data.

Comparing the two methods relatively large differences can be seen in the peptide concentrations needed to produce a 50% cytotoxic response. This could be due to differences in the properties of the cells but, it is more likely that it is due to differences in the overall experimental conditions. The concentration dependent activity of AMPs is very dependent on the number of cells it is tested against. Therefore, in some biophysical experiments where the experimental conditions can be highly controlled, it is common to describe their activity in terms of peptide to lipid

ratio which corrects for both the peptide and lipid concentration. In the haemolysis assay used in this study the concentration dependent activity was tested for 1h against a 10% erythrocyte suspension which would be expected to yield a cell concentration of around  $5 \times 10^8$  cells/ml (222). However, in the cell culture assay the cells were seeded at  $2 \times 10^5$  cells/ml and then grown for 24h before the peptides were added. Even if the cells had more than doubled in the 96 well plates, the concentration would still be around 1000 times lower than in the haemolysis assay and the cells were also exposed to the peptide for much longer, which could explain the lower peptide concentrations needed to kill the cells. Greco et al. compared the use of haemolysis and cell line assays and found that human cell lines are generally more robust against AMPs than erythrocytes (222), although other authors have found that the opposite to be the case (149, 223, 224). Furthermore, the specific values obtained from *in vitro* tests might not have much direct relevance to the concentrations needed to induce a cytotoxic response *in vivo*, where the pharmacokinetics of the drug molecule also play a large role.

Therefore, the *in vitro* cytotoxicity results are better utilised in a relative manner such as when comparing between the different analogs to identify in which direction the cytotoxicity trends. Although, with this viewpoint the results of the two assays still differ, with the differences between the peptides being more pronounced in the haemolysis assay than with the cell lines, something also found in other studies (222). This might indicate that different aspects of the mechanism of action are more or less important for the overall activity in each of the cytotoxicity models.

Smp20 shows the clearest reduction in cytotoxicity, with statistically significant shifts in both assays. Together with MIC results this further suggests a general activity reduction compared with Smp24. Comparing the MIC and the cell culture assay the peptide has around 1.66 and 1.45 times shifts in the activity respectively compared with the values for the parent peptide (in  $\mu\text{g/ml}$ ). However, for the haemolysis the  $\text{HC}_{50}$  value is shifted 2.78 times. This could indicate that structural changes that affect the selectivity and not just the activity have a larger impact in the haemolysis model. Most erythrocyte types contain either none or a very small fraction of negatively charged lipids in their outer membrane leaflet and therefore form a good basis for evaluating the lipid-based selectivity of antimicrobial peptides (225). Such lipid

compositions are also the case for other eukaryotic cell types under normal conditions. However, when a cell becomes cancerous one of the changes it undergoes can be an increase in the proportion of negatively charged lipids present in their outer leaflet (226). This change in their membranes is also thought to be the reason why some AMP like peptides can have anticancer properties (227). Little information exists in regard to the leaflet specific lipid composition of HEK293 and HepG2 cells, but as they are cancer cell-lines they could potentially have more negatively charged lipids in their outer leaflet than normal diminishing the effect of selectivity-based differences between the peptides. This could explain why the dose response curves differ between the two assays.

All truncated peptides show a reduced haemolytic activity compared with Smp24. This is in good correlation with the MD simulations showing an overall decrease in the binding energy with the neutral bilayer for all the truncated peptides. Furthermore, the interactions with the bilayers were also shown to be shifted away from hydrophobic interactions which have previously been indicated to be a key driver in the haemolytic activity (228). All three peptides had a relatively similar  $\Delta G$  when inserted into the neutral bilayer which corresponds with Smp14a and Smp18 also having similar molar based  $HC_{50}$  values. Smp20 deviates from the others, but this could be explained by the general loss of activity in addition to the change in selectivity.

The cytotoxicity levels against the two cell lines are very close between Smp24, Smp18 and Smp14a. However, when taking the change in their size into account the toxicity is somewhat reduced for both the truncated peptides compared to Smp24. Still, when considering the improved antimicrobial activity of these two peptides, it does indicate that the overall selectivity has been somewhat improved even against the HEK293 and HepG2 cell-lines.

One interesting observation is that Smp14a shows a lower maximum toxicity response than the other peptides in the cell culture assays. However, rather than this being due to an actual lower toxicity response it is more likely due to aggregation of the peptide. Smp14a has a higher ratio of hydrophobic residues than the other peptides due to removal of polar tail which could lower its solubility and even though its charge is

higher than Smp24 and Smp20, aggregation could likely occur at higher concentrations if the media has a relatively high ionic strength.

#### 6.2.6 Use of MD simulation for the design of truncated AMPs

Like in the previous chapter the use MD simulations relies on several assumptions, both inherited from the differences between synthetic bilayer models and bacterial cell membranes and from the differences between simulations and experimental observations. However, the assumptions that need to be made are even greater when it comes to predicting the behavior of a novel compound rather than contextualizing already obtained observations. The prediction of whether the new truncated analogs were likely to retain the antimicrobial activity of the parent peptide was based on the simulated inserted state of the peptides, prior to the pore formation itself. As previously mentioned, the presence of this state has been demonstrated for many helical amphiphilic AMPs using solid-state NMR (13) and many models created to describe the mechanism of action of AMPs includes this state as an intermediary state between the free peptide and the membrane disruption (15, 229). If these models are true, the ability for an AMP to adopt this state would be a critical aspect for achieving the endpoint of membrane disruption and thereby cell death. Therefore, the assumption is that if the conserved primary helical region of the peptides behaves similarly to the parent peptide the likelihood of the new analogs retaining their antimicrobial properties are higher than if they do not. However, this assumption does not consider any secondary targets of the peptides or how the truncations would affect the pore formation itself. Furthermore, there are also several examples of peptides with antimicrobial activity which do not adopt a helical inserted state (230), so this state is clearly not necessary in all cases.

The fact that the truncated Smp24 analogs do retain antimicrobial activity even after a significant reduction in their size could suggest that the predictive ability of the models was reasonable, but to say with a higher degree of confidence we would also need to demonstrate the ability of the simulations to predict when the activity of a new analog would be lost. Simulation of the first designed analog (Smp21) showed that the helical region of this peptide did not retain the behavior of the parent peptide, if this peptide

also had been evaluated *in vitro* and if it showed a significant reduction in the antimicrobial activity the validation of the assumptions made in the model design would have been much improved.

#### 6.2.7 Evaluation of the antibiofilm properties of the truncated peptides

In addition to their broad antimicrobial activity, AMPs have several other characteristics that make them attractive alternatives to the standard small molecule antibiotics. One of these is their potential ability to better combat biofilm related infections due to secondary mechanisms of action targeting some step in the biofilm formation process (231). This is also the case for Smp24 which has previously been shown to be able to inhibit biofilm growth at the MIC concentration of certain *E. coli* species (232). As mentioned previously, treating biofilm related infections is a massive healthcare challenge, so ideally the antibiofilm properties of an AMP should also be considered during the drug development process.

To help estimate if further evaluation of the biofilm inhibitory properties of Smp24 and the truncated analogs would be necessary the peptide sequences were run through the dPaBBs server (233). This server uses two machine learning models trained with two datasets, a positive dataset containing peptides with known antibiofilm activity and a negative one containing peptides associated with quorum sensing. Using these two models a score has been generated for Smp24 and each of the truncated peptides, indicative of the likelihood for each of them to possess antibiofilm activity. For the SVM score a positive value indicates that the peptide is biofilm-active with a greater value indicating higher certainty while the WEKA probability indicates the probability of antibiofilm activity from 0-1 (table 6.14).

While the SVM score for Smp24 is positive the WEKA probability is relatively low, thus giving no decisive prediction of whether the peptide would have anti-biofilm activity or not. However, with the next two truncations a stepwise increase in both values is seen, with Smp18 being predicted to have a high probability of having antibiofilm activity. However, with the final truncation down to Smp14a a large discrepancy between the two predictions models can now be seen, with the peptide having the lowest SVM score of all the peptides while the WEKA probability is still relatively high.

As the predictions indicated that some of the peptides were likely to have antibiofilm properties, this activity was tested *in vitro* using biofilm inhibition assays. *S. aureus* and *E. coli* biofilms were grown in media containing peptide concentrations around and below the MICs, followed by quantification of the cell viability and biomass using resazurin and crystal violet stains respectively (figure 6.15).

In most cases almost complete inhibition was seen at concentrations at or above the MICs, with the only exception being for Smp18 against *E. coli*. However, below the MICs clear differences in the inhibition curves can be seen between the two species. Against *S. aureus* all peptides show a significant reduction in the biofilm formation at 1/2 X MIC with Smp24 also showing a slight reduction at 1/4 X MIC, however at concentrations below this level no significant biofilm inhibition was observed ( $P > 0.280$ ). For all peptides except for Smp18, the reduction in cell viability and biomass follows each other closely, whereas for Smp18 the biomass is slightly lower than the cell viability at the lower concentrations.

Against *E. coli* all the peptides show a consistent difference between the inhibition of the cell viability and the biomass, with the biomass reduction being greater. In all cases biomass initially increases but then reaches a local minimum at 1/8 X MIC, with all peptides except Smp14a achieving greater than 50% reduction relative to the control. At concentrations below that point the biomass increases in a concentration dependent manner reaching around 80-86% of the control at 0.5 µg/ml. The cell variability curves run in parallel with the biomass curves although in most cases the local minimum at 1/8 X MIC is less pronounced. For all peptides the cell variability reaches close to 100% at the lowest concentration. The biofilm inhibition of Smp14a deviates the most from the other three peptides. At 1/2 X MIC the highest values for both the biomass and the cell variability were achieved, with the cell variability reaching almost 150% of the control.

To evaluate if the effect on the biofilm formation could be explained by the peptides affecting the growth rate below the MIC concentrations, growth curves were made for *E. coli* using the same conditions as used in the biofilm inhibition assay (data not shown).

In some cases, the initial growth rate was lower for samples at 1/2 X MIC but below

that there were no consistent concentration dependent differences in the growth rates for any of the peptides.

**Table 6.14 Anti-biofilm prediction scores for Smp24 and the truncated peptides.** \* C-terminal amidation not accounted for in calculations.

Name	SVM score	WEKA probability
Smp24	0.45	0.35
Smp20	0.80	0.47
Smp18	1.41	0.85
Smp14a	0.25*	0.71*

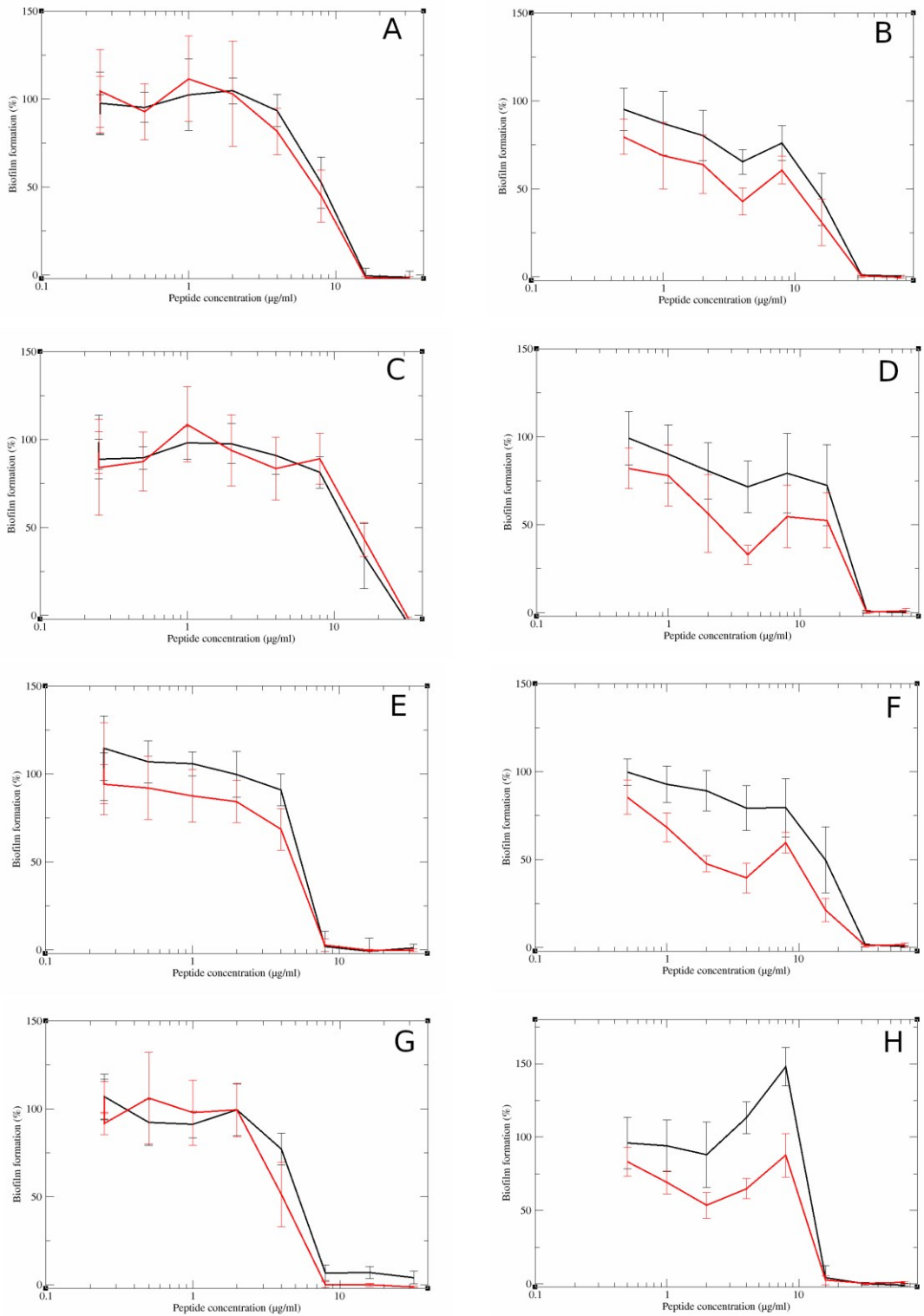


**Figure 6.15 Biofilm inhibition caused by Smp24 and the truncated peptides at different concentrations relative to untreated controls. Black = resazurin stain, red = crystal violet stain. A,C,E,G = *S. aureus*, B,D,F,H = *E. coli*. A,B = Smp24, C,D = Smp20, E,F = Smp18, G,H = Smp14a. N=1, n=8**

#### 6.2.6.1 Computer aided design of antibiofilm peptides

Due to the range of proposed mechanisms of action for the biofilm inhibition it is impossible to define a specific molecular level target that forms the underlying basis for the observed activity. Therefore, structure-based design approaches using tools such as MD simulations cannot easily be applied, to predict the antibiofilm properties of a novel peptide. Instead, sequence-based approaches have been developed that utilize machine learning in order to predict the activity of new or modified AMPs, such as with the dPaBBs server (233). This approach has a lot of limitations, as it does not consider the higher order structure of the peptide, is not based on a specific mechanistic relationship and does not account for the differences in the biofilm formation between different bacteria species. In the case of the dPabbs server, the result of the model also only relates to a prediction of whether the peptide has any antibiofilm activity or not and not if the activity is improved compared to another peptide.

The dPaBBs server uses two models based on different machine learning tools to predict the antibiofilm properties of peptides, however for the 4 peptides tested the results were not consistent between the two models. The SVM model predicted that all peptides would have antibiofilm activity, which corresponded to the observations in the biofilm inhibition assays, with the WEKA model only giving Smp18 and Smp14a more than a 50% chance of having antibiofilm activity. In addition, the two models disagreed with the effect the full truncation down to Smp14a would have on the probability.

These inconsistencies in the results from the models together with the binary nature of the result call into question how useful the server is in the design of new AMPs. For the purposes of an iterative design approach, such as that done with the truncation of Smp24, a more sophisticated output from the models would be necessary if the objective of the development were to improve the antibiofilm properties of the new variants. Ideally the output would give insight into if the activity of a modified peptide would be likely to have improved or not. With the current output, an increase in the likelihood of an analog having antibiofilm properties is not that useful for peptides such as Smp24 which are already known to have antibiofilm properties.

The models could still be useful as a secondary screening tool during the developing

process, highlighting if any modifications induce a drastic shift in the predicted properties, such as an analog suddenly having a very low probability of having antibiofilm activity. In such a case it could serve as an indication that *in vitro* evaluation of the antibiofilm activity would be necessary before further iteration is done on the new analog. Otherwise, the server might mostly be useful for predicting the properties of a large library of peptides with very different amino acids composition, where the properties of the individual peptides are more likely to deviate than for closely related analogs.

#### 6.2.6.2 Mechanisms of peptide mediated biofilm inhibition

The differences in the *in vitro* biofilm inhibitory activity of the peptides are much more dependent on the bacterial species than the structural differences between the peptides. Against *S. aureus* the inhibition only occurs consistently at 1/2 X MIC while against *E. coli* inhibition of especially the biofilm mass can be observed all the way down to 1/64 X MIC. The reduced biofilm formation against *S. aureus* at 1/2 X MIC could be due to a more general inhibition of bacterial growth at this peptide concentration and not directly mechanistically related to the inhibition of pathways of biofilm formation, whereas the concentration dependent response against *E. coli* strongly suggests that the peptide directly interacts with the biofilm formation in some way. Gram-negative and Gram-positive bacteria species have significant differences in the molecular components involved in the biofilm formation, starting at the beginning of the process with differences in their attachment due to the presence of LPS or teichoic acid, to differences in signalling and regulation due to differences in quorum sensing molecules with Gram-negative bacteria producing acyl-homoserine lactones and Gram-positive species producing autoinducing peptides (234). These molecular level differences could explain why the response to the peptide differs so drastically between the two bacteria species.

Two important observations can be made related to the biofilm inhibitory properties of the peptides against *E. coli*. Firstly, the biomass of the biofilm is consistently reduced to a much greater extent than the cell viability. This indicates that the primary mechanism of biofilm inhibition is related to the production of the extracellular matrix rather than the direct killing or inhibition of the cells within the matrix. The degree of

cell viability reduction that is still seen could be a downstream effect of the reduced matrix limiting the number of cells that can be positioned in the smaller biofilm volume. However, since AMPs can interact with the biofilm formation process in a variety of ways, multiple mechanisms of actions could likely still be taking place at the same time.

Secondly, the shape of the curve is not what would be expected for a direct concentration dependent relationship. At peptide concentrations below  $1/4 \times \text{MIC}$  the curve is linear (relative to  $\log(\text{Dose})$ ) as expected for a dose-response curve between the max and minimum response. However, between  $1/4 \times \text{MIC}$  and  $1 \times \text{MIC}$  the biofilm growth often seems higher than expected. This could be explained by two opposite peptide induced effects affecting the biofilm growth at the same time, an inhibitory effect that occurs at all peptide concentrations and a growth inducing effect at  $1/2$ - $1/4 \times \text{MIC}$ . Antimicrobial compounds such as ampicillin and triton X-100 that cause cell lysis and thereby release of intercellular DNA and RNA, have previously been shown to induce an increase in biofilm formation for *Enterococcus faecalis* at sub inhibitory concentrations (235). A similar effect could be present for Smp24 and the truncated peptides where at  $1/2$  and  $1/4 \times \text{MIC}$ , the peptide concentration is still high enough to cause some cell lysis or membrane disruption, releasing intercellular DNA and RNA and thereby inducing increased biofilm formation. At the same time a different mechanism could also cause a concentration dependent inhibition of the biofilm formation. At  $1/8 \times \text{MIC}$  the threshold peptide concentration for inducing biofilm growth is likely no longer reached. However, the biofilm inhibitory mechanism still occurs, leading to an overall greater reduction in biofilm growth than at  $1/4 \times \text{MIC}$ .

The bacterial response to Smp14a deviates the most from the other peptides. It is the only peptide that does not reach more than 50% biofilm inhibition at  $1/8 \times \text{MIC}$  against *E. coli* and the induced biofilm growth at  $1/2 \times \text{MIC}$  is much larger than for the other peptides. These differences could be due to the large structural change between Smp14a and the other peptides, with the complete removal of the polar tail region. Bose et al used machine learning to analyse a dataset of 242 antibiofilm peptides and found that the most important distinguishing characteristics of the antibiofilm peptides was the alternation between charged and hydrophobic groups (236). The presence of both the charged tail and more hydrophobic primary helical regions could

represent such an alternating motif, improving the biofilm inhibition compared with the primary helix only. Furthermore, the tail region has already been hypothesised to be involved in the binding between Smp24 bacteria secreted molecules such as siderophores (194), it could also be involved in binding to molecules related to biofilm formation.

#### 6.2.7 Biophysical evaluation of the pore formation

The last step in the evaluation of the new truncated analogs was to investigate if the truncations had affected the mechanisms of peptide induced pore formation. Like in the earlier chapter, the mechanisms of the membrane disruption were investigated using planar patch clamp with synthetic bilayers. However, some changes were made to the experimental parameters in this round of experiments.

Firstly, a few steps were taken to increase the success rate of the bilayer formation and improve its stability, leading to an increased experimental throughput. Firstly, the 1,2-dioleoyl-sn-glycero-3-phosphor type lipids (DOPX) were changed to the 1,2-diphytanoyl-sn-glycero-3-phosphor type lipids (4ME 16:0 PX). These lipids are more commonly used for synthetic bilayer for patch clamp experiments due to the improved stability and high membrane resistance (237). In addition, the buffer solutions were adjusted with  $\text{Ca}^{2+}$  ions, thought to improve the binding between the bilayer and the glass surface of the chip (238).

Secondly, to limit the total number of experimental runs needed, the peptides were only analysed at a single concentration each. For the optimal evaluation, the concentration needs to be high enough to consistently induce conductance events, however not so high that the bilayers are completely disrupted too soon in the recording. In addition, it would also be ideal if the concentrations could be adjusted to take into account the intrinsic differences in the dose-response of the peptides, as it is the mechanism of action that is investigated not the activity. Therefore, following some initial tests the final concentrations of 32  $\mu\text{g}/\text{ml}$  for Smp24 and Smp20 and 16  $\mu\text{g}/\text{ml}$  for Smp18 and Smp14a were chosen, corresponding to their MIC against *E. coli*. Lastly, due to the significant changes in the activity of the truncated peptides against

erythrocytes, the mechanisms of action of the peptides were also tested against a neutral PC:PE bilayer.

Like with the previous evaluation of the concentration dependent response of Smp24, the current traces were analysed both in relation to the kinetics of the membrane disruption and qualitative categorisation of the individually observed events in accordance with Chui et al. (105).

The time between the addition of peptide to the bilayer and the occurrence of the first current event and the time point where complete/irreversible membrane disruption occurred was calculated (figure 6.16). In some cases, no irreversible disruption occurred within the measurement period and as such in those cases the maximum timepoint of 80 minutes was used instead. For all peptides and both bilayer types, a high degree of variability was seen within each group of repeats. Therefore, further statistical modelling was utilised to evaluate any potential differences.

One aspect of the experimental setup that could contribute to the high variation could be differences in the biophysical properties of the individual bilayer. While factors such as the overall lipid composition and vesicle production parameters were kept constant for each type of bilayer, only a single bilayer is utilized in each experiment. Even within the same batch of vesicles the properties of each bilayer can vary slightly in aspects such as the lipid packing/order. In order to take this into account the baseline current was measured over 40s at the start of each experiment before the peptide was added. This baseline current was included in the statistical modelling as a covariate for each experiment.

The effect of the peptide and bilayer type on each of the kinetic responses was analysed using ANCOVA modelling. None of the variables had a significant influence on the time till the first event occurred ( $P > 0.05$ ) but the peptide type ( $P = 0.0347$ ) did significantly impact the time till irreversible membrane disruption.

Further post-hoc analysis was carried out using TukeyHSD showing that Smp20 is the biggest outlier although none of the specific comparisons were statistically significant ( $P_{\text{Smp20-Smp14a}} = 0.085$ ,  $P_{\text{Smp20-Smp18}} = 0.052$ ,  $P_{\text{Smp20-Smp24}} = 0.090$ ).

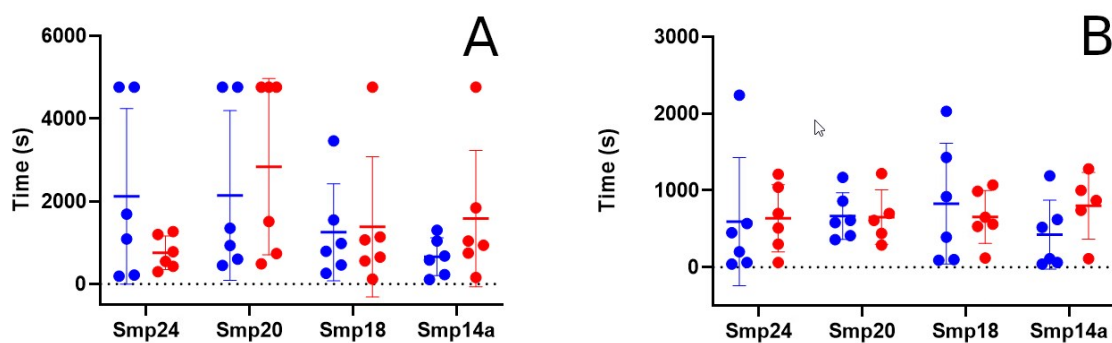
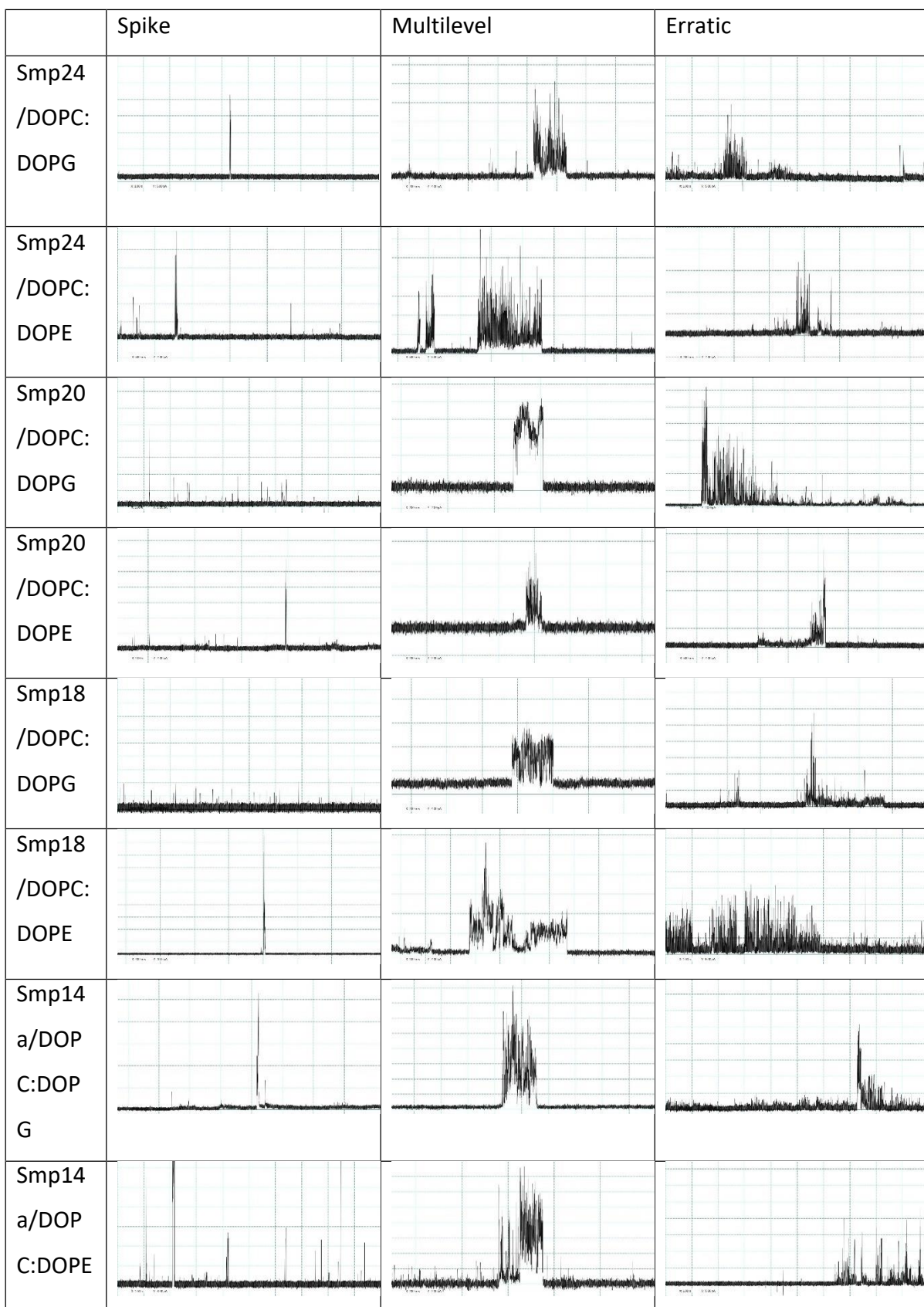


**Figure 6.16 Kinetics of pore formation observed for Smp24 and the truncated peptides during the patch clamp experiments with both negative and neutrally charged bilayers.** A = Time between addition of peptide to the bilayer and the occurrence of an irreversible disruption of the bilayer resistance. B = Time between the addition of peptide to the bilayer and the observation of the first conductance event. Blue = negative bilayer consistent of 1:1 4ME 16:0 PC:PG, red = neutral bilayer consistent of 1:1 4ME 16:0 PC:PE.

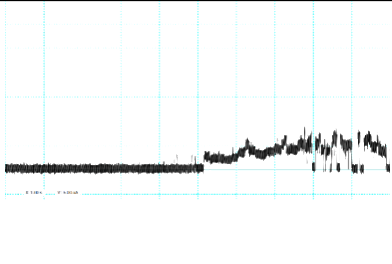
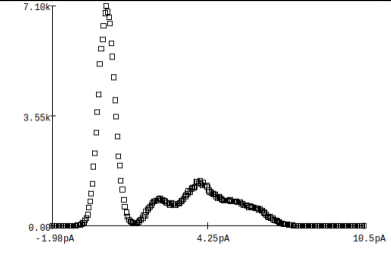
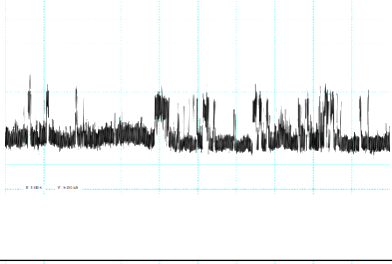
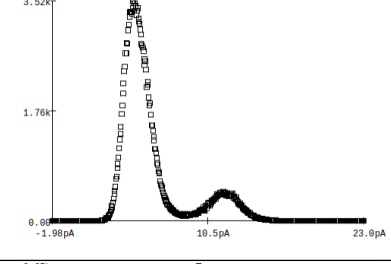
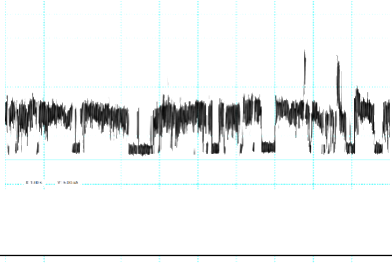
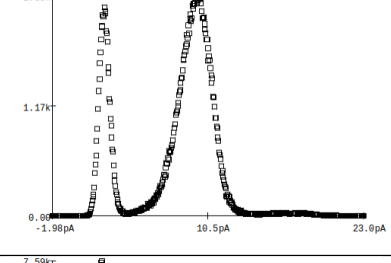
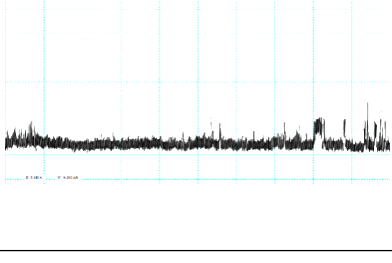
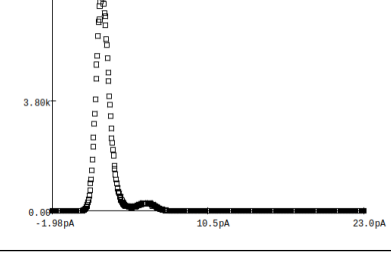
The qualitative analysis was carried out by characterising the individual current events from all the experiments, with 4 different general event types being found. As in the previous set of experiments with Smp24 and the DOPC:DOPG bilayers, spike, multilevel, and erratic conductance events dominated the current traces. Each of these three event types was observed at least once for all the peptide-bilayer combinations (table 6.15). In addition, spike events were again the first event to occur in the majority of experimental runs.

However, on rare occasions an additional previously unseen event type was also observed in this set of experiments, namely the flickering event type (table 6.16). Like for the spike and multilevel event types, individual flicker events also have a distinct beginning and end although the lifetime of each flicker can both be short like the spike or longer like the multilevel event. Thus, the distinguishing feature of flicker events relative to the other event types is their conductance rather than the shape of the current increase. Not only do individual flicker events only have one or two distinct conductance levels across their lifetime, when multiple flicker events occur in a row, they will all share similar conductance levels. Still, when comparing multiple experimental runs no consistent conductance level was found, with the average current for the events being 4.761 pA (Smp18), 7.692 pA (Smp20) and 3.289 pA (Smp20).

**Table 6.15** Examples of the spike, multilevel and erratic event types observed in the current traces for the different experimental combinations used in the study. All three event types were observed for all peptides with both bilayer types in at least one experimental run.



**Table 6.16 Examples of the current traces and corresponding amplitude histograms for the flicker event type.**

	Flicker	Amplitude histogram
Smp18_6		
Smp20_5		
Smp20_5		
Smp20_6		

Due to the large variation in the length of the period where distinct current events can be observed and the difficulty in distinguishing between what is a long single event vs multiple shorter events, direct comparison of the raw number of events between the different peptides is not straight forward. Instead, the different peptides were compared based on how many runs the different events occurred in (figure 6.17).

When added to the negative bilayer all the peptides except Smp20 have both spike, multilevel and erratic events occurring in all 6 runs. Those three event types were also the most consistently seen events for Smp20, although not in every run. Flicker events were by far the rarest event type, only seen in two Smp20 runs and one Smp18 run.

With the neutral bilayer the occurrence of the different event types is less consistent, however for all peptides spike, multilevel and erratic events occur at least once. No flicker events were observed using the neutral bilayer.

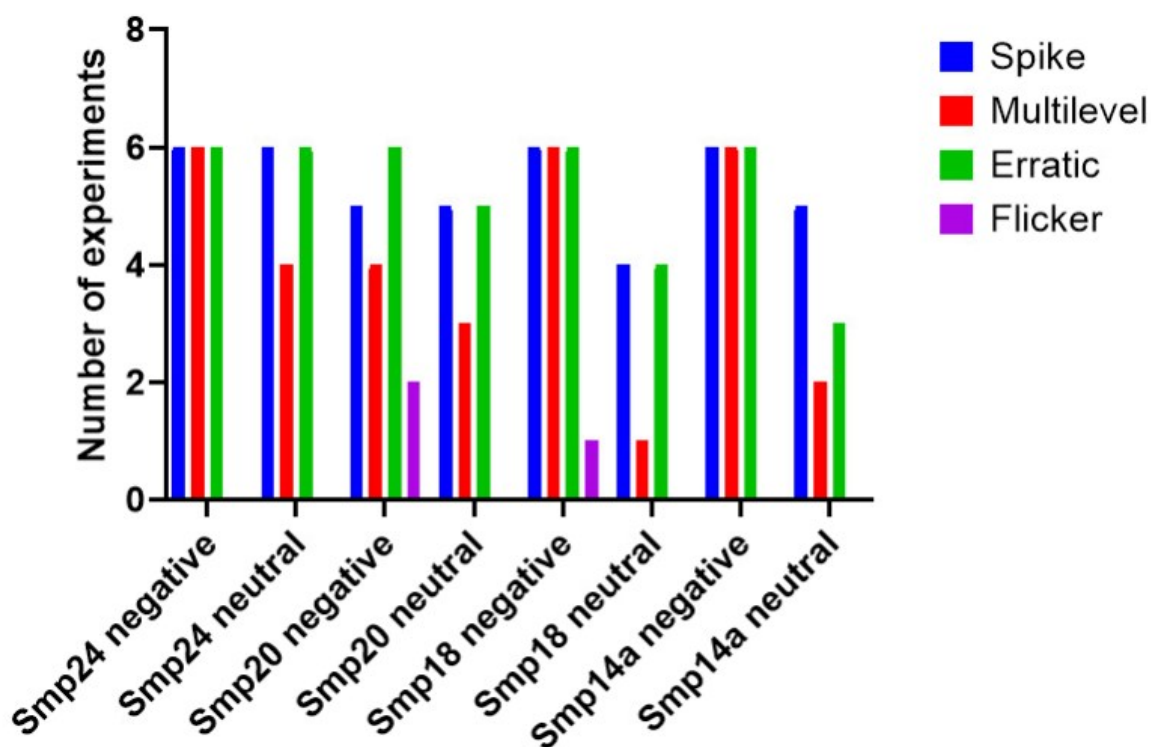


Figure 6.17 Overview of the number of experiments where each event type occurred for the different peptides and bilayers.

### 6.2.8 Effect of the truncations on the mechanisms of pore formation

While the biological results indicate that activity of the truncated peptides was not lost, it would not necessarily mean that the mechanism of action was unaffected. The reduced activity of Smp20 and slightly improved activity of Smp18 and Smp14a could be both cases be downstream effects from changes to how the peptides interacts with the bilayer during the pore formation. If such changes were observed, they could give valuable insight into the function of the truncated regions in Smp24 leading to an improved SMR which could aid in future designs. If no changes were observed, it would indicate that the truncated regions were not critical to the SMR and therefore further validate their selection as targets for truncation.

The kinetics of the membrane disruption and first conductance events follow similar trends as observed in the previous experiments with Smp24, especially in terms of the high degree of variation between individual experimental repeats. However, when considering that the peptide concentrations used in this set of experiments were considerably higher than even the maximum Smp24 concentration from the earlier chapter, the kinetics are much slower than would be expected. This can be explained by the change of lipid types used to form the bilayers. As seen from the kinetics, the 4ME 16:0 PX bilayers are much more stable than DOPX bilayers allowing for consistent evaluation of individual pore structures even at the elevated peptide concentrations. This is especially useful in this case where multiple peptides were evaluated, as it allowed for the evaluation of each peptide at one concentration without the need for extensive optimisation of the experiment's conditions for each peptide type.

The statistical evaluation of the membrane disruption kinetics did indicate that the peptide type affected the kinetics somewhat with the biggest difference being between Smp20 and the other peptides. Still, the overall similarity in the kinetics between most of the peptides indicate that the activity-concentration corrections made were relatively successful, meaning that the activity conditions were close enough between the peptides that their current traces could be compared in a qualitative way. If one change were to be made, it would have been to increase the Smp20 concentration somewhat, considering its consistently reduced activity in all of the biological assays. However, enough individual events were still seen for Smp20 to reasonably compare the mechanism of action with the other peptides.

A somewhat surprising observation related to the kinetics was that the bilayer composition did not show a significant effect even though the same peptide concentrations were used for both bilayers. Previous experiments have shown that Smp24 has higher selectivity towards negatively charged lipids resulting in a higher leakage from DOPC:DOPG vesicles compared to DOPC:DOPE (58). The increased selectivity for the truncated peptides towards prokaryotic cells suggests that this also would be the case for them. However, in the patch clamp experiments the kinetics and the probability for no irreversible membrane disruption to occur are almost the same. These discrepancies could be explained by a concentration dependency of the selectivity. The concentration of Smp24 used in these experiments was around 6-10

times greater than in the liposomal leakage experiments, which will likely greatly diminish any bilayer specific differences. However, the use of higher concentrations was needed in order to achieve consistent membrane disruption and therefore a greater number of events to analyse for the qualitative investigations.

When comparing between the two bilayer types for the individual peptides, the kinetics of Smp24 deviates from the rest. Its membrane disruption kinetics with the neutral bilayer were faster than for the other peptides which could be correlated with the lower membrane selectivity of the peptide as seen with its high haemolytic activity. However, it is still surprising that the kinetics were overall faster with the neutral bilayer compared with the more bacteria like negative bilayer. This could be due to intrinsic differences in the stability of the two bilayer types. The PE type lipids added to the neutral bilayer have a different shape than the PC or PG lipids, which could affect the elastic stress within the bilayer (239). Thus, even if the peptides are less selective towards the neutral bilayer, the conditions needed to induce complete disruption might still be reached more easily for other reasons.

In terms of the qualitative analysis of the conductance events there are also no significant differences between the two bilayer compositions. In both cases three event types (spike, multilevel and erratic) were by far the most dominant. However, in previous biophysical experiments some qualitative differences have been seen in how Smp24 affects bilayers depending upon their composition. Using AFM Smp24 was shown to create distinct pores of different sizes when added to DOPC:DOPG bilayers, while with DOPC:DOPE bilayers it instead created defect patterns which could eventually develop into holes in the bilayer at higher concentrations (58). As planar patch clamp can only measure changes in the bilayer that leads to a significant difference in the conductance, non-destructive effects on the bilayer such as membrane thinning, or de-mixing cannot be adequately investigated. Furthermore, as previously described, the small size and free-standing nature of the bilayers only allows for investigation of the early stages of the membrane disruption, contrary to the larger disruptions seen with AFM. Nevertheless, the previous results would indicate that the membrane disruption of a DOPC:DOPE bilayer should be less dominated by the formation of distinct pore structures. As the morphology of the observed event types are in complete agreement with the previous observations for Smp24 alone, the

proposed molecular level structures corresponding to the conductance increases should still be the same for the new bilayer types and new peptides. Therefore, based on the AFM results, one could expect to see a shift towards the erratic event type being the more dominant event type for the DOPC:DOPE bilayers. While all event types occur less consistently with the DOPC:DOPE bilayers, multilevel and flickering events do see the largest reduction in the consistency, indicating that stabilised pores are less likely to occur. The presence of spike events is still slightly more consistent than erratic events, but they are also by far the most frequent event type when comparing all the experiments. Another interesting observation is that the likelihood of an erratic event being the first observed event of a run also sees an increase from 25% to 46% when changing to the DOPC:DOPE bilayer. Taken together these observations could suggest that the distribution of the event types could be shifted towards an increased likelihood for erratic events to occur, but further experiments at different concentrations would be needed to confirm this.

The structural predictions from the MD simulations also correlate well with there not being any dramatic difference in the pore formation mechanisms. While the peptides do not insert into the DOPC:DOPE bilayers with the same consistency, if full insertion is achieved the structure and position of the individual peptides is very similar for both bilayer types. The main difference lies in the relative binding energies, but this would mainly affect the thermodynamic driving force for inserting into the DOPC:DOPE bilayer and not necessarily the pore formation itself. Based on the structure and position of the peptides, relatively similar local conditions for the pore formation and stabilisation should be possible for both systems. However, on a macroscopic scale a much greater diversity in peptide structure and insertion level would likely be prevalent in the DOPC:DOPE system. If assumed that the peptide needs to be in the helical configuration to best support the formation and stabilization of toroidal pores, the greater structural diversity would shift towards spike events and more generalized erratic membrane disruption.

The truncation of Smp24 did not change that the spike, multilevel and erratic events were the dominant event types. This indicates that reductions to the peptide size done in this study were not great enough to significantly change the mechanism of pore formation and early-stage membrane disruption.

In the case of the truncation of the tail and linker regions, these results corroborate the observations related to the simulations of the pore associated configurations of Smp24. In all cases, the peptide-pore configurations suggested that the tail region operated relatively independently of the pore and therefore it was deemed unlikely that it had much effect on the pore structure.

Predicting the effect of truncating the secondary helix was more complicated as it constitutes two structural changes that could be more likely to impact the mechanism of action. Firstly, it removes the kink in the helical region, thought for other AMPs to modulate how they associate with the pore structure and affect the activity (199, 200). The second aspect is the reduction of the overall length of the helical region which has also previously been shown to affect activity (240). However, as previously highlighted, the structure of the kink in Smp24 is somewhat unique compared with other AMPs. While the sequence position of the proline residue that induces the kink between the primary and secondary helix is consistent with other AMPs of similar length such as melittin or magainin 2, the second half of the Smp24 peptide has a much lower degree of helicity. It has previously been indicated that the effect of shortening the helix length of AMPs mainly works in threshold dependent manner, likely related to the ability of the peptides to span the thickness of the bilayer (240). Thus, if the helical regions of Smp24 were already too short to span the bilayer, as seems to be the case based on the MD simulations of Smp24, further reduction would not alter this and therefore no threshold length has been crossed by the truncated designs. Furthermore, even if this is the case, the short secondary helix could also make the impact of the kink motif much less significant.

These factors could explain why the impact of truncating the secondary helix was relatively minor both in terms of the mechanism of action and the overall activity level. While the previous MD simulations of the Smp24-pore configurations did indicate that the kink aided in the favourability of the pore interface associated structures at low peptide to lipid ratio, for the more extreme configurations at the higher peptide concentrations it seemed less critical. Therefore, pore formation and stabilisation still occur even if the secondary helix is truncated. The removal of the kink likely modulates how likely it is that a peptide is positioned around the pore interface as its ability to

adapt to the bilayer curvature is probably somewhat reduced, but this is not enough to completely change the mechanism of action or remove its antimicrobial activity.

One interesting observation for the truncated peptides is the occurrence of flickering events, although they were much rarer than the other types. The relatively consistent conductance level for both the individual events and between multiple events suggests that the molecular level pore structure responsible for these events is more ordered than for the other event types. Potentially indicating that Smp20 and Smp18 can form ordered toroidal pores in addition to the disordered toroidal pores and generalised membrane disruption seen for the other peptides.

There could be multiple explanations for why this additional event type is seen.

Experimental conditions can strongly affect which type of events are seen for a given peptide, such as for pleurocidin which has both been shown to predominantly form flickering events or multilevel and erratic events by different authors (83, 184).

However, the structural changes induced by the truncation could also theoretically increase the likelihood of the formation of more ordered peptide-pore assemblies.

Sengupta et al have previously highlighted the theoretical differences between the classical toroidal pore model and the disordered toroidal pore model (209). The disordered toroidal pore model requires the peptides to align with the high bilayer curvature near the opening of the pore and therefore favours high flexibility in the helical region, such as that induced by a kink motif. However, in the classical toroidal pore model the peptide adopts a transmembrane orientation within the centre of the pore, where the degree of peptide flexibility could be less important. Therefore, by removing the secondary helix, the truncated peptides could be pushed towards the formation of more ordered pore structures.

Overall, no clear link can be established between the qualitative aspects of the mechanism of pore formation/membrane disruption and the differences seen in the activity and toxicity for the truncated peptides relative to Smp24. This again highlights the complexity and multifaceted nature of the mechanism of action of AMPs, with pore formation only making up one aspect of the complete biological response to these types of peptides. Other aspects such as the initial peptide membrane interactions, peptide insertion, non-conductive peptide induced changes to the

membrane and secondary binding targets also play a key role in the activity and selectivity of the peptides.

### 6.3 Conclusions

The relatively large overall size of Smp24, high proportion of random coil structure in membrane mimicking systems and presence of multiple structural regions which were predicted to have limited impact on bacterial membrane binding, were all indications that truncation of the peptide sequence without significant loss of activity could be possible. Therefore, truncation of the peptide sequence was performed in a rational, stepwise fashion aided by MD simulations throughout the design process to ensure that the predicted behaviour of the conserved regions did not change in an unexpected way compared to the parent peptide. This led to the development of three novel truncated analogs, which were evaluated both *in silico* and *in vitro*. The two smallest analogs showed similar to slightly improved antimicrobial activity to the parent peptide, without affecting the cytotoxicity against secondary cell lines. In addition, all truncated analogs showed significantly reduced haemolytic activity and all peptide, including Smp24, showed the ability to reduce biofilm formation below their MICs. Biophysical evaluation via patch clamp experiments indicated that the truncations did not significantly affect the early-stage mechanism of membrane disruption/ pore formation, with the pores remain mostly disordered in nature although some examples of more ordered conductance events were also seen.

## 7. Optimisation of the primary sequence of Smp14a

### 7.1 Introduction

Setting out in the development process of Smp24 three main objectives were identified as reduction of the size of the peptide, improvement of the antimicrobial activity and improvement of the selectivity. With the development of Smp18 and Smp14a all three objectives were at least partially addressed, however further improvements to the therapeutic index were still deemed possible.

Both Smp18 and Smp14a have different advantages, making them promising candidates for further development. Smp18 has an interesting structural motif in the hydrophilic tail region and has shown promising anti-biofilm properties, while Smp14a has a smaller size and slightly improved antimicrobial activity.

In the end, Smp14a was chosen for further development for two main reasons. Most of the sequence of Smp14a is fully conserved in Smp18 and as such any residue substitutions leading to improvements in the properties of Smp14a could be transferred to Smp18 with a reasonable expectation of a comparable change in properties. This could significantly speed up any future development of Smp18 and allow for the focus to be on the more unique tail region. Secondly, the fully helical structure of Smp14a is also much more analogous to the structure of other AMPs of similar size. Therefore, knowledge gained related to the structure activity relationship of Smp14a could be more easily applicable to other peptides.

#### 7.1.1 Design of the first generation Smp14a analogs

The initial step in the design process was to identify different sites along the sequence where substitution of a residue could improve the properties of the peptide. This was mainly done based on the MD simulations described in chapter 5&6, supplemented with previously published findings regarding mutations of Smp24 and other AMPs. Three general design strategies were formulated, mainly focusing on affecting the early stages of the mechanism of action.

Improvement of hydrophilic/charged interactions between the peptide and bilayer:

From the previous results it was identified that electrostatic interaction between the peptide and bilayer were largely responsible for both the initial interactions with the bilayer and a major driving force for the insertion equilibrium. Therefore, the non-ionic residues along the structure, which after full insertion were oriented towards the lipid headgroups/solute, were identified as sites where residue substitution could be done. The RDFs shows that the serine3 residue already takes part in interaction with the lipid phosphate groups, however the per-residue breakdown indicates that the energy contribution of the serine residue is more than 30 times smaller than for the cationic lysine residues. This suggests that substituting the serine residue to a cationic residue could greatly improve the interactions. The serine to lysine substitution seemed to be the most obvious one as it is in line with the rest of the peptide composition and has previously shown promising results for Smp24 (149). In addition, the serine to histidine substitution was also evaluated. Even though histidine is not fully protonated at physiological pH the protrusion length of the sidechain is closer to serine, which could be a factor affecting the insertion as the 3 position is inserted within the bilayer in the early stages of the insertion process.

Further functionality could also be added to the peptide via the substitution. A histidine residue in the third position from the N-terminal is the key feature of the structural motif called the amino-terminal copper and nickel (ATCUN) binding unit. As the name suggests, this structural motif allows the peptide to bind Cu(II) ions which can be involved in the generation of reactive oxygen species (ROS), leading to cell damage. AMPs have previously been modified with ATCUN units in order to utilise the selectivity of the AMP and the oxidative properties of Cu(II) to improve the overall antimicrobial efficacy, with varying degrees of success (112, 241, 242).

Another polar residue positioned towards the lipid headgroups is threonine10, however the RDF indicates that the interactions of the native residue with the phosphate groups are minimal. Instead thr10 forms a relatively consistent hydrogen bond with the backbone carbonyl group of Ile6 and thus could be important for structural stability of the helix. In this configuration the methyl group of the sidechain is positioned upwards, away from the lipids and thus contributes minimally to any hydrophobic interactions.

The increased reach of a lysine substitution could allow the residue to interact with the lipid phosphate groups and the positive charge could improve the strength of the

interaction.

In addition, a substitution to Ser was also performed in order to evaluate minor optimisation of the structure. The per-residue decompositional analysis of the binding energy for Smp24 revealed that the Van der Waals energy component for thr10 was not significantly greater than for the two serine residues (-2.281 kcal/mol vs -2.210 kcal/mol and -2.510 kcal/mol) and thus in thermodynamic terms the additional methyl group of the threonine residue does not seem to improve the binding. Substitution with serine would reduce the overall size and hydrophobicity of the peptide.

#### Improvement of hydrophobic interactions between the peptide and bilayer:

Another way to improve the binding could be by increasing the hydrophobic interactions. Therefore, residues which were oriented towards the centre of the bilayer were identified and substituted for residues with larger hydrophobic sidechains. However, quantification of the overall hydrophobicity of the different hydrophobic amino acids is not a simple matter. Multiple different scales have been made, ranking the hydrophobicity of the 20 common amino acids and often there is a significant difference when comparing the internal rankings of the most hydrophobic residues such as Leu, Iso, Phe and Trp. These variations are due to differences in the underlying experimental methodology and observations used to formulate the individual scale (243). Therefore, for the modification aimed at increasing the hydrophobicity of the peptide two residues were chosen, phenylalanine and leucine, which also differ in the overall structure of the sidechain.

Isoleucine 1 faces the core for the bilayer both during and after insertion and is therefore one of the residues where the hydrophobic interactions might have the largest impact on the activity. As Ile is already relatively similar to Leu, so only a substitution to Phe was made.

Both Ala8 and Ala9 were identified as potential modification targets but based on visual evaluation of their position in previous simulations Ala9 seems to be positioned towards the centre of the bilayer most consistently. Substitutions with both Leu and Phe were investigated.

### Reduction of potential cation- $\pi$ interactions between the peptide and cationic lipid headgroups:

The overall objective with the further development of Smp14a is not only to improve its interactions with the bilayer/membrane but also the selectivity towards bacteria. One way to achieve this could be to limit any interactions which are more specific towards the eukaryotic membrane. The previous simulations showed that the peptides often have difficulty in establishing the initial consistent interactions with the neutral bilayer which could be an avenue of the selectivity that could be further exploited. During this part of the insertion process the interactions are driven by electrostatic interactions, but these might not be limited to only the charged and polar amino acids. Previous studies have highlighted that electrostatic interactions between  $\pi$  electron systems of aromatic residues and the cationic choline and amine lipid headgroups could play a significant role for the anchoring of membrane proteins (244-246). As zwitterionic lipids are much more common in the outer leaflet of eukaryotic membranes, especially compared with the Gram-positive membrane, limiting the ability of the peptide to form cation- $\pi$  interactions could improve the selectivity. Smp14a contains two aromatic residues that could take part in cation- $\pi$  interactions, namely Trp2 and Phe13, with Trp in general being known to form stronger interactions compared with Phe (247). Therefore, Trp2 was chosen as a substitution to investigate if a reduction in the peptide's potential for cation- $\pi$  interactions could reduce the cytotoxicity. The orientation of the Trp sidechain after insertion indicated that the residue still needed to be hydrophobic and as such substitutions to both Leu and Phe were investigated, with Phe serving as a reduction and Leu as a complete elimination of the cation- $\pi$  potential of the 2nd position.

Following the first round of simulations an initial rough evaluation of the simulations was done in order to choose a few of the single residue substitutions that could be combined into dual and triple substitutions. Under ideal circumstances each single residue substitution would have been fully evaluated both *in silico* and *in vitro* before higher order substitutions would be made but due to time constraints these substitutions were done within the same drug design iteration.

The following Smp14a analogs were designed and evaluated *in silico* during the first block of simulations (table 7.1):

**Table 7.1 Overview of the physicochemical properties of the first generation Smp14a analogs.** Hydrophobic moment calculated using <https://heliquest.ipmc.cnrs.fr/>, \* C-terminal amidation not accounted for in calculations.

Name	Sequence	Mw (g/mol)	Charge at pH 7	Hydrophobic moment*
Smp14a	IWSFLIKAATKLFK- NH <sub>2</sub>	1665.07	4	0.626
Smp14a_I1F	FWSFLIKAATKLFK- NH <sub>2</sub>	1699.09	4	0.626
Smp14a_W2L	ILSFLIKAATKLFK-NH <sub>2</sub>	1592.02	4	0.596
Smp14a_W2F	IFSFLIKAATKLFK-NH <sub>2</sub>	1626.04	4	0.601
Smp14a_S3K	IWKFLIKAATKLFK- NH <sub>2</sub>	1706.17	5	0.678
Smp14a_S3H	IWHFLIKAATKLFK- NH <sub>2</sub>	1715.13	4.1	0.617
Smp14a_A9L	IWSFLIKALTKLFK-NH <sub>2</sub>	1707.15	4	0.721
Smp14a_A9F	IWSFLIKAFTKLFK-NH <sub>2</sub>	1741.17	4	0.727
Smp14a_T10K	IWSFLIKAACKLFK-NH <sub>2</sub> IWSFLIKAASKLFK-	1692.14	5	0.673
Smp14a_T10S	NH <sub>2</sub> FLSFLIKAATKLFK-NH <sub>2</sub>	1651.05	4	0.636
Smp14a_I1F_W2L	ILKFLIKAATKLFK-NH <sub>2</sub>	1626.04	4	0.595
Smp14a_W2L_S3K	ILSFLIKALTKLFK-NH <sub>2</sub>	1633.11	5	0.649
Smp14a_W2L_A9L	IWKFLIKALTKLFK-	1634.10	4	0.690
Smp14a_S3K_A9L	NH <sub>2</sub> ILKFLIKALTKLFK-NH <sub>2</sub>	1748.25	5	0.771
Smp14a_W2L_S3K_A9L		1675.19	5	0.741

### 7.1.2 In silico evaluation strategy

Due to the large number of novel peptides to be evaluated in the first round of the drug design process the range of simulations and analysis methods had to be refined. In the previous computer aided design process where Smp24 was truncated down to Smp14a, the most useful set of simulations were by far the baseline bilayer simulations (7 nm<sup>2</sup> DOPC:DOPG bilayer). The solution-based models gave very little critical information that could not also be determined from the base bilayer simulation. The information from the variant 1 simulations (DOPC:DOPE bilayer) was more useful but they had a low success rate in terms of achieving full peptide insertion making them very inefficient when investigating a larger library of peptides. The additional simulations used for the initial evaluation of Smp24 (variant 2-4) were either very complex, computationally expensive or resulted in less quantifiable data that would be difficult to use for comparisons between closely related peptides. Therefore, only base bilayer models were used in this round of simulations.

For the analysis of the simulations a focus was put on aspects that could be reduced to a single value for each simulation. For some analysis methods this such as the relative binding energy this was already the case with their previous use, while for other such as the partial density profiles an additional step was added to further refine the output.

In addition, based on the specific residue modification additional analysis method were sometimes added if more context were to evaluate the effect of changing that specific residue.

## 7.2 Results and discussion

### 7.2.1 In silico screening of Smp14a analogs

For the *in silico* design process of the first generation Smp14a analogs a total of 42 simulations were performed. Full insertion of the peptides was achieved within 1000 ns simulation time in more than 90% of these simulations. In three simulations only a partial peptide insertion was observed, with a significant proportion of the peptide being unstructured and positioned around the surface of the bilayer rather than having

the expected structure and position. In one simulation, only adsorption of the peptide to the bilayer surface was achieved.

As expected, the insertion mechanism of the Smp14a analogs in most cases followed the stepwise mechanism previously described for Smp24 (table 7.2). In around 12% of the simulations the peptides skipped the N-terminal inserted stages going directly from the initial interactions to the rotation stage, but with the number of simulations it is not unexpected that in some cases the local lipid conditions would allow this to happen.

Overall, the kinetics of the insertion processes were consistent with observations from the previous rounds of simulations. The initial lag period was on average the shortest stage taking  $57 \pm 101$  ns. The N-terminal insertion stage was on average the longest stage and the most variable taking  $160 \pm 192$  ns, with as mentioned some simulations where it is completely skipped. The rotation stage was the most consistent, taking on average  $81 \pm 53$  ns and overall, the full insertion process took on average  $279 \pm 191$  ns.

The relatively large variations in the kinetics of the insertion process makes it difficult to determine any specific effects on this due to the amino acid substitution. However, no modifications seemed to be completely detrimental to the insertion process with even Smp14a\_S3K\_A9L, that did not achieve full insertion in one of the simulations, behaving in an equivalent fashion to the other peptides in the remaining two simulations.

**Table 7.2 Overview of the insertion kinetics for Smp14a and the first-generation analogs. All values are in ns.**

Simulation name	Overall Insertion level	Initial lag period	N-terminal inserted	Rotation	Inserted
bpg_I1F_1	Full	0-105	105-155	155-250	250-500
bpg_I1F_2	Full	0-55	55-122	122-169	196-500
bpg_I1F_3	Full	0-54	na	54-337	337-500
bpg_W2L_1	Full	0-74	74-107	107-165	165-500
bpg_W2L_2	Full	0-27	27-109	109-162	162-500
bpg_W2L_3	Full	0-6	6-44	44-110	110-500
bpg_W2F_1	Full	0-2	2-265	265-307	307-500
bpg_W2F_2	Full	0-220	na	220-350	350-500
bpg_W2F_3	Full	0-4	4-236	236-246	246-500
bpg_S3K_1	Full	0-6	6-80	80-117	117-500
bpg_S3K_2	Full	0-513	na	513-555	550-750
bpg_S3K_3	Full	0-13	13-126	126-192	192-500
bpg_S3H_1	Full	0-17	17-38	38-122	122-500
bpg_S3H_2	Full	0-161	161-211	211-266	266-500
bpg_S3H_3	Full	0-134	na	134-309	309-500
bpg_A9L_1	Full	0-15	15-43	43-162	162-500
bpg_A9L_2	Full	0-320	320-364	364-515	515-750
bpg_A9L_3	Full	0-13	13-34	34-115	115-500
bpg_A9F_1	Full	0-5	5-136	136-330	330-500
bpg_A9F_2	Full	0-19	19-80	80-128	128-500
bpg_A9F_3	Full	0-10	10-139	139-208	208-500
bpg_T10K_1	Full	0-5	5-122	122-195	195-500
bpg_T10K_2	Partial	0-5	5-823	823-842	842-1000
bpg_T10K_3	Partial	0-24	24-788	788-895	895-1000
bpg_T10S_1	Full	0-1	1-11	11-74	74-500
bpg_T10S_2	Full	0-6	6-365	365-446	446-750
bpg_T10S_3	Full	0-2	2-467	467-572	572-750

bpg_I1F_W2L_1	Full	0-80	na	80-112	112-500
bpg_I1F_W2L_2	Full	0-3	3-12	12-30	30-500
bpg_I1F_W2L_3	Full	0-31	31-134	134-245	245-500
bpg_W2L_S3K_1	Full	0-6	6-495	495-516	516-750
bpg_W2L_S3K_2	Full	0-6	6-194	194-293	293-500
bpg_W2L_S3K_3	Full	0-5	5-60	60-152	152-500
bpg_W2L_A9L_1	Full	0-18	18-148	148-207	207-500
bpg_W2L_A9L_2	Full	0-72	72-92	92-152	152-500
bpg_W2L_A9L_3	Full	0-12	12-74	74-108	108-500
bpg_S3K_A9L_1	Full	0-32	32-111	111-196	196-500
bpg_S3K_A9L_2	Surface	0-43	43-1000	na	na
bpg_S3K_A9L_3	Full	0-9	9-198	198-303	303-500
bpg_W2L_S3K_A9L_1	Full	0-17	17-102	102-138	138-500
bpg_W2L_S3K_A9L_2	Partial	0-230	230-415	415-500	500-750
bpg_W2L_S3K_A9L_3	Full	0-17	17-205	205-355	355-500

As previously shown, the helicity of the Smp14a was relatively consistent and relatively high after the insertion into the bilayer, having an average helicity of  $84.6 \pm 0.9\%$ . Therefore, there is likely limited opportunity for increasing the overall helicity of the peptide by substituting any individual amino acids. However, substitutions could still have a disruptive effect to the overall or local structure which might lead to a reduced activity of the peptide *in vitro*.

As expected, none of the modified peptides had a higher % of helical structure than Smp14a but 21% of them retained an average helicity above 80% while 43% had an average helicity above 70% (figure 7.1). Several general trends could be observed related to the effect of the amino acid substitutions on helicity of the structure. Firstly, substitution to larger aromatic residues generally induced a reduction in the helicity both in comparison to the native peptide and the other substitution types. Examples of this could be the substitution to a leucine residue in 2<sup>nd</sup> or 9<sup>th</sup> position

which in both cases only led to a small disruption of the helical structure while the equivalent substitution to phenylalanine residues more consistently reduced the helicity. This was also the case for the isoleucine1 to phenylalanine substitution which reduced the helicity both with the single and dual modifications. This phenomenon was not just isolated to the hydrophobic residues with the serine3 to histidine also reducing the helicity compared with both the native peptide and the lysine modification. Li Ping Lu et al investigated the propensity of different residues to induce the formation of a helical structure in a membrane mimicking environment and found residues with aliphatic hydrophobic sidechains such as leucine and isoleucine generally were better than aromatic residues such as tryptophan and phenylalanine, corresponding well with the observations from the simulations (248).

Secondly, substitution to non-aromatic residues in general do not markedly affect the helicity. The main outlier for this observation was the threonine10 to lysine modification which could indicate that this residue position has a larger influence on the overall peptide structure. Lastly, there was not always a direct correlation between the single amino acid substitutions and the multi amino acid substitutions. Individually, both the serine3 to lysine and alanine9 to leucine modifications did not affect the structure substantially, however when combined the helicity was consistently reduced. In other cases, such as the combination of the isoleucine1 to phenylalanine or the serine3 to lysine with the tryptophan2 to leucine the behaviour is more expected, yielding a helicity of the dual modifications somewhere between the average helicities of the individual modifications.

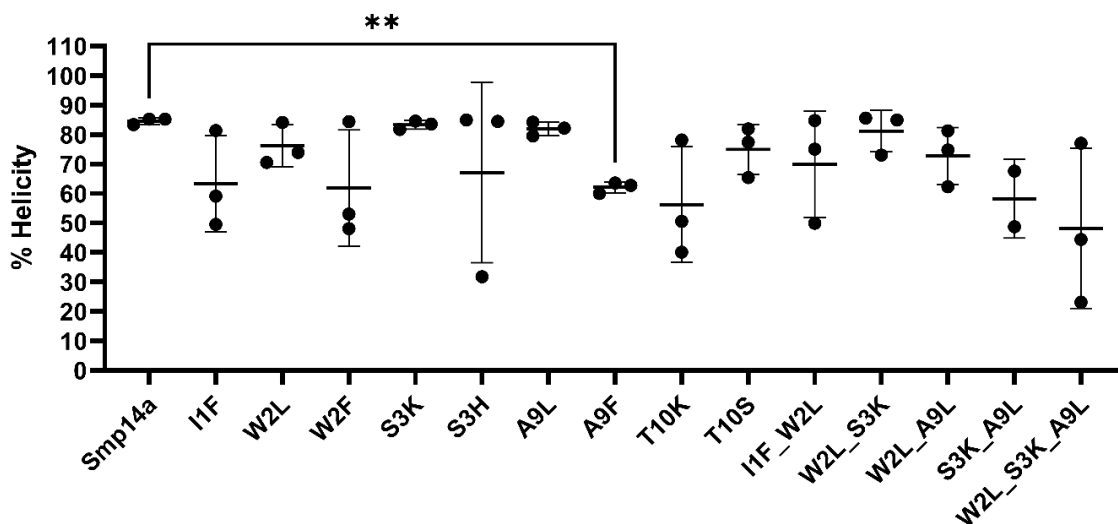


**Figure 7.1 Average helicity of the first generation Smp14a analogs.** \* Statistically significant difference from parent peptide (Smp14a) calculated based on two-sided, unpaired, independent t-test.

Ensuring that the modified peptides retain their level of insertion within the bilayer could be a key indicator that they would be likely to retain their antimicrobial properties *in vitro*. Most of the peptide analogs retained a mean distance from the centre of the bilayer of around 1.25-1.30 nm similar to that of the native Smp14a (figure 7.2). While none of insertion depths were significantly different from Smp14a a few trends could still be observed.

Again, substitution to the larger aromatic residues seemed to have a relatively consistent effect leading to a slight reduction in the insertion depth compared to both the native peptide and other modifications at the same residue position. As expected, the threonine10 to lysine substitution led to the largest reduction in the insertion depth due to the peptide only achieving a partial insertion state in two of the simulations.

One might have expected that substituting the small downwards facing alanine 9 residue to a residue with a larger hydrophobic sidechain could have increased the overall insertion depth of the peptide, but this did not seem to be the case. Both the alanine9 to leucine and to phenylalanine substitutions led to a reduction of the average insertion depth of above 1.3 nm from the bilayer centre.

Surprisingly the substitution which led to the greatest increase in the insertion depth was the serine3 to lysine modification, with the single substitution and one of the dual

substitutions being the only two modified peptides with improved insertion level compared with Smp14a. The W2L\_S3K peptide was especially improved with a more than 5% increase in the insertion depth.

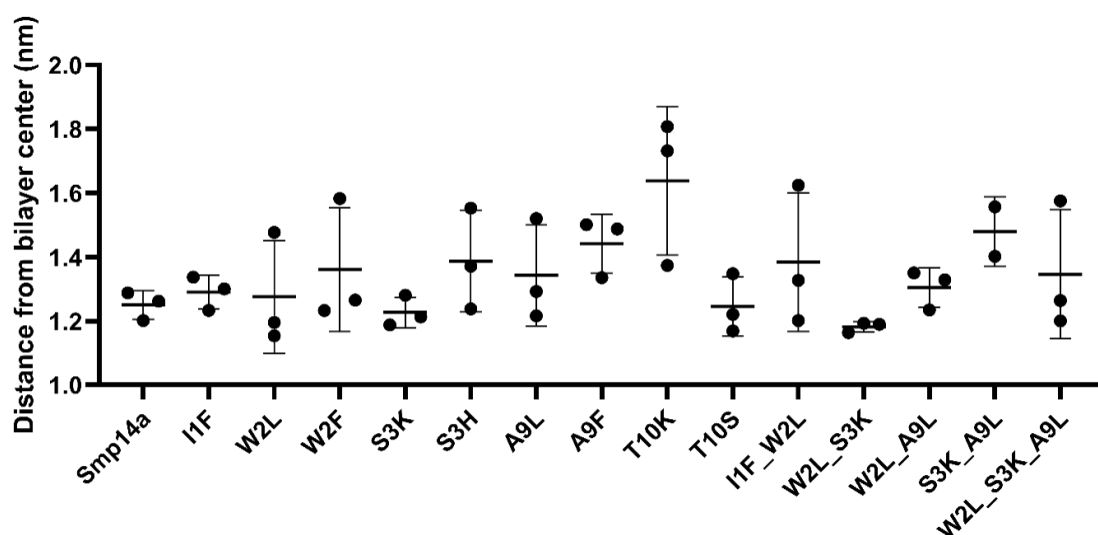


**Figure 7.2 Average distance from the centre of the bilayer of the first generation Smp14a analogs.** \* Statistically significant difference from parent peptide (Smp14a) calculated based on two-sided, unpaired, independent t-test.

The relative binding energy is one of the key characteristics where the modified peptides could more readily show potential improvements over the parent peptide. As expected, the greatest impact seen on the  $\Delta G$  was when the overall charge of the peptide was increased by substituting in another lysine residue (figure 7.3). While the binding energy was increased for all peptides with this lysine modification compared with the parent peptide, the largest and most statistically significant increases were seen for the S3K ( $P=0.0027$ ) and W2L\_S3K ( $P=0.0165$ ) peptides. The average  $\Delta G$  increases were smaller and more variable for the other peptides with a +5 charge likely due to increased variability in their structure. A few other peptides had smaller but statistically insignificant increases, most notably the I1F and W2L peptides which both have an average  $\Delta G$  of above  $-86$  kcal/mol. The I1F\_W2L peptide was the only one with an average  $\Delta G$  below that of the parent peptide although the difference was less than 0.2 kcal/mol.

By breaking the binding energy further down into its electrostatic and hydrophobic components further context could be obtained related to the changes in the overall binding energies (figure 7.4 & 7.5). As expected, the lysine substitutions significantly increased the electrostatic energy in all cases. The tryptophan<sup>2</sup> to leucine modification seems to facilitate a small but relatively consistent increase in the electrostatic energy seen for both the W2L, I1F\_W2L, W2L\_S3K and W2L\_S3K\_A9L peptides. This is somewhat surprising as the leucine residue would not be expected to impact the electrostatic interactions much by itself. The change could therefore instead be one that indirectly improves the electrostatic interactions of other residues as seen previously with the truncation of the secondary helix of Smp24.

The most notable reduction in the electrostatic energy is for the S3H peptide which was a modification of one of the key non-charged residues responsible for the overall electrostatic interactions. This is one indication that the histidine residue was not able to form stronger interactions with the bilayer than the serine residue, at least under the conditions used in the simulations.

Two of the modified peptides had a statistically significant increase in the hydrophobic component of the binding energy. First was the I1F peptide ( $P=0.046$ ) which could be expected based on the substitution to another phenylalanine residues, as this residue type did show a generally higher energy contribution than leucine and isoleucine residues in previous per-residue energy breakdowns of Smp24 and the truncated peptides. The specific increase to the energy contribution would also be somewhat dependent on the position of the residue, but with the observed position of the sidechain of the N-terminal residue the increase in the van der Waals energy would likely be a direct result of the increased energy contribution of the larger sidechain. The second and more surprising significant increase was seen for the S3K peptide ( $P=0.019$ ). Neither a serine or a lysine residue itself would be expected to have a large impact on the hydrophobic interactions, so the energy increase could likely instead be a secondary effect of the substitution improving the interactions of the other residues. This observation does line up with the slight increase in the insertion depth also seen for this peptide.

While several of the modified peptides had a slight decrease in the van der Waals energies, taking the large variations between the replicate simulations into account

these reductions could be explained by the coinciding structural variation of these peptides. However, one notable outlier is the W2L peptide which had reduced van der Waals energy with a relatively small variation. This suggests that the opposite of what happened for the I1F modification is occurring with the direct interactions between the leucine residue and the bilayer being less energetically favourable than with the tryptophan residue.

Another set of peptides with notable Van der Waals energies are the A9L and A9F peptides. One could expect that the substitution of the small alanine residue to the larger more hydrophobic leucine and phenylalanine residues would have led to an overall increase in the hydrophobic interactions, but this was not the case. Again, the explanation is likely due to an indirect effect of the substitutions reducing the overall structural stability and causing a reduced overall insertion depth of the peptides limiting the hydrophobic interactions of the peptides as a whole.

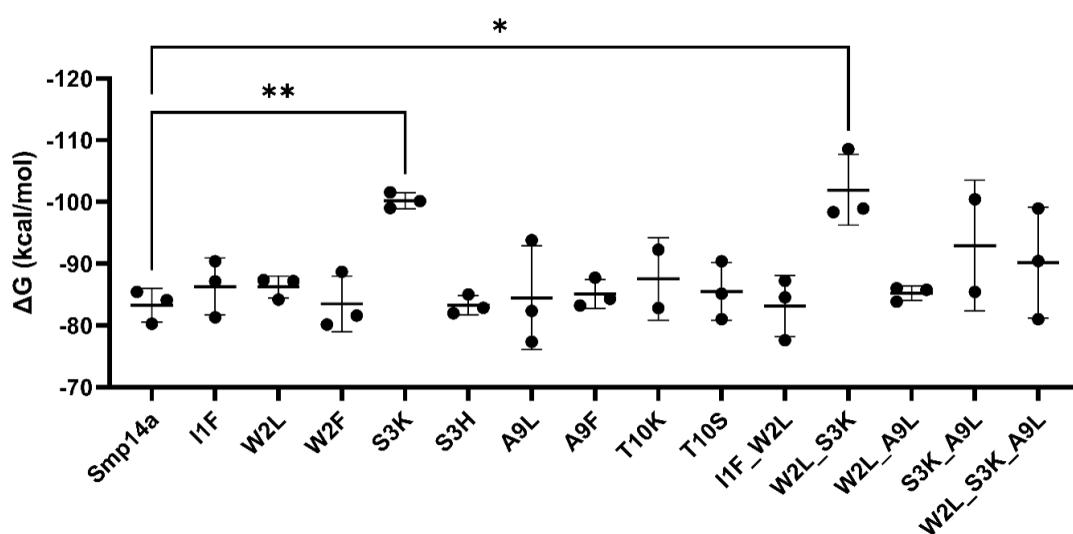


**Figure 7.3 Average relative free binding energy of the first generation Smp14a analogs. \*** Statistically significant difference from parent peptide (Smp14a) calculated based on two-sided, unpaired, independent t-test.

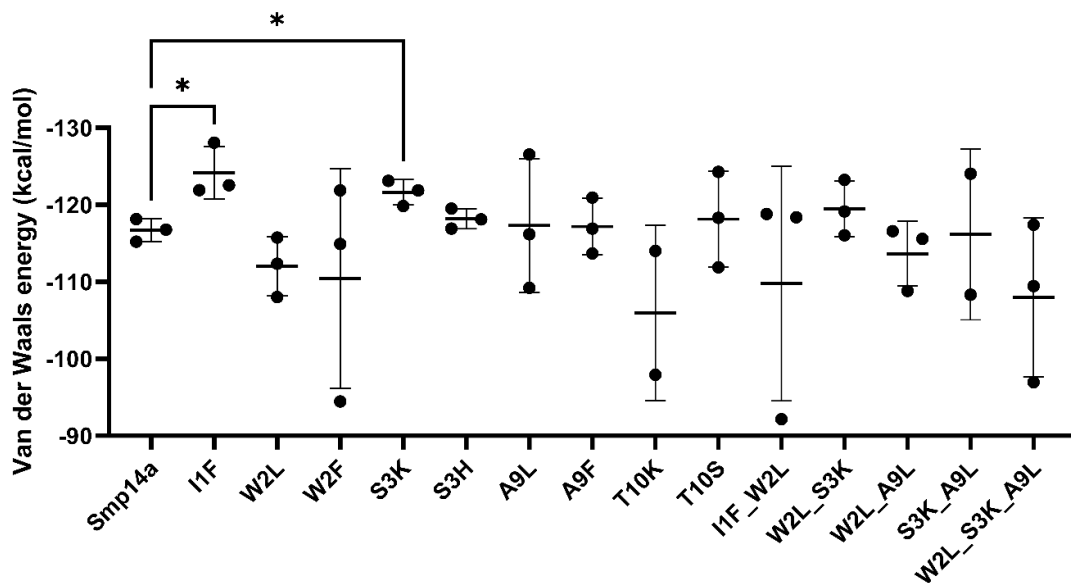


Figure 7.4 Average Van der Waals energy of the first generation Smp14a analogs as calculated as part of MMPBSA analysis. \* Statistically significant difference from parent peptide (Smp14a) calculated based on two-sided, unpaired, independent t-test.

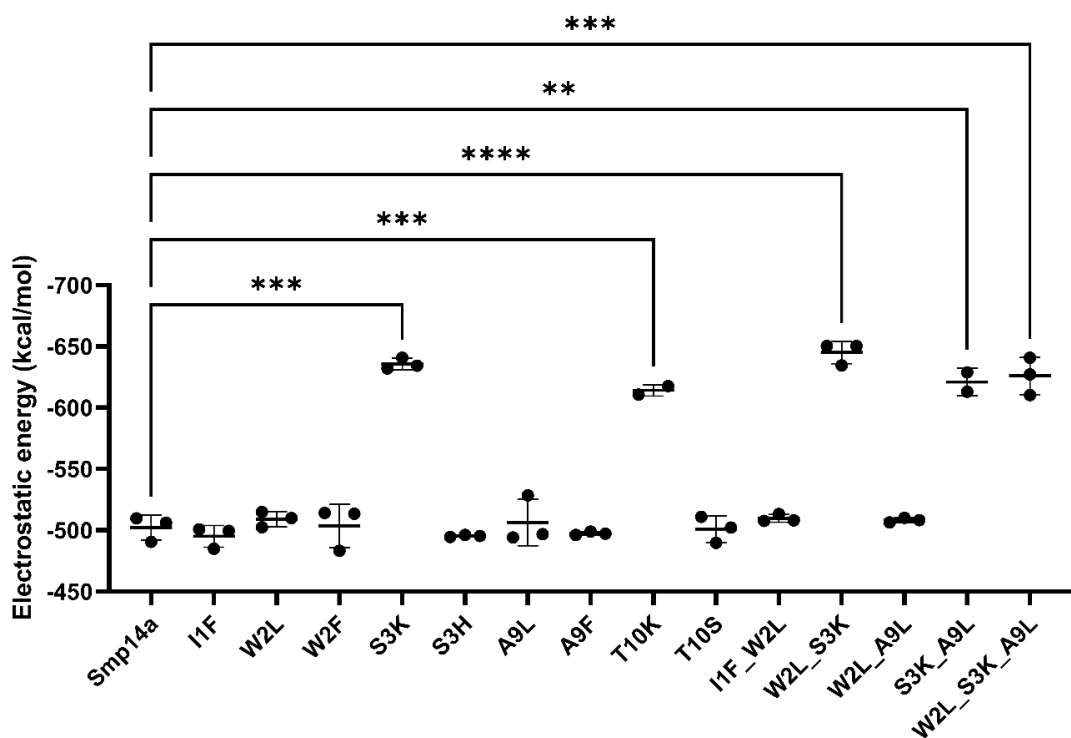


Figure 7.5 Average electrostatic energy of the first generation Smp14a analogs as calculated as part of MMPBSA analysis. \* Statistically significant difference from parent peptide (Smp14a) calculated based on two-sided, unpaired, independent t-test.

In addition to the previous sets of characteristics analysed for all the peptides some more specific analysis methods were utilised to investigate the local effects that the individual amino acid substitutions had on the analogs.

A key aspect of modifying the polar residues in the 3<sup>rd</sup> and 10<sup>th</sup> position was to investigate if the polar interactions between the residues in these positions and the phospholipids could be improved. To evaluate if this was achieved the RDFs between the main polar sidechain atom and the phosphate groups of the lipid were calculated (figure 7.6).

In the 3<sup>rd</sup> residue position the serine residue previously did show some interactions with the phosphate groups as indicated by the peak at around 0.38-0.40 nm. However, as expected from the energy calculations, substitution to a lysine residue strongly improved these interactions leading to a higher and more consistent peak due to the increased strength of the fully charged interaction.

A similar effect was not seen when substituting in the histidine residue, again consistent with the energy calculations. The main reason for this is that the non-protonated form of histidine was used in the simulations, as the majority of histidine residues would be non-protonated in the experimentally relevant pH range. Polar interactions between the histidine hydrogen bond donor and the phosphate groups still occurred, but RDF indicates that they were even smaller than with the serine residue. Part of the explanation for this could be the larger size of the histidine sidechain limiting the consistency of the interactions. *In vitro* a small proportion of the histidine residues would still be charged likely allowing for interactions more akin to those observed for the lysine residue. Thus, it is difficult to estimate if the interactions between the residue and the lipids would be improved or reduced as a whole.

At the 10<sup>th</sup> position the threonine residue of the native Smp14a peptide showed almost no interactions with the lipid phosphate groups even though the relative position/orientation of the side could in theory allow for interactions to occur. However, this changes for both substitutions. As expected, the substitution to the lysine residue had the greatest impact on the interactions, however compared to what has been observed for other lysine residues the variation in the interactions between the repeated simulations were much greater. This is likely an effect caused by the greater variation in the structure and insertion level observed for this peptide analog.

However, when investigating the RDF for the bpg\_T10K\_1 simulation where the best insertion was achieved, a clear peak at 3.9 nm was observed (data not shown). The substitution to the serine residue did significantly increase the peak compared with the native threonine residue, although compared to the peak seen for the serine residue in the 3<sup>rd</sup> position it was still relatively small.

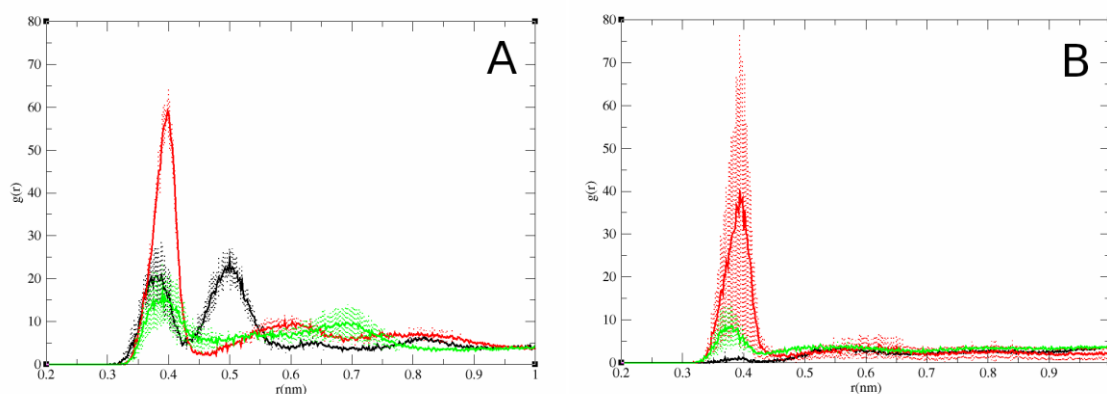


**Figure 7.6 Radial distribution functions between select polar residues and the lipid phosphorus atoms.** A = Comparison between the average RDFs of the different residues in the 3<sup>rd</sup> position of the peptide sequence. Black = the serine3 in Smp14a, red = the lysine3 in the S3K analog, green = the histidine3 residue in S3H analog. B = Comparison between the average RDFs of the different residues in the 10<sup>th</sup> position of the peptide sequence. Black = the threonine10 in Smp14a, red = the lysine10 in the T10K analog, green = the serine10 in the T10S analog.

To further investigate why the polar interactions between the position 10 residues and the lipid phosphate groups were smaller than expected, the occurrence of intermolecular hydrogen bonds facilitated by the position 10 sidechain were explored (table 7.3). For the native Smp14a peptide a very consistent hydrogen bond was formed between the hydroxy group of the of the threonine sidechain and the backbone of the isoleucine6 residues. When the substitution to the serine residue is performed the occurrence of this bond was almost halved, explaining why interactions instead could occur with the lipid phosphate groups. Substitution to the lysine eliminated the formation of this intramolecular hydrogen bond.

**Table 7.3 Hydrogen bond occupancy of the hydrogen bond between the residue 10 side chain doner and the Ile6 backbone after full insertion into the DOPC:DOPG bilayer.**

Peptide	Hydrogen bond occupancy
Smp14a	91.91 ± 1.47 %
T10K	0.00 ± 0.00 %
T10S	47.39 ± 16.55 %

Another key hydrogen bond that might be affected by the amino acid substitutions could be related to the residue in the 2<sup>nd</sup> position. The native peptide contains a tryptophan residue which not only could interact with the bilayer through hydrophobic interactions but also via the formation of a hydrogen bond facilitated by the nitrogen atom in the indole ring structure. Substitution of this residue to either leucine or phenylalanine would eliminate the possibility of such a hydrogen bond to be formed. The average number of hydrogen bonds between the whole of the 2<sup>nd</sup> position residue and the bilayer was calculated for the relevant peptides to account not only for the loss of the hydrogen bond doner of the indole ring but also to see if the side chain affected the hydrogen bond formation coming from the backbone of the residue (table 7.4).

As expected, the substitution of the tryptophan residue led to a reduction of the average number of hydrogen bonds in all cases. The reduction was the largest when the larger aromatic phenylalanine residue was added, either in the 1<sup>st</sup> or 2<sup>nd</sup> residue position. The change was smaller when the substitution was made to the leucine residue but consistent for both the W2L and W2L\_S3K peptides.

**Table 7.4 Average number of hydrogen bonds between the 2<sup>nd</sup> residue in the peptide sequence and the lipid bilayer.**

Peptide	Average number of hydrogen bonds
Smp14a	1.073 ± 0.2829
W2L	0.7065 ± 0.022
W2F	0.4687 ± 0.1320
I1F_W2L	0.4507 ± 0.1383
W2L_S3K	0.7389 ± 0.1511

The modifications of the hydrophobic residues in the 1<sup>st</sup> and 9<sup>th</sup> positions were performed in order to improve the hydrophobic interactions with the bilayer and potentially lead to a deeper level of insertion of these residues among the lipid acyl chains. Therefore, the mean distance between the centre of the bilayer and the individual residues was investigated (table 7.5).

The substitution of the N-terminal isoleucine residue to a phenylalanine did induce a very small but non-significant increase in the insertion depth of the residue. The small effect could be due to the charged N-terminal amine forming strong interactions with the phosphate groups limiting any effect of changing the sidechain.

For the substitutions of the 9<sup>th</sup> residue the effects were larger but not necessarily what would be expected. In both cases the larger residues were positioned further away from the bilayer centre than the original alanine residue, which correlates with the observations for the insertion depth of the entire peptide.

**Table 7.5 The average distance from the centre of the bilayer between select residues in the Smp14a analogs.**

Peptide	Residue 1 distance from bilayer centre (nm)
Smp14a	1.0496 ± 0.0210
I1F	1.0417 ± 0.1190
I1F_W2L	1.0280 ± 0.1024
	Residue 9 distance from bilayer centre (nm)
Smp14a	1.0827 ± 0.0543
A9L	1.1252 ± 0.1248
A9F	1.2038 ± 0.1956

### 7.2.2 Selection of the most promising analogs

Based on the totality of the *in silico* investigations, predictions can be made as to if their antimicrobial activity would be improved, reduced or be unchanged compared with the parent peptide. In all cases a predicted improvement would be ideal but as

the modifications might also affect other aspects of the behaviour of the peptides such as their selectivity a prediction of a similar level of antimicrobial activity might also be considered a success. To allow for a complete analysis of the validity of the previously described design principles, a minimum of one Smp14a variant was chosen for each of the modification sites to move on to *in vitro* evaluation.

For the residue 1 substitution site only one modification was made, that being the substitution of the isoleucine to a phenylalanine residue. While the simulations did indicate that the substitution to the larger aromatic residue could potentially reduce the stability of the helical structure, the energy calculations indicated that the hydrophobic interaction between the peptide and the bilayer had been increased thereby fulfilling the main objective of the substitution. In all other aspects the modified peptide behaved within the limits of what would be expected for a peptide with a similar level of activity as its parent peptide.

The increased hydrophobic interactions of the N-terminal could also impact other aspects of the behaviour of the peptide not directly investigated in this set of simulations. As indicated by the original simulations for Smp24, the sidechain of the N-terminal is one of the few hydrophobic residues which might play a role during the insertion and surface adhesion of the peptide. While no clear effect of the substitution on the insertion kinetics could be observed, a small effect might still be relevant *in vitro* when averaging over many orders of magnitudes more peptides.

When comparing the two modifications of the position 2 substitution site the tryptophan to leucine substitution would be predicted to be the most successful, as the greater helical disruption of the phenylalanine residue is not compensated by a significant improvement in the other properties of the peptide. The slightly helical disruptive tendency of the leucine substitution could be due to the elimination of the hydrogen bond between the tryptophan and the lipids providing some local stability to the helix. However, even with the slightly reduced helicity of the peptide, it still had similar or slightly improved properties in the other aspects evaluated and therefore the W2L variant would be predicted to have similar antimicrobial properties as the parent peptide.

As mentioned previously, the substitution of the serine 3 residue to a lysine residue was expected to yield an improved peptide based on previous modifications of Smp24 (149). The *in silico* modelling agrees with these expectations showing a large increase in the electrostatic interactions, while retaining the other properties of the parent peptide.

The effect of the substitution to the histidine residue is less clear. Overall, the S3H peptide is predicted to be slightly worse than the parent peptide in most of the investigated aspects. Although to some extent this can be explained by one of the simulations deviating significantly from the rest, lowering the average value and increasing the variance. While the interactions between the phospholipids of the histidine sidechain might be overall slightly worse than with the serine residue they still occur and were reasonably consistent, so the modified peptide would be predicted to have an antimicrobial activity around the same level or slightly lower than the parent peptide. In addition, with the potential presence of an ATCUN motif the S3H peptide does show enough promise to warrant further *in vitro* evaluation.

Improvement of the hydrophobic interactions between the peptide and the bilayer through substitution of the alanine9 residue was seemingly less successful than the residue 1 modification. Like at the other modification sites the addition of a phenylalanine seemed to disrupt the helical structure of the peptide while not providing any significant improvements over the parent peptide in any of the other investigated aspects. The behaviour of the A9L peptide was more complex. While the helical structure of the peptide in the simulations was very consistent, the other properties of the peptide such as the insertion depth and the binding energies varied much more than would be expected based on the structural variation alone. This makes it more difficult to predict the behaviour of the peptide *in vitro*. In one simulation the insertion depth of the peptide was deeper than for the parent peptide also leading to an increased binding energy, however in the others the opposite was the case. This was also the case when looking at the insertion depth of the leucine residue only, potentially indicating that it is difficult for this residue to achieve a consistent/optimal position within the parameters of the simulations. The ability of the peptide to adopt the most optimal position within the bilayer might be more dependent on the specific configuration of the lipids surrounding it as it could be more

difficult for the larger leucine sidechain to properly align with the lipid acyl chains. This could increase the amount of time it takes for the peptide to reach its true fully inserted state leading to greater variation within the short timeframe of the simulations. However, in an *in vitro* setting such kinetic differences might not be as relevant, while the potentially increased hydrophobic interactions could lead to an overall increase in the activity of the peptide.

Many of the amino acid substitutions indicate that a balancing act might exist between trying to improve the interactions between the peptide and the bilayer without disrupting the helical structure of the peptide too much. For the T10K peptide such a balance did not seem to be reached. While the lysine residue did increase the electrostatic interactions with the bilayer, the helical structure and insertion level were both consistently disrupted. This could be related to the loss of the intramolecular hydrogen bond between the threonine sidechain and the peptide backbone which is completely lost following the lysine substitution. Some structural stability could in principle instead come from the interactions with the surrounding phospholipids but the relative position/orientation of residue sidechain might not be optimal for such interactions while in a helical configuration.

The substitution to the serine residue seemed to instead facilitate a middle point between favouring internal and external interactions. The increased structural flexibility of the serine sidechain relative to the threonine allowed for interactions with both the lipids and the peptide backbone. The modification could thus allow for an investigation into how critical this intramolecular hydrogen bond is and if even a slight change to its stability would impact the activity of the peptide. Based on the simulations no difference in the antimicrobial activity would be expected which is consistent with the very minor structural difference between the threonine and serine residues. However, it would still be interesting to get an indication about how large the modifications need to be in order to have an *in vitro* impact on the activity. This would both help answer the question whether it is worth substituting polar residues such as threonine for other non-charged residues and would help validate whether the modelling is accurate enough to predict activity changes based on such small structural modifications.

Out of the 5 analogs containing 2-3 residue modifications two were chosen for further evaluation. Based on the simulations the W2L\_S3K peptide was overall the most promising analog, with a good helicity, the deepest insertion level and the largest increase in both the binding energy all giving the indication that the activity is likely improved.

The second dual modified analog chosen was the I1F\_W2L peptide which had more mixed *in silico* results indicating that the analog was more likely to have a similar antimicrobial activity as Smp14a. However, it was still chosen as it seemed to improve the helicity slightly compared to the I1F, potentially due to increasing the space between the large aromatic residues located near the N-terminal.

### 7.2.3 Biological evaluation of Smp14a analogs

To assess the *in vitro* properties of the peptides, the antimicrobial, haemolytic and cytotoxic activity of a new batch of Smp14a (new manufacturer) and the 8 chosen analogs were evaluated (table 7.6). The new batch of Smp14a had a slightly lower antimicrobial efficacy than the previous batch, shifting the MIC values against *S. aureus* from 4-8 to 8 µg/ml and against *P. aeruginosa* from 16 to 16-32 µg/ml, however these changes are within the expected range of batch-to-batch variation. The A9L variant was found to have very limited solubility in the test media making it impossible to determine any consistent MIC values. Several of the other peptides showed some degree of aggregation at the highest test concentration leading to slightly elevated absorbance readings in these wells. However, as the peptide concentration was reduced the absorbance conformed with the negative growth control until the MIC had been surpassed.

Excluding the A9L analog only one of the remaining Smp14a analogs had a consistently reduced antimicrobial efficacy, with the activity of the I1F\_W2L analog being reduced against all the tested bacteria species by up to a factor of 2. However, the remaining 6 analogs all showed an overall equivalent efficacy with some cases of small improvements against specific species.

The only analog which had an improved activity against *S. aureus* was the W2L peptide, achieving an MIC of 4 µg/ml which is a 2-fold increase compared with Smp14a and a 4-

fold increase relative to Smp24. However, this improvement did not carry over to any of the Gram-negative species. Both double modified peptides which included the W2L modification lost the activity increase against *S. aureus*, with the W2L\_S3K peptide instead having a similar MIC to Smp14a.

Several analogs had an improved activity against the Gram-negative species *E. coli* and *P. aeruginosa*, with all of them sharing a common motif relating to the substitution of the serine3 residue. The overall best activity was achieved for the double mutant W2L\_S3K which had a factor 2 improvement against both *E. coli* and *P. aeruginosa* compared with Smp14a and a 4-fold improvement against *E. coli* compared with Smp24.

These results correlate well with the predicted properties of the peptides based on the MD simulations. Most of the peptides were expected to have a similar activity to the parent peptide and this seems to be the case. The peptide analogs with an increased charge (S3K and W2L\_S3K) were expected to have an improved antimicrobial activity based on their increased binding energy but this was only against the Gram-negative species. The effect of increasing the charge was smaller in this round of designs compared with the difference between Smp20 and Smp18 where the charge increase led to 2-4 fold improvements in the MIC against all the bacteria species. Similar observations have been made for other AMPs in the past, showing both a general diminishing return on the activity increase when increasing the charge of the peptide and that this diminishing return happens faster against Gram-positive species (220, 249).

The improved activity of the W2L analog was less expected based on the MD simulations, indicating that the activity change might be related to other aspects of the peptide-bilayer interactions not well modelled in the simple peptide-bilayer simulations, such as changes to the pore formation itself.

The activity increase of the S3H analog could either be due to increased interactions with the bacterial membrane or an effect of the ACTUN motif. Previous studies of AMPs modified by ACTUN motifs show that an activity increase simply due to the presence of a potential ACTUN motif is not a given. The specific residues coming before the position three histidine can have a large effect on how efficiently reactive

oxygen species can be produced, with the IWH motif found in the S3H analog not being previously explored or found in nature (242). Most studies have previously found inconsistent effects even when adding the same ACTUN motif to different peptides and often do not take into account how much of the activity increase is simply due to increasing the size of the peptide (112, 241, 242). When Agbale et al tested their most promising ACTUN modified AMP analogs in the presence of a Cu(II) chelator which should eliminate the effect of the peptide-copper binding, only a 2-fold change in the MIC was observed, indicating that the real effect of the ACTUN motif is relatively minor (112). Since the activity changes of S3H mimic those seen for the S3K analog it is more likely that the slight improvement is due to the partial protonation of the histidine sidechain under the experimental conditions.

The observations related to the A9L analog highlight that solubility should also be a key concern when designing AMPs. While the relatively high proportion of hydrophobic residues can be somewhat counterbalanced by the inclusion of cationic residues, this still makes the solubility of the peptide very dependent on the ionic strength of the surrounding solution. The low solubility can in practice reduce the concentration of active peptides and thereby reduce the measured antimicrobial activity or lead to loss of peptides during the sample preparation.

**Table 7.6 MIC values for Smp14a and the first-generation analogs in µg/ml. N=2, n=3**

Peptide	<i>S. aureus</i>	<i>E. coli</i>	<i>P. aeruginosa</i>
Smp14a	8	16	16-32
Smp14a_I1F	8	16	32
Smp14a_W2L	4	16	16-32
Smp14a_S3K	8	8	16
Smp14a_S3H	8	8	16-32
Smp14a_A9L	>128	>128	>128
Smp14a_T10S	8	16	16-32
Smp14a_I1F_W2L	8-16	32	32
Smp14a_W2L_S3K	8	8	8-16

The first round of peptide analogs showed both improvements and reductions in the selectivity against erythrocytes (table 7.7). The solubility of the A9L analog was better in PBS allowing for the evaluation of its haemolytic activity which was by far the highest of any of the peptides, with a significantly decreased  $HC_{50}$  value compared to Smp14a ( $P=0.006$ ). Most of the remaining analogs had a haemolytic activity relatively close to that of Smp14a.

The  $HC_{50}$  values of the S3H and T10S analogs both deviated by less than 10% from that of Smp14a. Larger but still nonsignificant changes were seen for the I1F ( $P=0.086$ ), W2L ( $P=0.1187$ ) and I1F\_W2L ( $P=0.2812$ ) showing a higher haemolytic activity for the first and a reduced activity for the latter two. However, two of the peptide analogs did show a significantly reduced activity, namely S3K ( $P=0.0254$ ) and W2L\_S3K ( $P=0.0024$ ). The haemolytic activity is especially reduced for the W2L\_S3K analog shifting the  $HC_{50}$  value 2.99-fold relative to Smp14a and 4.65-fold relative to Smp24.

Focusing further on the 4 peptides with reduced haemolytic activity, an interesting observation can be made in terms of the shape of the dose response curve (figure 7.7). While the S3K analog has a higher  $HC_{50}$  value than the W2L and I1F\_W2L analogs at the lower concentrations the %lysis is lower for these two peptides. However, at 64  $\mu\text{g/ml}$  for I1F\_W2L and 128  $\mu\text{g/ml}$  for the W2L peptide their %lysis overtakes that of the S3K peptide and reaches similar levels to Smp14a at either 254 or 512  $\mu\text{g/ml}$ . This difference in the shape of the curve could give some insight into how the W2L modification has affected the mechanism of action of the peptide. The reduced activity at the lower concentrations could indicate that the modification inhibits the ability of the peptide to insert into the membrane of the erythrocytes which is likely the rate limiting step of the mechanism of action at these conditions. This correlates well with the hypothesis that the removal of the tryptophan residue would inhibit the initial interactions between the peptide and zwitterionic lipids through cation pi interactions. If this is the case, a lower proportion of peptides would reach the fully inserted stage necessary for the membrane disruption under these conditions explaining the low %lysis. However, as the concentration of peptides in the surrounding solution is increased the actual number of inserted peptides will reach a critical point where pore formation and membrane disruption can more readily occur. Furthermore, the fact that the W2L and I1F\_W2L peptides reaches similar levels of lysis as Smp14a at the

higher concentration could indicate that the W2L modification increases the efficiency of the membrane disruption after the critical concentration has been reached. An increased membrane disruption efficiency could also explain the increased antimicrobial activity of the W2L peptide against *S. aureus*.

A potential explanation for why the W2L modification leads to an increased membrane disruption efficiency could be the removal of the hydrogen bond between the tryptophan and surrounding lipids. Previous studies have indicated that limiting the polar interactions between an AMP and the lipid bilayer coming from the areas near the terminals of the peptide could allow the peptide to more easily adopt a tilted configuration that could serve as an initial step in the pore formation (188, 240). This concept could also explain the reduced activity of the S3K peptide as the lysine residue would also make it more difficult for the N-terminal end of the peptide to insert more deeply into the bilayer, yielding more of a direct shift of the dose response curve as a lower membrane disruption efficiency affects the lysis at all concentrations.

As such, both the W2L and S3K modifications seem to facilitate a reduced haemolytic activity at the lower peptide concentration but via different effects on the mechanism of action. This might explain why their combined effect in the W2L\_S3K analog seem to be synergistic with the reduction in the haemolytic activity being several times greater.

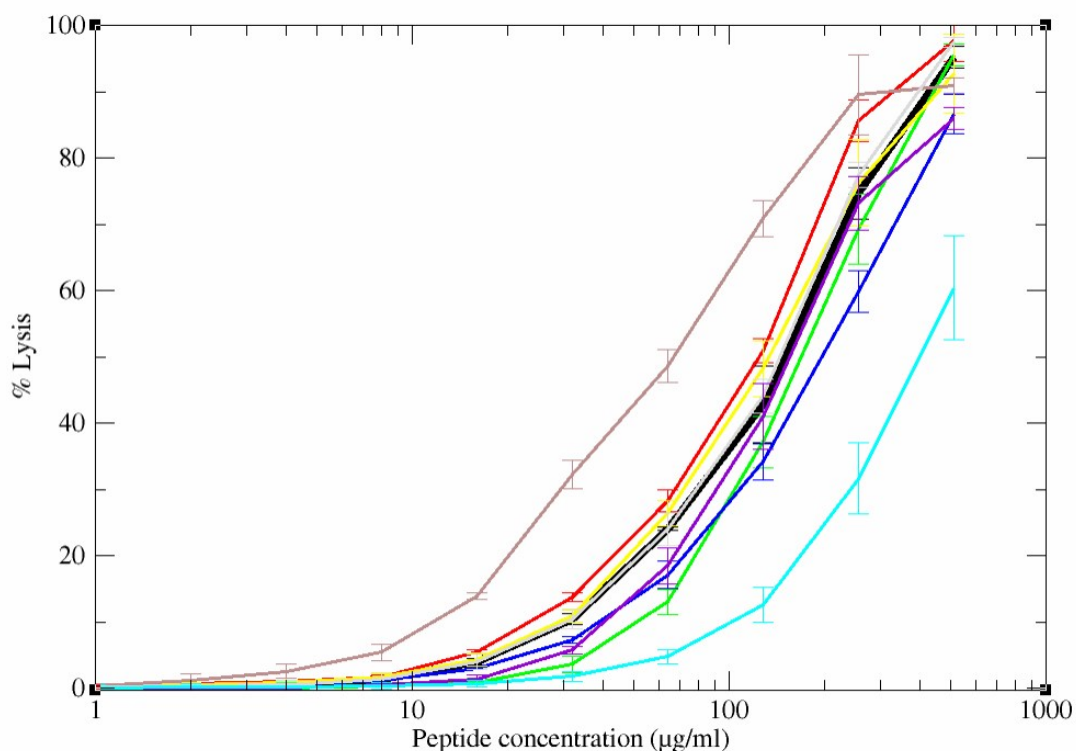


**Figure 7.7 Concentration dependent haemolysis of sheep erythrocytes by Smp14a and analogs.** Black = Smp14a, red = Smp14a\_I1F, green = Smp14a\_W2L, blue = Smp14a\_S3K, yellow = Smp14a\_S3H, brown = Smp14a\_A9L, grey = Smp14a\_T10S, violet = Smp14a\_I1F\_W2L, cyan = Smp14a\_W2L\_S3K, N=3, n=3.

**Table 7.7 HC<sub>50</sub> values for Smp14a and the first-generation analogs based on the haemolysis of sheep erythrocytes.** \* Value is significantly different from Smp14a based on two-sided two-sample independent t-test (P<0.05).

Peptide	HC <sub>50</sub> (µg/ml)
Smp14a	137.37 ± 12.23
Smp14a_I1F	110.70 ± 2.29
Smp14a_W2L	165.91 ± 15.86
Smp14a_S3K	187.91 ± 15.73*
Smp14a_S3H	128.10 ± 14.97
Smp14a_A9L	63.15 ± 5.10*
Smp14a_T10S	131.40 ± 7.94
Smp14a_I1F_W2L	154.79 ± 15.40
Smp14a_W2L_S3K	410.62 ± 72.77*

As with the previous set of experiments related to the truncation of Smp24, the effect of the peptide modifications on their selectivity seems to be much smaller against the cell lines such as the HEK293 cells compared with the erythrocytes (table 7.8). As with Smp14a all the modified analogs have a reduced cytotoxic response at the highest 1-3 concentration levels, likely due to aggregation in the culture media. As such, these data points were not used for calculating the EC<sub>50</sub> values. The average maximal cytotoxic response for the peptides was also relatively low, reaching  $30.42 \pm 1.00$  % over the three replicate experimental runs. This leads to an apparent shift in the EC<sub>50</sub> values compared with the previous set of experiments where they were calculated based on the maximum response of the larger peptides such Smp24 at around  $52.2 \pm 5.71$  % LDH release, with the EC<sub>50</sub> value for Smp14a going from  $37.01 \pm 4.61$  µg/ml to  $23.40 \pm 0.80$  µg/ml in this new set of experiments. However, if the EC<sub>50</sub> values for the first set of experiments were calculated using 30.42% as the maximum response, the average EC<sub>50</sub> value would not be significantly different from the  $23.40 \pm 0.80$  µg/ml found in the new set of experiments (P=0.2025).

The only Smp14a analog with a statistically significantly different EC<sub>50</sub> value was the S3K analog (P=0.0262), producing a lower cytotoxic response than the parent peptide at similar concentrations, correlating with the observations for the haemolytic activity of the peptide. However, the other three peptides that showed a reduced haemolytic activity did not have a significantly reduced cytotoxic response, with the W2L analog even having a slightly lower EC<sub>50</sub> value than the parent peptide. The reduced response at the lower peptide concentrations for the analogs containing the W2L substitution were still seen but to a much smaller extent than in the haemolysis assay (figure 7.8). These observations could again indicate that the different aspects of the mechanism of action of the peptides do not have the same impact on the selectivity in the two toxicity models. If as hypothesised the W2L modification mainly impacts the initial interactions/insertion of the peptide into the membranes the differences in the membrane compositions might result in this effect being less significant in the cell line assay. However, if the S3K modification instead impacts the membrane disruption efficiency it would explain why this peptide shows reduced toxicity in both assays.

This might also explain why the W2L\_S3K analog shows no significant reduction in its toxicity in the cell line assay. If the effect of the W2L substitution on the initial

interaction/insertion is insignificant, the slight increase in the membrane disruption caused by the substitution might balance out the slight reduction caused by the S3K modification, similarly to what was observed with the antimicrobial efficacy against *S. aureus*.

Like Smp14a the 20-residue long AMP CA-MA also contains a tryptophan residue in the 2<sup>nd</sup> position. Donghoon et al substituted this tryptophan to a leucine residue and as for Smp14a this substitution did not inhibit the antimicrobial activity of the peptide. While the haemolytic activity of the peptides was not investigated the cytotoxicity against a range of cell lines was reduced (250).

Bi et al substituted several leucine residues to tryptophan residues in the 13-residue long AMP L-K6 and found that adding the tryptophan residues near the N-terminal in general improved the antimicrobial activity while tryptophan residues near the C-terminal reduced it. The parent peptide showed no haemolytic activity and this was not significantly changed by adding the tryptophan residues (251).

For the 16-residue long peptide dCATH(1–16) substitution of the position 4 tryptophan residue led to both reduced antimicrobial activity and cytotoxicity (252). However, as the substitution was made to a much smaller alanine residue rather than a leucine residue a general activity reduction is not surprising.

Overall, 3 (W2L, S3K and W2L\_S3K) out of the 8 peptide analogs showed clear improvements to their *in vitro* biological properties with only one peptide (A9L) being clearly worse. With the overall best antimicrobial activity and by far the lowest haemolytic activity the W2L\_S3K analog was chosen as the basis for the next round of the iterative drug design process.

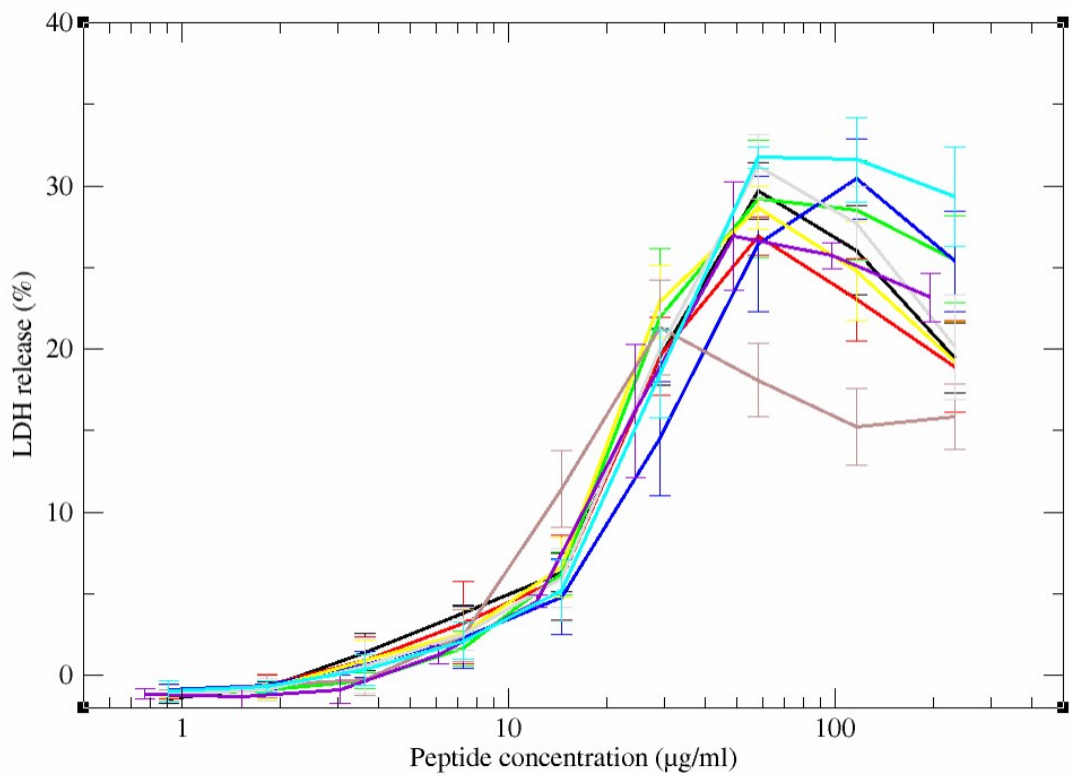


**Figure 7.8 Concentration dependent LDH release from HEK293 cell caused by Smp14a and the first-generation analogs.** Black = Smp14a, red = Smp14a\_I1F, green = Smp14a\_W2L, blue = Smp14a\_S3K, yellow = Smp14a\_S3H, brown = Smp14a\_A9L, grey = Smp14a\_T10S, violet = Smp14a\_I1F\_W2L, cyan = Smp14a\_W2L\_S3K. N=3, n=3.

**Table 7.8 EC<sub>50</sub> values for Smp14a and the first-generation analogs based on the LDH release from the HEK293 cell line.** The EC<sub>50</sub> values for all peptides are calculated against the average maximum LDH release rate for all peptides excluding A9L relative to the positive control. Average maximum LDH release was 30.42 ± 1.00% against the HEK293 cell line. \* Value is significantly different from Smp14a based on one-sided two-sample independent t-test (P<0.05).

Peptide	EC <sub>50</sub>
Smp14a	23.40 ± 0.80
Smp14a_I1F	24.22 ± 3.17
Smp14a_W2L	22.78 ± 3.59
Smp14a_S3K	32.45 ± 2.47 *
Smp14a_S3H	21.12 ± 1.49
Smp14a_A9L	19.64 ± 2.94
Smp14a_T10S	23.00 ± 2.34
Smp14a_I1F_W2L	24.70 ± 5.66
Smp14a_W2L_S3K	24.52 ± 1.50

#### 7.2.4 Design of the second generation Smp14a analogs

Following the *in vitro* evaluation of the first generation of Smp14a analogs a second iteration of peptides were designed based on the W2L\_S3K variant. Two new design strategies were implemented with the hope that they might lead to improvements in the antimicrobial efficacy.

Building on the hypothesised effect seen for the W2L modification where removal of polar interactions between the bilayer and the area of the peptide near the N-terminal potentially led to an improved membrane disruption efficiency, the N-terminal amine was acetylated to remove the positive charge and thereby eliminating the strong interactions between it and the lipid phosphate groups. While removing this charge is likely to negatively impact the strength of the binding between the peptide and the bilayer, the hope is that it will make it much easier for the N-terminal region to adapt a deeper insertion level which could lead to greater pore formation.

The second strategy was to try to reintroduce the helical kink motif, removed from Smp24 during the truncation stage of the drug design. While in that case the impact of removing the kink could be counteracted by increasing the charge, a kink motif could potentially be a way to improve the activity of Smp14a\_W2L\_S3K against *S. aureus* where further increases of the charge seem likely to have a limited effect.

As previously mentioned, two different residues can be used to introduce bending in a helical region. Proline residues create a distinct kink due to a loss of a backbone hydrogen bond and due to steric interactions between the proline ring and the carbonyl oxygens in the preceding turn of the helix. Glycine residues can also induce an increased curvature of the helix due to its small size and high torsional flexibility (253). As both types of residues can be found in other AMPs (199), substitutions were made to both proline and glycine residues.

The next question was then which residue in the sequence should be substituted to the proline/glycine. Ideally a residue should be chosen which is not by itself critical for the activity of the peptide and the position should be relatively central in the helical region to facilitate the creating of a reasonably sized helical region on each side of the kink. Another question is where the kink is introduced relative to the rotational orientation of the helix. In Smp24 the proline residue is positioned on the side of the helix relative to its orientation when the peptide is inserted in a bilayer. With these considerations in mind the two most obvious choices for modification sites are the 8th position alanine and the 10th position threonine. Both native residues are expected to have a relatively minor impact on the peptide-bilayer interactions, so the substitutions should not impact the binding directly. The main concern is instead to which degree the substitutions would impact the structural stability of the peptide and how much such structural disruptions would impact the *in vitro* activity.

Based on these design strategies 5 new second-generation analogs were designed and evaluated *in silico* (table 7.9).

For the *in silico* evaluation of this generation of peptide analogs, a few changes were made to the base bilayer model leading to the creating of the 5<sup>th</sup> bilayer model variant. The first change was to reduce the overall size of the bilayer. This was done as the bilayer size in the original model was chosen based on the size of Smp24. However, with the now much smaller Smp14a and its derivatives a smaller model should be able

to serve the same role without leading to artifacts and at the same time significantly reduce the computational cost of the simulations.

A second change made was to increase the salt concentration in the solution phase of the simulation. While there is a consensus that enough ions should be added to a model to at least neutralise the overall charge of the system, the addition of extra ions beyond that varies between authors. Therefore, the change was made to explore the effect of the salt concentration on the simulation of the interactions between AMPs and bilayers, in order to inform future model design.

**Table 7.9 Overview of the physicochemical properties of the second generation Smp14a analogs.** Hydrophobic moment calculated using <https://heliquet.ipmc.cnrs.fr/>, \* C-terminal amidation not accounted for in calculations.

Name	Sequence	Mw (g/mol)	Charge at pH 7	Hydrophobic moment*
Smp14a	IWSFLIKAATKLFK- NH <sub>2</sub>	1665.07	4	0.626
Smp14a_W2L_S3 K	ILKFLIKAATKLFK- NH <sub>2</sub>	1633.11	5	0.649
Smp14x_ACE	<b>ACE-</b> ILKFLIKAATKLFK- NH <sub>2</sub>	1675.18	4	0.649
Smp14x_A8G	ILKFLIKGATKLFK- NH <sub>2</sub>	1619.11	5	0.644
Smp14x_A8P	ILKFLIKPATKLFK- NH <sub>2</sub>	1659.18	5	0.657
Smp14x_T10G	ILKFLIKAAGKLFK- NH <sub>2</sub>	1589.09	5	0.660
Smp14x_T10P	ILKFLIKAAPKLFK- NH <sub>2</sub>	1629.15	5	0.632

### 7.2.5 In silico evaluation of the second generation smp14a analogs

For the second generation of the Smp14a analog designs a total of 18 simulations were done. Simulations for the W2L\_S3K peptide were repeated to take into account the differences in the bilayer size and ion concentration.

Full insertion was achieved within 1000 ns for 83.33% of the simulations with two simulations yielding a partially inserted peptide due to major but not complete loss of the helical structure and one simulation where the peptide only achieved a surface level association with the bilayer. All three simulations where full peptide insertion was not achieved were related to peptide analogs with the threonine10 residues substituted. All kinetics of the insertion were within the range expected based on the previous rounds of simulations (table 7.10).

As the charged N-terminal previously has been shown to be one of the key structural characteristics that drives the specific insertion mechanism for Smp24 and its derivatives, one might expect that the acetylation of the charged amine group would significantly impact the mechanism. However, based on the positions of the peptide and the N-terminal the effect seemed to be relatively minor (figure 7.9). In 2/3 simulations the peptide still seemed to have adopted an N-terminal inserted state, where the N-terminal was positioned below the rest of the peptide, around the same level as the phosphate groups, before the full insertion was achieved. The position of the N-terminal was not as consistent or as deep within the bilayer as seen in previous simulations, but the behaviour was still clearly different than in the case where only a lag period was observed (figure 7.9C). However, visual inspection of the simulation trajectories revealed that this pseudo N-terminal inserted stage was more likely due to the orientation of the lysine3 sidechain (figure 7.10). Compared with the other lysine residues, the sidechain of lysine3 was oriented in line with the helical axis rather than tangentially to it. This means that the charged sidechain to some extent mimics the behaviour of the charged N-terminal allowing the peptide to adopt a tilted configuration where some hydrophobic interactions between the bilayer and residues such as the acetylated N-terminal can occur at the same times as the charged interactions via the lysine residues. The position of the acetylated N-terminal is therefore still often positioned more deeply within the bilayer during the insertion, but the function has changed compared to with the nonacetylated N-terminal.

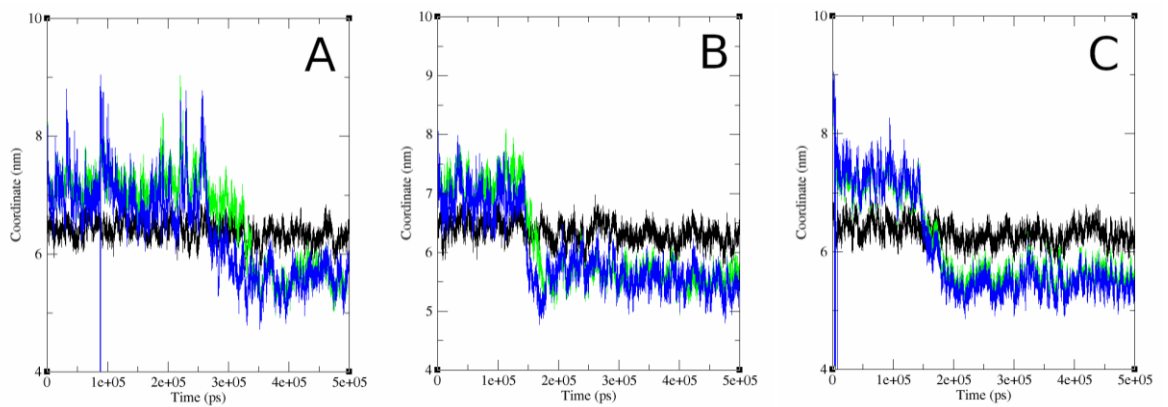


**Figure 7.9** Changes to the centre of mass over time for the three Smp14a\_W2L\_S3K\_ACE simulations. Black = Top leaflet phosphate groups, green = whole peptide, blue = acetylated N-terminal. A = bpgs\_ACE\_1, B = bpgs\_ACE\_2, C= bpgs\_ACE\_3.

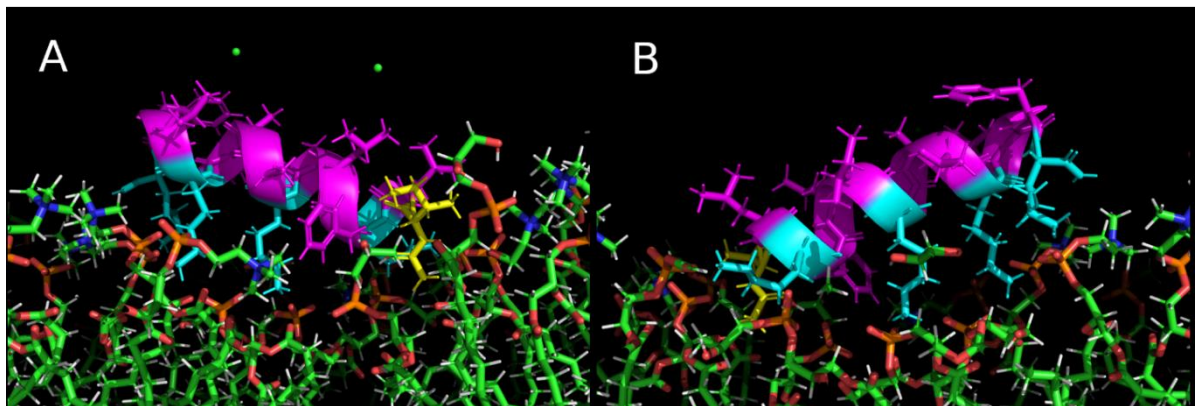


**Figure 7.10** 3D structure of the surface associated (pseudo N-terminal inserted) configuration of Smp14a\_W2L\_S3K\_ACE. The acetylated N-terminal is labelled yellow and the lysine residues in cyan. A = side showing the orientation of the N-terminal, B = side showing the orientation of the lysine3 sidechain.

**Table 7.10 Overview of the insertion kinetics for the second-generation analogs.** All values are in ns.

Simulation name	Overall Insertion level	Initial lag period	N-terminal inserted	Full insertion/rotation	Inserted
bpgs_W2L_S3K_1	Full	0-6	6-358	358-440	440-750
bpgs_W2L_S3K_2	Full	0-20	20-239	239-620	620-750
bpgs_W2L_S3K_3	Full	0-6	6-60	60-144	144-500
bpgs_ACE_1	Full	0-109	109-258	258-355	355-500
bpgs_ACE_2	Full	0-7	7-142	142-178	178-500
bpgs_ACE_3	Full	0-144	na	144-212	212-500
bpgs_A8G_1	Full	0-119	119-205	205-247	247-500
bpgs_A8G_2	Full	0-27	27-52	52-233	233-500
bpgs_A8G_3	Full	0-5	5-11	11-82	82-500
bpgs_A8P_1	Full	0-93	na	93-185	185-500
bpgs_A8P_2	Full	0-15	15-70	70-302	302-750
bpgs_A8P_3	Full	0-47	47-231	231-533	533-750
bpgs_T10G_1	Surface	0-36	36-51	51-177	177-500
bpgs_T10G_2	Partial	0-6	6-139	139-209	209-500
bpgs_T10G_3	Full	0-55	55-400	400-866	866-1000
bpgs_T10P_1	Partial	0-9	9-62	62-107	107-500
bpgs_T10P_2	Full	0-38	38-53	53-94	94-500
bpgs_T10P_3	Full	0-76	76-214	214-370	370-500

The helicity of the W2L\_S3K parent peptide was slightly lower in this round of simulations compared with the previous one (figure 7.11) This could be due to the increased salt concentration used in the simulation, with the additional chloride ions somewhat shielding the interactions between the bilayer and the cationic residues of the peptide which play a key role in stabilising the helical structure while the peptide is still mostly located in the solution phase. The A8G analog has a similar level of average helicity while the acetylated analog has an average helicity of above 80% similarity to the maximum helicity found for the peptides in the previous round of simulations. The

remaining three peptides (T10G, A8P, T10P) all had a lower average helicity although due to the relatively high variations between the repeat simulations, only the result of the A8P analog was significantly different from the parent peptide (P=0.0417).

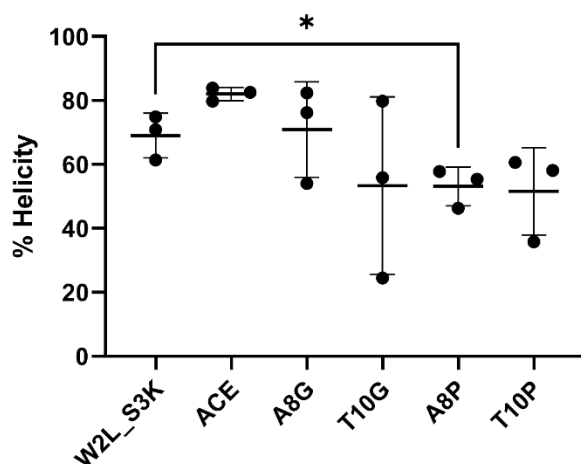


**Figure 7.11 Average helicity of the second generation Smp14a analogs.** \* Statistically significant difference from parent peptide (Smp14a) calculated based on two-sided, unpaired, independent t-test.

In terms of the insertion level of the peptides, the results for the W2L\_S3K parent peptide again deviates somewhat from the values found in the previous round of simulations (figure 7.12). This could be due to the different size of the bilayer leading to a change in the peptide to lipid ratio, but more likely this is a downstream effect of the slightly lower average helicity. The main outlier from the other peptides was the acetylated analog which reached an average insertion level around 0.2 nm or more closer to the bilayer centre than the other peptides. This could be due to the acetylation of the N-terminal allowing the peptide to insert deeper as the strong interaction between the N-terminal and the lipid phosphate groups was removed. However, it could also again be explained by the more consistent helical structure of the peptide analog. If compared to the previous round of simulations, the insertion level of the acetylated analog is in line with the insertion level of the W2L\_S3K analog.

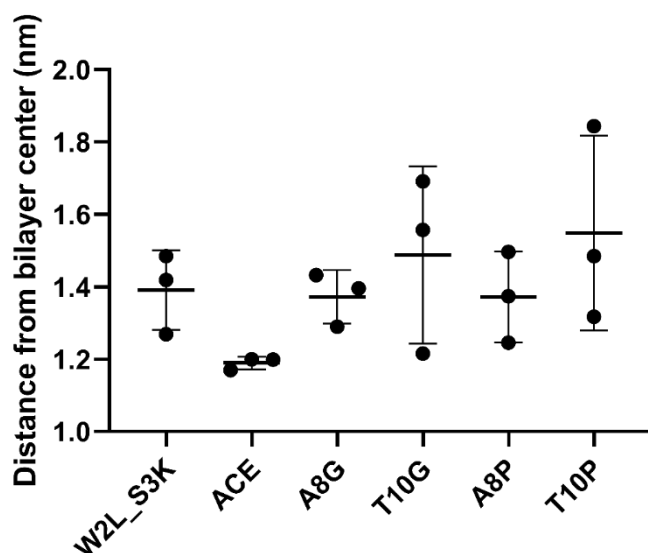


**Figure 7.12 Average distance from the centre of the bilayer of the second generation Smp14a analogs.** \* Statistically significant difference from parent peptide (Smp14a) calculated based on two-sided, unpaired, independent t-test.

The binding energy of the W2L\_S3K parent peptide was around 25 kcal/mol lower than what was found in the previous simulations (figure 7.13). When broken down into the electrostatic and hydrophobic energy components the main contributor to the overall  $\Delta G$  reductions seems to come from the electrostatic energy which was reduced by around 33% compared with the original set of simulations (figure 7.14 & 7.15). However, again this change can be explained by the increased salt concentration used in the new simulations shielding the electrostatic interactions between the peptide and the bilayer.

The A8G analog had the best overall relative binding energy which was also in line with the parent peptide in terms of the Van der Waals and electrostatic energy contributions. Following that comes the A8P analog with an average binding energy that is around 5% lower than that of the parent peptide but taking the lower average helicity into account this difference is smaller than could be expected. Both analogs with the threonine substituted have an even lower relative binding energy which could be explained by reductions in the Van der Waals interactions, likely due to the less consistent insertion of these peptides. The acetylated analog also showed an overall reduction in the relative binding energy which can be explained by a significant

reduction in the electrostatic interaction energy ( $P=0.017$ ). This reduction is due to the removal of the cationic charge of the N-terminal residue which for Smp14a was shown to be the single residue with the highest energy contribution.

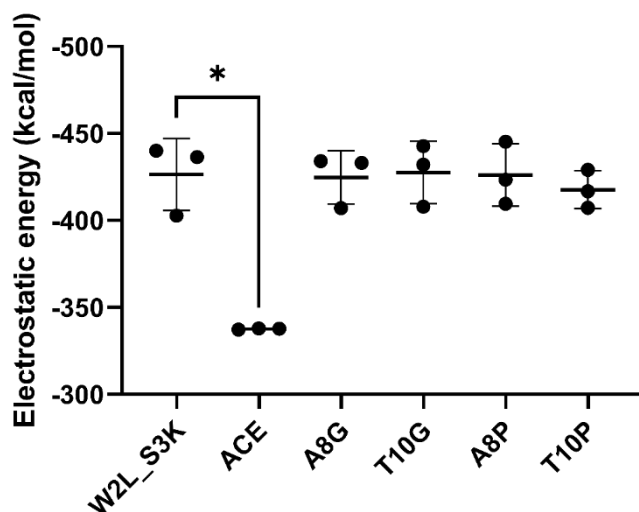


**Figure 7.13 Average relative free binding energy of the second generation Smp14a analogs.** \* Statistically significant difference from parent peptide (Smp14a) calculated based on two-sided, unpaired, independent t-test.

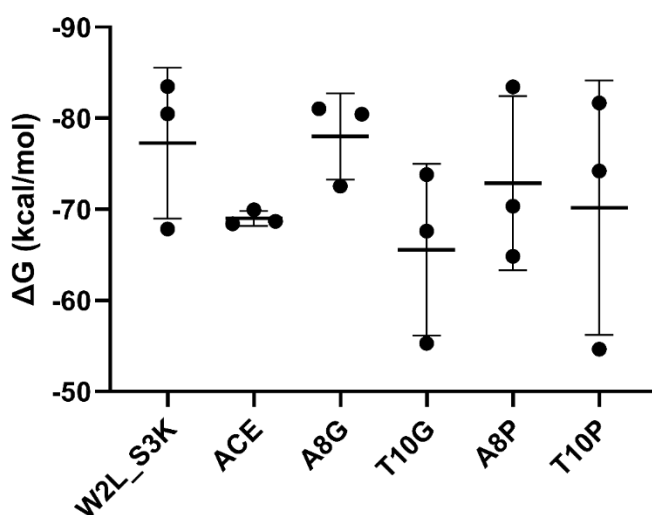


**Figure 7.14 Average Van der Waals energy of the second generation Smp14a analogs as calculated as part of MMPBSA analysis.** \* Statistically significant difference from parent peptide (Smp14a) calculated based on two-sided, unpaired, independent t-test.

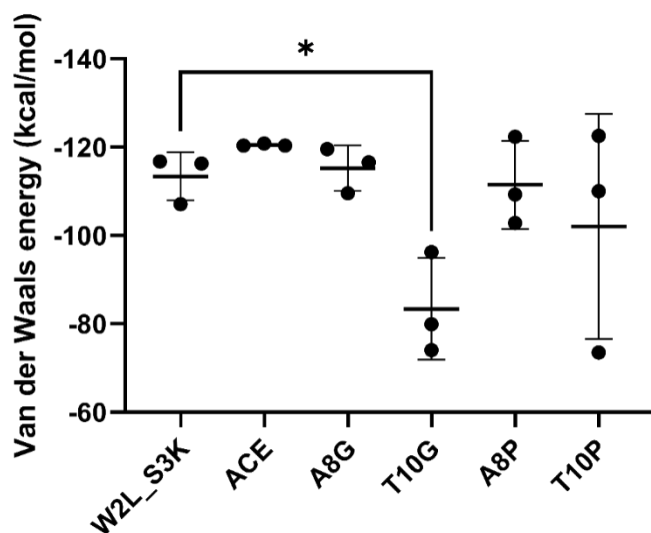


**Figure 7.15 Average electrostatic energy of the second generation Smp14a analogs as calculated as part of MMPBSA analysis. \*** Statistically significant difference from parent peptide (Smp14a) calculated based on two-sided, unpaired, independent t-test.

As one of the key aspects of most of the modifications was to improve the ability of the helical structures to bend, the natural curvature of a select set of the peptide analogs was investigated. The W2L\_S3K peptide was chosen to represent the baseline for the helical curvature while the alanine8 modified peptides were chosen for comparison as their helical structure was more consistent than the analogs based on modifications of the threonine10 residue. The investigations showed that in the simulations the parent peptide had on average a slight curvature with a maximum cumulative angle of just over 5 degrees at the 8<sup>th</sup> residue (figure 7.16). Substituting this 8<sup>th</sup> residue to a glycine had only a limited effect on the curvature, shifting the maximum bend slightly to residue 6 and 7 but not increasing it by much. However, when the residue was substituted to a proline the curvature was greatly increased, with a maximum curvature located at residue 7-8 at on average above 20 degrees.

This highlights the structural differences between the proline or glycine residues with the proline residue introducing a distinct kink in the helical structure leading to a high curvature even when the peptide is insertion into a flat bilayer. On the other hand, the effect of the glycine residue is more related to an increased flexibility of the helical curvature. This means that while the peptide is inserted into a flat bilayer no significant effect can be observed, but if the peptide were to be position in a higher curvature

environment such as when associated with a membrane pore the increased flexibility would at least in theory allow the peptide to better align with the bilayer. Still, the effect would likely be smaller than with the distinct kink of the proline residue.

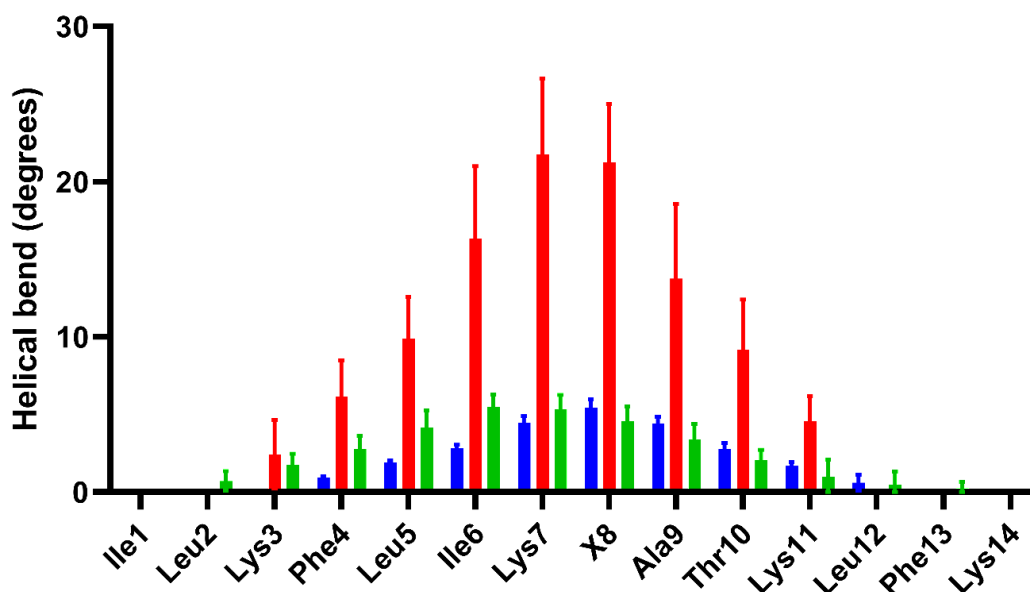


Figure 7.16 Average degree of cumulative helical curvature for each residue in select Smp14a analogs. Blue = W2L\_S3K, red = A8P, green = A8G.

Due to the more complex nature of the effects of the modifications on the structure and behaviour of the peptide analogs, predicting their activity is more difficult. The results for the acetylated analog were very polarising, being either clearly the most promising candidate as with the helicity and insertion depth or showing one of the clearest worsening of its properties as with the binding energy. Based on the relative binding energy alone one would expect to see a reduction in the antimicrobial properties compared with the parent peptide, however this could be somewhat counteracted by the good helicity and deep insertion. Furthermore, the previous round of experiments showed that a change in the binding energy/reduction in the overall charge would most likely affect the activity against the Gram-negative species to the greatest extent.

Predicting the activity of the analogs which had the glycine or proline residues added is even more difficult as the part of the mechanism of action that they are likely to affect

(pore formation/stabilization) is not well modelled within this set of simulations. Overall, the modifications to the alanine8 residue performed better in all aspects compared with the threonine10 modified peptides. This is likely because of the effect the specific residue position has on the stability of the helical structure. Substitution of the threonine residue not only removes the intramolecular hydrogen bond from the side chain, but it is also much closer to the end of the helix furthering the disruptive effect. The A8G analog behaves relatively similarly to the parent peptide in the simulations, so a similar antimicrobial activity could be expected, potentially with an upside if the increased flexibility improves the pore formation. The activity of the A8P analog could go either way depending on whether the increased curvature of the helix further improves the pore formation or if the disruption to the helical structure is too great for the peptide to consistently fold into the active configuration.

#### 7.2.6 In vitro evaluation of the second generation Smp14a analogs

None of the second generation analogs showed improvements in their antimicrobial activity relative to the Smp14a\_W2L\_S3K peptide (table 7.11).

The acetylated analog retained its activity against *S. aureus* but lost activity against both Gram-negative species. This is consistent with previous studies for other AMPs showing that acetylation generally lowers the activity against Gram-negative species while in some cases leading to improvements against Gram-positives (189, 254). This is likely due to the change in the overall charge of the peptide which, as seen in the previous set of MICs, was critical for the activity against the Gram-negatives.

**Table 7.11 MIC values for Smp14a and the second-generation analogs in µg/ml. N=2, n=3**

Peptide	<i>S. aureus</i>	<i>E. coli</i>	<i>P. aeruginosa</i>
Smp14a	8	16	16-32
Smp14a_W2L_S3K	8	8	8-16
Smp14a_W2L_S3K_ACE	8	16	16-32
Smp14a_W2L_S3K_A8G	16	16	16-32
Smp14a_W2L_S3K_A8P	>256	256	32-64

Both modifications to the alanine8 residue led to a general reduction in the antimicrobial activity. As the differences in the physiochemical properties between the alanine and the glycine or proline residues are relatively minor, the most likely explanation for the activity reduction is the helical disruptive properties of the new residues.

Previous studies have shown that incorporation of such residues into helical AMPs can lead to an overall reduction of the helicity (198). Proline residues are known to disrupt the helical structure to a larger extent than glycine residues (253), which also correlates with the relative reduction of the antimicrobial activity being much greater for the proline modified analog. The structure disruptive effect seems to have the greatest impact against *S. aureus* with the A8P analog completely losing its activity against this species although it still retaining some activity against *P. aeruginosa* especially. While the activity of the A8G analogs is reduced overall compared with the W2L\_S3K parent peptide, the activity against the Gram-negative species is still comparable to Smp14a and the activity against *S. aureus* is like that of Smp24.

While no activity improvements were achieved, the results still correlate well with the predicted properties from the MD simulations. The acetylated peptide did show a large reduction in the binding energy which would be expected to inhibit the ability of the peptide to bind to the bacterial cell membrane. Against *S. aureus* these reduced interactions are likely balanced with an improved membrane disruption efficiency leading to an equivalency in the overall activity change.

The simulations for the two remaining peptides both showed a reduction in their helicity which again could explain the activity reduction. However, the difference between the W2L\_S3K and W2L\_S3K\_A8G peptides was not enough to clearly predict an activity reduction. This might indicate that the effect of introducing the glycine residue is more pronounced during stages of the mechanism of action not modelled in the simulations. The structure disruptive effect of the glycine residue could be more relevant during the transition of the peptide from its unstructured to helical configurations rather than once the structure of the peptide is already fully helical. The helical structure of the fully inserted peptide might be relatively consistent and stable even with the glycine residue, but if the energy cost of folding into the helix is greater a smaller proportion of peptides are likely to reach that point at a given concentration.

The antimicrobial activity of several helical AMPs of similar size to Smp14a with and without glycine and proline residues have been investigated previously. The 17-residue long AMP P18 derived from parts of both Cecropin and Magainin 2 has a kink in its helix induced by a proline residue in the 9<sup>th</sup> position. Substituting this residue to either a leucine or serine led to general reductions in the antimicrobial activity relative to the parent peptide (255). However, compared with the Smp14a analogs P18 is both larger and has a greater charge (+8.1 at pH 7) which might help counteract the structure disruptive properties of the proline residue and thereby instead allowing the improved pore formation caused by the kink to dominate the overall effect on the activity.

The 13-residue peptide GHaR has two glycine residues, one at the 7<sup>th</sup> and one at the 10<sup>th</sup> position. Substitution of the 7<sup>th</sup> position glycine to an arginine reduced the antimicrobial activity of the peptide against most pathogens even though the charge of the peptide was increased (256). A notable difference between GHaR and Smp14a\_W2L\_S3K\_A8G is the position of the central glycine residue relative to the hydrophobic and hydrophilic sides of the helix. The glycine residue in GHaR is positioned on the hydrophilic side of the helix contrary to the glycine's position in the Smp14a analog. This could indicate that the specific position of the glycine residue in the helix could be critical for the effect on the activity, as the improved helical flexibility should preferably align with the peptide-pore assembly structure.

The 14-residue peptide mastoparan-C does not contain a proline or glycine residue. However, when the 7<sup>th</sup> position leucine residue was substituted to a glycine residue a general reduction in the antimicrobial activity was seen, especially against *S. aureus* (257).

It thus seems that the effect of inserting these residues into smaller AMPs is very dependent on the specific peptide and potentially on where in the sequence the substitution is performed.

Even if none of the modifications led to improved antimicrobial properties, improvements to the selectivity of the peptides were still possible. The haemolytic activity of the acetylated analog was significantly increased compared to the W2L\_S3K parent peptide ( $P=0.0003$ ) with the  $HC_{50}$  value reaching a level more comparable to Smp14a (table 7.12). However, for the two remaining peptide analogs the haemolytic activity was greatly reduced even compared with the W2L\_S3K analog. For both

analogs a single run with an addition higher peptide concentration (1024 µg/ml) was done in order to ensure a concentration dependent haemolysis increase could be detected. Even at this elevated concentration less than 10% haemolysis was achieved making it impossible to accurately calculate the HC<sub>50</sub> values.

These results are consistent with similar modifications for other AMPs. N-terminal acetylation has previously been shown to both increase or decrease the haemolytic activity compared to parent peptides (189, 254). The inclusion of proline or glycine residues have consistently led to reduced haemolytic activity compared with their analogs without helix disruptive residues (255-257).

The large reduction in the haemolytic activity for glycine and proline analogs indicates that the ability of the peptides to fold into their helical configuration is critical for their activity. This is also the case against bacterial cells but in this case the structure transition is aided by the increased electrostatic interactions with the membrane surface, helping the peptide overcome the entropy cost of folding into the helical configuration. Structure disruptive residues such as glycine or proline could thus improve the selectivity of the peptides by disproportionately inhibiting the structural transition when the peptides are interacting with eukaryotic cell membranes.

**Table 7.12 HC<sub>50</sub> values for Smp14a and the second-generation analogs based on the haemolysis of sheep erythrocytes.** \* Value is significantly different from Smp14a\_W2L\_S3K based on two-sided two-sample independent t-test (P<0.05).

Peptide	HC <sub>50</sub> (µg/ml)
Smp14a	137.37 ± 12.23
Smp14a_W2L_S3K	410.62 ± 72.77
Smp14a_W2L_S3K_ACE	112.99 ± 3.01*
Smp14a_W2L_S3K_A8G	NA (7.32% at 1024 µg/ml)
Smp14a_W2L_S3K_A8P	NA (1.70% at 1024 µg/ml)

The cell line cytotoxicity assays again show smaller differences in the selectivity between the peptides compared with the haemolysis assay (table 7.13). However, relatively large reductions in the cytotoxicity were still observed for the W2L\_S3K\_A8G

and W2L\_S3K\_A8P analogs. The EC<sub>50</sub> value for the W2L\_S3K\_A8G analog was shifted more than 3-fold compared with the parent peptide meaning that the therapeutic index for the peptide is still improved even when taking the 2-fold antimicrobial activity reduction into account. The cytotoxicity for the W2L\_S3K\_A8P was reduced to such an extent that a significant LDH release was only measured at the highest evaluated peptide concentration.

These results indicate that the selectivity improvements created by impacting the structure of the peptides translate better to the cell line assay compared to the modifications inhibiting the initial interaction with the eukaryotic membrane.

**Table 7.13 EC<sub>50</sub> values for Smp14a and the second-generation analogs based on the LDH release from the HEK293 cell line.** The EC<sub>50</sub> values for all peptides are calculated against the average maximum LDH release rate for all peptides excluding A9L relative to the positive control. Average maximum LDH release was 30.42 ± 1.00% against the HEK293 cell line. \* Value is significantly different from Smp14a\_W2L\_S3K based on one-sided two-sample independent t-test (P<0.05).

Peptide	EC <sub>50</sub>
Smp14a	23.40 ± 0.80
Smp14a_W2L_S3K	24.52 ± 1.50
Smp14a_W2L_S3K_ACE	21.91 ± 4.59
Smp14a_W2L_S3K_A8G	75.48 ± 14.66 *
Smp14a_W2L_S3K_A8P	NA (6.32% at 465 µg/ml)

Overall, the optimization of the sequence of Smp14a only led to limited improvements to the antimicrobial efficacy of the peptide. However, significant improvements were achieved regarding the selectivity of the peptides towards prokaryotic rather than eukaryotic cells. This was especially the case when it comes to their ability to attack red blood cells, with the haemolytic activity of both the best first-generation analog (Smp14a\_W2L\_S3K) and the best second-generation analog (Smp14a\_W2L\_S3K\_A8G) being significantly reduced each time.

### 7.2.7 Computer aided drug design of AMPs using MD simulations

Like in previous chapters, the use of MD simulation for the drug design purposes comes with several assumptions and limitations. These limitations are even greater for this chapter as we not only try to predict if new analogs behave in a similar way to the parent peptide but also if the antimicrobial activity is likely to be improved. The results indicate that the ability for the simulations to be used for this purpose is relatively limited. For some analogs such as Smp14a\_W2L, the improved activity was not clearly predicted, while all peptides with the S3K showed a large increase in the relative binding energy but only minor improvement in the antimicrobial activity. Furthermore, the simulations could not predict the large reduction in activity of the Smp14a\_A9L peptide as factors such as aggregation were not taken into account in the model. To improve the further use of MD simulations in computer aided drug design of AMPs would require the determination of a clearer *in silico in vitro* correlation, by investigating AMPs with a range of antimicrobial activity and correlating the activity to the corresponding *in silico* variables, likely with help of a machine learning. However, the overall complexity of the mechanism of action of AMPs might limit how strong an *in silico in vitro* correlation can be found, even for a large dataset.

To conclude if the use of MD simulations could be a successful drug design approach, a systemic comparison with other approaches would need to be performed, to identify if this new approach would be better at finding analogs based on the same parent peptide with improved properties that would be missed by other approaches. As this was not done, the best we can do to get some indication of the usefulness of the approach would be to compare with previous design efforts for similar peptides. Amino acid substitutions have previously been done for both Smp24 (149) and Smp43 (232), with 11 and 8 new analogs being designed for each respectively. These analogs were also designed based on structural predictions but using much simpler computational methods without explicit simulation of the surrounding solvent or bilayer. Table 7.14 shows an overview of the antimicrobial activity of the designed analogs relative to each of their parent peptides.

**Table 7.14 Overview of outcomes from amino acids substitutions for the Smp family of AMPs.** Similar activity as the parent peptide defined as maximum 1 factor 2 deviation in the MIC against a maximum of one species. Improved activity is defined as at least 1 factor 2 improvement in the MIC against one or more species. Consistently reduced activity is defined as a factor 2 reduction in the MIC against at least 2 species or a greater than factor 2 reduction against one species.

	Smp24	Smp43	Smp14a
Similar activity as the parent peptide	9%	38%	36%
Improved activity compared to the parent peptide	36%	0%	36%
Consistently reduced activity compared to the parent peptide	45%	63%	27%

For the Smp24 and Smp43 the most common outcome for a new modification was a reduction in the activity of the new peptide, however with the use of the MD simulation approach this outcome was the least common for the Smp14a analogs. This could be an indication that the MD simulations could help sort out analogs which are likely to have a reduced activity, but it could also be down to an intrinsic difference between the parent peptides. The Smp24 analogs had a similar rate of modifications with lead to improved activity as with the Smp14a analogs, and in both cases these improvements were mainly driven by increasing the charge of the peptide. This again indicates that the MD simulation approach is not that much better at identifying modifications directly leading to improvements of the antimicrobial activity. Many of the modifications that yielded the improved activity for the Smp24 analogs would likely also have been identified using the new approach and vice versa. However, some examples can be found where the MD simulation approach might have eliminated one of the "bad" analogs from the Smp24 study. The Smp24\_D23F analog has a relatively major modification with the substitution of the negatively charged Asp23 to a hydrophobic Phe residue. This design choice was likely done based on the simple

structural prediction, which predicted that the 23rd residue would be positioned and oriented similarly to most of the hydrophobic residues of the peptide. However, if MD simulations had been used, this residue would have been predicted to be positioned among the lipid headgroups and a more appropriate substitution to a polar or cat ionic residue could have been done.

### 7.3 Conclusions

While Smp14a have a significantly smaller size than Smp24 further improvements regarding the antimicrobial activity and selectivity would still be needed in order to make the peptide a more attractive drug candidate. Optimization of the peptide sequence was performed by amino acid substitution of 6 different residues across two design iterations leading to the design of 18 new analogs evaluated *in silico*, 11 of which were also evaluated *in vitro*. Out of the synthesised analogs, 72% had comparable antimicrobial properties to the parent peptide with 36% showing small improvements against at least one of the bacteria species tested, however overall the improvements to antimicrobial activity that could be achieved were relatively minor. Contrary to this, much greater improvements to the selectivity of the peptides could be achieved, especially regarding their haemolytic activity, with multiple analogs showing several fold increases in their HC<sub>50</sub> values. Substitution of polar residues with cat ionic residues seemed to be the most consistent way of improving the antimicrobial activity of the analogs while reduction in the ability of the peptides to form cation pi interactions and especially the addition of helix disruptive residues improved the selectivity. However, it seems that the addition of such structure disruptive residues needs to be done in a balanced approach as the addition of a highly disruptive proline residues also almost completely eliminated the antimicrobial properties of the peptide against several bacteria species.

## 8. General discussion and future perspectives

### 8.1 Advanced formulation of antimicrobial peptides

While the cytotoxic activity of AMPs to a large extent can be addressed using drug design, the cell line cytotoxicity assays of Smp24 and its derivatives show that there are some limitations to the efficacy of this approach. While the haemolytic activity, which is the first concern for intravenous systemic administration, can be relatively efficiently reduced as was the case for Smp14a\_W2L\_S3K\_A8G other toxicity concerns still arise as the peptides are distributed throughout the body. Limited knowledge exists as to the *in vivo* cytotoxicity mechanisms of AMPs with the most widely studied AMP-like antimicrobial agent being the lipopeptide colistin (polymyxin E) (258). For colistin nephrotoxicity is a major concern, due to the reabsorption of colistin by specific carrier systems in the renal tubules leading to an elevated peptide exposure for these cells (259). Such a toxicity mechanism could also be a concern for AMPs such as Smp24 and its derivatives limiting their possibilities for clinical use via a systemic administration route. Therefore, avoiding kidney exposure to the AMPs via local administration of the peptides via an advanced drug delivery system could be a critical step towards the clinical use of AMPs.

The intrinsic antibiofilm properties shown by the peptides (Smp24-14a) could make them very attractive candidates for uses in antimicrobial coatings such as those described in chapter 3. A key property of such antimicrobial coatings would be the ability for its behaviour to be adapted to the different demands set by different clinical applications. Some applications might require a longer or shorter time period of peptide elution, and for some a high burst release might be critical to eliminate an initial bacterial load.

The coating could be used with medical implants such as those used during hip replacements to prevent biofilm formation from external pathogens that have colonized the surface of the implant during the procedure. The broad spectrum of activity of the peptides could be an advantage for this purpose as the diversity of pathogens that can cause biofilm infections on devices such as prosthetic joints can be relatively high (260). However, for many medical devices such as prosthetic joints, central venous catheters and mechanical heart valves the coating would in practice

lead to a delayed release parental administration and thus cytotoxicity could still be a concern.

There is however still one type of medical device where the AMP loaded coating could have an obvious use, namely for urinary catheters. Around 80-90% of urinary tract infections are due to *E. coli* (261), so the strong biofilm inhibitory properties shown by Smp24 and the truncated analogs against *E. coli* biofilms might make the sol-gel coating especially effective for this purpose. The ability of Smp24 to eradicate biofilms formed by clinical strains of uropathogenic *E. coli* has previously been shown to be limited with an MBEC of 256 µg/ml (232). However, in practice the ability for the peptide to inhibit the biofilm growth might be more relevant for a catheter coating as the peptides would not be exposed to a preformed biofilm in this situation. Biofilm inhibition properties of the peptide even below the MIC might also allow the coating to still be effective towards the end of the use period as the drug elution rate decreases. Depending on the type, the use period for a single urinary catheter can vary greatly with long term catheters being in place for over a month (262). Therefore, it is important for the coating to be able to release the peptides over a long time period as shown for the coatings with PDMS-OH in the formulation. It is also important for the formulation to facilitate a relatively constant release of peptide as the infection risk is not just associated with the initial insertion of the catheter but persists throughout the entire use period. This also means that the initial burst release would be less important for a coating when used on urinary catheters.

Alternatively, the sol-gel coating could be used as a wound dressing. However, this purpose would likely completely change what the most optimal behaviour of the coating would look like. Antimicrobial wound dressings are often not used until the wound shows clinical signs of an infection, so when the formulations would be applied there would likely already be a pre-formed biofilm present (263). Therefore, the initial burst release from the coating becomes critical as enough API needs to be released in order to fight the initial biofilm which likely has a high tolerance against the antimicrobial agent. The broad spectrum of activity for Smp24 and its derivatives would again be an advantage as wound infections are often polymicrobial in nature (19). However, as the biofilm eradication efficiency of the peptides are likely much lower than their inhibitory properties, their effectiveness in a wound dressing would

be limited. This could potentially be improved by formulating the peptides together with another antimicrobial compound, given that they together could combat the biofilms in a synergistic way. The properties of the sol-gel coating could be well suited for the formulations of such combination therapies due to the different drug release mechanisms. If the AMP were formulated together with a polar small molecule antibiotic, the initial burst release would likely consist of both compounds facilitating the eradication of the initial biofilm, while the hydrophobic domains would ensure that it would be followed by a slow release of AMPs, perfect for preventing the formation of a new biofilm.

Due to the two distinct peptide release mechanisms from the sol-gel coatings with PDMS-OH in the formulation, customisation of the behaviour of the coating relevant to the different applications could be achievable. However, a prerequisite for this would be that each mechanism of release could be controlled relatively independently. Based on the proposed microscopic structure for the sol-gel formulations one would expect that the burst release mechanism is mainly determined by the pore size of the sol-gel network. If this is the case the most obvious way to control the rate of the burst release would be to change the water to silica precursor ratio. Previous studies have shown that the water/precursor ratio affects the hydrolysis rate during the polymerisation which can lead to changes in the pore size and a thereby a faster or slower drug release rate (264, 265).

Control of the slower release rate would instead mainly rely on the properties of the hydrophobic domains. This release rate could be modified in two different ways. It could be done in a direct way by changing how tightly the peptides are bound to the hydrophobic domains, such as by changing the physiochemical properties of the surface of the domains by changing their composition. Alternatively, it could be done in an indirect way by changing the proportion of peptides bound to the hydrophobic domains. As seen when comparing the formulations with the low or high levels of PDMS-OH, when the hydrophobic domains are smaller a higher proportion of the peptides are bound to them leading to a faster effective release rate after the initial burst has concluded, even though the release rate of each individual peptide is likely similar. There might be other approaches to changing the size of the hydrophobic domain that would have a smaller impact on bulk properties of the coating rather than

changing the level of PDMS-OH in the formulation. The properties of the solvent phase during the curing process might be one such alternative aspect that could affect the domain size, as indicated by the accumulation of very large PDMS-OH deposits during the initial optimization of the coating process. If the domain size could be affected by changing the amount of water or 2-propanol added to the formulation during the step just before the coating procedure it could be an easy way to indirectly affect the peptide elution profile.

The complexity of the peptide release mechanisms seen for the sol-gel coatings highlights the potential interplay between the drug formulation and the drug design. The initial lag period seen for the formulations without PDMS-OH could potentially be alleviated using smaller peptides such as Smp14a which may be able to diffuse through the pores of the silica polymer network without the need for it to partially break down. The smaller Smp14a peptides might also affect the number of peptides that could be bound to the hydrophobic domains at a given peptide loading, shifting the elution profile toward relying more on the slower gradual release rate. Furthermore, as the slow release rate is likely directly dependent on the strength of the interactions between the peptides and the formulation, modifying the sequence of the peptide such as done during the optimization of Smp14a could also greatly affect the elution behaviour of the coating. More hydrophobic peptides such as Smp14a\_A9L might be more tightly bound to the hydrophobic domains, slowing the overall release rate down.

Some questions remain regarding the interactions between the peptides and the sol-gel formulations. Other methods not used in the project could be used to further explore the microscopic accumulation of the peptides within the coating. With the relatively high transparency of the coating, fluorescence microscopy could potentially be used to visualize the location of peptides if they were tagged with a fluorophore. If such microscopy could be used to show the peptide localized at a higher concentration on/around the hydrophobic domains, it could serve as key evidence for the proposed microscopic structure of the coating and the two distinct release mechanisms. Furthermore, it is unknown what the secondary structure of the peptides is while encapsulated within the coating. As AMPs such as Smp24 can change their secondary structure based on their environment one would expect them to at least to some

extent adopt a helical structure when interacting with the hydrophobic domains. Other studies have indicated that pre-folding AMPs into their alpha-helical structure could potentially improve their activity, which could further explain the improved biofilm inhibitory abilities of the formulations with PDMS-OH (266). Secondary structure of proteins encapsulated in sol-gels has previously been investigated using FTIR, as certain amine bonds shift dependent on the secondary structure (267). This method could potentially also be used to investigate the secondary structure of Smp24 in the sol-gel coating.

Other than antimicrobial coatings, polymeric nanoparticles are one of the main drug delivery systems that researchers try to use in combination with AMPs (268, 269). This is often done because of the rationale that encapsulating the peptides within the nanoparticles could improve their ability to penetrate biofilms as the peptides are shielded from the many components of the extra cellular matrix that they otherwise would bind to. One of the unique properties of sol-gels are that they can either create bulk polymeric networks (such as used for the coatings) or smaller nanoparticles networks depending on the conditions used during the polymerization process (38). As such the fundamentals of the formulations used for the coatings in this study could, at least in principle, relatively easily be converted into nanoparticle formulations instead. A key criterion that could limit the feasibility of such a conversion is that nanoparticles require the polymeric network to facilitate a much higher encapsulation efficiency of the drug molecule than what is needed for a sol-gel coating where most of the solvent is evaporated during the curing process. However, based on the slow release of Smp24 from the formulations containing PDMS-OH, it is likely that a high encapsulation efficiency could be achieved for sol-gel nanoparticles if they have a similar structure as seen in the sol-gel coatings. Thus, formulating the peptide with sol-gel nanoparticles using the principles learned from this study could potentially be worth exploring in the future.

## 8.2 Structure activity relationship and structure based design of Smp24 and analogs

The SAR of AMPs is difficult to define for two main reasons. Firstly, the structural properties of both the peptide and the target are much more variable and dynamic compared with a traditional small molecule-protein system, highlighted by the previous discussions of the mechanism of pore formation. Secondly, the overall mechanism of action involves several steps, from the initial interaction of the peptide with the membrane(s) up to cell death. Accounting for the entire process at once can obfuscate which underlying biophysical processes are affected by a change in the peptide structure.

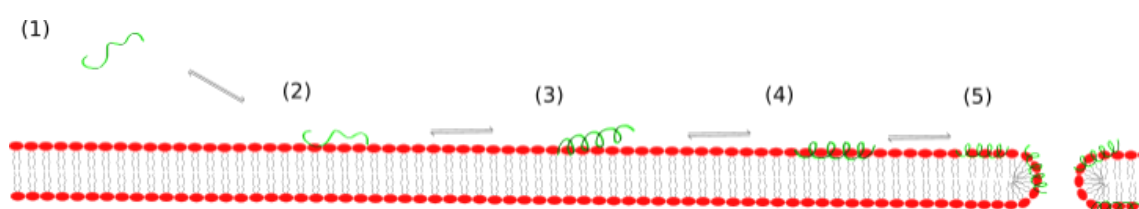


**Figure 8.1 Schematic of the different stages in the mechanism of action of antimicrobial peptides, making up the partial structure activity relationships.** 1) Peptide is unstructured in solution, 2) Initial unstructured surface associated state, 3) surface associated but helical state, 4) full inserted state, 5) pore formation.

The mechanism of action of the AMPs can be broadly separated into four different intermediate equilibria, being the transition of the peptide from solution to a bilayer surface associated state, transition to the helical structure, insertion into the top membrane leaflet and creation of membrane pores/membrane disruption (figure 8.1). Together these equilibria form a cascade leading from the unbound peptide to membrane disruption. While in reality these separations are not rigid, with the processes likely overlapping to some extent, from a drug design perspective it can be useful to separate and thereby simplify them. Each of these equilibria can be viewed as giving rise to a distinct structure activity relationship for that part of the overall process, with each of these partial SARs together making up the SAR for the entire process. The equilibria can be pushed to further the progress through the cascade by optimising the interactions between the peptide and the bilayer for each end point and thereby increasing the difference in the standard Gibbs free energy. The

thermodynamic driving force for each step can also be optimised to favour one type of lipid environment over another and thereby facilitate the selectivity of the peptide. However, changes to the peptide structure might affect more than one of the equilibriums and the effect might pull the cascade in opposite directions. If one intermediate structure is favoured too greatly it might inhibit the next step.

In addition to the changes to the structure of the peptides that occur throughout the process, so too does it affect the bilayer. The most significant change is of course in the pore formation step, but as previously shown the peptide insertion can also affect other properties of the bilayer such as the lipid packing and thickness in a concentration dependent manner. These changes might affect the different equilibriums, making the concentration dependency more complex than at first glance. However, from a drug design perspective we can only control the system from the point of view of the peptide, and this somewhat “peptide centric” approach will allow for simpler but still relatively good partial SARs.

The design of new AMPs can be more readily done by focusing on just one or two of these partial SAR depending on the objective of the modification.

To efficiently improve the selectivity of the AMP, focus should be put on the first two steps of the cascade. If a high degree of selectivity can be achieved in these early parts of the process the proportion of peptides that reach the full insertion and pore formation will be greatly reduced in the eukaryotic membrane. Thereby optimisation of these steps can be fully focused on improving the activity and do not need to take selectivity into account.

One challenge with designing based on these partial SARs is that the peptide is unstructured at this stage and therefore, the positions of individual residues in the peptide-bilayer can be difficult to predict. The peptide design must thus mainly rely on the overall physiochemical properties and residue composition, with less focus needed on the sequence order itself.

If improving the activity of the peptide is the main objective the partial SAR of the final two steps should be the focus. Optimizing configuration (4) and (5) could help to push the cascade to the conclusion and thereby membrane disruption and cell death.

While the pore formation step is the most critical for the peptide activity, several factors make it a more difficult partial SAR to use for design purposes. The variations in peptide positions and orientations, the likely requirement for multiple peptides to take part in the pore structure and a greater impact of the bilayers physiochemical properties that can be affected both by external factors and the peptide concentration all make it much more difficult to establish a reliable partial SAR. However, some characteristics such as the insertion depth in configuration (4) might be indirectly linked to the pore formation and thus the partial SAR could be explored in indirect but simpler ways such that the peptides still can be rationally optimised for pore formation.

The fully inserted configuration (4) might be the most useful partial SAR from a drug design point of view. At this step the peptide is folded into a stable structure with a consistent position and orientation relative to the bilayer. While the dynamic nature of the bilayer still makes the peptide-bilayer structure complex, it is simpler and more consistent than all the other configurations, improving the predictive capabilities of methods such as MD simulations. Another aspect is how this configuration relates to the concentration dependency for the overall process. The stoichiometry of the final equilibrium is different from the rest, requiring multiple peptides in configuration (4) to transition to configuration (5). Therefore, making configuration (4) as energetically favourable as possible could improve the overall activity, even if on a per molecule basis it makes the transition to the pore formation less favourable.

This highlights that improving the activity of the peptide based on the two final SARs is somewhat of a balancing act. Some peptide modification, such as with the S3K analog, might at the same time improve the insertion efficiency of the peptide while reducing membrane disruption efficiency. The biological effect of such a modification is thus very dependent on the properties of the specific target membrane with the improved electrostatic interactions leading to an improved activity against Gram-negative bacteria while the reduced membrane disruption efficiency led to a reduced activity against the eukaryotic cells.

### 8.3 Improving the therapeutic index of Smp24 using drug design

Improving the therapeutic index of an AMP can be achieved in two different ways, either by increasing the activity against the target pathogens or by reducing the activity against the off target cells/tissues. However, from a drug design perspective this binary viewpoint mainly works if the mechanism of action is different between the target and the off target. That way an SAR can be established for each process, and either be optimized or deoptimized depending on the objective, in such a way that the second SAR is unaffected. However, for AMPs such as Smp24 a clear mechanistic distinction between how the peptides kill prokaryotic and eukaryotic cells cannot be seen, with loss of membrane integrity being observed in both cases (137). Thus, as the mechanisms seem to be linked, reducing the intrinsic activity against eukaryotic cells is also likely to reduce the activity against bacteria and vice versa. In this case, thinking of the antimicrobial activity and cytotoxic activity as two distinct things is not the most productive approach.

A more effective approach would be to view the therapeutic index as a measure of the selectivity of the compound. Instead of focusing on how well the peptide disrupts the different cell membrane types, the focus should be on how many peptides reach the pore formation step at a given concentration in the different membrane environments. Even if a peptide is intrinsically very good at disrupting the membrane of eukaryotic cells once inserted into the membrane, if very few peptides reach full insertion at clinically relevant concentrations the therapeutic index will still be good. The key step in achieving this is to identify the differences and similarities between the membrane systems and how to best exploit them. In this regard, the most important difference between the prokaryotic and eukaryotic cell membranes is the higher proportion of negatively charged lipids in the outer leaflet of the prokaryotic cell membrane(s). The clearest way of exploiting this is by the inclusion of cationic residues in the peptide sequence, an idea supported in the MD simulations by the observation that electrostatic interactions are the main factor discriminating the relative binding energy between the two bilayer types. This is also supported experimentally with peptides with an increased charge such as Smp18, Smp14a and Smp14a\_S3K all showing increased selectivity at least when comparing between bacteria and erythrocytes. Contrary to this, hydrophobic interactions do not seem to impact the

selectivity much in the MD simulations. In the synthetic membrane models the hydrophobic core of the bilayers are very similar, while in reality a greater diversity exists such as with the inclusion of cholesterol in the eukaryotic membrane. This difference could affect some of the more complex concentration dependent peptide-membrane interactions (thinning, lipid disordering, lateral diffusion etc.), but these are likely more difficult to exploit. If only the favourability of the inserted peptide is measured, the contribution of the hydrophobic interactions seems to be almost independent of the bilayer type and likely has a negative correlation with selectivity. The experimental observations in the study support this, showing that increasing the hydrophobicity negatively impacts the selectivity. The best example of this is Smp14a\_A9L which has the most direct increase in hydrophobicity relative to its parent compound. While the low solubility in MHB made it impossible to detect a consistent MIC value, the toxicity could be evaluated showing increased activity. However, altering the hydrophobicity of a peptide could still be used as a potential strategy for improving the selectivity by instead substituting larger hydrophobic residues such as Leu or Ile with residues such as Ala to reduce the overall hydrophobicity of the peptide. As the overall binding to the prokaryotic membranes is much more favourable, such reduction in the hydrophobic interactions might disproportionately inhibit the interactions with the eukaryotic membrane. However, some hydrophobic interactions are necessary to ensure a deep insertion and correct orientation of the peptide into the prokaryotic membranes as well. The question is then where in the structure hydrophobic residues could be substituted without affecting the peptide position and orientation in the negatively charged bilayer? To ensure that the fully inserted structure is achieved, an overall hydrophobic side of the helix is necessary, but the intensity of these hydrophobic interactions do not need to be the same across the entire helix. For the peptide to adopt the orientation in parallel with the bilayer surface it is only necessary to anchor the two ends of the helix. Thus, any hydrophobic residues in the centre of the helical axis could likely be substituted without affecting the orientation too much. However, for Smp24 and its analogs the two most central hydrophobic residues alanine 8 and 9 are already relatively small making this strategy difficult to test for these peptides.

In addition to selectivity based on the overall differences between the relative strength of the electrostatic and hydrophobic interactions between the peptide and the membranes, smaller more niche differences in the membrane compositions can also be exploited. Since the charged interactions between the peptide and the lipid phosphate groups are reduced for the zwitterionic lipids making up the eukaryotic membrane other sources of electrostatic interactions might become more critical for the initial peptide-bilayer interactions. A strategy for improving the selectivity could be to inhibit these niche interactions as it would disproportionately affect the overall electrostatic interactions between the peptide and the eukaryotic bilayer. In this project this was done by replacing the tryptophan<sup>2</sup> residue with a leucine residue to retain the hydrophobic nature of the sidechain but eliminate its ability to form cation- $\pi$  interactions with the cationic lipid headgroups. Peptides such as Smp14a\_W2L showed that this approach was somewhat successful, reducing the haemolytic activity of the analog when the peptide was added in low concentrations. However, very little effect was seen in the cell line cytotoxicity assay indicating that the thermodynamic driving force caused by the cation- $\pi$  interactions quickly becomes overshadowed by other electrostatic interactions. Thus, the effect of removing tryptophan residues is limited and very dependent on the membrane composition of the target membrane, containing either a completely neutral or very small negative charge.

Perhaps the most impactful individual strategy for improving the selectivity of the peptides is to modify their ability to fold into the activity helical configuration. To a large extent this selectivity based on the helical folding is downstream from the selectivity based on the electrostatic interactions, as these interactions are the main driving force for the transition from the unstructured to the helical state. Since the electrostatic interactions between the peptide and the bilayer are greater for the prokaryotic membrane it is also easier for the peptide to fold into the helical configuration when associated with it. In thermodynamic terms, the entropy cost associated with the structural transition is intrinsically determined by the properties of the peptide itself while the enthalpy saved due to the formation of bonds and interactions between the peptide and the bilayer is much greater for the prokaryotic membrane. Thus, if the entropy cost is increased by a set amount it will disproportionately impact the structural transition when the peptide is interacting with

the eukaryotic bilayer. Therefore, making it more difficult for the peptide to transition to its helical structure can be seen as a secondary way to further exploit the differences in the electrostatic interactions between the membrane systems. In this project this was most effectively done with the Smp14a\_W2L\_S3K\_A8G peptide with the flexible glycine residue likely increasing the entropy cost of the transition. However, if the cost of transition is increased too much as was the case with the proline substituted variant the folding can be made so unfavourable that the proportion of peptides that reach their active configuration is reduced to such a degree that activity is lost even when interacting with the more enthalpically favourable prokaryotic membrane(s).

Another key observation in relation to optimising the selectivity of the peptides is that synergy can occur between the different approaches. The best example of this is with the Smp14a\_W2L\_S3K analog where the relatively minor reductions in the haemolytic activity seen for the individual residue substitutions were greatly improved when combined. Mechanistically this makes sense when looking at the mechanism of action in a stepwise manner as described in the previous section (figure 8.1). If the initial interactions between the peptide and the eukaryotic membrane are reduced, a smaller proportion of peptide will reach the surface associated stage. Furthermore, if the transition to the helical structure is made more difficult a smaller proportion of an already smaller proportion will make it to the next stage etc. further and further reducing the number of peptides that reaches the final pore formation stage. The synergistic approach for improving the selectivity of the peptide would therefore be to optimise the selectivity in as many ways as possible rather than inhibiting the interactions between the peptide and the eukaryotic membrane in one step to such a great degree that it also starts to significantly impact the interactions with prokaryotic membranes.

Overall, the strategy for improving the selectivity should be first to identify differences and similarities in the interactions between the peptides and the two bilayer types (figure 8.2). Secondly, to try to exploit these differences and similarities such that the interactions between the peptide and the eukaryotic membrane are disproportionately inhibited. And lastly, to combine different approaches to obtain a synergistic effect.

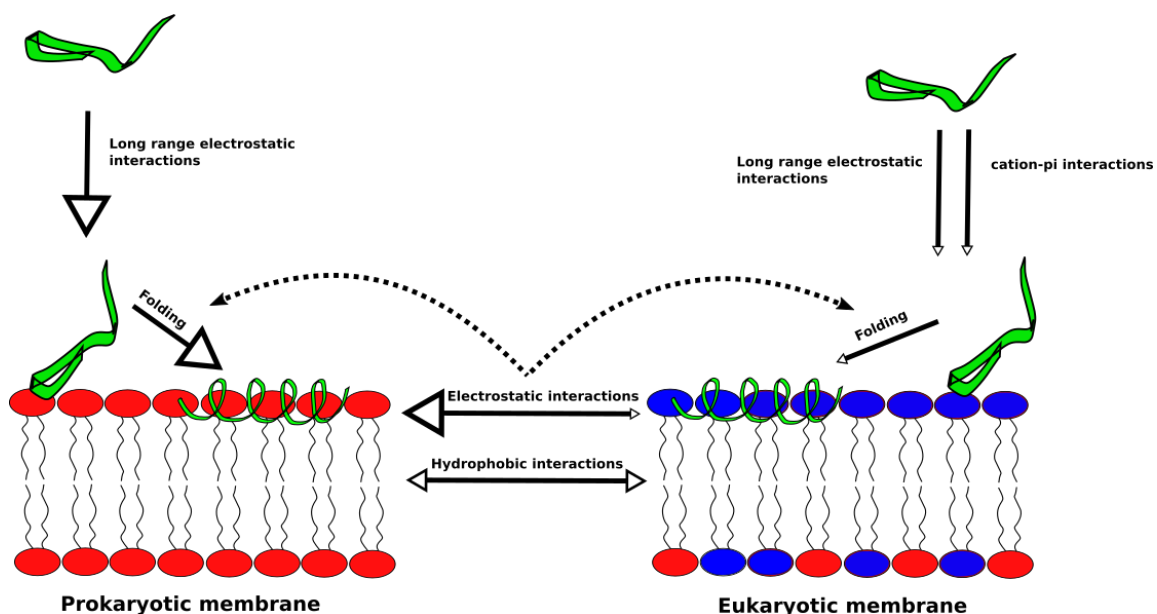


**Figure 8.2 Schematic highlighting the relative size of the different interactions and energy costs during the first three processes of the mechanism of action of the AMPs when compared between a prokaryotic and a eukaryotic membrane.**

A critical way of evaluating the overall selectivity of a peptide is to create a therapeutic index comparing the concentration needed to reach a therapeutic effect with the concentration needed to observe a toxic response. This was done for Smp24 and the best of its derivatives from each generation of the design created in this project (figure 8.3). The values are based on the MIC for the individual peptide vs the concentration needed to induce 5% haemolysis in the haemolysis assay or 10% release of LDH against HEK293 cells in the cell line cytotoxicity assay. The figures show a clear trend that the therapeutic index is generally improved for each new generation of the development process. The biggest differences are seen when comparing against the haemolytic activity with the Smp14a\_W2L\_S3K\_A8G having a therapeutic index 63-126 times greater than Smp24. The differences are much smaller when comparing against the cell line cytotoxicity, but the therapeutic indexes are still improved by 3.5-7 times between Smp24 and Smp14a\_W2L\_S3K\_A8G. These stepwise improvements to the therapeutic indexes validate the efficacy of the rational, iterative design process used throughout this project.

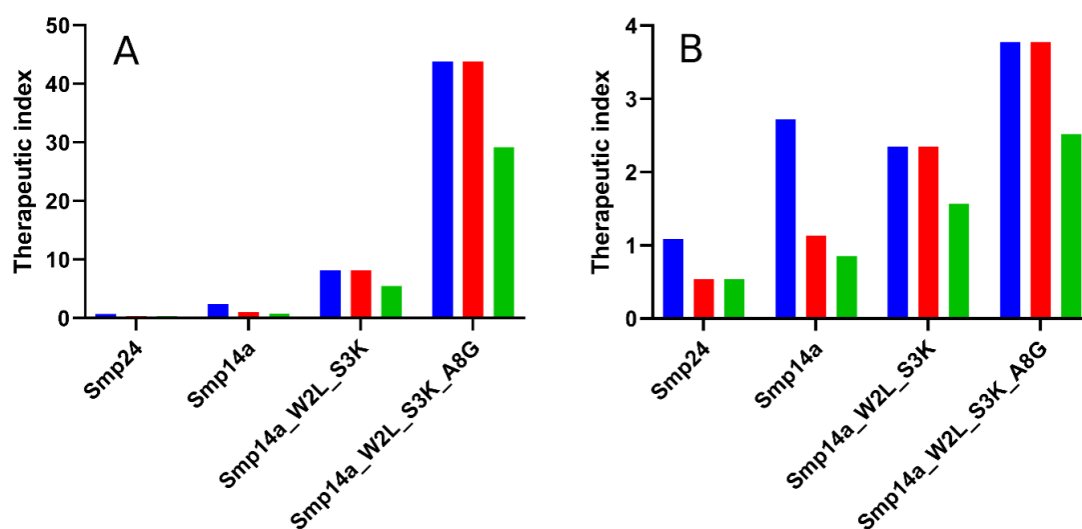


**Figure 8.3. Therapeutic indexes for Smp24 and select peptide designed through this study.** A = MICs relative to the concentration needed to induce 5% haemolytic activity, B= MICs relative to the concentration needed to induce 10% LDH release against HEK293 cells. Blue = based on the MIC against *S. aureus*, red = based on the MIC against *E. coli*, green = based on the MIC against *P. aeruginosa*.

#### 8.4 Mechanism of membrane disruption and drug design

When looking at the mechanism of membrane disruption of AMPs from a perspective focusing purely on the activity and selectivity of the peptide there is not strong evidence that one mechanism of action is better than another. However, from a drug design perspective this is not the case. The complex and disordered ways peptides like Smp24 and its derivatives disrupt the membrane makes it difficult to design new analogs based on the pore formation and structure. A key aspect of rational drug design is the ability to predict the outcome of a modification and the greater variation and complexity in the structures underlying the SAR the more difficult it is to make accurate predictions. Therefore, if the objective is to perform rational drug design based on the partial SAR highlighted in configuration (5) (figure 8.1), the first step should be to modify the peptide such that the peptide-pore assembly is more consistent.

One way could be to make the transmembrane pore associated configuration more favourable than the standard surface-oriented configuration (Figure 8.1 (5) (4)). For the peptide to adopt a more consistent configuration there must be a strong thermodynamic driving force in place to facilitate the transition between the two

configurations. As mentioned in chapter 5 this does not seem to be the case for Smp24 with the transition instead being driven by the concentration dependent effect the peptide has on the bilayer's properties. If the peptide should be modified to have a greater intrinsic preference for the transmembrane configuration the differences in the structure of the bilayer between the two configurations must first be identified. The clearest difference is the curvature of the bilayer. If the peptide could be designed to strongly prefer the high curvature of the pore lumen it could both push the equilibrium towards the pore state and give a more consistent structure. This principle is already observed to a lesser extent for Smp24 with the two pore interface associated configuration observed in the MD simulations. However, even if the peptide alignment with the high curvature pore is made more favourable it would still not necessarily lead to a sufficiently consistent peptide-pore structure for drug design purposes. If the improved alignment is achieved by increasing the flexibility of the helix the peptide will still be able to adopt a multitude of different relatively favourable configurations within different positions of the pore and the pore-bilayer interface. To avoid this the helical curvature could be made more ridged by including certain intramolecular interactions, retaining the curvature of the helix but reducing the flexibility. This could limit the range of favourable configurations that the peptide could adopt within the pore. The disadvantage is that locking the peptide structure could negatively impact the selectivity of the peptide, by limiting or even eliminating the step of the mechanism of action where the peptide transitions from unstructured into the active configuration.

Another approach could be to introduce interactions between the peptide and some other molecular component less dynamic than the lipids in the bilayer. This could be done using two different AMPs with a strong and specific interaction between them such as between their terminal ends. One peptide could serve as an anchor peptide, strongly preferring to be positioned in the pore interface rather than inside the pore itself. In contrast, the second peptide could be designed to more readily adopt a configuration within the pore. However, due to the interactions with the anchor peptide, the range of different pore-associated configurations that this peptide could adopt would be greatly reduced compared with the peptide on its own, leading to an overall much more consistent pore-peptide-peptide assembly.

An example of this principle in nature could be the heterodimeric interactions of Magainin 2 and PGLa, two AMPs found in the skin of the African frog species *Xenopus laevis*. When used together, these two peptides show a synergistic effect with maximum membrane permeabilization at a 1:1 molar ratio, indicating that a dimeric assembly is formed. Strandberg et al have investigated the structure of the peptide-peptide-pore assembly using solid-state NMR and MD simulations, showing that PGLa adopts a more extreme tilt angle compared to Magainin 2, indicating a difference in their positions in the pore assembly. The interaction between the peptides could be facilitated by charged interactions between the C-terminal regions as the C-terminal region of Magainin 2 contains two negative charges which if removed reduces the synergistic effect. The proposed model for the pore complex is that Magainin 2 is positioned around the pore interface while PGLa is inserted deeper with the two C-terminal regions overlapping, securing the relative positions of the peptides (270, 271). As the regions of the two peptides which interact with each other are relatively small it should be possible to modify other peptides to gain a similar heterodimeric function by only modifying the C-terminal region of each peptide, potentially gaining a more consistent pore structure and a synergistic effect.

#### 8.5 Further development of Smp24 and its analogs

While large improvements to the overall properties of the antimicrobial peptide have been achieved going from Sm24 to Smp14a\_W2L\_S3K\_A8G further structural improvements could still be made.

While the modification from Smp14a to Smp14a\_W2L\_S3K did show signs of the peptide reaching the point where further increase of the cationic charge would likely have diminishing returns, the alanine to glycine substitution could potentially change this. Based on the reduction in the antimicrobial activity seen for the W2L\_S3K\_A8G peptide and the observation that electrostatic interactions are the main thermodynamic driving force for the structure change, adding another lysine residue to the Smp14a\_W2L\_S3K\_A8G could potentially improve the antimicrobial activity of the peptide by allowing it to more readily fold into the active helical configuration. However, further lysine substitutions start to become challenging. Obvious targets for polar substitutions are few compared to in the earlier stages of the development process with residues such as serine3 still being part of the peptide. The threonine10

residue is the only non-charged polar residue left in the peptide structure, but as seen for several of the analogs evaluated *in silico*, substitution of this residue seems to disrupt the structure of the peptide. Another option could be the isoleucine6 residue which while hydrophobic is still the hydrophobic residue which is positioned the furthest up the side of the helix. Due to these positional challenges, it might be necessary to rearrange which positions the other lysine residues occupy. This could for example be changing the position of the threonine10 and lysine11 such that substituting the isoleucine6 residue to a lysine becomes more feasible as the change to the size of the polar face of the peptide helix would be smaller.

Another structural modification that might be worth trying could be the truncation of the lysine14 residue. As previously discussed, eliminating charges/polar interaction near the terminal of the peptide could improve membrane disruption efficiency by making it easier for the peptide to adapt a tilted configuration in the bilayer. This strategy was tried with limited success for the Smp14a\_W2L\_S3K\_ACE analog, however the removal of the N-terminal charge was seemingly a big detriment especially for the activity against the Gram-negative species. Some explanation of the limited effect could also be due to the cationic lysine3 residue being positioned so close to the N-terminal, locking the position of this end of the helix even if the N-terminal charge is neutralized. Employing the strategy at the other end of the peptide could be a better approach as the critical N-terminal would be unaffected and similar modifications has been shown to lead to improved activity for other peptides (240).

While efforts have been made towards improving both the antimicrobial activity and selectivity of Smp24 and its variants, there is another aspect of the properties of the peptide which might require improvements via structural modifications. In several administration routes, the peptides will encounter different proteolytic enzymes excreted by cells or bacteria which can break down the peptides before they reach their actual target and thereby reducing the overall activity. Thus, modifying the structure of the peptide to inhibit such degradation could potentially be a must before the peptide could see clinical use. Several studies have shown that the antimicrobial activity of AMPs is significantly reduced if evaluated in physiological fluids such as serum rather than microbiological broths (272, 273). Common strategies to circumvent the low proteolytic stability of AMPs are to incorporate unnatural amino acids,

changing some amino acids to their D-configuration, modifying the terminals of the peptide such as by acetylation or by removal of known enzymatic cleavage sites (221, 274, 275). Several of these design strategies are yet to be explored with Smp24 and its derivatives.

Lastly, a natural next step in the development process of the peptide would be to move into some *in vivo* animal testing. As the activity of AMPs is very dependent on the conditions of the surrounding environment a strong *in vitro* activity is not a guarantee that the peptide would be effective in a *in vivo* setting. The pharmacokinetic properties of the drug such as the stability, off-target binding and excretion will also greatly affect the overall efficacy. *In vivo* animal models such as neutropenic mouse thigh and lung infection models could be used to investigate the PK/PD index and further demonstrate the overall effectiveness of the peptides (276). Furthermore, animal *in vivo* toxicity studies could also be performed to get a better understanding of which tissues are most effected by the peptides and determine a more realistic therapeutic index for the peptides (277).

While most of the structural exploration and optimisation in the latter parts of this project have been focused on Smp14a due its small size and favourable biological properties, the larger peptides still have some interesting structural motifs such as the distinct tail region which could warrant more investigation. One key property of the tail region is that it serves as a natural spacer between the C-terminal and the main helical body of the peptide. This could allow for further modifications to be investigated at the C-terminal end of the peptide potentially without disrupting the function of the rest of the peptide. One strategy to potentially increase the potency of AMPs is to conjugate them with something, such as a small molecule antibiotic, giving it a secondary activity (278). The rationale for this approach is that it can exploit the cell selectivity of the AMP to deliver the high potency small molecule more effectively to the bacterial cells. To take full advantage of this approach the small molecule antibiotic should be relatively polar and thereby have a low ability to penetrate the cell membrane by itself. In this case the tail region of Smp24 or Smp18 would be ideal for the conjugation as it would position the polar compound far away from the hydrophobic region of the lipid bilayer.

## References

### References

1. Prestinaci, F.; Pezzotti, P.; Pantosti, A. Antimicrobial resistance: a global multifaceted phenomenon. *Pathogens and global health* **2015**, *109*, 309-318.
2. Nikaido, H. Multidrug resistance in bacteria. *Annu. Rev. Biochem.* **2009**, *78*, 119-146.
3. O'Neill, J. Tackling drug-resistant infections globally: final report and recommendations. **2016**.
4. Murray, C. J.; Ikuta, K. S.; Sharara, F.; Swetschinski, L.; Aguilar, G. R.; Gray, A.; Han, C.; Bisignano, C.; Rao, P.; Wool, E. Global burden of bacterial antimicrobial resistance in 2019: a systematic analysis. *The Lancet* **2022**, *399*, 629-655.
5. Huan, Y.; Kong, Q.; Mou, H.; Yi, H. Antimicrobial peptides: classification, design, application and research progress in multiple fields. *Frontiers in microbiology* **2020**, 2559.
6. Lei, J.; Sun, L.; Huang, S.; Zhu, C.; Li, P.; He, J.; Mackey, V.; Coy, D. H.; He, Q. The antimicrobial peptides and their potential clinical applications. *American journal of translational research* **2019**, *11*, 3919.
7. Assoni, L.; Milani, B.; Carvalho, M. R.; Nepomuceno, L. N.; Waz, N. T.; Guerra, M. E. S.; Converso, T. R.; Darrieux, M. Resistance Mechanisms to Antimicrobial Peptides in Gram-Positive Bacteria. *Frontiers in Microbiology* **2020**, *11*, 2362.
8. Rima, M.; Rima, M.; Fajloun, Z.; Sabatier, J.; Bechinger, B.; Naas, T. Antimicrobial peptides: A potent alternative to antibiotics. *Antibiotics* **2021**, *10*, 1095.
9. Magana, M.; Pushpanathan, M.; Santos, A. L.; Leanse, L.; Fernandez, M.; Ioannidis, A.; Giulianotti, M. A.; Apidianakis, Y.; Bradfute, S.; Ferguson, A. L. The value of antimicrobial peptides in the age of resistance. *The Lancet Infectious Diseases* **2020**, *20*, e216-e230.
10. Hale, J. D. F.; Hancock, R. E. W. Alternative mechanisms of action of cationic antimicrobial peptides on bacteria. *Expert Review of Anti-Infective Therapy* **2007**, *5*, 951-959.
11. Brogden, K. A. Antimicrobial peptides: pore formers or metabolic inhibitors in bacteria? *Nature Reviews Microbiology* *2005* **3:3** **2005**, *3*, 238-250.
12. Bechinger, B. Structure and functions of channel-forming peptides: magainins, cecropins, melittin and alamethicin. *The Journal of membrane biology* **1997**, *156*, 197-211.

13. Bechinger, B. The structure, dynamics and orientation of antimicrobial peptides in membranes by multidimensional solid-state NMR spectroscopy. *Biochimica et Biophysica Acta (BBA) - Biomembranes* **1999**, *1462*, 157-183.
14. Ashrafuzzaman, M.; Andersen, O. S.; McElhane, R. N. The Antimicrobial Peptide Gramicidin S Permeabilizes Phospholipid Bilayer Membranes Without Forming Discrete Ion Channels. *Biochimica et biophysica acta* **2008**, *1778*, 2814.
15. Bechinger, B. The SMART model: Soft Membranes Adapt and Respond, also Transiently, in the presence of antimicrobial peptides. *Journal of Peptide Science* **2015**, *21*, 346-355.
16. Percival, S. L.; Suleman, L.; Vuotto, C.; Donelli, G. Healthcare-associated infections, medical devices and biofilms: risk, tolerance and control. *Journal of medical microbiology* **2015**, *64*, 323-334.
17. Veerachamy, S.; Yarlagadda, T.; Manivasagam, G.; Yarlagadda, P. K. Bacterial adherence and biofilm formation on medical implants: a review. *Proceedings of the Institution of Mechanical Engineers. Part H, Journal of engineering in medicine* **2014**, *228*, 1083-1099.
18. Singha, P.; Locklin, J.; Handa, H. A review of the recent advances in antimicrobial coatings for urinary catheters. *Acta biomaterialia* **2017**, *50*, 20-40.
19. Simões, D.; Miguel, S. P.; Ribeiro, M. P.; Coutinho, P.; Mendonça, A. G.; Correia, I. J. Recent advances on antimicrobial wound dressing: A review. *European Journal of Pharmaceutics and Biopharmaceutics* **2018**, *127*, 130-141.
20. Chung, P. Y.; Khanum, R. Antimicrobial peptides as potential anti-biofilm agents against multidrug-resistant bacteria. *Journal of Microbiology, Immunology and Infection* **2017**, *50*, 405-410.
21. De Breij, A.; Riool, M.; Kwakman, P. H. S.; De Boer, L.; Cordfunke, R. A.; Drijfhout, J. W.; Cohen, O.; Emanuel, N.; Zaat, S. A. J.; Nibbering, P. H.; Moriarty, T. F. Prevention of Staphylococcus aureus biomaterial-associated infections using a polymer-lipid coating containing the antimicrobial peptide OP-145. *Journal of Controlled Release* **2016**, *222*, 1-8.
22. Lim, K.; Saravanan, R.; Chong, K. K. L.; Goh, S. H. M.; Chua, R. R. Y.; Tambyah, P. A.; Chang, M. W.; Kline, K. A.; Leong, S. S. J. Anhydrous polymer-based coating with sustainable controlled release functionality for facile, efficacious impregnation, and delivery of antimicrobial peptides. *Biotechnology and bioengineering* **2018**, *115*, 2000-2012.
23. Raman, N.; Lee, M. R.; Rodríguez López, A. d. L.; Palecek, S. P.; Lynn, D. M. Antifungal activity of a  $\beta$ -peptide in synthetic urine media: Toward materials-

based approaches to reducing catheter-associated urinary tract fungal infections. *Acta biomaterialia* **2016**, *43*, 240-250.

24. Riool, M.; de Breij, A.; de Boer, L.; Kwakman, P. H. S.; Cordfunke, R. A.; Cohen, O.; Malanovic, N.; Emanuel, N.; Lohner, K.; Drijfhout, J. W.; Nibbering, P. H.; Zaat, S. A. J. Controlled Release of LL-37-Derived Synthetic Antimicrobial and Anti-Biofilm Peptides SAAP-145 and SAAP-276 Prevents Experimental Biomaterial-Associated Staphylococcus aureus Infection. *Advanced Functional Materials* **2017**, *27*, 1606623.
25. Shukla, A.; Fleming, K. E.; Chuang, H. F.; Chau, T. M.; Loose, C. R.; Stephanopoulos, G. N.; Hammond, P. T. Controlling the release of peptide antimicrobial agents from surfaces. *Biomaterials* **2010**, *31*, 2348-2357.
26. Cassin, M. E.; Ford, A. J.; Orbach, S. M.; Saverot, S. E.; Rajagopalan, P. The design of antimicrobial LL37-modified collagen-hyaluronic acid detachable multilayers. *Acta biomaterialia* **2016**, *40*, 119-129.
27. Forbes, S.; McBain, A. J.; Felton-Smith, S.; Jowitt, T. A.; Birchenough, H. L.; Dobson, C. B. Comparative surface antimicrobial properties of synthetic biocides and novel human apolipoprotein E derived antimicrobial peptides. *Biomaterials* **2013**, *34*, 5453-5464.
28. Fulmer, P. A.; Wynne, J. H. Development of broad-spectrum antimicrobial latex paint surfaces employing active amphiphilic compounds. *ACS Applied Materials and Interfaces* **2011**, *3*, 2878-2884.
29. He, Y.; Zhang, Y.; Shen, X.; Tao, B.; Liu, J.; Yuan, Z.; Cai, K. The fabrication and in vitro properties of antibacterial polydopamine-LL-37-POPC coatings on micro-arc oxidized titanium. *Colloids and surfaces. B, Biointerfaces* **2018**, *170*, 54-63.
30. Rodríguez López, A. d. L.; Lee, M. R.; Ortiz, B. J.; Gastfriend, B. D.; Whitehead, R.; Lynn, D. M.; Palecek, S. P. Preventing S. aureus biofilm formation on titanium surfaces by the release of antimicrobial  $\beta$ -peptides from polyelectrolyte multilayers. *Acta biomaterialia* **2019**, *93*, 50-62.
31. Kazemzadeh-Narbat, M.; Lai, B. F. L.; Ding, C.; Kizhakkedathu, J. N.; Hancock, R. E. W.; Wang, R. Multilayered coating on titanium for controlled release of antimicrobial peptides for the prevention of implant-associated infections. *Biomaterials* **2013**, *34*, 5969-5977.
32. Tian, J.; Shen, S.; Zhou, C.; Dang, X.; Jiao, Y.; Li, L.; Ding, S.; Li, H. Investigation of the antimicrobial activity and biocompatibility of magnesium alloy coated with HA and antimicrobial peptide. *Journal of materials science. Materials in medicine* **2015**, *26*.

33. Kazemzadeh-Narbat, M.; Kindrachuk, J.; Duan, K.; Jenssen, H.; Hancock, R. E. W.; Wang, R. Antimicrobial peptides on calcium phosphate-coated titanium for the prevention of implant-associated infections. *Biomaterials* **2010**, *31*, 9519-9526.
34. Townsend, L.; Williams, R. L.; Anuforom, O.; Berwick, M. R.; Halstead, F.; Hughes, E.; Stamboulis, A.; Oppenheim, B.; Gough, J.; Grover, L.; Scott, R. A. H.; Webber, M.; Peacock, A. F. A.; Belli, A.; Logan, A.; De Cogan, F. Antimicrobial peptide coatings for hydroxyapatite: electrostatic and covalent attachment of antimicrobial peptides to surfaces. *Journal of the Royal Society Interface* **2017**, *14*.
35. Rapsch, K.; Bier, F. F.; Tadros, M.; Von Nickisch-Roseneck, M. Identification of antimicrobial peptides and immobilization strategy suitable for a covalent surface coating with biocompatible properties. *Bioconjugate chemistry* **2014**, *25*, 308-319.
36. Muszanska, A. K.; Rochford, E. T. J.; Gruszka, A.; Bastian, A. A.; Busscher, H. J.; Norde, W.; Van Der Mei, H. C.; Herrmann, A. Antiadhesive polymer brush coating functionalized with antimicrobial and RGD peptides to reduce biofilm formation and enhance tissue integration. *Biomacromolecules* **2014**, *15*, 2019-2026.
37. Paris, J. B.; Seyer, D.; Jouenne, T.; Thébault, P. Various methods to combine hyaluronic acid and antimicrobial peptides coatings and evaluation of their antibacterial behaviour. *International journal of biological macromolecules* **2019**, *139*, 468-474.
38. Owens, G. J.; Singh, R. K.; Foroutan, F.; Alqaysi, M.; Han, C. M.; Mahapatra, C.; Kim, H. W.; Knowles, J. C. Sol-gel based materials for biomedical applications. *Progress in Materials Science* **2016**, *77*, 1-79.
39. Santos, E. M.; Radin, S.; Ducheyne, P. Sol-gel derived carrier for the controlled release of proteins. *Biomaterials* **1999**, *20*, 1695-1700.
40. Radin, S.; Ducheyne, P.; Kamplain, T.; Tan, B. H. Silica sol-gel for the controlled release of antibiotics. I. Synthesis, characterization, and in vitro release. **2001**.
41. Aughenbaugh, W.; Radin, S.; Ducheyne, P. Silica sol-gel for the controlled release of antibiotics. II. The effect of synthesis parameters on the in vitro release kinetics of vancomycin. *Journal of Biomedical Materials Research: An Official Journal of The Society for Biomaterials, The Japanese Society for Biomaterials, and The Australian Society for Biomaterials and the Korean Society for Biomaterials* **2001**, *57*, 321-326.
42. Radin, S.; Ducheyne, P. Controlled release of vancomycin from thin sol-gel films on titanium alloy fracture plate material. *Biomaterials* **2007**, *28*, 1721-1729.

43. Bhattacharyya, S.; Agrawal, A.; Knabe, C.; Ducheyne, P. Sol-gel silica controlled release thin films for the inhibition of methicillin-resistant *Staphylococcus aureus*. *Biomaterials* **2014**, *35*, 509-517.
44. Radin, S.; Bhattacharyya, S.; Ducheyne, P. Nanostructural control of the release of macromolecules from silica sol-gels. *Acta biomaterialia* **2013**, *9*, 7987-7995.
45. Adams, C. S.; Antoci, V.; Harrison, G.; Patal, P.; Freeman, T. A.; Shapiro, I. M.; Parvizi, J.; Hickok, N. J.; Radin, S.; Ducheyne, P. Controlled release of vancomycin from thin sol-gel films on implant surfaces successfully controls osteomyelitis. *Journal of orthopaedic research : official publication of the Orthopaedic Research Society* **2009**, *27*, 701-709.
46. Mena, B.; Herrero, M.; Rives, V.; Lavrenko, M.; Eggers, D. K. Favourable influence of hydrophobic surfaces on protein structure in porous organically-modified silica glasses. *Biomaterials* **2008**, *29*, 2710-2718.
47. Shams, E.; Yeganeh, H.; Naderi-Manesh, H.; Gharibi, R.; Mohammad Hassan, Z. Polyurethane/siloxane membranes containing graphene oxide nanoplatelets as antimicrobial wound dressings: in vitro and in vivo evaluations. *Journal of materials science. Materials in medicine* **2017**, *28*.
48. Gharibi, R.; Yeganeh, H.; Gholami, H.; Hassan, Z. M. Aniline tetramer embedded polyurethane/siloxane membranes and their corresponding nanosilver composites as intelligent wound dressing materials. *RSC Advances* **2014**, *4*, 62046-62060.
49. Gharibi, R.; Kazemi, S.; Yeganeh, H.; Tafakori, V. Utilizing dextran to improve hemocompatibility of antimicrobial wound dressings with embedded quaternary ammonium salts. *International journal of biological macromolecules* **2019**, *131*, 1044-1056.
50. Izquierdo-Barba, I.; Vallet-Regí, M.; Kupferschmidt, N.; Terasaki, O.; Schmidtchen, A.; Malmsten, M. Incorporation of antimicrobial compounds in mesoporous silica film monolith. *Biomaterials* **2009**, *30*, 5729-5736.
51. Braun, K.; Pochert, A.; Lindén, M.; Davoudi, M.; Schmidtchen, A.; Nordström, R.; Malmsten, M. Membrane interactions of mesoporous silica nanoparticles as carriers of antimicrobial peptides. *Journal of Colloid and Interface Science* **2016**, *475*, 161-170.
52. Diosa, J.; Guzman, F.; Bernal, C.; Mesa, M. Formation mechanisms of chitosan-silica hybrid materials and its performance as solid support for KR-12 peptide adsorption: Impact on KR-12 antimicrobial activity and proteolytic stability. *Journal of Materials Research and Technology* **2020**, *9*, 890-901.

53. Aquila, M.; Benedusi, M.; Milani, A.; Rispoli, G.; Aquila, M.; Benedusi, M.; Milani, A.; Rispoli, G. Enhanced Patch-Clamp Technique to Study Antimicrobial Peptides and Viroporins, Inserted in a Cell Plasma Membrane with Fully Inactivated Endogenous Conductances. *Patch Clamp Technique* **2012**.
54. Rispoli, G. Studying the Mechanism of Membrane Permeabilization Induced by Antimicrobial Peptides Using Patch-Clamp Techniques. *Methods in molecular biology (Clifton, N.J.)* **2017**, *1548*, 255-269.
55. Martinac, B.; Rohde, P. R.; Cranfield, C. G.; Nomura, T. Patch clamp electrophysiology for the study of bacterial ion channels in giant spheroplasts of *E. coli*. *Methods in molecular biology (Clifton, N.J.)* **2013**, *966*, 367-380.
56. Fasoli, A.; Salomone, F.; Benedusi, M.; Boccardi, C.; Rispoli, G.; Beltram, F.; Cardarelli, F. Mechanistic insight into CM18-Tat11 peptide membrane-perturbing action by whole-cell patch-clamp recording. *Molecules (Basel, Switzerland)* **2014**, *19*, 9228-9239.
57. Aquila, M.; Benedusi, M.; Koch, K. W.; Dell'Orco, D.; Rispoli, G. Divalent cations modulate membrane binding and pore formation of a potent antibiotic peptide analog of alamethicin. *Cell calcium* **2013**, *53*, 180-186.
58. Harrison, P. L.; Heath, G. R.; Johnson, B. R. G.; Abdel-Rahman, M. A.; Strong, P. N.; Evans, S. D.; Miller, K. Phospholipid dependent mechanism of smp24, an  $\alpha$ -helical antimicrobial peptide from scorpion venom. *Biochimica et Biophysica Acta - Biomembranes* **2016**, *1858*, 2737-2744.
59. Gallucci, E.; Meleleo, D.; Micelli, S.; Picciarelli, V. Magainin 2 channel formation in planar lipid membranes: the role of lipid polar groups and ergosterol. *European biophysics journal : EBJ* **2003**, *32*, 22-32.
60. Jiang, Y.; Idikuda, V.; Chanda, B. Preparation of Giant Escherichia coli spheroplasts for Electrophysiological Recordings. *Bio-protocol* **2021**, *11*, e4261.
61. Kikuchi, K.; Sugiura, M.; Nishizawa-Harada, C.; Kimura, T. The application of the Escherichia coli giant spheroplast for drug screening with automated planar patch clamp system. *Biotechnology Reports* **2015**, *7*, 17.
62. Kuo, M. M. C.; Saimi, Y.; Kung, C.; Choe, S. Patch Clamp and Phenotypic Analyses of a Prokaryotic Cyclic Nucleotide-gated K<sup>+</sup> Channel Using Escherichia coli as a Host. *J. Biol. Chem.* **2007**, *282*, 24294-24301.
63. Martinac, B.; Rohde, P. R.; Cranfield, C. G.; Nomura, T. Patch clamp electrophysiology for the study of bacterial ion channels in giant spheroplasts of *E. coli*. *Methods in Molecular Biology* **2013**, *966*, 367-380.

64. Wei, L.; LaBouyer, M. A.; Darling, L. E. O.; Elmore, D. E. Bacterial Spheroplasts as a Model for Visualizing Membrane Translocation of Antimicrobial Peptides. *Antimicrob. Agents Chemother.* **2016**, *60*, 6350.
65. Sun, Y.; Sun, T. L.; Huang, H. W. Mode of Action of Antimicrobial Peptides on E. coli Spheroplasts. *Biophys. J.* **2016**, *111*, 132-139.
66. Benedusi, M.; Fasoli, A.; Bobone, S.; Orioni, B.; De Zotti, M.; Formaggio, F.; Toniolo, M. C.; Stella, L.; Rispoli, G. In *In Single-Channel Properties of Peptides Inserted in Natural and Artificial Membranes*; 22nd American Peptide Symposium; WILEY-BLACKWELL: 2011; Vol. 96, pp 497.
67. Benedusi, M.; Milani, A.; Aquila, M.; Rispoli, G. Divalent Cations Regulate Pore Formation of Synthetic, Naturally Occurring Alamethicin and Selected Analogs. *Biophys. J.* **2010**, *98*, 107a.
68. Madan, V.; Sánchez-Martínez, S.; Vedovato, N.; Rispoli, G.; Carrasco, L.; Nieva, J. L. Plasma Membrane-porating Domain in Poliovirus 2B Protein. A Short Peptide Mimics Viroporin Activity. *Journal of Molecular Biology* **2007**, *374*, 951-964.
69. Milani, A.; Benedusi, M.; Aquila, M.; Rispoli, G. Pore Forming Properties of Cecropin-Melittin Hybrid Peptide in a Natural Membrane. *Molecules* **2009**, *Vol. 14*, Pages 5179-5188 **2009**, *14*, 5179-5188.
70. Rispoli, G.; Milani, A.; Infanti, M.; Benedusi, M.; Aquila, M.; Vedovato, N. Pore forming properties of antimicrobial peptides in different natural lipid environment. *Biophys. J.* **2009**, *96*, 535a.
71. Vedovato, N.; Baldini, C.; Toniolo, C.; Rispoli, G. Pore-Forming Properties of Alamethicin F50/5 Inserted in a Biological Membrane. *Chemistry & Biodiversity* **2007**, *4*, 1338-1346.
72. Vedovato, N.; Rispoli, G. A novel technique to study pore-forming peptides in a natural membrane. *European Biophysics Journal* **2007**, *36*, 771-778.
73. Yue, G.; Merlin, D.; Selsted, M. E.; Lencer, W. I.; Madara, J. L.; Eaton, D. C. Cryptdin 3 forms anion selective channels in cytoplasmic membranes of human embryonic kidney cells. *American journal of physiology. Gastrointestinal and liver physiology* **2002**, *282*.
74. Ye, J. S.; Zheng, X. J.; Leung, K. W.; Chen, H. M.; Sheu, F. S. Induction of transient ion channel-like pores in a cancer cell by antibiotic peptide. *Journal of biochemistry* **2004**, *136*, 255-259.

75. Souza, A. L. A.; Faria, R. X.; Calabrese, K. S.; Hardoim, D. J.; Taniwaki, N.; Alves, L. A.; De Simone, S. G. Temporizin and Temporizin-1 Peptides as Novel Candidates for Eliminating *Trypanosoma cruzi*. *PLOS ONE* **2016**, *11*, e0157673.
76. Haimovich, B.; Tanaka, J. C. Magainin-induced cytotoxicity in eukaryotic cells: kinetics, dose-response and channel characteristics. *Biochimica et biophysica acta* **1995**, *1240*, 149-158.
77. Kouri, K.; Lemmens, M.; Lemmens-Gruber, R. Beauvericin-induced channels in ventricular myocytes and liposomes. *Biochimica et Biophysica Acta - Biomembranes* **2003**, *1609*, 203-210.
78. Cociancich, S.; Ghazi, A.; Hetru, C.; Hoffmann, J. A.; Letellier, L. Insect defensin, an inducible antibacterial peptide, forms voltage-dependent channels in *Micrococcus luteus*. *Journal of Biological Chemistry* **1993**, *268*, 19239-19245.
79. Llanos, P.; Henriquez, M.; Minic, J.; Elmorjani, K.; Marion, D.; Riquelme, G.; Molgó, J.; Benoit, E. Puroindoline-a and alpha1-purothionin form ion channels in giant liposomes but exert different toxic actions on murine cells. *The FEBS journal* **2006**, *273*, 1710-1722.
80. Cosette, P.; Rebuffat, S.; Bodo, B.; Molle, G. The ion-channel activity of longibrachins LGA I and LGB II: effects of pro-2/Ala and gln-18/Glu substitutions on the alamethicin voltage-gated membrane channels. *Biochimica et biophysica acta* **1999**, *1461*, 113-122.
81. Higashimoto, Y.; Kodama, H.; Jelokhani-Niaraki, M.; Kato, F.; Kondo, M. Structure-function relationship of model Aib-containing peptides as ion transfer intermembrane templates. *Journal of biochemistry* **1999**, *125*, 705-712.
82. Lougheed, T.; Borisenko, V.; Hand, C. E.; Woolley, G. A. Fluorescent gramicidin derivatives for single-molecule fluorescence and ion channel measurements. *Bioconjugate Chemistry* **2001**, *12*, 594-602.
83. Saint, N.; Cadiou, H.; Bessin, Y.; Molle, G. Antibacterial peptide pleurocidin forms ion channels in planar lipid bilayers. *Biochimica et Biophysica Acta (BBA) - Biomembranes* **2002**, *1564*, 359-364.
84. Bertrand, B.; Munusamy, S.; Espinosa-Romero, J. F.; Corzo, G.; Arenas Sosa, I.; Galván-Hernández, A.; Ortega-Blake, I.; Hernández-Adame, P. L.; Ruiz-García, J.; Velasco-Bolom, J. L.; Garduño-Juárez, R.; Muñoz-Garay, C. Biophysical characterization of the insertion of two potent antimicrobial peptides-Pin2 and its variant Pin2[GVG] in biological model membranes. *Biochimica et Biophysica Acta - Biomembranes* **2020**, *1862*, 183105.

85. Christensen, B.; Fink, J.; Merrifield, R. B.; Mauzerall, D. Channel-forming properties of cecropins and related model compounds incorporated into planar lipid membranes. *Proceedings of the National Academy of Sciences of the United States of America* **1988**, *85*, 5072.
86. Luchian, T. The Modulatory Effect of Calcium Ions Upon Alamethicin Monomers Uptake on Artificial Phospholipid Membranes. *Journal of Biological Physics* **2005**, *31*, 23.
87. Fennouri, A.; Mayer, S. F.; Schroeder, T. B. H.; Mayer, M. Single channel planar lipid bilayer recordings of the melittin variant MelP5. *Biochimica et Biophysica Acta (BBA) - Biomembranes* **2017**, *1859*, 2051-2057.
88. Pham, T.; Perry, J. L.; Dosey, T. L.; Delcour, A. H.; Hyser, J. M. The Rotavirus NSP4 Viroporin Domain is a Calcium-conducting Ion Channel. *Scientific Reports* **2017** *7*:1 **2017**, *7*, 1-11.
89. Rangel, M.; dos Santos Cabrera, M. P.; Kazuma, K.; Ando, K.; Wang, X.; Kato, M.; Nihei, K. i.; Hirata, I. Y.; Cross, T. J.; Garcia, A. N.; Faquim-Mauro, E. L.; Franzolin, M. R.; Fuchino, H.; Mori-Yasumoto, K.; Sekita, S.; Kadowaki, M.; Satake, M.; Konno, K. Chemical and biological characterization of four new linear cationic  $\alpha$ -helical peptides from the venoms of two solitary eumenine wasps. *Toxicon : official journal of the International Society on Toxinology* **2011**, *57*, 1081-1092.
90. Song, C.; Weichbrodt, C.; Salnikov, E. S.; Dynowski, M.; Forsberg, B. O.; Bechinger, B.; Steinem, C.; De Groot, B. L.; Zachariae, U.; Zeth, K. Crystal structure and functional mechanism of a human antimicrobial membrane channel. *Proceedings of the National Academy of Sciences of the United States of America* **2013**, *110*, 4586-4591.
91. Kazuma, K.; Ando, K.; Nihei, K. i.; Wang, X.; Rangel, M.; Franzolin, M. R.; Mori-Yasumoto, K.; Sekita, S.; Kadowaki, M.; Satake, M.; Konno, K. Peptidomic analysis of the venom of the solitary bee *Xylocopa appendiculata circumvolans*. *The Journal of Venomous Animals and Toxins Including Tropical Diseases* **2017**, *23*.
92. Silva, J. C.; Neto, L. M.; Neves, R. C.; Gonçalves, J. C.; Trentini, M. M.; Mucury-Filho, R.; Smidt, K. S.; Fensterseifer, I. C.; Silva, O. N.; Lima, L. D.; Clissa, P. B.; Vilela, N.; Guilhelmelli, F.; Silva, L. P.; Rangel, M.; Kipnis, A.; Silva-Pereira, I.; Franco, O. L.; Junqueira-Kipnis, A. P.; Bocca, A. L.; Mortari, M. R. Evaluation of the antimicrobial activity of the mastoparan Polybia-MPII isolated from venom of the social wasp *Pseudopolybia vespiceps testacea* (Vespidae, Hymenoptera). *International journal of antimicrobial agents* **2017**, *49*, 167-175.
93. Chooduang, S.; Surya, W.; Torres, J.; Boonserm, P. An aromatic cluster in *Lysinibacillus sphaericus* BinB involved in toxicity and proper in-membrane folding. *Archives of Biochemistry and Biophysics* **2018**, *660*, 29-35.

94. Manzo, G.; Ferguson, P. M.; Hind, C.; Clifford, M.; Gustilo, V. B.; Ali, H.; Bansal, S. S.; Bui, T. T.; Drake, A. F.; Atkinson, R. A.; Sutton, M. J.; Lorenz, C. D.; Phoenix, D. A.; Mason, A. J. Parallel evolution of frog antimicrobial peptides produces identical conformations but subtly distinct membrane and antibacterial activities. *bioRxiv* **2018**, 388967.
95. Manzo, G.; Ferguson, P. M.; Gustilo, V. B.; Hind, C. K.; Clifford, M.; Bui, T. T.; Drake, A. F.; Atkinson, R. A.; Sutton, J. M.; Batoni, G.; Lorenz, C. D.; Phoenix, D. A.; James Mason, A. Minor sequence modifications in temporin B cause drastic changes in antibacterial potency and selectivity by fundamentally altering membrane activity. *Scientific Reports* **2019**, *9*, 1-16.
96. Manzo, G.; Ferguson, P. M.; Hind, C. K.; Clifford, M.; Gustilo, V. B.; Ali, H.; Bansal, S. S.; Bui, T. T.; Drake, A. F.; Atkinson, R. A.; Sutton, J. M.; Lorenz, C. D.; Phoenix, D. A.; Mason, A. J. Temporin L and aurein 2.5 have identical conformations but subtly distinct membrane and antibacterial activities. *Scientific Reports* **2019**, *9*, 10934.
97. Fertig, N.; Meyer, C.; Blick, R. H.; Trautmann, C.; Behrends, J. C. Microstructured glass chip for ion-channel electrophysiology. *Physical review. E, Statistical, nonlinear, and soft matter physics* **2001**, *64*, 4.
98. Zhang, M.; Zhu, P. P.; Xin, P.; Si, W.; Li, Z. T.; Hou, J. L. Synthetic Channel Specifically Inserts into the Lipid Bilayer of Gram-Positive Bacteria but not that of Mammalian Erythrocytes. *Angewandte Chemie International Edition* **2017**, *56*, 2999-3003.
99. Watanabe, H.; Kawano, R. Channel Current Analysis for Pore-forming Properties of an Antimicrobial Peptide, Magainin 1, Using the Droplet Contact Method. *Analytical Sciences* **2016**, *32*, 57-60.
100. Sondermann, M.; George, M.; Fertig, N.; Behrends, J. C. High-resolution electrophysiology on a chip: Transient dynamics of alamethicin channel formation. *Biochimica et Biophysica Acta (BBA) - Biomembranes* **2006**, *1758*, 545-551.
101. Matsuoka, S.; Shinohara, N.; Takahashi, T.; Iida, M.; Inoue, M. Functional Analysis of Synthetic Substructures of Polytheonamide B: A Transmembrane Channel-Forming Peptide. *Angewandte Chemie International Edition* **2011**, *50*, 4879-4883.
102. Chistyulin, D. K.; Rokitskaya, T. I.; Kovalchuk, S. I.; Sorochkina, A. I.; Firsov, A. M.; Kotova, E. A.; Antonenko, Y. N. pH-Dependent properties of ion channels formed by N-terminally glutamate substituted gramicidin A in planar lipid bilayers. *Biochimica et Biophysica Acta (BBA) - Biomembranes* **2017**, *1859*, 896-902.
103. Kara, S.; Afonin, S.; Babii, O.; Tkachenko, A. N.; Komarov, I. V.; Ulrich, A. S. Diphtanoyl lipids as model systems for studying membrane-active peptides. *Biochimica et biophysica acta. Biomembranes* **2017**, *1859*, 1828-1837.

104. Fadda, G. C.; Lairez, D.; Guennouni, Z.; Koutsioubas, A. Peptide pores in lipid bilayers: Voltage facilitation pleads for a revised model. *Physical Review Letters* **2013**, *111*, 028102.
105. Chui, J. K. W.; Fyles, T. M. Ionic conductance of synthetic channels: analysis, lessons, and recommendations. *Chemical Society Reviews* **2011**, *41*, 148-175.
106. Hollingsworth, S. A.; Dror, R. O. Molecular Dynamics Simulation for All. *Neuron* **2018**, *99*, 1129-1143.
107. Durrant, J. D.; McCammon, J. A. Molecular dynamics simulations and drug discovery. *BMC Biology* **2011**, *9*, 1-9.
108. González, M. A. Force fields and molecular dynamics simulations. *École thématique de la Société Française de la Neutronique* **2011**, *12*, 169-200.
109. Abraham, M. J.; Murtola, T.; Schulz, R.; Páll, S.; Smith, J. C.; Hess, B.; Lindah, E. Gromacs: High performance molecular simulations through multi-level parallelism from laptops to supercomputers. *SoftwareX* **2015**, *1-2*, 19-25.
110. Kutzner, C.; Páll, S.; Fechner, M.; Esztermann, A.; de Groot, B. L.; Grubmüller, H. More bang for your buck: Improved use of GPU nodes for GROMACS 2018. *Journal of Computational Chemistry* **2019**, *40*, 2418-2431.
111. Bobone, S.; Bocchinfuso, G.; Park, Y.; Palleschi, A.; Hahm, K. S.; Stella, L. The importance of being kinked: role of Pro residues in the selectivity of the helical antimicrobial peptide P5. *Journal of Peptide Science* **2013**, *19*, 758-769.
112. Agbale, C. M.; Sarfo, J. K.; Galyuon, I. K.; Juliano, S. A.; Silva, G. G. O.; Buccini, D. F.; Cardoso, M. H.; Torres, M. D. T.; Angeles-Boza, A. M.; De La Fuente-Nunez, C.; Franco, O. L. Antimicrobial and Antibiofilm Activities of Helical Antimicrobial Peptide Sequences Incorporating Metal-Binding Motifs. *Biochemistry* **2019**, *58*, 3802-3812.
113. Borocci, S.; Pelle, G. D.; Ceccacci, F.; Olivieri, C.; Buonocore, F.; Porcelli, F. Structural analysis and design of chionodracine- derived peptides using circular dichroism and molecular dynamics simulations. *International Journal of Molecular Sciences* **2020**, *21*.
114. Aschi, M.; Perini, N.; Bouchemal, N.; Luzi, C.; Savarin, P.; Migliore, L.; Bozzi, A.; Sette, M. Structural characterization and biological activity of Crabrolin peptide isoforms with different positive charge. *Biochimica et Biophysica Acta - Biomembranes* **2020**, *1862*.
115. Ramos-Martín, F.; Herrera-León, C.; Antonietti, V.; Sonnet, P.; Sarazin, C.; D'Amelio, N. Antimicrobial Peptide K11 Selectively Recognizes Bacterial

Biomimetic Membranes and Acts by Twisting Their Bilayers. *Pharmaceuticals* 2021, Vol. 14, Page 1 **2020**, 14, 1.

116. AnnaVal, T.; Ramos-Martín, F.; Herrera-León, C.; Adélaïde, M.; Antonietti, V.; Buchoux, S.; Sonnet, P.; Sarazin, C.; D'Amelio, N. Antimicrobial Bombinin-like Peptide 3 Selectively Recognizes and Inserts into Bacterial Biomimetic Bilayers in Multiple Steps. *Journal of Medicinal Chemistry* **2021**, 64, 5185-5197.
117. Jahangiri, S.; Jafari, M.; Arjomand, M.; Mehrnejad, F. Molecular insights into the interactions of GF-17 with the gram-negative and gram-positive bacterial lipid bilayers. *Journal of Cellular Biochemistry* **2018**, 119, 9205-9216.
118. Mihailescu, M.; Sorci, M.; Seckute, J.; Silin, V. I.; Hammer, J.; Perrin, B. S.; Hernandez, J. I.; Smajic, N.; Shrestha, A.; Bogardus, K. A.; Greenwood, A. I.; Fu, R.; Blazyk, J.; Pastor, R. W.; Nicholson, L. K.; Belfort, G.; Cotten, M. L. Structure and Function in Antimicrobial Piscidins: Histidine Position, Directionality of Membrane Insertion, and pH-Dependent Permeabilization. *Journal of the American Chemical Society* **2019**, 141, 9837-9853.
119. Chakraborty, A.; Kobzev, E.; Chan, J.; Zoysa, G. H. d.; Sarojini, V.; Piggot, T. J.; Allison, J. R. Molecular Dynamics Simulation of the Interaction of Two Linear Battacin Analogs with Model Gram-Positive and Gram-Negative Bacterial Cell Membranes. *ACS Omega* **2020**, 6, 388-400.
120. Bédard, F.; Fliss, I.; Biron, E. Structure-Activity Relationships of the Bacteriocin Bactofencin A and Its Interaction with the Bacterial Membrane. *ACS Infectious Diseases* **2019**, 5, 199-207.
121. Ulmschneider, J. P.; Smith, J. C.; Ulmschneider, M. B.; Ulrich, A. S.; Strandberg, E. Reorientation and Dimerization of the Membrane-Bound Antimicrobial Peptide PGLa from Microsecond All-Atom MD Simulations. *Biophysical Journal* **2012**, 103, 472-482.
122. Liscano, Y.; Salamanca, C. H.; Vargas, L.; Cantor, S.; Laverde-Rojas, V.; Oñate-Garzón, J. Increases in hydrophilicity and charge on the polar face of alyteserin 1c helix change its selectivity towards gram-positive bacteria. *Antibiotics* **2019**, 8.
123. Jafari, M.; Mehrnejad, F.; Aghdami, R.; Chaparzadeh, N.; Razaghi Moghadam Kashani, Z.; Doustdar, F. Identification of the Crucial Residues in the Early Insertion of Pardaxin into Different Phospholipid Bilayers. **2017**.
124. Chen, C. H.; Starr, C. G.; Guha, S.; Wimley, W. C.; Ulmschneider, M. B.; Ulmschneider, J. P. Tuning of a Membrane-Perforating Antimicrobial Peptide to Selectively Target Membranes of Different Lipid Composition. *The Journal of Membrane Biology* 2021 254:1 **2021**, 254, 75-96.

125. Ma, R.; Wong, S. W.; Ge, L.; Shaw, C.; Siu, S. W. I.; Kwok, H. F. In Vitro and MD Simulation Study to Explore Physicochemical Parameters for Antibacterial Peptide to Become Potent Anticancer Peptide. *Molecular Therapy - Oncolytics* **2020**, *16*, 7-19.
126. Ghafari, M. D.; Rasooli, I.; Khajeh, K.; Dabirmanesh, B.; Owlia, P. Molecular Dynamics Study of the Human Beta-defensins 2 and 3 Chimeric Peptides with the Cell Membrane Model of *Pseudomonas aeruginosa*. *International Journal of Peptide Research and Therapeutics* **2020**, *26*, 2039-2056.
127. Vasudevan, S. V.; Kumar, A. Antimicrobial peptide ROAD-1 triggers phase change in local membrane environment to execute its activity. *Journal of Molecular Modeling* **2019**, *25*, 1-15.
128. Sayyed-Ahmad, A.; Khandelia, H.; Kaznessis, Y. N. Relative free energy of binding between antimicrobial peptides and SDS or DPC micelles. *Molecular Simulation* **2009**, *35*, 986-997.
129. Lipkin, R.; Lazaridis, T. Computational studies of peptide-induced membrane pore formation. *Phil. Trans. R. Soc. B* **2017**, *372*, 20160219.
130. Cheraghi, N.; Hosseini, M.; Mohammadinejad, S. Pore formation and the key factors in antibacterial activity of aurein 1.2 and LLAA inside lipid bilayers, a molecular dynamics study. *Biochimica et Biophysica Acta (BBA) - Biomembranes* **2018**, *1860*, 347-356.
131. Talandashti, R.; Mehrnejad, F.; Rostamipour, K.; Doustdar, F.; Lavasanifar, A. Molecular Insights into Pore Formation Mechanism, Membrane Perturbation, and Water Permeation by the Antimicrobial Peptide Pleurocidin: A Combined All-Atom and Coarse-Grained Molecular Dynamics Simulation Study. *The Journal of Physical Chemistry B* **2021**, *125*, 7163-7176.
132. Sun, D.; Forsman, J.; Woodward, C. E. Multistep Molecular Dynamics Simulations Identify the Highly Cooperative Activity of Melittin in Recognizing and Stabilizing Membrane Pores. *Langmuir* **2015**, *31*, 9388-9401.
133. Puentes, P. R.; Henao, M. C.; Torres, C. E.; Gómez, S. C.; Gómez, L. A.; Burgos, J. C.; Arbeláez, P.; Osma, J. F.; Muñoz-Camargo, C.; Reyes, L. H.; Cruz, J. C. Design, Screening, and Testing of Non-Rational Peptide Libraries with Antimicrobial Activity: In Silico and Experimental Approaches. *Antibiotics* **2020**, *Vol. 9*, Page 854 **2020**, *9*, 854.
134. Ruiz Puentes, P.; Henao, M. C.; Cifuentes, J.; Muñoz-Camargo, C.; Reyes, L. H.; Cruz, J. C.; Arbeláez, P. Rational Discovery of Antimicrobial Peptides by Means of Artificial Intelligence. *Membranes* **2022**, *12*, 708.

135. Pandit, G.; Biswas, K.; Ghosh, S.; Debnath, S.; Bidkar, A. P.; Satpati, P.; Bhunia, A.; Chatterjee, S. Rationally designed antimicrobial peptides: Insight into the mechanism of eleven residue peptides against microbial infections. *Biochimica et Biophysica Acta - Biomembranes* **2020**, *1862*, 183177.
136. Huynh, L.; Velásquez, J.; Rabara, R.; Basu, S.; Nguyen, H. B.; Gupta, G. Rational design of antimicrobial peptides targeting Gram-negative bacteria. *Computational Biology and Chemistry* **2021**, *92*, 107475.
137. Harrison, P. L.; Abdel-Rahman, M. A.; Strong, P. N.; Tawfik, M. M.; Miller, K. Characterisation of three alpha-helical antimicrobial peptides from the venom of *Scorpio maurus palmatus*. *Toxicon* **2016**, *117*, 30-36.
138. Elrayess, R. A.; Mohallal, M. E.; El-Shahat, Y. M.; Ebaid, H. M.; Miller, K.; Strong, P. N.; Abdel-Rahman, M. A. Cytotoxic Effects of Smp24 and Smp43 Scorpion Venom Antimicrobial Peptides on Tumour and Non-tumour Cell Lines. *International Journal of Peptide Research and Therapeutics* **2020**, *26*, 1409-1415.
139. Nichol, T.; Callaghan, J.; Townsend, R.; Stockley, I.; Hatton, P. V.; Le Maitre, C.; Smith, T. J.; Akid, R. The antimicrobial activity and biocompatibility of a controlled gentamicin-releasing single-layer sol-gel coating on hydroxyapatite-coated titanium. *Bone and Joint Journal* **2021**, *103 B*, 522-529.
140. Horsburgh, M. J.; Aish, J. L.; White, I. J.; Shaw, L.; Lithgow, J. K.; Foster, S. J.  $\sigma$ B modulates virulence determinant expression and stress resistance: characterization of a functional rsbU strain derived from *Staphylococcus aureus* 8325-4. *J. Bacteriol.* **2002**, *184*, 5457-5467.
141. Skogman, M. E.; Vuorela, P. M.; Fallarero, A. A platform of anti-biofilm assays suited to the exploration of natural compound libraries. *Journal of Visualized Experiments* **2016**, *2016*, e54829.
142. Brüggemann, A.; Farre, C.; Haarmann, C.; Haythornthwaite, A.; Kreir, M.; Stoelzle, S.; George, M.; Fertig, N. Planar patch clamp: Advances in electrophysiology. *Methods in Molecular Biology* **2008**, *491*, 165-176.
143. Mark, D. F.; Chase, J. W.; Richardson, C. C. Genetic mapping of *trxA*, a gene affecting thioredoxin in *Escherichia coli* K12. *Molecular and General Genetics MGG* **1977**, *155*, 145-152.
144. Holloway, B. W. Genetic recombination in *Pseudomonas aeruginosa*. *Microbiology* **1955**, *13*, 572-581.
145. Andrews, J. M. Determination of minimum inhibitory concentrations. *Journal of Antimicrobial Chemotherapy* **2001**, *48*, 5-16.

146. Corzo, G.; Escoubas, P.; Villegas, E.; Barnham, K. J.; He, W.; Norton, R. S.; Nakajima, T. Characterization of unique amphipathic antimicrobial peptides from venom of the scorpion *Pandinus imperator*. *Biochem. J* **2001**, *359*, 35-45.
147. Graham, F. L.; Smiley, J.; Russell, W. C.; Nairn, R. Characteristics of a human cell line transformed by DNA from human adenovirus type 5. *J. Gen. Virol.* **1977**, *36*, 59-72.
148. Aden, D. P.; Fogel, A.; Plotkin, S.; Damjanov, I.; Knowles, B. B. Controlled synthesis of HBsAg in a differentiated human liver carcinoma-derived cell line. *Nature* **1979**, *282*, 615-616.
149. Rawson, K. M.; Lacey, M. M.; Strong, P. N.; Miller, K. Improving the Therapeutic Index of Smp24, a Venom-Derived Antimicrobial Peptide: Increased Activity against Gram-Negative Bacteria. *International Journal of Molecular Sciences* **2022**, *23*, 7979.
150. Lemkul, J. A. From proteins to perturbed Hamiltonians: a suite of tutorials for the GROMACS-2018 molecular simulation package [article v1. 0]. *Living Journal of Computational Molecular Science* **2018**, *1*, 33011.
151. Lamiable, A.; Thevenet, P.; Rey, J.; Vavrusa, M.; Derreumaux, P.; Tuffery, P. PEP-FOLD3: faster de novo structure prediction for linear peptides in solution and in complex. *Nucleic Acids Research* **2016**, *44*, W449.
152. Gerig, J. T. Toward a molecular dynamics force field for simulations of 40% trifluoroethanol-water. *Journal of Physical Chemistry B* **2014**, *118*, 1471-1480.
153. Lee, J.; Cheng, X.; Swails, J. M.; Yeom, M. S.; Eastman, P. K.; Lemkul, J. A.; Wei, S.; Buckner, J.; Jeong, J. C.; Qi, Y.; Jo, S.; Pande, V. S.; Case, D. A.; Brooks, C. L. I., II; MacKerell, A. D. J.; Klauda, J. B.; Im, W. CHARMM-GUI Input Generator for NAMD, GROMACS, AMBER, OpenMM, and CHARMM/OpenMM Simulations Using the CHARMM36 Additive Force Field. *J. Chem. Theory Comput.* **2016**, *12*, 405-413.
154. Wang, C.; Greene, D.; Xiao, L.; Qi, R.; Luo, R. Recent Developments and Applications of the MMPBSA Method. *Frontiers in Molecular Biosciences* **2018**, *0*, 87.
155. Miller, B. R.; McGee, T. D.; Swails, J. M.; Homeyer, N.; Gohlke, H.; Roitberg, A. E. MMPBSA.py: An efficient program for end-state free energy calculations. *Journal of Chemical Theory and Computation* **2012**, *8*, 3314-3321.
156. Wang, H.; Akid, R. A room temperature cured sol-gel anticorrosion pre-treatment for Al 2024-T3 alloys. *Corrosion science* **2007**, *49*, 4491-4503.

157. Akid, R.; Wang, H.; Smith, T. ; Greenfield, D.; Earthman, J. Biological Functionalization of a Sol-Gel Coating for the Mitigation of Microbial-induced Corrosion. *Advanced functional materials* **2008**, *18*, 203-211.
158. Suleiman, R.; Gittens, J.; Khaled, M.; Smith, T. J.; Akid, R.; El Ali, B.; Khalil, A. Assessing the Anticorrosion and Antifouling Performances of a Sol–Gel Coating Mixed with Corrosion Inhibitors and Immobilised Bacterial Endospores. *Arab J Sci Eng* **2017**, *42*, 4327-4338.
159. Promvongsa, J.; Fungtammasan, B.; Gerard, G.; Saengkaew, S.; Vallikul, P. A Study on the Evaporation of Water-Ethanol Mixture Using Rainbow Refractometry. *Journal of Energy Resources Technology, Transactions of the ASME* **2017**, *139*.
160. Li, D.; Xu, F.; Liu, Z.; Zhu, J.; Zhang, Q.; Shao, L. The effect of adding PDMS-OH and silica nanoparticles on sol–gel properties and effectiveness in stone protection. *Applied Surface Science* **2013**, *266*, 368-374.
161. Chaurand, P.; Luetzenkirchen, F.; Spengler, B. Peptide and protein identification by matrix-assisted laser desorption ionization (MALDI) and MALDI-post-source decay time-of-flight mass spectrometry. *Journal of the American Society for Mass Spectrometry* **1999**, *10*, 91-103.
162. Wetzel, S. J.; Guttman, C. M.; Girard, J. E. The influence of matrix and laser energy on the molecular mass distribution of synthetic polymers obtained by MALDI-TOF-MS. *International Journal of Mass Spectrometry* **2004**, *238*, 215-225.
163. Yoo, H. J.; Kim, D. H.; Choi, Y. J.; Choi, J. H.; Park, M.; Shin, D.; Oh, Y.; Kim, Y.; Cho, K. Comparison of Matrices for Optimal Analysis of Synthetic Polymers Using MALDI-TOF Mass Spectrometry. *Mass Spectrometry Letters* **2020**, *11*, 77-81.
164. Liu, X. M.; Maziarz, E. P.; Heiler, D. J.; Grobe, G. L. Comparative studies of poly(dimethyl siloxanes) using automated GPC-MALDI-TOF MS and on-line GPC-ESI-TOF MS. *Journal of the American Society for Mass Spectrometry* **2003**, *14*, 195-202.
165. Zheng, Y.; He, L.; Asiamah, T. K.; Otto, M. Colonization of Medical Devices by Staphylococci. *Environmental microbiology* **2018**, *20*, 3141.
166. Pollitt, E. J. G.; Diggle, S. P. Defining motility in the Staphylococci. *Cellular and Molecular Life Sciences* **2017**, *74*, 2943.
167. Dima, A.; Carlsson, A.; Broo, K.; Arwin, H. Advanced substrates in sol-gel technology for MALDI mass spectrometry. *Proceedings of the International Semiconductor Conference, CAS* **2004**, *1*, 81-84.

168. Lin, Y. S.; Chen, Y. C. Laser desorption/ionization time-of-flight mass spectrometry on sol-gel-derived 2,5-dihydroxybenzoic acid film. *Analytical Chemistry* **2002**, *74*, 5793-5798.
169. Careri, M.; Elviri, L.; Lorenzi, A.; Mangia, A.; Penna, A.; Predieri, G. Improved silica xerogel film processing for MALDI-TOF-MS quantitative analysis of peptides and small molecules. *Journal of Sol-Gel Science and Technology* **2011**, *60*, 359-365.
170. Park, E. J.; Han, S. W.; Jeong, B.; Park, S. H.; Kim, Y. G.; Kim, Y. H.; Kim, Y. D. Effect of polydimethylsiloxane (PDMS) coating on TiO<sub>2</sub>-based MALDI matrix for dimethyl methylphosphonate (DMMP) analysis. *Applied Surface Science* **2015**, *353*, 342-349.
171. Falaize, S.; Radin, S.; Ducheyne, P. In vitro behavior of silica-based xerogels intended as controlled release carriers. *Journal of the American Ceramic Society* **1999**, *82*, 969-976.
172. Sayyed-Ahmad, A.; Khandelia, H.; Kaznessis, Y. N. Relative free energy of binding between antimicrobial peptides and SDS or DPC micelles. *Molecular Simulation* **2009**, *35*, 986-997.
173. Kłodzińska, S. N.; Pletzer, D.; Rahanjam, N.; Rades, T.; Hancock, R. E. W.; Nielsen, H. M. Hyaluronic acid-based nanogels improve in vivo compatibility of the anti-biofilm peptide DJK-5. *Nanomedicine: Nanotechnology, Biology and Medicine* **2019**, *20*, 102022.
174. Prokopowicz, M.; Szewczyk, A.; Łunio, R.; Sawicki, W. Monolithic polydimethylsiloxane-modified silica composites prepared by a low-temperature sol-gel micromolding technique for controlled drug release. *Reactive and Functional Polymers* **2017**, *114*, 136-145.
175. Kim, G.; Lee, D.; Moon, J.; Kim, J.; Park, J. Synthesis and Applications of TEOS/PDMS Hybrid Material by the Sol-gel Process. *Appl. Organometal. Chem.* **1999**, *13*, 361-372.
176. Loose, C.; Jensen, K.; Rigoutsos, I.; Stephanopoulos, G. LETTERS A linguistic model for the rational design of antimicrobial peptides. **2006**, *443*.
177. Huan, Y.; Kong, Q.; Mou, H.; Yi, H. Antimicrobial Peptides: Classification, Design, Application and Research Progress in Multiple Fields. *Frontiers in Microbiology* **2020**, *11*, 2559.
178. Yacoub, T.; Rima, M.; Karam, M.; Sabatier, J. M.; Fajloun, Z. Antimicrobials from Venomous Animals: An Overview. *Molecules* **2020**, *25*.

179. Kadaoluwa Pathirannahalage, S. P.; Meftahi, N.; Elbourne, A.; Weiss, A. C. G.; McConville, C. F.; Padua, A.; Winkler, D. A.; Costa Gomes, M.; Greaves, T. L.; Le, T. C.; Besford, Q. A.; Christofferson, A. J. Systematic Comparison of the Structural and Dynamic Properties of Commonly Used Water Models for Molecular Dynamics Simulations. *Journal of Chemical Information and Modeling* **2021**, *61*, 4521-4536.
180. Gerig, J. T. Further Efforts Toward a Molecular Dynamics Force Field for Simulations of Peptides in 40% Trifluoroethanol-Water. *Journal of Physical Chemistry B* **2015**, *119*, 5163-5175.
181. Amos, S. B. T. A.; Vermeer, L. S.; Ferguson, P. M.; Kozłowska, J.; Davy, M.; Bui, T. T.; Drake, A. F.; Lorenz, C. D.; Mason, A. J. Antimicrobial Peptide Potency is Facilitated by Greater Conformational Flexibility when Binding to Gram-negative Bacterial Inner Membranes. *Scientific Reports* **2016**, *6*, 1-13.
182. Manzo, G.; Ferguson, P. M.; Gustilo, V. B.; Hind, C. K.; Clifford, M.; Bui, T. T.; Drake, A. F.; Atkinson, R. A.; Sutton, J. M.; Batoni, G.; Lorenz, C. D.; Phoenix, D. A.; James Mason, A. Minor sequence modifications in temporin B cause drastic changes in antibacterial potency and selectivity by fundamentally altering membrane activity. *Scientific Reports* **2019**, *9*, 1-16.
183. Duclohier, H.; Molle, G.; Spach, G. Antimicrobial peptide magainin I from *Xenopus* skin forms anion-permeable channels in planar lipid bilayers. *Biophysical Journal* **1989**, *56*, 1017-1021.
184. Manzo, G.; Hind, C. K.; Ferguson, P. M.; Amison, R. T.; Hodgson-Casson, A. C.; Ciazynska, K. A.; Weller, B. J.; Clarke, M.; Lam, C.; Man, R. C. H.; Shaughnessy, B. G. O.; Clifford, M.; Bui, T. T.; Drake, A. F.; Atkinson, R. A.; Lam, J. K. W.; Pitchford, S. C.; Page, C. P.; Phoenix, D. A.; Lorenz, C. D.; Sutton, J. M.; Mason, A. J. A pleurocidin analogue with greater conformational flexibility, enhanced antimicrobial potency and in vivo therapeutic efficacy. *Communications Biology* **2020** *3:1* **2020**, *3*, 1-16.
185. Arouri, A.; Dathe, M.; Blume, A. Peptide induced demixing in PG/PE lipid mixtures: A mechanism for the specificity of antimicrobial peptides towards bacterial membranes? *Biochimica et Biophysica Acta (BBA) - Biomembranes* **2009**, *1788*, 650-659.
186. Henderson, J. M.; Waring, A. J.; Separovic, F.; Lee, K. Y. C. Antimicrobial Peptides Share a Common Interaction Driven by Membrane Line Tension Reduction. *Biophysical Journal* **2016**, *111*, 2176-2189.
187. Bechinger, B.; Lohner, K. Detergent-like actions of linear amphipathic cationic antimicrobial peptides. *Biochimica et Biophysica Acta (BBA) - Biomembranes* **2006**, *1758*, 1529-1539.

188. Alvares, D. S.; Wilke, N.; Ruggiero Neto, J. Effect of N-terminal acetylation on lytic activity and lipid-packing perturbation induced in model membranes by a mastoparan-like peptide. *Biochimica et Biophysica Acta (BBA) - Biomembranes* **2018**, *1860*, 737-748.
189. Li, D.; Yang, Y.; Li, R.; Huang, L.; Wang, Z.; Deng, Q.; Dong, S. N-terminal acetylation of antimicrobial peptide L163 improves its stability against protease degradation. *Journal of Peptide Science* **2021**, e3337.
190. B. Scott Perrin, J.; Tian, Y.; Fu, R.; Grant, C. V.; Chekmenev, E. Y.; Wieczorek, W. E.; Dao, A. E.; Hayden, R. M.; Burzynski, C. M.; Venable, R. M.; Sharma, M.; Opella, S. J.; Pastor, R. W.; Cotten, M. L. High-Resolution Structures and Orientations of Antimicrobial Peptides Piscidin 1 and Piscidin 3 in Fluid Bilayers Reveal Tilting, Kinking, and Bilayer Immersion. *Journal of the American Chemical Society* **2014**, *136*, 3491-3504.
191. Strandberg, E.; Horn, D.; Reißer, S.; Zerweck, J.; Wadhvani, P.; Ulrich, A. S. H-NMR and MD Simulations Reveal Membrane-Bound Conformation of Magainin 2 and Its Synergy with PGLa. *Biophysical journal* **2016**, *111*, 2149-2161.
192. Guilhelmelli, F.; Vilela, N.; Smidt, K. S.; Oliveira, M. A. d.; Álvares, A. d. C. M.; Rigonatto, M. C. L.; Costa, P. H. d. S.; Tavares, A. H.; Freitas, S. M. d.; Nicola, A. M.; Franco, O. L.; Derengowski, L. d. S.; Schwartz, E. F.; Mortari, M. R.; Bocca, A. L.; Albuquerque, P.; Silva-Pereira, I. Activity of Scorpion Venom-Derived Antifungal Peptides against Planktonic Cells of *Candida* spp. and *Cryptococcus neoformans* and *Candida albicans* Biofilms. *Frontiers in Microbiology* **2016**, *7*, 1844.
193. Neves, R. C. d.; Mortari, M. R.; Schwartz, E. F.; Kipnis, A.; Junqueira-Kipnis, A. P. Antimicrobial and Antibiofilm Effects of Peptides from Venom of Social Wasp and Scorpion on Multidrug-Resistant *Acinetobacter baumannii*. *Toxins* **2019**, *11*.
194. Tawfik, M. M.; Bertelsen, M.; Abdel-Rahman, M. A.; Strong, P. N.; Miller, K. Scorpion Venom Antimicrobial Peptides Induce Siderophore Biosynthesis and Oxidative Stress Responses in *Escherichia coli*. *mSphere* **2021**, *6*.
195. Ramirez, L. S.; Pande, J.; Shekhtman, A. Helical Structure of Recombinant Melittin. *Journal of Physical Chemistry B* **2019**, *123*, 356-368.
196. Gesell, J.; Zasloff, M.; Opella, S. J. Two-dimensional <sup>1</sup>H NMR experiments show that the 23-residue magainin antibiotic peptide is an  $\alpha$ -helix in dodecylphosphocholine micelles, sodium dodecylsulfate micelles, and trifluoroethanol/water solution. *Journal of Biomolecular NMR* **1997**, *9*, 127-135.
197. Timmons, P. B.; O'Flynn, D.; Conlon, J. M.; Hewage, C. M. Structural and positional studies of the antimicrobial peptide brevinin-1BYa in membrane-mimetic environments. *Journal of Peptide Science* **2019**, *25*.

198. Suh, J.; Lee, Y.; Park, C.; Lee, K.; Kim, S.; Choi, B. Structural and functional implications of a proline residue in the antimicrobial peptide gaegurin. *European Journal of Biochemistry* **1999**, *266*, 665-674.
199. Tuerkova, A.; Kabelka, I.; Králová, T.; Sukeník, L.; Pokorná, Š; Hof, M.; Vácha, R. Effect of helical kink in antimicrobial peptides on membrane pore formation. *eLife* **2020**, *9*.
200. Lee, J. K.; Gopal, R.; Park, S.; Ko, H. S.; Kim, Y.; Hahm, K.; Park, Y. A Proline-Hinge Alters the Characteristics of the Amphipathic  $\alpha$ -helical AMPs. *PLOS ONE* **2013**, *8*, e67597.
201. Yamaguchi, S.; Huster, D.; Waring, A.; Lehrer, R. I.; Kearney, W.; Tack, B. F.; Hong, M. Orientation and dynamics of an antimicrobial peptide in the lipid bilayer by solid-state NMR spectroscopy. *Biophysical Journal* **2001**, *81*, 2203.
202. Jeong, J. H.; Kim, J. S.; Choi, S. S.; Kim, Y. NMR Structural Studies of Antimicrobial Peptides: LPcin Analogs. *Biophysical Journal* **2016**, *110*, 423-430.
203. Strandberg, E.; Tremouilhac, P.; Wadhvani, P.; Ulrich, A. S. Synergistic transmembrane insertion of the heterodimeric PGLa/magainin 2 complex studied by solid-state NMR. *Biochimica et Biophysica Acta (BBA) - Biomembranes* **2009**, *1788*, 1667-1679.
204. Kawaguchi, K.; Suita, K.; Suzuki, Y.; Umemoto, K.; Nakazawa, Y.; Asakura, T. Orientation of the antimicrobial peptide, Cecropin A-Magainin 2 hybrid, in a lipid bilayer studied by  $^{15}\text{N}$  solid-state NMR. *Polymer Journal* **2005**, *37*, 229-233.
205. Reißer, S.; Strandberg, E.; Steinbrecher, T.; Elstner, M.; Ulrich, A. S. Best of Two Worlds? How MD Simulations of Amphiphilic Helical Peptides in Membranes Can Complement Data from Oriented Solid-State NMR. *J. Chem. Theory Comput* **2018**, *14*, 6002-6014.
206. Sohlenkamp, C.; Geiger, O. Bacterial membrane lipids: diversity in structures and pathways. *FEMS Microbiology Reviews* **2016**, *40*, 133-159.
207. Grage, S. L.; Afonin, S.; Kara, S.; Buth, G.; Ulrich, A. S. Membrane thinning and thickening induced by membrane-active amphipathic peptides. *Frontiers in Cell and Developmental Biology* **2016**, *4*, 65.
208. Chen, F. Y.; Lee, M. T.; Huang, H. W. Evidence for Membrane Thinning Effect as the Mechanism for Peptide-Induced Pore Formation. *Biophysical Journal* **2003**, *84*, 3751.

209. Sengupta, D.; Leontiadou, H.; Mark, A. E.; Marrink, S. J. Toroidal pores formed by antimicrobial peptides show significant disorder. *Biochimica et Biophysica Acta (BBA) - Biomembranes* **2008**, *1778*, 2308-2317.
210. Leontiadou, H.; Mark, A. E.; Marrink, S. J. Antimicrobial Peptides in Action. *Journal of the American Chemical Society* **2006**, *128*, 12156-12161.
211. Zhao, H.; Kinnunen, P. K. J. Binding of the antimicrobial peptide temporin L to liposomes assessed by Trp fluorescence. *Journal of Biological Chemistry* **2002**, *277*, 25170-25177.
212. Lam, Y. -.; Wassall, S. R.; Morton, C. J.; Smith, R.; Separovic, F. Solid-State NMR Structure Determination of Melittin in a Lipid Environment. *Biophysical journal* **2001**, *81*, 2752-2761.
213. Strahl, H.; Errington, J. Bacterial membranes: structure, domains, and function. *Annu. Rev. Microbiol.* **2017**, *71*, 519-538.
214. Isidro-Llobet, A.; Kenworthy, M. N.; Mukherjee, S.; Kopach, M. E.; Wegner, K.; Gallou, F.; Smith, A. G.; Roschangar, F. Sustainability Challenges in Peptide Synthesis and Purification: From R&D to Production. *The Journal of Organic Chemistry* **2019**, *84*, 4615-4628.
215. Glukhov, E.; Stark, M.; Burrows, L. L.; Deber, C. M. Basis for Selectivity of Cationic Antimicrobial Peptides for Bacterial Versus Mammalian Membranes. *Journal of Biological Chemistry* **2005**, *280*, 33960-33967.
216. Dathe, M.; Wieprecht, T. Structural features of helical antimicrobial peptides: their potential to modulate activity on model membranes and biological cells. *Biochimica et Biophysica Acta (BBA) - Biomembranes* **1999**, *1462*, 71-87.
217. Chen, X.; Zhang, L.; Wu, Y.; Wang, L.; Ma, C.; Xi, X.; Bininda-Emonds, O. R. P.; Shaw, C.; Chen, T.; Zhou, M. Evaluation of the bioactivity of a mastoparan peptide from wasp venom and of its analogues designed through targeted engineering. *International Journal of Biological Sciences* **2018**, *14*, 599.
218. Bommineni, Y. R.; Dai, H.; Gong, Y. X.; Soulages, J. L.; Fernando, S. C.; DeSilva, U.; Prakash, O.; Zhang, G. Fowlicidin-3 is an  $\alpha$ -helical cationic host defense peptide with potent antibacterial and lipopolysaccharide-neutralizing activities. *The FEBS Journal* **2007**, *274*, 418-428.
219. Qu, P.; Gao, W.; Chen, H.; Li, D.; Yang, N.; Zhu, J.; Feng, X.; Liu, C.; Li, Z. The central hinge link truncation of the antimicrobial peptide fowlicidin-3 enhances its cell selectivity without antibacterial activity loss. *Antimicrobial Agents and Chemotherapy* **2016**, *60*, 2798-2806.

220. Jiang, Z.; Vasil, A. I.; Hale, J. D.; Hancock, R. E. W.; Vasil, M. L.; Hodges, R. S. Effects of net charge and the number of positively charged residues on the biological activity of amphipathic  $\alpha$ -helical cationic antimicrobial peptides. *Peptide Science* **2008**, *90*, 369-383.
221. Ma, Y.; Yao, A.; Chen, X.; Wang, L.; Ma, C.; Xi, X.; Chen, T.; Shaw, C.; Zhou, M. Generation of truncated derivatives through in silico enzymatic digest of peptide GV30 target MRSA both in vitro and in vivo. *Computational and Structural Biotechnology Journal* **2021**, *19*, 4984-4996.
222. Greco, I.; Molchanova, N.; Holmedal, E.; Jensen, H.; Hummel, B. D.; Watts, J. L.; Håkansson, J.; Hansen, P. R.; Svenson, J. Correlation between hemolytic activity, cytotoxicity and systemic in vivo toxicity of synthetic antimicrobial peptides. *Scientific Reports* **2020**, *10*, 1-13.
223. Chen, S. P.; Chen, E. H. L.; Yang, S. Y.; Kuo, P. S.; Jan, H. M.; Yang, T. C.; Hsieh, M. Y.; Lee, K. T.; Lin, C. H.; Chen, R. P. Y. A Systematic Study of the Stability, Safety, and Efficacy of the de novo Designed Antimicrobial Peptide PepD2 and Its Modified Derivatives Against *Acinetobacter baumannii*. *Frontiers in Microbiology* **2021**, *12*, 1621.
224. Le, C. F.; Yusof, M. Y. M.; Hassan, H.; Sekaran, S. D. In vitro properties of designed antimicrobial peptides that exhibit potent antipneumococcal activity and produces synergism in combination with penicillin. *Scientific Reports* **2015**, *5*.
225. Virtanen, J. A.; Cheng, K. H.; Somerharju, P. Phospholipid composition of the mammalian red cell membrane can be rationalized by a superlattice model. *Biophysics Communicated by John A. Glomset* **1998**, *95*, 4964-4969.
226. Preta, G. New Insights Into Targeting Membrane Lipids for Cancer Therapy. *Frontiers in Cell and Developmental Biology* **2020**, *8*, 876.
227. Chiangjong, W.; Chutipongtanate, S.; Hongeng, S. Anticancer peptide: Physicochemical property, functional aspect and trend in clinical application (Review). *International Journal of Oncology* **2020**, *57*, 678-696.
228. Chen, Y.; Guarnieri, M. T.; Vasil, A. I.; Vasil, M. L.; Mant, C. T.; Hodges, R. S. Role of Peptide Hydrophobicity in the Mechanism of Action of  $\alpha$ -Helical Antimicrobial Peptides. *Antimicrobial Agents and Chemotherapy* **2007**, *51*, 1398.
229. Nguyen, L. T.; Haney, E. F.; Vogel, H. J. The expanding scope of antimicrobial peptide structures and their modes of action. *Trends in Biotechnology* **2011**, *29*, 464-472.

230. Mahlapuu, M.; Håkansson, J.; Ringstad, L.; Björn, C. Antimicrobial peptides: an emerging category of therapeutic agents. *Frontiers in cellular and infection microbiology* **2016**, 194.
231. Yasir, M.; Willcox, M. D. P.; Dutta, D. Action of Antimicrobial Peptides against Bacterial Biofilms. *Materials* **2018**, Vol. 11, Page 2468 **2018**, 11, 2468.
232. Rawson, K. M. Antimicrobial Peptides from Venom: Structure, Function and Toxicity, Sheffield Hallam University, 2019.
233. Sharma, A.; Gupta, P.; Kumar, R.; Bhardwaj, A. dPABBs: A Novel in silico Approach for Predicting and Designing Anti-biofilm Peptides. *Scientific Reports* **2016** 6:1 **2016**, 6, 1-13.
234. Ruhel, R.; Kataria, R. Biofilm patterns in gram-positive and gram-negative bacteria. *Microbiological Research* **2021**, 251, 126829.
235. Yu, W.; Hallinen, K. M.; Wood, K. B. Interplay between antibiotic efficacy and drug-induced lysis underlies enhanced biofilm formation at subinhibitory drug concentrations. *Antimicrobial Agents and Chemotherapy* **2018**, 62.
236. Bose, B.; Downey, T.; Ramasubramanian, A. K.; Anastasiu, D. C. Identification of Distinct Characteristics of Antibiofilm Peptides and Prospection of Diverse Sources for Efficacious Sequences. *Frontiers in Microbiology* **2022**, 12, 4409.
237. Baba, T.; Toshima, Y.; Minamikawa, H.; Hato, M.; Suzuki, K.; Kamo, N. Formation and characterization of planar lipid bilayer membranes from synthetic phytanyl-chained glycolipids. *Biochimica et Biophysica Acta (BBA) - Biomembranes* **1999**, 1421, 91-102.
238. Priel, A.; Gil, Z.; Moy, V. T.; Magleby, K. L.; Silberberg, S. D. Ionic Requirements for Membrane-Glass Adhesion and Giga Seal Formation in Patch-Clamp Recording. *Biophysical Journal* **2007**, 92, 3893-3900.
239. Findlay, H. E.; Booth, P. J. The folding, stability and function of lactose permease differ in their dependence on bilayer lipid composition. *Scientific Reports* **2017**, 7.
240. Gagnon, M. C.; Strandberg, E.; Grau-Campistany, A.; Wadhvani, P.; Reichert, J.; Bürck, J.; Rabanal, F.; Auger, M.; Paquin, J. F.; Ulrich, A. S. Influence of the Length and Charge on the Activity of  $\alpha$ -Helical Amphipathic Antimicrobial Peptides. *Biochemistry* **2017**, 56, 1680-1695.
241. Bouraguba, M.; Glattard, E.; Naudé, M.; Pelletier, R.; Aisenbrey, C.; Bechinger, B.; Raibaut, L.; Lebrun, V.; Faller, P. Copper-binding motifs Xxx-His or Xxx-Zzz-His (ATCUN) linked to an antimicrobial peptide: Cu-binding, antimicrobial activity and ROS production Copper-binding motifs Xxx-His or Xxx-Zzz-His (ATCUN) linked to an

- antimicrobial peptide: Cu-binding, antimicrobi. *Journal of Inorganic Biochemistry* **2018**.
242. Libardo, M. D.; Cervantes, J. L.; Salazar, J. C.; Angeles-Boza, A. M. Improved Bioactivity of Antimicrobial Peptides by Addition of Amino-Terminal Copper and Nickel (ATCUN) Binding Motifs. *ChemMedChem* **2014**, *9*, 1892-1901.
243. Simm, S.; Einloft, J.; Mirus, O.; Schleiff, E. 50 years of amino acid hydrophobicity scales: revisiting the capacity for peptide classification. *Biological Research* **2016**, *49*, 31.
244. Grauffel, C.; Yang, B.; He, T.; Roberts, M. F.; Gershenson, A.; Reuter, N. Cation- $\pi$  interactions as lipid specific anchors for phosphatidylinositol-specific phospholipase-C. *Journal of the American Chemical Society* **2013**, *135*, 5740.
245. Infield, D. T.; Rasouli, A.; Galles, G. D.; Chipot, C.; Tajkhorshid, E.; Ahern, C. A. Cation- $\pi$  Interactions and their Functional Roles in Membrane Proteins. *Journal of Molecular Biology* **2021**, *433*, 167035.
246. Waheed, Q.; Khan, H. M.; He, T.; Roberts, M.; Gershenson, A.; Reuter, N. Interfacial Choline-Aromatic Cation-Pi Interactions Can Contribute as Much to Peripheral Protein Affinity for Membranes as Aromatics Inserted Below the Phosphates. *ChemRxiv* **2019**.
247. Dougherty, D. A. Cation- $\pi$  Interactions Involving Aromatic Amino Acids. *The Journal of Nutrition* **2007**, *137*, 1504S-1508S.
248. Liu, L. P.; Deber, C. M. Uncoupling hydrophobicity and helicity in transmembrane segments.  $\alpha$ - helical propensities of the amino acids in non-polar environments. *Journal of Biological Chemistry* **1998**, *273*, 23645-23648.
249. Dathe, M.; Nikolenko, H.; Meyer, J.; Beyermann, M.; Bienert, M. Optimization of the antimicrobial activity of magainin peptides by modification of charge. *FEBS Letters* **2001**, *501*, 146-150.
250. Donghoon Oh; Song Yub Shin; Sangwon Lee; Joo Hyun Kang; Sun Don Kim; Pan Dong Ryu; Kyung-Soo Hahm; Yangmee Kim Role of the Hinge Region and the Tryptophan Residue in the Synthetic Antimicrobial Peptides, Cecropin A(1-8)-Magainin 2(1-12) and Its Analogues, on Their Antibiotic Activities and Structures. *Biochemistry* **2000**, *39*, 11855-11864.
251. Bi, X.; Wang, C.; Ma, L.; Sun, Y.; Shang, D. Investigation of the role of tryptophan residues in cationic antimicrobial peptides to determine the mechanism of antimicrobial action. **2013**.

252. Feng, X.; Jin, S.; Wang, M.; Pang, Q.; Liu, C.; Liu, R.; Wang, Y.; Yang, H.; Liu, F.; Liu, Y. The Critical Role of Tryptophan in the Antimicrobial Activity and Cell Toxicity of the Duck Antimicrobial Peptide DCATH. *Frontiers in Microbiology* **2020**, *11*, 1146.
253. Bright, J. N.; Sansom, M. S. P. The flexing/twirling helix: Exploring the flexibility about molecular hinges formed by proline and glycine motifs in transmembrane helices. *Journal of Physical Chemistry B* **2003**, *107*, 627-636.
254. Crusca, E.; Rezende, A. A.; Marchetto, R.; Mendes-Giannini, M. J. S.; Fontes, W.; Castro, M. S.; Cilli, E. M. Influence of N-terminus modifications on the biological activity, membrane interaction, and secondary structure of the antimicrobial peptide hylin-a1. *Peptide Science* **2011**, *96*, 41-48.
255. Kim, Y.; Hahm, K. S.; Lee, D.; Lee, M.; Lee, S. H.; Kim, J.; Song, W.; Eom, S.; Park, E.; Yang, S. T.; Shin, S. Antibacterial, antitumor and hemolytic activities of  $\alpha$ -helical antibiotic peptide, P18 and its analogs. *The Journal of Peptide Research* **2001**, *58*, 504-514.
256. Wei, H.; Xie, Z.; Tan, X.; Guo, R.; Song, Y.; Xie, X.; Wang, R.; Li, L.; Wang, M.; Zhang, Y. Temporin-Like Peptides Show Antimicrobial and Anti-Biofilm Activities against *Streptococcus mutans* with Reduced Hemolysis. *Molecules* **2020**, *25*.
257. Zhu, N.; Zhong, C.; Liu, T.; Zhu, Y.; Gou, S.; Bao, H.; Yao, J.; Ni, J. Newly designed antimicrobial peptides with potent bioactivity and enhanced cell selectivity prevent and reverse rifampin resistance in Gram-negative bacteria. *European Journal of Pharmaceutical Sciences* **2021**, *158*, 105665.
258. Wang, G.; Mechesso, A. F. Realistic and critical review of the state of systemic antimicrobial peptides. *ADMET & DMPK* **2022**, *10*, 91.
259. Jafari, F.; Elyasi, S. Prevention of colistin induced nephrotoxicity: a review of preclinical and clinical data. *Expert Rev Clin Pharmacol* **2021**, *14*, 1113-1131.
260. Benito, N.; Franco, M.; Ribera, A.; Soriano, A.; Rodriguez-Pardo, D.; Sorlí, L.; Fresco, G.; Fernández-Sampedro, M.; Dolores del Toro, M.; Guío, L.; Sánchez-Rivas, E.; Bahamonde, A.; Riera, M.; Esteban, J.; Baraia-Etxaburu, J. M.; Martínez-Alvarez, J.; Jover-Sáenz, A.; Dueñas, C.; Ramos, A.; Sobrino, B.; Euba, G.; Morata, L.; Pigrau, C.; Coll, P.; Mur, I.; Ariza, J.; Barcenilla, F.; Pérez-Villar, F.; Prats-Gispert, L.; Cisterna, R.; Ibarra, S.; López; Santamaría, J. M.; Cabo, J.; García, D.; Lora-Tamayo, J.; Murillo, O.; Pedrero, S.; Álvarez-Parrondo, S.; Muedra-Font, R.; Raya-Fernández, C.; Rodríguez-Alonso, C.; Moreno, A.; Blanco-Martínez-de-Morentin, M. A.; Cabo-Magadan, R.; Combalia, A.; García, S.; Martínez-Pastor, J. C.; Tornero, E.; Merino-Pérez, J.; Montejo, J. M.; Alier, A.; Horcajada, J. P.; Plasencia, V.; Puig, L.; Auñón; Blanco, A.; García-Cañete, J.; Sandoval, E.; Fakkas-Fernández, M.; Garcés-Zarzalejo, C.; Fariñas-Alvarez, C.; Fariñas, M. C.; Martinez-Martinez, L.; Salas-Venero, C.; Cobo, J.; Ruiz-Carbajosa, P.; Jordán, M.; Crusi, X.; Marinescu, C.;

- Montaner, F.; Ramírez, A.; Corona, P. S.; Lung, M.; Muniain-Ezcurra, M.; Peñas-Espinar, C.; Suárez, A. I.; Álvarez, R.; Cordero, J. A.; López-Pliego, M.; Palomino, J.; Puente, A. Time trends in the aetiology of prosthetic joint infections: a multicentre cohort study. *Clinical Microbiology and Infection* **2016**, *22*, 732.e1-732.e8.
261. Marrs, C. F.; Zhang, L.; Foxman, B. Escherichia coli mediated urinary tract infections: Are there distinct uropathogenic E. coli (UPEC) pathotypes? *FEMS Microbiology Letters* **2005**, *252*, 183-190.
262. Lachance, C. C.; Grobelna, A. Management of Patients with Long-Term Indwelling Urinary Catheters: A Review of Guidelines. *Canadian Agency for Drugs and Technologies in Health* **2019**, 1-25.
263. NICE Antimicrobial dressings | Wound management .  
<https://bnf.nice.org.uk/wound-management/antimicrobial-dressings/>.
264. Azolin, D. R.; Moro, C. C.; Costa, T. M. H.; Benvenuti, E. V. Effects of organic content and H<sub>2</sub>O/TEOS molar ratio on the porosity and pore size distribution of hybrid naphthaleneaminepropylsilica xerogel. *Journal of Non-Crystalline Solids* **2004**, *337*, 201-206.
265. Kortesuso, P.; Ahola, M.; Kangas, M.; Jokinen, M.; Leino, T.; Vuorilehto, L.; Laakso, S.; Kiesvaara, J.; Yli-Urpo, A.; Marvola, M. Effect of synthesis parameters of the sol-gel-processed spray-dried silica gel microparticles on the release rate of dexmedetomidine. *Biomaterials* **2002**, *23*, 2795-2801.
266. Zhu, X.; Tang, W.; Cheng, X.; Wang, H.; Sang, T.; Ye, Z. Roles of Self-Assembly and Secondary Structures in Antimicrobial Peptide Coatings. *Coatings* **2022**, *12*, 1456.
267. Delfino, I.; Portaccio, M.; Ventura, B. D.; Mita, D. G.; Lepore, M. Enzyme distribution and secondary structure of sol-gel immobilized glucose oxidase by micro-attenuated total reflection FT-IR spectroscopy. *Materials Science and Engineering: C* **2013**, *33*, 304-310.
268. Biswaro, L. S.; Sousa, M. G. d. C.; Rezende, T. M. B.; Dias, S. C.; Franco, O. L. Antimicrobial peptides and nanotechnology, recent advances and challenges. *Frontiers in Microbiology* **2018**, *9*, 855.
269. Kłodzińska, S. N.; Wan, F.; Jumaa, H.; Sternberg, C.; Rades, T.; Nielsen, H. M. Utilizing nanoparticles for improving anti-biofilm effects of azithromycin: A head-to-head comparison of modified hyaluronic acid nanogels and coated poly (lactic-co-glycolic acid) nanoparticles. *Journal of Colloid and Interface Science* **2019**, *555*, 595-606.
270. Strandberg, E.; Tremouilhac, P.; Wadhwani, P.; Ulrich, A. S. Synergistic transmembrane insertion of the heterodimeric PGLa/magainin 2 complex studied

by solid-state NMR. *Biochimica et Biophysica Acta (BBA) - Biomembranes* **2009**, *1788*, 1667-1679.

271. Strandberg, E.; Horn, D.; Reißer, S.; Zerweck, J.; Wadhvani, P.; Ulrich, A. S. Article 2 H-NMR and MD Simulations Reveal Membrane-Bound Conformation of Magainin 2 and Its Synergy with PGLa. **2016**.
272. Yeaman, M. R.; Gank, K. D.; Bayer, A. S.; Brass, E. P. Synthetic Peptides That Exert Antimicrobial Activities in Whole Blood and Blood-Derived Matrices. *Antimicrobial Agents and Chemotherapy* **2002**, *46*, 3883.
273. Nguyen, L. T.; Chau, J. K.; Perry, N. A.; de Boer, L.; Zaat, S. A. J.; Vogel, H. J. Serum Stabilities of Short Tryptophan- and Arginine-Rich Antimicrobial Peptide Analogs. *PLoS ONE* **2010**, *5*, 1-8.
274. Lu, J.; Xu, H.; Xia, J.; Ma, J.; Xu, J.; Li, Y.; Feng, J. D- and Unnatural Amino Acid Substituted Antimicrobial Peptides With Improved Proteolytic Resistance and Their Proteolytic Degradation Characteristics. *Frontiers in Microbiology* **2020**, *11*, 2869.
275. Li, D.; Yang, Y.; Li, R.; Huang, L.; Wang, Z.; Deng, Q.; Dong, S. N-terminal acetylation of antimicrobial peptide L163 improves its stability against protease degradation. *Journal of peptide science : an official publication of the European Peptide Society* **2021**, *27*.
276. Andes, D. R.; Lepak, A. J. In vivo infection models in the pre-clinical pharmacokinetic/pharmacodynamic evaluation of antimicrobial agents. *Current Opinion in Pharmacology* **2017**, *36*, 94-99.
277. Narayana, J. L.; Mishra, B.; Lushnikova, T.; Wu, Q.; Chhonker, Y. S.; Zhang, Y.; Zarena, D.; Salnikov, E. S.; Dang, X.; Wang, F.; Murphy, C.; Foster, K. W.; Gorantla, S.; Bechinger, B.; Murry, D. J.; Wang, G. Two distinct amphipathic peptide antibiotics with systemic efficacy. *Proceedings of the National Academy of Sciences of the United States of America* **2020**, *117*, 19446-19454.
278. Reinhardt, A.; Neundorff, I. Design and Application of Antimicrobial Peptide Conjugates. *International Journal of Molecular Sciences* **2016**, *17*.